

# **Structural investigations of isolated neutral molecules, aggregates and metal complexes in molecular beams**

Vom Fachbereich Chemie der Technischen Universität Kaiserslautern zur  
Verleihung des akademischen Grades “Doktor der Naturwissenschaften”  
genehmigte Dissertation

D 386



vorgelegt von

M. Sc. Pol Boden

geboren in Luxemburg-Stadt

Tag der wissenschaftlichen Aussprache: 28.07.2022

Betreuer: Priv.-Doz. Dr. Christoph Riehn  
Prof. Dr. Markus Gerhardt†



Die vorliegende Arbeit wurde im Zeitraum von Oktober 2018 bis Juni 2022 im Fachbereich Chemie der Technischen Universität Kaiserslautern unter Betreuung von Prof. Dr. Markus Gerhardt† und Priv.-Doz. Dr. Christoph Riehn angefertigt.

Datum des Antrags der Eröffnung des Promotionsverfahrens: 21.06.2022

Datum der wissenschaftlichen Aussprache: 28.07.2022

Promotionskommission:

Vorsitzender	Prof. Dr. Werner R. Thiel
1. Berichterstatter	Priv.-Doz. Dr. Christoph Riehn
2. Berichterstatterin	Jun.-Prof. Dr. Jennifer D. Meyer





### **Eidesstattliche Erklärung:**

Hiermit bestätige ich, Pol Jean Boden, dass ich die vorliegende Arbeit gemäß der Promotionsordnung des Fachbereichs Chemie der Technischen Universität Kaiserslautern selbstständig verfasst habe und nur die angegebenen Quellen und Hilfsmittel verwendet wurden.

Kaiserslautern, im Juli 2022

Pol Jean Boden



***„Ich will euch mein Erfolgsrezept verraten: Meine ganze Kraft ist nichts als Ausdauer.“***

Louis Pasteur



## **Mein besonderer Dank gilt...**

...Herrn Priv.-Doz. Dr. Christoph Riehn für die Betreuung während der abschließenden Phase meiner Promotion, für die Unterstützung des ehemaligen AK Gerhards, für die konstruktiven „Flur-Gespräche“ und für den ergiebigen Freiraum bei der wissenschaftlichen Arbeit.

...Frau Jun.-Prof. Dr. Jennifer D. Meyer für die Übernahme des Zweitgutachtens und ebenso für die Unterstützung des ehemaligen AK Gerhards.

...Herrn Prof. Dr. Werner R. Thiel für die Übernahme des Vorsitzes der Prüfungskommission.

...meinem leider viel zu früh verstorbenen ehemaligen Betreuer Prof. Dr. Markus Gerhards für die freundliche Aufnahme in seine Arbeitsgruppe und die stete (abendliche) Diskussionsbereitschaft.

...meinem Kollegen Patrick Strebert für die hervorragende Teamarbeit im Gasphasenlabor, auch wenn es mal nicht so lief wie erwünscht.

...Dr. Kirsten Schwing für das Korrekturlesen dieser Arbeit, für die Unterstützung bei organisatorischen/verwaltungstechnischen Angelegenheiten und für Ihre Diskussionsbereitschaft.

...allen einstigen und aktuellen Mitarbeitern des ehemaligen Arbeitskreises Gerhards für das angenehme Arbeitsklima. An der Stelle möchte ich mich insbesondere bei den verbleibenden Doktoranden Patrick Strebert, Sophie Steiger, Daniel Marhöfer und meinem Bruder (Dr.) Pit Boden für die schöne gemeinsame Zeit bedanken.

...Dr. Fabian Dietrich für sein sehr engagiertes Mitarbeiten an den Dispersions-Projekten, auch lange nach seiner Zeit in Kaiserslautern.

...der „alten Garde“ des Gasphasenlabors mit Dr. Markus Becherer, Dr. Dominic Bernhard und Dr. Dominique Maué für die detaillierte Einführung in die Gebiete der anspruchsvollen Molekularstrahlapparaturen und der Lasertechnik.

...Michael Borchers und Marcel Meta für ihre tatkräftige Unterstützung während ihrer Zeit als Masteranden.

...den AKs GNS, Riehn und Meyer für die angenehme Atmosphäre auf dem „PC“-Flur.

...Frau Stemler, Frau Wetzler und Frau Heieck für die Unterstützung bei verwaltungstechnischen Angelegenheiten.

...dem Chemikalienlager für das nette Entgegenkommen, vor allem für das Ausgeben von Chemikalien außerhalb der regulären Öffnungszeiten.

...der Deutschen Forschungsgemeinschaft (DFG) für die finanzielle Unterstützung.

...meinen Eltern für die zuverlässige Unterstützung außerhalb der Uni. Dies gab mir die Möglichkeit während Jahren nahezu vollständig in der (physikalischen) Chemie zu versinken!

...meinem Zwillingbruder (Dr.) Pit Boden für den großen Zusammenhalt während Studium und Promotion.

....allen, die ich in dieser Auflistung vergessen haben sollte.



## Table of contents

1	Introduction.....	1
2	Spectroscopic methods .....	6
2.1	R2PI spectroscopy.....	6
2.2	IR/R2PI spectroscopy .....	8
2.3	IR <sub>fixed</sub> /IR/R2PI Spectroscopy .....	10
2.4	UV/IR/UV Spectroscopy .....	11
2.5	IR(M)PD Spectroscopy .....	12
2.6	UV/UV/IR spectroscopy .....	13
3	Experimental setups.....	14
3.1	Laser systems .....	14
3.1.1	UV laser setups .....	14
3.1.2	IR laser setups.....	15
3.2	Molecular beam technique.....	17
3.3	Experiments with thermal sources – molecular beam apparatus (I).....	19
3.4	Laser desorption experiments – molecular beam apparatus (II).....	23
3.4.1	Introduction .....	23
3.4.2	History of the laser desorption technique.....	23
3.4.3	The laser desorption process – physical aspects.....	25
3.4.4	Molecular beam apparatus (II) with implemented laser desorption source.....	26
4	Theoretical methods .....	38
4.1	Density Functional Theory (DFT).....	38
4.2	<i>Ab initio</i> methods.....	41
4.2.1	Coupled-Cluster Methods.....	41
4.2.2	Algebraic Diagrammatic Construction (ADC) Methods .....	43
5	Results and discussion.....	44
5.1	Laser desorption experiments .....	44
5.1.1	Successful implementation of R2PI- and IR/R2PI experiments .....	45
5.1.2	Investigations on isolated contact ion pairs (CIPs) .....	55
5.1.2.1	Introduction.....	55
5.1.2.2	Isolated alkali/ <i>para</i> -aminobenzoate contact ion pairs in gas phase: insights into nuclear and electronic structure by laser spectroscopy (see manuscript draft [1]) .....	58
5.1.2.3	Metal <i>para</i> -aminobenzoate complexes with divalent metal centers (Mg <sup>2+</sup> , Ca <sup>2+</sup> and Ba <sup>2+</sup> )	66
5.1.2.4	Alkali <i>para</i> -methoxybenzoate (M <sup>+</sup> PMBA <sup>-</sup> ) and alkali benzoate (M <sup>+</sup> BA <sup>-</sup> ) ion pairs	68

5.1.2.5	Investigations on the metal complex tris(8-hydroxyquinolato)aluminium.....	80
5.2	Non-covalent interactions .....	82
5.2.1	Introduction .....	82
5.2.2	Chromone–methanol cluster in the electronic ground and lowest triplet state: A delicate interplay of non-covalent interactions (see publication [2]).....	85
5.2.3	AcTyr(Me)OMe–methanol cluster .....	87
5.3	Metal ion–peptide interactions .....	93
5.3.1	Introduction .....	93
5.3.2	Theoretical and Spectroscopic Investigations on Monovalent Cationic Metal–AcTrpOMe Clusters in the Gas Phase (see manuscript draft [3]) .....	95
6	References.....	98
7	Publications and manuscript drafts.....	107
7.1	Manuscript draft [1].....	107
7.2	Publication [2].....	146
7.3	Manuscript draft [3].....	177
8	Summary and Outlook.....	237
9	Zusammenfassung und Ausblick .....	243



# 1 Introduction

The present work deals with the laser spectroscopic structural analysis of neutral isolated molecules, aggregates and metal complexes in the gas phase under molecular beam conditions. Spectroscopic investigations on isolated compounds enable the characterization of the intrinsic properties of a specific species without environmental effects. On top of that, *e.g.* the effects of a stepwise microsolvation of a compound can also be probed by successively adding solvent molecules to an analyte by application of a supersonic coexpansion (*e.g.* <sup>[1,2]</sup>). In such gas phase studies, the main focus is commonly put on the structure elucidation of the respective species, since there is a tight relation between structure and functionality of a compound. As presented further down in the text and in figure 1, different types of molecular systems are of interest in this thesis, with the structure-function relationship playing a key role across all task areas.

Furthermore, the cold isolated conditions reached in molecular beams, in cryo-cooled ion traps or in helium droplets have the advantage that (in absence of any kinetic trapping effects) the chosen analyte is cooled down to its lowest vibrational (and rotational) levels. Additionally, the occurrence of hot bands in the vibrational and vibronic spectra is avoided (see subchapter 3.2). Likewise, if compounds of high conformational flexibility are studied, merely the most stable conformers are populated. This leads to less crowded spectra, which facilitates interpretation of the results.

Within studies on charged compounds, an isolated gas phase analyte is most frequently generated by applying an electrospray ionization (ESI) source (*e.g.* <sup>[3,4]</sup>) or a laser vaporization (LVAP) source (*e.g.* <sup>[5,6]</sup>). Alternatively, isolated ions can be obtained *via* laser-induced liquid bead ion desorption (LILBID)<sup>[7]</sup>, matrix-assisted laser desorption/ionization (MALDI)<sup>[8]</sup>, desorption electrospray ionization (DESI)<sup>[9]</sup>, direct analysis in real time (DART)<sup>[10]</sup> or atmospheric-pressure solids analysis probe (ASAP)<sup>[11]</sup>. Few studies report on the desorption of initially neutral molecules from a surface by using a so-called ultrasonic cutter, prior to ionization of the analyte by a dielectric barrier discharge (DBD) ion source.<sup>[12]</sup> For the investigation of neutral isolated compounds *via* laser spectroscopy, however, thermal molecular beam sources are most commonly applied. In case of neutral compounds of high molecular weight, insufficient vapor pressure and/or limited thermal stability, such as larger biomolecules (*e.g.* <sup>[13]</sup>), ion pairs (*e.g.* <sup>[14,15]</sup>) and transition metal complexes<sup>[16]</sup>, laser desorption sources could be a valid alternative. The laser desorption technique with all its variants is introduced in subchapter 3.4.2 of this work. Optionally, the rather unique so-called Laser-induced acoustic desorption (LIAD) technique<sup>[17]</sup> might be applied, which was specifically developed to transfer thermally labile neutral molecules into the gas phase.

At this point, it should also be noted that neutral species cannot be analyzed by applying setups with cold ion traps. Hence, molecular beam machines are ideal tools for this purpose.

In the studies presented here, insights regarding structures and electronic properties of the investigated systems are obtained by applying UV as well as combined IR/UV laser spectroscopic methods in molecular beam experiments. With the applied techniques, the electronic and ionic ground states ( $S_0$  and  $D_0$ ) as well as electronically excited states ( $S_1$  or  $T_1$ ) can be probed. A comparison of the recorded experimental spectra with geometries and harmonic vibrational frequencies predicted by quantum chemical simulations (mainly density functional theory (DFT) calculations) enables clear structural assignments as well as a deeper understanding of electronic effects. In the projects presented in this work, the respective theoretical analyses were either performed by other group members (for the aromatic molecule–solvent aggregates) or by myself (regarding metal–amino acid aggregates and all projects related to laser desorption).

Basically, the present thesis can be subdivided into three distinct task areas, as illustrated in figure 1 below.

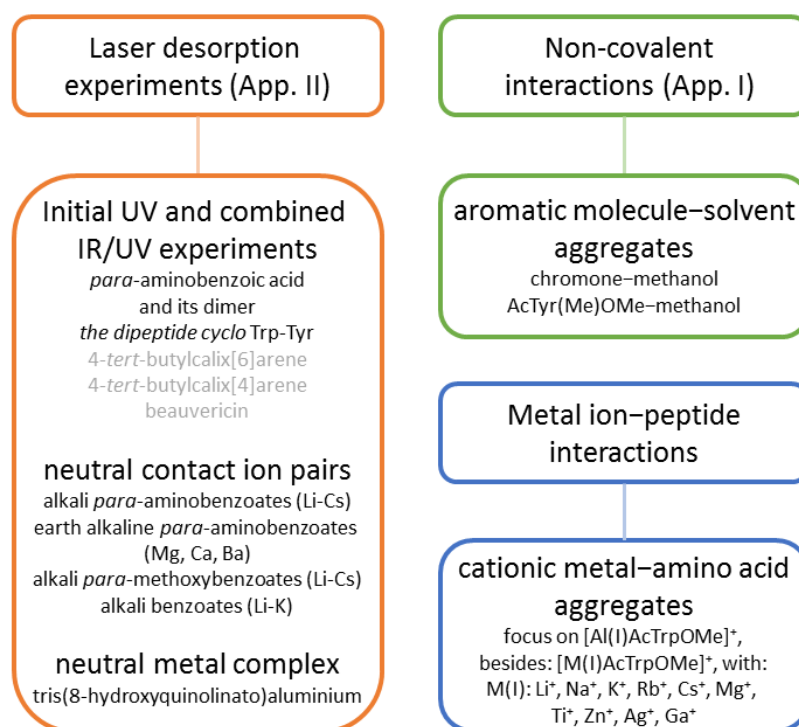


Figure 1: Topics covered in the present thesis, with the three main task areas highlighted in orange (Laser desorption experiments), green (Experiments with thermal source) and blue (Quantum chemical simulations). For each subproject, the investigated compounds are indicated in smaller font.

Beforehand, it should also be mentioned that experiments with two independent molecular beam machines (named apparatus (I) and apparatus (II) in the following) were performed. As indicated in

figure 1, all laser desorption experiments were performed using apparatus (II), while the studies on aromatic molecule–solvent aggregates were carried out with apparatus (I), featuring a thermal molecular beam source.

The applied laser desorption setup had been developed and implemented into apparatus (II) by the former group member Dr. Markus Becherer<sup>[18]</sup>. However, at the beginning of this thesis, the experimental achievements were still limited to at most some mass spectra. Hereby, the ion signal intensity and stability were inadequate for any valuable spectroscopic studies. Therefore, some crucial experimental refinements were required, which could finally be realized during the work described in the present thesis. All optimization steps are discussed together with the whole experimental setup in subchapter 3.4.4. On that basis, initial UV and combined IR/UV experiments could be performed. Hereby, various compounds were investigated (see figure 1) with a focus on the improvement of the setup rather than on the characterization of the analytes. At this point, it is to note that highly resolved spectra were obtained, emphasizing the successful optimization of all relevant parameters.

After these initial experiments the focus was put on the investigation of neutral isolated contact ion pairs. Studies on neutral ion pairs consist of a still new field in molecular beam spectroscopy, which is of interest due to the huge relevance of ion pairs in nature (*e.g.* <sup>[19,20]</sup>), in therapeutics (*e.g.* <sup>[21,22]</sup>) or in organic synthesis (*e.g.* <sup>[23,24]</sup>). Therefore, it is not surprising that ion pairs have already been studied in depth, predominantly *via* experiments in condensed media. However, spectroscopic investigations on isolated ion pairs in solution have the disadvantage that different types of ion pairs, *i.e.*, contact ion pairs (CIPs, without any solvent molecules separating cation and anion)<sup>[25]</sup>, solvent-shared ion pairs (SIPs, with a single solvent layer between cation and anion)<sup>[25]</sup> and solvent-separated ion pairs (SSIPs, with intact primary solvation shells around both counterions)<sup>[25]</sup> may coexist. This limitation can be overcome by probing free ion pairs in the gas phase. In that manner, the intrinsic properties of isolated CIPs can be elucidated. Even so, only a few studies on isolated contact ion pairs have been published up to now. This may be partly explained by the fact that most ion pairs (salts) cannot be transferred into the gas by simple heating. Yet, laser desorption sources, like the one applied in this work, are ideally suited for this purpose. In this work various sorts of ion pairs were investigated (see figure 1), whereby the main focus was put on the alkali (Li-Cs) *para*-aminobenzoates. Within that, the influence of the size of the alkali ion on the structural and electronic behavior of the *para*-aminobenzoate chromophore was followed in detail. These investigations are further motivated in subchapter 5.1.2.1, while the results are discussed in subchapter 5.1.2.2 and in publication draft [1]. For comparison, the alkali (Li-Cs) *para*-methoxybenzoates and unsubstituted alkali (Li-K) benzoates were also probed, revealing further information, especially regarding the (photo)stability of isolated ion pairs. In order to increase molecular complexity and find model systems for neutral metal complexes in the gas phase, investigations of the earth alkaline *para*-aminobenzoates (comprising two *para*-aminobenzoate

ligands coordinated to the divalent metal center) were performed. In a further pilot experiment, the neutral OLED-relevant (OLED: organic light emitting diode) complex tris(8-hydroxyquinolino)aluminium (Alq<sub>3</sub>) was successfully desorbed, photoionized and subsequently detected in the mass spectrometer.

In the second part of this work, aromatic molecule–solvent aggregates were analyzed with regard to non-covalent (mainly dispersion) interactions. The attractive London dispersion interactions<sup>[26,27]</sup> are part of the long-range van der Waals interactions,<sup>[28]</sup> together with the also attractive inductive Debye interactions<sup>[29]</sup> and the ambivalent Keesom (dipole–dipole) forces.<sup>[30]</sup> As these interactions exhibit an  $1/r^6$  dependence, with  $r$  being the distance separating two interacting atoms or molecules, van der Waals interactions are of particular relevance in larger molecules.<sup>[31,32]</sup> London dispersion forces may be considered as weak, but their importance successively grows with increasing system size. In fact, dispersion interactions can already be decisive for the structure of medium-sized molecules or aggregates (*e.g.* <sup>[31,33,34]</sup>). Thus, a deeper understanding of dispersion forces and their interplay with other non-covalent interactions is crucially needed. Molecular beam experiments on isolated weakly bound aggregates, in combination with thorough computational studies, should contribute to a better understanding of London dispersion forces and their delicate interplay with other inter- or intramolecular interactions. Furthermore, the experimental results obtained for isolated aromatic molecule–solvent aggregates are ideally suited as benchmark values for theoretical methods, often struggling to describe non-covalent interactions. Over the last few years, ketone solvation balances were in the focus of these studies.<sup>[35–37]</sup> Herein, complexes formed between (mainly aromatic) ketones, exhibiting two very similar free electron lone pairs as docking sites, and various alcohols were investigated. Within this context, the chromone–methanol complex was analyzed in this work. For this system, a tight competition between two distinct isomers, stabilized *via* distinct CH $\cdots$ O contacts, was observed. Up to that point, all published studies on ketone solvation balances were limited to clusters in their electronic ground state. For chromone–methanol, however, the electronic ground and electronically excited states were probed. Most interestingly, the chromone unit undergoes a fast and efficient intersystem crossing (ISC) into the triplet manifold upon electronic excitation,<sup>[38]</sup> which also occurs for the respective methanol clusters. Thus, the performed studies on non-covalent interactions could for the first time be extended to an aromatic molecule–solvent aggregate in an electronically excited triplet state. This study is further introduced in subchapters 5.2.1 and 5.2.2, while the obtained results are discussed in detail in publication [2].

In addition, investigations on the aggregation behavior between the protected amino-acid AcTyr(Me)OMe and methanol as solvent were performed. Such protected amino acids, exhibiting various potential binding motifs and sites for an alcohol molecule, are ideally suited to probe peptide

backbone solvations.<sup>[41]</sup> At the same time, AcTyr(Me)OMe–methanol is another convenient system to probe the delicate interplay between competing non-covalent interactions. The experimental results obtained for AcTyr(Me)OMe–methanol are discussed in subchapter 5.2.3, together with the predictions from DFT simulations.

The last part of this work deals with the topic of metal ion–protein interactions. At first instance, the structure of proteins primarily depends on the amino acid sequence in the protein chain. However, several proteins found in nature bind to cofactors (*e.g.* solvent molecules or metal cations), which often have a crucial influence on their conformation and functionality.<sup>[39–41]</sup> In particular, it is to note that almost half of all natural proteins bind to metal atoms, whereby the formed metalloproteins<sup>[41,42]</sup> frequently play a decisive role in biological processes (*e.g.* <sup>[42]</sup>). Despite this, the specific role of metallic cofactors is still not well understood for many biochemical reactions. Therefore, a so-called bottom-up approach, starting with structural investigations on small isolated metal ion–amino acid aggregates, can be a valuable approach towards a better understanding of metal ion–protein interactions.<sup>[39,40,42]</sup> In this context, the [AlAcTrpOMe]<sup>+</sup> cluster, formed by complexation between the protected amino acid AcTrpOMe and a monovalent aluminium ion (Al<sup>+</sup>), was investigated here. For this adduct, an extensive conformational search was performed at the DFT level, followed by harmonic vibrational frequency calculations. The obtained predictions were further underpinned by simulations at coupled cluster level (DLPNO-CCSD(T)). Additional DFT calculations for aggregates with other monovalent metal ions were also performed, emphasizing the features that are unique to the Al<sup>+</sup> species. Finally, the theoretical outcome was discussed in combination with experimental results achieved by former group members. The project is further discussed in subchapter 5.3, as well as in manuscript draft [3].

## 2 Spectroscopic methods

In the following subchapters the UV and combined IR/UV laser spectroscopic techniques applied in this work are presented. For better understanding, all methods are illustrated on the basis of simplified term schemes.

All these techniques belong to so-called action spectroscopy<sup>[43]</sup>, where, in contrast to transmission spectroscopy (such as FTIR spectroscopy), the effects of light excitation are detected indirectly by recording *e.g.* the intensity of mass signals as function of laser wavelength. With this approach, the sensitivity towards spectroscopic effects is considerably increased, which is a significant advantage regarding the extremely low sample density in molecular beams.

### 2.1 R2PI spectroscopy

The Resonant two-photon Ionization (R2PI) technique<sup>[44]</sup> provides information about the (vertical) excitation energies into the electronically excited state ( $S_n$ ) (most often the first excited singlet state ( $S_1$ )) as well as the low frequency vibrational modes of this electronically excited state.

The R2PI technique is a UV-spectroscopic method where the absorption of a first UV photon leads to electronic excitation into an electronically excited singlet state ( $S_n$ ) (generally the  $S_1$  state). Upon absorption of a second UV photon within the lifetime of the electronically excited state the molecule is ionized. The singly ionized molecule or aggregate is then detected in a time-of-flight (TOF) mass spectrometer, where the measured time-of-flight correlates with the mass-to-charge ratio  $m/z$  of the species:  $TOF \sim \sqrt{m/z}$ . The described resonant two-photon ionization process is particularly efficient if the vibrational ground state or a higher vibrational level of this electronically excited state is resonantly reached upon electronic excitation.

An R2PI process can principally be isomer-selective if two isomers of a compound exhibit different electronic excitation energies. This ideally leads to distinct peaks in the R2PI spectrum, which is obtained by recording the ion signal intensity as function of the UV excitation laser wavelength. Thus, an R2PI process is basically mass-selective and, if different isomers exhibit distinct electronic excitation energies, also isomer-selective. The mass-selectivity is a significant advantage compared to the alternative laser-induced fluorescence (LIF) technique<sup>[45,46]</sup>. However, one should notice that, especially if clusters are investigated, the R2PI spectrum recorded on a certain mass trace can likely be affected by UV fragmentation of larger aggregates upon their electronic excitation and ionization. This means that the R2PI spectrum recorded for a specific cluster can thus show (often broad) features belonging to the R2PI resonances of larger aggregates.

An efficient photoionization *via* R2PI can in principle be realized for systems exhibiting electronically allowed transitions. Further preconditions are a sufficient lifetime of the electronically excited state as well as favorable Franck-Condon factors<sup>[47]</sup>, which are decisive for the number and the intensity of the observed vibronic transitions. It should also be noted that vibrational modes of higher frequency, such as the structure-sensitive NH- and OH-stretching vibrations, have generally no or a too low Franck-Condon activity to be experimentally detected. Therefore, the combined IR/UV techniques, presented in the following subchapters, are often applied.

The term schemes for all variants of the R2PI technique are depicted in figure 2.

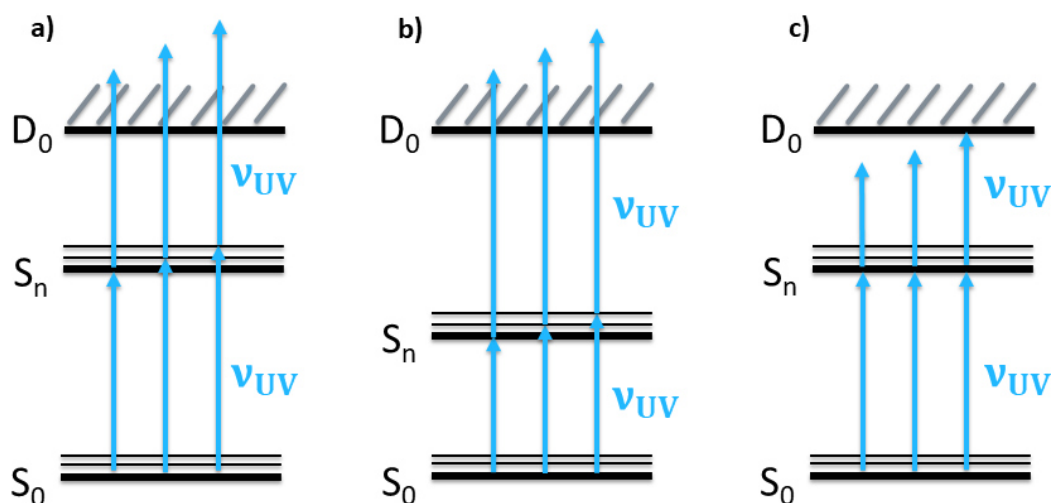


Figure 2: Term schemes for the R2PI-based techniques: a) one color (1C)-R2PI method, 1 + 1 process; b) two color (2C)-R2PI method, 1 + 1' process; c) ion current curve (2C-R2PI, whereby the ionization laser wavelength is scanned).

As long as the ionization potential of an investigated molecule or cluster is lower than twice the excitation energy, two photons of the same energy can be applied for excitation and successive ionization (one color (1C)-R2PI process, 1 + 1 process). In this case, only one UV laser system is required, which is experimentally convenient.

If, however, the ionization potential is higher than twice the electronic excitation energy, a second UV photon of distinct (shorter) wavelength is required for ionization (two color (2C)-R2PI process, 1 + 1' process). A 2C-R2PI spectrum is then obtained by scanning the excitation laser wavelength while keeping the ionization laser frequency-fixed. This increases the experimental effort, as two independent UV laser systems are required. Hereby, both UV laser beams have to be spatially overlapped and the ionization laser has to be irradiated within the lifetime of the electronically excited state. When investigating compounds where a 2C-R2PI experiment is indispensable, this has the advantage that the excess energy (in the  $D_0$  state) upon ionization can be reduced. In this manner, UV

fragmentation effects occurring upon ionization (discussed above) can be suppressed, especially if larger weakly bound clusters are investigated.

In addition, ionization potentials can also be obtained *via* 2C-R2PI, by measuring so-called ion current curves (figure 2 c)). Within that, the excitation laser is frequency-fixed at a resonance obtained from the (1C- or 2C-)R2PI spectrum, while the ionization laser-wavelength is tuned. Hereby, an (ideally sharp) step-like increase of the ion signal is observed when the ionization potential is reached. However, further sharp steps in the ion signal may be observed on the blue side of the ionization potential if higher vibrational levels of the  $D_0$  state are accessed. If a more precise value regarding an ionization potential is of interest, even more demanding techniques like ZEKE (zero-electron kinetic energy)<sup>[48]</sup> and MATI (mass analyzed threshold ionization)<sup>[49–51]</sup> are required.

Finally, it should be pointed out that 2C-R2PI investigations on compounds that can also be resonantly ionized by 1C-R2PI are always challenging, as the efficient 1C-R2PI process has to be suppressed in the way to obtain a two color effect. For this purpose the pulse intensities of both, exciting and ionizing laser, have to be adjusted appropriately.

## 2.2 IR/R2PI spectroscopy

The Infrared/Resonant two-photon Ionization (IR/R2PI) technique<sup>[52,53,54]</sup> combines IR spectroscopy with the R2PI technique described above. This method is an ideal tool to measure infrared spectra of isolated neutral molecules or aggregates in the electronic ground state ( $S_0$ ), which is also termed “IR/UV hole burning” or “resonant ion dip IR (RIDIR)” spectroscopy in the literature.

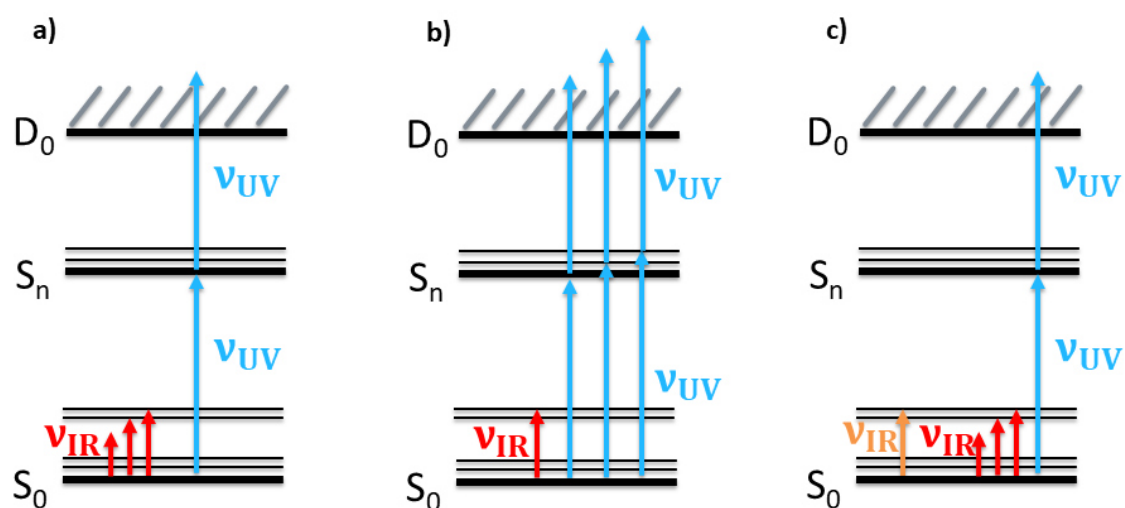


Figure 3: Term schemes for the combined IR/UV techniques in the  $S_0$  state: a) IR/R2PI method; b)  $IR_{\text{fixed}}$ /R2PI method; c)  $IR_{\text{fixed}}$ /IR/R2PI method.



When performing an IR/R2PI experiment (see figure 3 a)), first a resonant ion signal is required, which has to be stable over time and can be obtained by either 1C-R2PI or 2C-R2PI. Therefore, the UV excitation laser is frequency fixed at a specific band obtained from the R2PI spectrum. If 2C-R2PI is applied, the ionization laser frequency is also set to a specific wavelength, whereby the excess energy upon photoionization should be kept moderate. The IR laser pulse irradiates the sample about 50 ns prior to the UV excitation laser and its wavelength is tuned. If the IR laser is resonant with a vibrational mode of the investigated molecule or cluster, the vibrational ground state is depopulated. This means that fewer molecules are available for the subsequent (1C- or 2C-)R2PI process, which thus results in a less intense ion signal. In consequence, a depletion of the initially stable ion signal is observed, whereby the intensity of the observed IR effect mainly depends on the oscillator strength of the respective vibrational mode and on the pulse energy of the IR laser.

As mentioned, IR/R2PI spectroscopy yields mass selective IR spectra which can also be isomer selective, provided that the isomers occurring in the molecular beam exhibit clearly distinct R2PI resonances. In this case, an IR spectrum of one single isomer is obtained by recording an IR/R2PI spectrum *via* an isomer-specific R2PI resonance. Thus, the number of isomers in the molecular beam can be determined by successively measuring IR/R2PI spectra *via* all resonances observed in the R2PI experiment. In the case of overlapping R2PI resonances, the measured IR spectra show features from more than one isomer, whereby isomer selectivity may be regained by performing an IR<sub>fixed</sub>/IR/R2PI experiment (see subchapter 2.3).

Regarding species selectivity it should however be noted that, as discussed in chapter 2.1 for the R2PI spectroscopy, UV fragmentation effects can influence the IR spectra measured for a specific cluster. The mass signal observed for a certain  $m/z$  often partly results from UV fragmentation of larger aggregates down onto the respective lower mass trace. If the larger cluster undergoing UV fragmentation is vibrationally excited by the IR laser (prior to UV irradiation), not only the ionization efficiency of this heavier cluster decreases, but also the UV fragmentation efficiency onto lower mass traces. This means that the IR scans recorded for a particular cluster size can show vibrational features of larger aggregates, which impedes interpretation of the spectra.

Frequently, the vibrational pattern obtained in the IR spectra provides first hints about the structure of the investigated compound (for *e.g.* free and hydrogen-bonded groups). In most cases, a specific structural motif can then be assigned to the experiment by consulting the optimized geometries and corresponding vibrational frequencies predicted by quantum chemical (for example DFT) calculations.

Occasionally, the application of an alternative variant of the IR/R2PI technique, namely the IR<sub>fixed</sub>/R2PI method<sup>[33,55,56]</sup> is helpful. Here, the IR laser is frequency-fixed at a (if possible isomer-selective) band of the measured IR/R2PI spectrum, while the UV excitation laser is scanned (see figure 3 b)). As a result,

all R2PI bands belonging to the vibrationally excited isomer(s) show decreased intensity relative to the R2PI features of the isomers that are not resonantly excited by the IR laser, remaining unchanged compared to the conventional R2PI spectrum. Finally, this method is a tool to assign observed R2PI transitions to specific isomers occurring in the molecular beam.

As an alternative approach to the described IR/R2PI method, IR spectra can also be obtained by recording the resonant IR depletion of a laser induced fluorescence (LIF) signal. This technique, known as fluorescence-detected or fluorescence-dip IR (FDIR) spectroscopy<sup>[46,54,57–59]</sup>, has the disadvantage that the IR spectra are recorded without mass selection.

In this subchapter the ionization loss stimulated Raman spectroscopy (ILSRS)<sup>[60–64]</sup> as well as the ionization gain stimulated Raman spectroscopy (IGSRS)<sup>[60–64]</sup>, which have been developed as complementary methods to the described IR/R2PI spectroscopy, should also be mentioned. Here, a vibrational excitation is realized *via* a stimulated Raman scattering process. Over the last years, these demanding techniques, being particularly appropriate if structurally relevant vibrational modes exhibit too low IR but higher Raman activities, have additionally been established in the Gerhards group.<sup>[34,65]</sup>

### 2.3 IR<sub>fixed</sub>/IR/R2PI Spectroscopy

As mentioned above, the IR<sub>fixed</sub>/IR/R2PI technique (also called IR/IR hole burning technique)<sup>[33,55,66–68]</sup> can be applied to achieve isomer selectivity if no isomer selective IR/R2PI spectra are obtained due to the presence of two or more isomers with overlapping UV resonances. As illustrated in figure 3 c), an additional IR laser (“burn” laser) is irradiated about 50 ns prior to the scanned IR laser and is frequency fixed at a preferably intense isomer specific band obtained from the IR/R2PI spectrum. Thus, the vibrational ground state of the isomer which is excited by the IR burn laser is depopulated, so that fewer molecules are available for the subsequent IR/R2PI process. In the obtained IR<sub>fixed</sub>/IR/R2PI spectrum, all IR bands belonging to the burned isomer are weakened compared to the pattern observed in the IR/R2PI scans without burn laser. At the same time, all the isomers which are not excited by the burn laser show unaffected IR bands in the IR<sub>fixed</sub>/IR/R2PI spectrum. In this way, ideally all IR bands observed in the “common” IR/R2PI spectrum can be assigned to specific isomers by successively setting the IR burn laser to various vibrational transitions and performing IR<sub>fixed</sub>/IR/R2PI scans.

It should be emphasized that the presence of isomer specific IR transitions in the IR/R2PI spectrum, allowing for the spectroscopic “burning” of single isomers, is mandatory for a successful IR<sub>fixed</sub>/IR/R2PI experiment.

Besides the described IR<sub>fixed</sub>/IR approach used for isomer discrimination, IR-induced rearrangement reactions in isolated aggregates can also be investigated by IR<sub>fixed</sub>/IR/R2PI spectroscopy. Within that, the first frequency fixed IR laser triggers the isomerization, while the scanned IR laser probes the generated species. First examples giving strong hints that “new” structural motifs can be formed in the molecular beam upon IR excitation were found in the Gerhards group.<sup>[55,69]</sup>

## 2.4 UV/IR/UV Spectroscopy

The UV/IR/UV technique<sup>[55,70,71,72]</sup>, illustrated in figure 4 a), is applied to measure IR spectra of neutral molecules or aggregates in their electronically excited state. Alternatively, the fluorescence dip IR (FDIR) approach<sup>[73]</sup> can be used, with the IR laser being fired after electronic excitation. However, the lack of mass selectivity is a significant disadvantage of the latter technique.

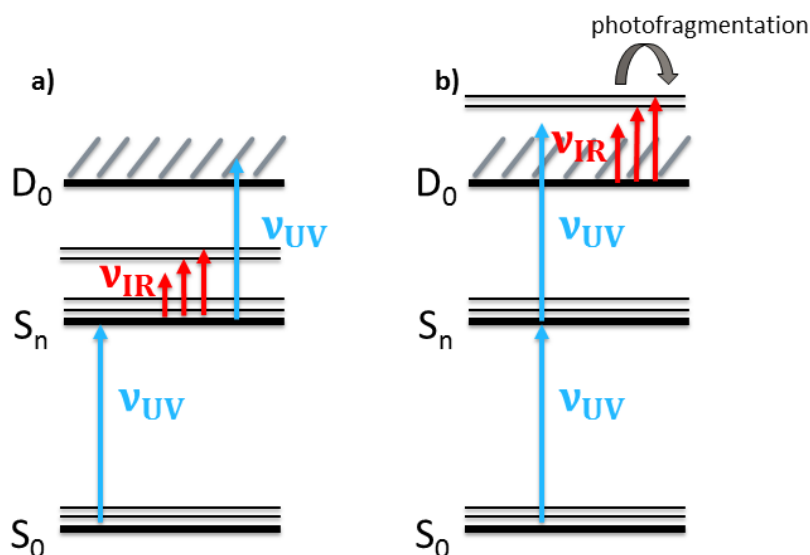


Figure 4: Term schemes for the combined IR/UV techniques in the  $S_1$  and  $D_0$  states: a) UV/IR/UV method; b) UV/UV/IR method.

In contrast to the IR/R2PI technique in the  $S_0$  state, the UV/IR/UV method is only applicable in combination with a 2C-R2PI process, whereby the UV excitation and ionization lasers have to be synchronized with a delay of (if possible) at least a few nanoseconds. The scanned IR laser is fired between both UV laser pulses to probe the electronically excited state. If the IR laser is resonant with a vibrational mode of the electronically excited compound, the vibrational ground state of the electronically excited state is depopulated, so that fewer molecules can be ionized by the ionization laser. Thus, a depletion of the corresponding ion signal is observed.

As the singlet excited state lifetimes of the investigated organic compounds are often relatively short (mostly below 10 ns), both UV laser pulses must be fired within a time span of no more than a few

nanoseconds between electronic excitation and ionization. Due to an IR laser pulse width of about 10 ns, a temporal overlap between the IR laser pulse and both UV laser pulses (for electronic excitation and ionization) cannot be avoided in these cases, so that IR transitions of the electronic and ionic ground state ( $S_0$  and  $D_0$ ) likely appear in the excited state IR spectrum ( $S_1$ ). Specific IR transitions can then be assigned to the electronically excited state by comparing the UV/IR/UV spectra with the respective IR/R2PI and UV/UV/IR spectra. In this work, however, UV/IR/UV spectra of chromone–MeOH clusters were recorded with the UV excitation and ionization lasers separated in time to about 70 ns due to a long lifetime of the electronically excited (triplet) state. In this way, a temporal overlap of the IR and UV pulses could be avoided.

Finally, it should be mentioned that in cases where no isomer selective UV/IR/UV spectra can be obtained due to congested electronic transitions of multiple isomers, the IR/UV/IR/UV scheme<sup>[55,67]</sup>, also developed in the Gerhards group, can be applied to regain isomer selectivity. In specific cases, this sophisticated method can even be used to support the assignment of vibrational transitions observed in  $S_0$  state IR spectra.<sup>[55]</sup>

## 2.5 IR(M)PD Spectroscopy

The infrared (multi-)photon dissociation (IR(M)PD) technique is commonly used to measure IR spectra of ionic clusters or metal complexes in (cryo-cooled) ion traps<sup>[74]</sup> and rarely in molecular beams<sup>[75–77]</sup> (in combination with *e.g.* ESI<sup>[3,4]</sup> or laser ablation/vaporization sources<sup>[5,6]</sup>).

If the IR laser is resonant with a vibrational mode of the ionic species, an infrared (multi-)photon dissociation (IR(M)PD) process can be induced. Hereby, the number of IR photons which have to be absorbed to induce dissociation depends on the dissociation energy of the compound. If weakly bound clusters such as hydrates are investigated the absorption of one single IR photon may already lead to fragmentation. In case of strongly bound systems, however, multiple IR photons may be required to induce dissociation (of *e.g.* covalent bonds). This is the rationale for the establishment of the so-called “tagging” or “messenger” technique<sup>[78,79]</sup>, where a weakly-bound “messenger” (for example Ar,  $H_2$ ,  $N_2$ ,...) is linked to the investigated ionic species. Hereby, the attached atom or small molecule does not significantly disturb the intrinsic properties of the probed system and can be split off by absorption of only one IR photon.

In case of a too high dissociation limit to apply the common IR(M)PD technique, the more complex IR+UV method may also be helpful, developed in the group of Fujii for neutral systems<sup>[80]</sup> and adapted for the investigation of cationic clusters in the Gerhards group<sup>[75]</sup>. The main advantage of this technique is that principally only one IR photon is required to induce cluster dissociation. This new approach can

also be useful if no efficient dissociation channel is reached by excitation of a certain vibrational mode (dark mode effect).

When using the IR+UV technique the UV laser frequency is fixed about  $1000\text{ cm}^{-1}$  below the resonant excitation (and also dissociation) energy determined by recording a UV photodissociation spectrum. The tuned IR laser is irradiated about 10 ns prior to the UV laser. Thus, similarly as within conventional IR(M)PD experiments, an IR photodissociation spectrum is obtained by recording the ion signal intensity in function of the IR laser wavelength. It should however be noted that the IR+UV technique was merely used to investigate cationic clusters that were generated by using a combined thermal and ablation source, but has never been applied to probe photoionized species.

## 2.6 UV/UV/IR spectroscopy

The UV/UV/IR technique<sup>[2,78,81,82]</sup>, illustrated in figure 4 b), is applied to measure IR photodissociation spectra of molecules or aggregates in the ionic ground state ( $D_0$ ). Hereby, the aromatic radical cations are obtained by 1C-R2PI or 2C-R2PI, while the IR laser is fired about 50 ns after the UV ionization process. In a UV/UV/IR experiment, IR dissociation yields can be detected on both the parent and fragment mass traces. A dip of the ion signal is obtained on the parent mass trace, while a mirror-inverted ion gain is observed on the fragment mass trace. Hereby, the ion signal on the parent mass trace is always subjected to the ordinary fluctuations. If, in contrast, the fragment mass signal only appears upon resonant IR photodissociation, the signal-to-noise ratio on this mass trace is superb (due to the vanishing background signal), so that even weak transitions can be recorded.

When applying the UV/UV/IR technique, the measured IR photodissociation spectrum can also be influenced by the available amount of excess energy for the cation (in the  $D_0$  state) after the R2PI process. This can be an obstacle if the investigated ions are formed within a 1C-R2PI process, where the energy of the ionizing photon cannot be specifically adjusted to the ionization potential. A large excess energy may lead to band broadening due to the high internal energy and vibrational frequency shifts due to vibrational coupling between the probed transitions and other (low frequency) modes. However, previous work illustrates that IR photodissociation spectra do not significantly depend on the amount of excess energy, since this coupling is very small if localized vibrational transitions (such as NH- or OH-stretch) are probed.<sup>[82,83]</sup> It should also be noted that a considerable excess energy introduced by the R2PI process can facilitate IR effects in case of a high photodissociation barrier.

### 3 Experimental setups

#### 3.1 Laser systems

When applying the spectroscopic techniques described in chapter 2, up to four independent tunable laser systems are required. All laser setups are pulsed nanosecond laser systems, running at a repetition rate of 10 Hz. The operating principles of the UV and IR laser setups are described in the following subchapters.

##### 3.1.1 UV laser setups

All UV laser systems used in this work basically consist of a frequency-doubled dye laser (Cobra Stretch or PrecisionScan, Sirah) pumped by a Nd:YAG laser (Spitlight 600, Spitlight 1000 or Spitlight 1000.2, Innolas). A schematic view of such a UV laser setup is depicted in figure 5.

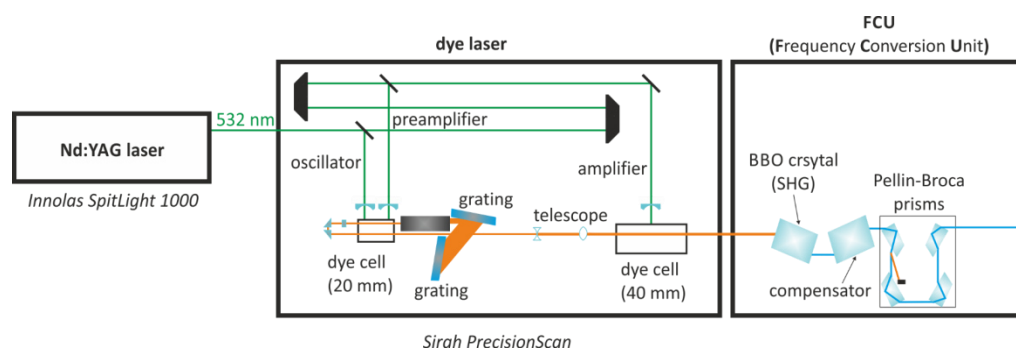


Figure 5: Schematic view of the UV laser setups; here for a pump wavelength of 532 nm. It should be noted that for one of the used setups the FCU was integrated into the dye laser housing, while it was mounted into a separate unit for all other systems.

The fundamental (1064 nm) of the Nd:YAG laser is frequency-doubled (second harmonic generation (SHG), 532 nm) or -tripled (third harmonic generation (THG), 355 nm) in nonlinear optical processes in  $KD^*P(KH_2PO_4)$  crystals. The required pump wavelength depends on the absorption spectrum of the used laser dye, whereby the choice of a specific dye depends on the electronic excitation or ionization energy of the investigated compound.

In a frequency conversion unit (FCU), the dye laser radiation is frequency-doubled using a BBO ( $\beta$ - $BaB_2O_4$ ) crystal. Then, the beam passes through the compensator in order to reverse its spatial shift. Finally, a Pellin-Broca unit (composed of two or four Pellin-Broca prisms) separates the generated (second harmonic, SH) UV radiation from the fundamental dye laser radiation.

By selecting the suitable laser dyes as well as the correspondingly cut BBO crystals for frequency-doubling a tuning range of 206 to about 450 nm is principally accessible with a bandwidth of  $0.07\text{ cm}^{-1}$ . In this work, visible light in the region of 380 to 475 nm was applied in some experiments, so that the fundamental of the dye laser could be used directly.

The laser pulse energies were adjusted according to the applied experimental techniques (UV excitation or ionization laser, 1C-R2PI or 2C-R2PI,...) and ranged from  $50\text{ }\mu\text{J}$  to  $1.5\text{ mJ}$  per pulse.

### 3.1.2 IR laser setups

The IR laser systems A and B used in this work, schematically depicted in figure 6, can generate mid IR radiation in the range of  $2600\text{ to }4200\text{ cm}^{-1}$ , so that NH-, OH- and also CH-stretching modes can be probed. For setup A, the region from  $600\text{ to }1800\text{ cm}^{-1}$ , where CO-stretching modes as well as NH-, CH- and OH-bending modes are found, is also accessible.

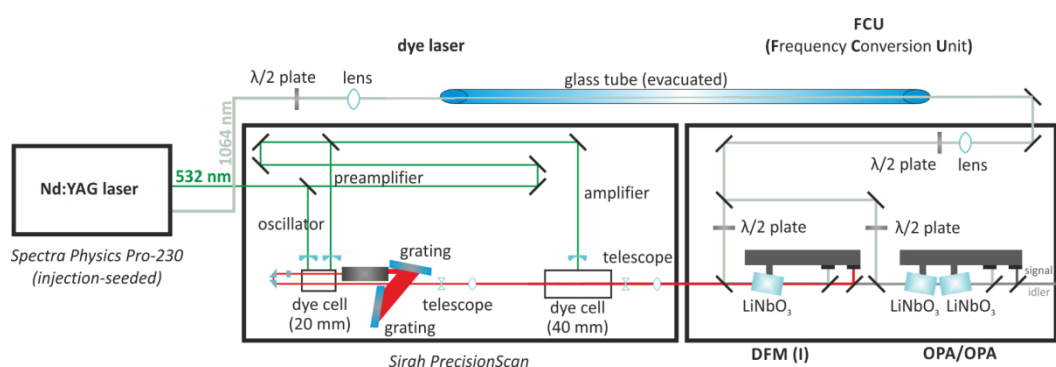


Figure 6: Schematic view of the IR laser setups A and B.

The fundamental (1064 nm) of a (for system A also injection seeded) Nd:YAG laser (Quanta-Ray, PRO-230, Spectra Physics) is frequency-doubled by a  $\text{KD}^*\text{P}(\text{KH}_2\text{PO}_4)$  crystal. The generated 532 nm radiation is separated from the residual of the fundamental by a dichroic mirror and serves as dye laser (PrecisionScan, Sirah) pump source. Regarding both IR laser setups, the laser dyes styryl 8 (solved in DMSO) or styryl 9 (solved in MeOH), or optionally a mixture of both (solved in DMSO), are systematically used.

The dye laser output is spatially and temporally overlapped with about 30% of the remaining 1064 nm radiation (separated from the other 70% by a dichroic mirror) in a  $\text{LiNbO}_3$  crystal, whereby the mid-IR radiation, with a spectral range of  $2600\text{ to }4200\text{ cm}^{-1}$ , is generated by difference frequency mixing (DFM). The remaining dye laser radiation as well as the 1064 nm beam are separated from the generated IR-radiation by dichroic mirrors, before optical parametrical amplification (OPA process) *via* mixing with the other 70% of the fundamental radiation in a second  $\text{LiNbO}_3$  crystal. Simultaneously,

so-called “signal” radiation in the region of 5200–6800  $\text{cm}^{-1}$  is generated within the latter non-linear optical process. The remaining fundamental of the Nd:YAG laser as well as the “signal” radiation are split off, while the “idler” radiation (corresponding to the amplified mid IR-radiation), with a spectral resolution of  $< 0.1 \text{ cm}^{-1}$ , is used for the experiments. For laser system B a second OPA crystal is occasionally installed to obtain “idler” radiation with a pulse energy of about 19 mJ at a dye laser output wavelength of 765.55 nm, corresponding to an “idler” wavenumber of 3664  $\text{cm}^{-1}$ . Regarding laser system A higher output energies of 28 mJ (“idler”) per pulse at 765.55 nm are reached, even with only one OPA crystal for amplification.

For both systems A and B, the so-called “relay imaging technique” is applied in order to improve the beam profile quality of the 1064 nm radiation at a distance of about four meters from the Nd:YAG laser. Using this technique, the beam profile is projected over a distance of two meters by two convex lenses ( $f = 1 \text{ m}$ ), which are separated from each other by their double focal length (2 m, 1:1 imaging telescope with focus). In order to avoid air-breakdown in the beam focus, an evacuated glass tube with Brewster angle windows is installed between both lenses. The described approach is required because a spatially homogeneous laser beam profile is mandatory for efficient DFM and OPA processes. Furthermore, any hotspots in the laser beam profile would likely damage the sensitive  $\text{LiNbO}_3$  crystals or its anti-reflective coatings.

These highly efficient IR laser setups have the disadvantage that the output energy is drastically lower in the spectral region of 3460–3520  $\text{cm}^{-1}$ , due to self-absorption of the generated IR radiation by the  $\text{LiNbO}_3$  crystals. This spectral region can still be accessed by a high-grade MgO-doped  $\text{LiNbO}_3$  crystal, where the self-absorption is shifted to 3520–3550  $\text{cm}^{-1}$ . However, no MgO-doped OPA crystals have been available (up to now), so that a pulse energy of less than 3.5 mJ is reached between 3460 and 3520  $\text{cm}^{-1}$ . For this work, the laser power was adequate for most experiments, but unfortunately turned out to be insufficient when probing weak vibrational transitions in combination with the newly established laser desorption setup. When the laser desorption source is used, the ion signal is subjected to strong fluctuations (see chapter 3.4.4), so that small absorptions cannot be detected at low IR laser pulse energy. Furthermore, the beam path between the IR laser setup and the molecular beam apparatus II (applied for the desorption experiments) is particularly long, which additionally reduces the IR laser power.

For laser system A, the region of 600–1800  $\text{cm}^{-1}$  can also be accessed by a further difference-frequency mixing process (DFM II) in an additional frequency conversion unit. Hereby, the “idler” and “signal” radiation, obtained as described above, are mixed in an  $\text{AgGaSe}_2$  crystal to generate radiation in this low-frequency spectral range.<sup>[84]</sup> In order to avoid damage to the delicate  $\text{AgGaSe}_2$  crystal, input



powers are kept at moderate values of about 15 mJ (“idler” + “signal”), to reach final output energies of about 0.5 mJ per pulse.

However, measurements in this spectral region were not part of this work. It should also be noted that laser desorption experiments requiring the DFM II setup are out of reach due to the low laser power (compared to the spectral region above  $3000\text{ cm}^{-1}$ ).

### 3.2 Molecular beam technique

As described in the following, molecular beam experiments are ideal tools for investigations on (especially neutral) isolated molecules and clusters in the gas phase.<sup>[85]</sup> The collision-free environment obtained by expanding a gas from a high-pressure reservoir through a small hole (nozzle) into the vacuum provides the cold conditions required for spectroscopy on isolated molecules or aggregates. Within molecular beam experiments, the expansion gas, also denoted as carrier gas, is enriched with the investigated sample molecules. In this way, not only the carrier gas is cooled down during the expansion, but also the respective analyte. At the same time, the multiple collisions which occur during the expansion are at the basis of cluster formation. Since the probed molecules are co-expanded with the carrier gas, the described method is often termed as “seeded beam technique”.

In case of a high backing pressure in the gas reservoir, the mean free path of the atoms or molecules is small relative to the diameter of the hole, so that the expansion process can be described by a hydrodynamic model. As the expansion is rapid, almost no thermal exchange with the environment occurs, so that it is an adiabatic process. Therefore, the term “adiabatic expansion” is frequently mentioned in the context of molecular beam spectroscopy.

Efficient cooling during the expansion is attained if the internal energy  $U$  of a molecule in the molecular beam, with  $U = U_{\text{trans}} + U_{\text{rot}} + U_{\text{vib}}$ , is almost entirely transformed into kinetic energy. Ideally, an internal relative energy of  $U = 0$  should be reached, thus with a temperature of  $T = 0$ . However, as described further down, this cannot be fully realized experimentally.

The adiabatic cooling process can be explained by the atomic model system illustrated in figure 7. During the expansion, molecules with a higher relative velocity in propagation direction of the molecular beam undergo elastic collisions with relatively slower molecules. Hereby, translational energy is transmitted up to the point where the molecules’ relative velocity distribution (in propagation direction of the molecular beam) is significantly narrowed and the particle density is so low that no further collisions may occur. Figure 7 shows velocity distributions before the adiabatic expansion and in the collision-free region of the molecular beam.

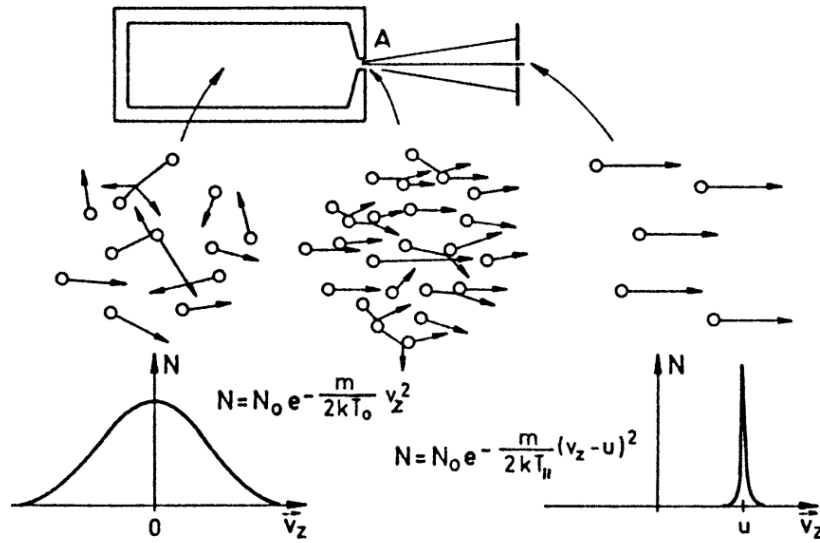


Figure 7: Atomic model of a molecular beam expansion from a high-pressure reservoir into the vacuum, with the relative velocity distributions before and after the adiabatic expansion.<sup>[85]</sup>

Molecules undergoing transversal collisions are deviated and are thus unlikely to pass through the skimmer, peeling off the outer turbulent region of the molecular beam. In this way, the transversal velocity distribution in the skimmed and collimated molecular beam is also narrowed, so that Doppler broadening of spectral lines is reduced.

For spectroscopic investigations the reduction of rotational energy  $U_{\text{rot}}$  and vibrational energy  $U_{\text{vib}}$  of a molecule through adiabatic collisions is of particular relevance. However, the cross sections for rotation-translation energy transfers are generally less efficient than for elastic collisions, so that rotational energy cannot be completely dissipated within the expansion. Regarding vibrational energies  $U_{\text{vib}}$ , the adiabatic cooling is considerably less efficient than for the rotational energies  $U_{\text{rot}}$ . As the relative velocity distribution is crucially reduced during the expansion, translational temperatures  $T_{\text{trans}}$  are cooled down to almost 0 Kelvin. However, rotational temperatures  $T_{\text{rot}}$  merely reach a few Kelvin, while vibrational temperatures  $T_{\text{vib}}$  usually drop to a few ten Kelvin:

$$T_{\text{vib}} > T_{\text{rot}} > T_{\text{trans}}$$

Efficient adiabatic cooling leads to less crowded spectra as hot bands are eliminated effectively and Doppler broadening is reduced.

As mentioned, the adiabatic expansion conditions can also favor cluster formation. Due to the small relative energies, the aggregation of two molecules can be supported by the interaction with a third collision partner (the carrier gas) taking up the remaining relative energy. In the experiment, the

formation of specific clusters can be optimized by adjusting expansion parameters such as the type of carrier gas (mostly helium, neon or argon) or the backing pressure (2-3 bar relative to lab atmosphere).

### 3.3 Experiments with thermal sources – molecular beam apparatus (I)

In this chapter the technical aspects of the molecular beam apparatus (I) and the implemented thermal source are described. Apparatus (I) can be used for investigations on all compounds with sufficient vapor pressures and (if strong heating of the substance is necessary) sufficient thermal stability. As the design of apparatus (I) is principally similar to the setup of apparatus (II), described in detail in subchapter 3.4.4, only the main aspects and singularities are described in the following.

#### *Vacuum system and operation*

In contrast to machine (II), apparatus (I) has only three vacuum chambers, namely a source chamber (a), in which the thermal source is implemented, an ionization chamber (b) and a flight tube (c). A schematic view of the setup is depicted in figure 8.

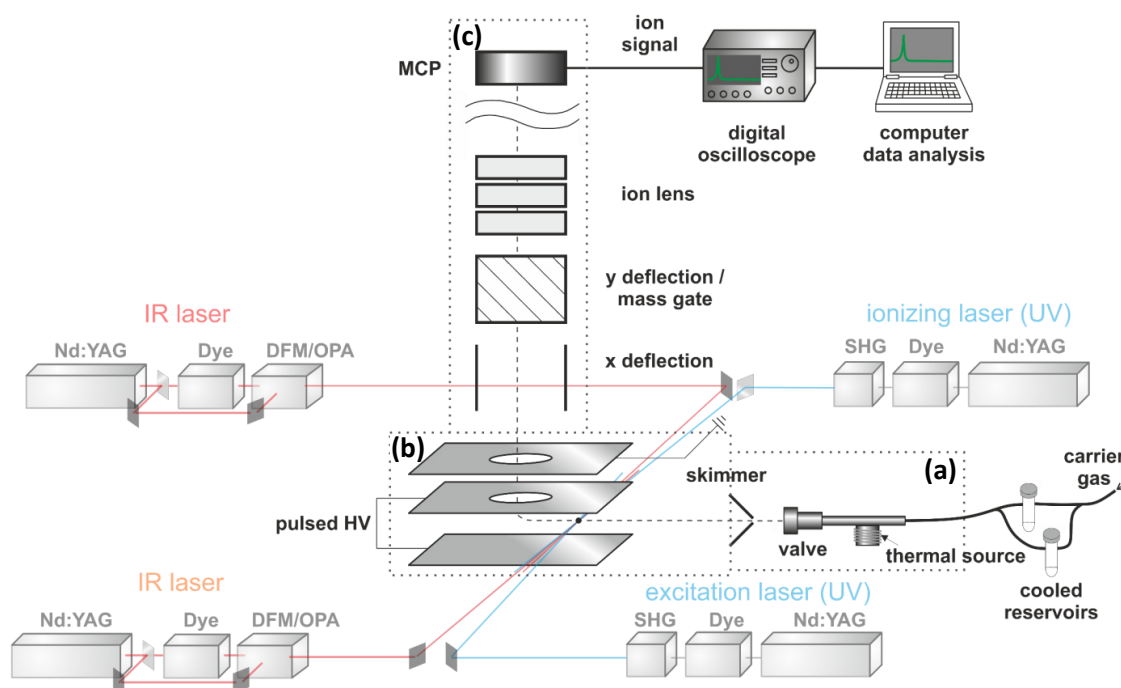


Figure 8: Schematic view of the molecular beam apparatus (I), showing the most relevant parts.

The molecular beam source, composed of a pulsed valve (General Valve, Series 9, 500  $\mu\text{m}$  orifice) linked to the carrier gas line and to the heatable sample supply, is implemented in the source chamber (a). Chamber (a) is pumped by an oil diffusion pump (DI 3000, 3000 l/s  $\cong$  10800  $\text{m}^3/\text{h}$ , Leybold), with the required pre-vacuum being generated by a two-stage rotary vane pump (TRIVAC D65B, 65  $\text{m}^3/\text{h}$ ,

Leybold) combined with a roots-pump (250 m<sup>3</sup>/h, Alcatel). With running pulsed valve, the pressure in the source chamber (a) is between  $2 \cdot 10^{-5}$  and  $2 \cdot 10^{-4}$  mbar, while a pressure of about  $5 \cdot 10^{-6}$  mbar is reached if the pulsed valve is switched off. The ionization chamber (b), separated from chamber (a) by a skimmer, is pumped by a turbomolecular pump (1150 l/s  $\hat{=}$  4140 m<sup>3</sup>/h, Turbovac 1000, Leybold), using the same pre-vacuum pumps as chamber (a). Thereby, a pressure of about  $5 \cdot 10^{-7}$  mbar is obtained. The flight tube (c) is pumped by a turbomolecular pump (Turbovac 361, 1242 m<sup>3</sup>/h, Leybold) to attain a pressure of  $1-5 \cdot 10^{-8}$  mbar, with the pre-vacuum being provided by a two-stage rotary vane pump (TRIVAC D8B, 8 m<sup>3</sup>/h, Leybold).

A difference to apparatus (II) is the longer field-free drift zone of about 30 mm (instead of only about 20 mm) between the interaction region with the laser beams and the center of the Wiley-McLaren arrangement. This longer drift zone was required for the MATI<sup>[49-51]</sup> experiments performed in the past. Although apparatus (I) is not equipped with a reflectron, which is not necessarily required for the performed IR/UV experiments, a very good mass resolution of  $m/\Delta m = 1800$  (for a mass of 110 amu) is achieved. Overall, apparatuses (I) and (II) both have very similar operating principles, but the applied voltages are specific to each setup. For apparatus (I) acceleration voltages of VA1: +4130 V and VA2: +3520 V are applied, while a voltage of VX1 = +230 V is applied to the deflection plate to compensate for the remaining horizontal drift after ion extraction.

Additionally, setup (I) is equipped with a further deflection plate which can be used to specifically draw away ions in a specific mass range, so that no or less ions of this  $m/z$  can reach the detector. Here, a push-pull switch with adjustable rise and fall times is used (HTS 31-03 GSM, Behlke), whereby a voltage between +10 and +200 V is applied, depending on the size of the ion signal to be suppressed. This option is primarily utilized if an ion signal is so intense that it could damage the sensitive MCP detector. At the MCP detector a voltage of -1700 V (VD1) is applied, which is then split up (VD2 = 54.5 %, VD3 = 9.1 %).

### Thermal sources – heatable sample supply

The sample supply is depicted in figure 9, together with the pulsed valve and the carrier gas line.

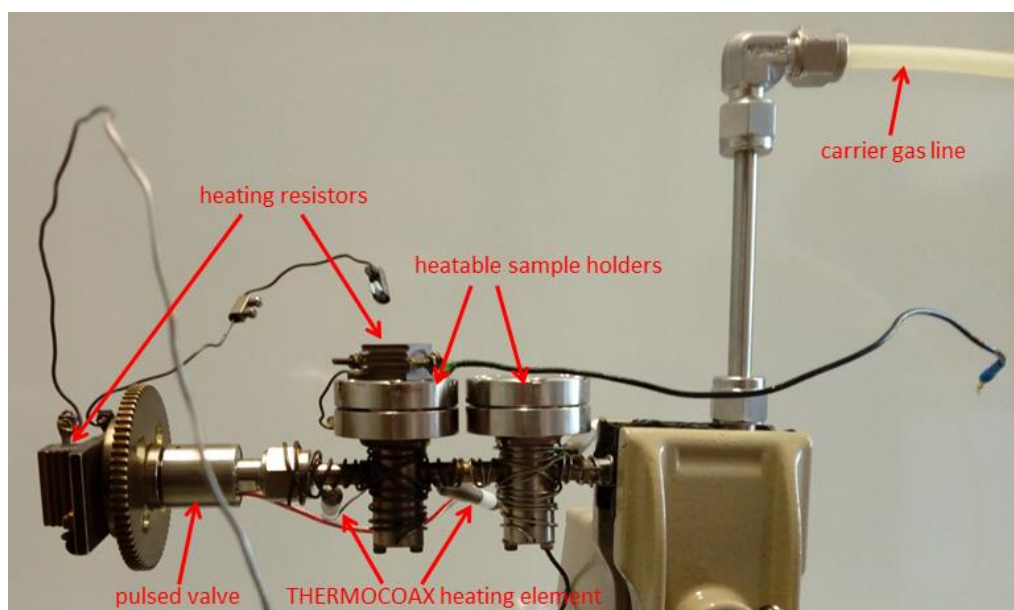


Figure 9: The heatable sample supply with the pulsed valve and the carrier gas line, implemented in apparatus (I).

This stainless steel assembly is composed of two sample holders that can be heated separately by heating resistors and THERMOCOAX heating elements, which are wrapped around the holders. This allows the co-expansion of two non-volatile compounds of individual vapor pressure (which are therefore heated up to different temperatures) to investigate mixed clusters such as heterodimers. If (like in this work) only one non-volatile compound is co-expanded with the carrier gas, solely the first sample holder, being closer to the pulsed valve, is filled with substance and heated. In the way to avoid any reaction between the compound and the stainless steel surface, the substance is filled into a small tailor-made glass pot, which is inserted into the sample holder. The carrier gas (mostly helium or neon) streams over the sample holders, so that it is enriched with the investigated substance before the expansion into the vacuum *via* the pulsed valve. It should be noted that the pulsed valve is also heated, since an increasing temperature gradient from the sample holder(s) towards the valve is required to avoid any recondensation of the compound(s).

*Thermal sources – cooled reservoirs*

If compounds with a high vapor pressure, such as methanol, are co-expanded, they are not filled into a heatable sample holder, since in that case cooling of the substance instead of heating is required. Therefore, two external cooled glass reservoirs containing the respective solvents are integrated into a bypass of the carrier gas line. Hereby, each sample reservoir is placed into a well, milled out of a brass cylinder, which is filled with the cooling liquid ethylene glycol. The brass cylinder is placed on a thermoelectric cooling plate (Peltier cooling element). The amount of solvent in the expansion is varied by case-dependently adapting the reservoir temperature, and is further regulated *via* metering valves.

## 3.4 Laser desorption experiments – molecular beam apparatus (II)

### 3.4.1 Introduction

Apparatus (I), described in subchapter 3.3, is equipped with a thermal molecular beam source, whereby the investigated compound is brought into the gas phase *via* mild heating. Thus, a precondition is that the substance of interest exhibits a sufficiently high vapor pressure and, if stronger heating is necessary, also shows a high thermal stability. In other words, all experiments were limited to compounds that can be transferred into the gas phase without undergoing thermal decomposition. To overcome this limitation, a new laser desorption source was developed by the former group member Dr. Markus Becherer<sup>[18]</sup>. Apparatus (II), which had been almost exclusively used for the investigation of charged metal–alcohol<sup>[76,77,86]</sup> or metal–protected amino acid clusters<sup>[75]</sup> in previous works, was extended by an additional source chamber for implementation of the new desorption source. In the following, preliminar test runs and preoptimization steps were performed, but at the beginning of the present thesis the experimental achievements were still limited to at most rather unstable ion signals of too low intensity for thorough spectroscopic studies. Thus, some major refinements regarding the setup and especially the experimental procedure were required in order to successfully realize the first resonant two-photon ionization (R2PI) and in particular IR/R2PI (and UV/UV/IR) experiments with the new laser desorption setup. This could finally be achieved within this work, whereby all relevant experimental improvements are discussed in subchapter 3.4.4. The initial R2PI and IR/R2PI spectra are presented in section 5.1.1.

### 3.4.2 History of the laser desorption technique

In the 60s and 70s of the 20<sup>th</sup> century various techniques were developed to transfer larger non-volatile and labile or thermally unstable molecules into the gas phase. Hereby, solid samples were irradiated either with light pulses, electrons or neutral/charged particles to obtain neutral but also charged isolated molecules in the gas phase, which could then be detected in a time-of-flight mass spectrometer.<sup>[87]</sup> Although there are major technical differences between these different methods, they have in common that the desorption process and the ionization process occur simultaneously at the same point. Thus, the ionization parameters crucially depend on the possibly harsh conditions required for an efficient vaporization of the sample molecules, which often leads to strong fragmentation effects. Furthermore, only a small fraction of the desorbed molecules is also ionized to be then detected. On top of that, often mainly cluster ions are formed within such a combined

desorption and ionization process, so that an interpretation of the obtained spectra gets more complicated.<sup>[87–90]</sup>

The idea to separate the desorption and ionization processes in time and space goes back to 1980, when R. J. Cotter desorbed guanosine with a CO<sub>2</sub> laser from a solid sample prior to ionization through chemical ionization upon collision with a reagent gas.<sup>[91]</sup> Then, the groups of Schlag and Gillen combined the laser desorption with multiphoton-ionization (MPI).<sup>[87–90]</sup> Gillen and coworkers desorbed small clusters from a NBS copper C1252 surface by pulsed Ar<sup>+</sup> probe beam bombardment, followed by ionization with an excimer laser (248 nm).<sup>[90]</sup> The group of Schlag used a CO<sub>2</sub> (IR) laser to desorb tryptophan and retinal from solid sample pills (free of any matrix compound), prior to ionization at 266 nm and 355 nm, respectively. Then, they moved on to larger molecules, with chlorophyll *a* and porphyrin derivatives being successfully desorbed and ionized by resonance enhanced multiphoton-ionization (REMPI) using a frequency-doubled dye laser. Hereby, the parameters could be adjusted to detect the intact species without any strong limitations due to adduct formation or fragmentation.<sup>[87,89]</sup> Over the following years, laser desorption sources with diverse variations regarding target shape, target preparation as well as desorption laser wavelength and power were designed by different groups. For example, the group of Zare used a CO<sub>2</sub> laser to desorb molecules from a sample film deposited on a rotating glass cup.<sup>[92]</sup> Lubman and coworkers desorbed their compounds from the surface of a rotating ceramic rod with a CO<sub>2</sub> laser. Meijer and de Vries *et al.* desorbed molecules from a thin sample layer brought on fritted glass by using a KrF excimer (248 nm) desorption laser.<sup>[93,94]</sup> In the case of rather volatile compounds, they opted for an activated carbon substrate.<sup>[93,95]</sup> Levy and coworkers, from their side, investigated various dipeptides by doping the sample with a certain amount of Rhodamine 6G, to then desorb it from a rotating brass disc with a 530 nm laser.<sup>[96]</sup> Later on, the group of de Vries systematically used graphite as substrate.<sup>[97,98,99]</sup> In 2000, Piuze, Mons and coworkers took up the concept of graphite matrices by mixing the investigated compound with graphite powder and pressing it to a solid disc.<sup>[100]</sup> Since then, few other groups designed various source types where graphite matrices are applied. The groups of Fujii and Kleinermanns use rotating graphite discs with the substance being desorbed from its lateral surface.<sup>[101,102]</sup> The Müller, Müller-Dethlefs and Fernández groups desorb the samples from a rotating graphite rod.<sup>[103,104]</sup> These setups are similar to the laser ablation source type developed by Smalley<sup>[5]</sup>, also used in the Gerhards group<sup>[75]</sup>. Desorption sources using translatable graphite sample bars (similar to the targets used in this work) are employed in the groups of de Vries<sup>[98]</sup>, Rijs<sup>[105]</sup>, Küpper<sup>[106]</sup>, Zehnacker<sup>[107]</sup> and Zwier<sup>[108]</sup>. Thus, the latter source type is nowadays definitely one of the most common laser desorption setups in the field. All details regarding the desorption source applied in this work are discussed in chapter 3.4.4.



### 3.4.3 The laser desorption process – physical aspects

In this paragraph, the physical concepts of the laser desorption techniques should be illustrated, while the development of laser desorption over the last 40 years with all its variants was actually discussed in the preceding subchapter.

In general, the investigated sample is either deposited on or mixed with a substrate or matrix, to be then desorbed by laser irradiation (mostly a ns or even a ps laser<sup>[109]</sup>). The desorption process is a thermal process, where the laser energy absorbed by the substrate is very rapidly transferred into thermal energy, with extremely high heating rates in the range of  $10^8$ – $10^{13}$  K/s.<sup>[110]</sup> Regarding the mechanism of thermal desorption processes different variants have been proposed and the role of each of these mechanisms crucially depends on parameters like the desorption laser wavelength and power. Furthermore, the optical and thermal properties of the probed molecule and the substrate definitely play a role. However, a desorption of intact molecules should in all cases result from the abrupt temperature increase induced by the laser pulse, whereby surface reactions or decomposition of the investigated compound are unlikely due to the high heating rate.<sup>[110,111]</sup>

### 3.4.4 Molecular beam apparatus (II) with implemented laser desorption source

In this chapter, the molecular beam apparatus used for the laser desorption experiments is described in detail. Important technical aspects are discussed, together with the crucial optimization steps that were realized during this thesis. In figure 10 below, a detailed view of the molecular beam apparatus (II), consisting of a four-chambered differentially pumped vacuum system, is depicted.

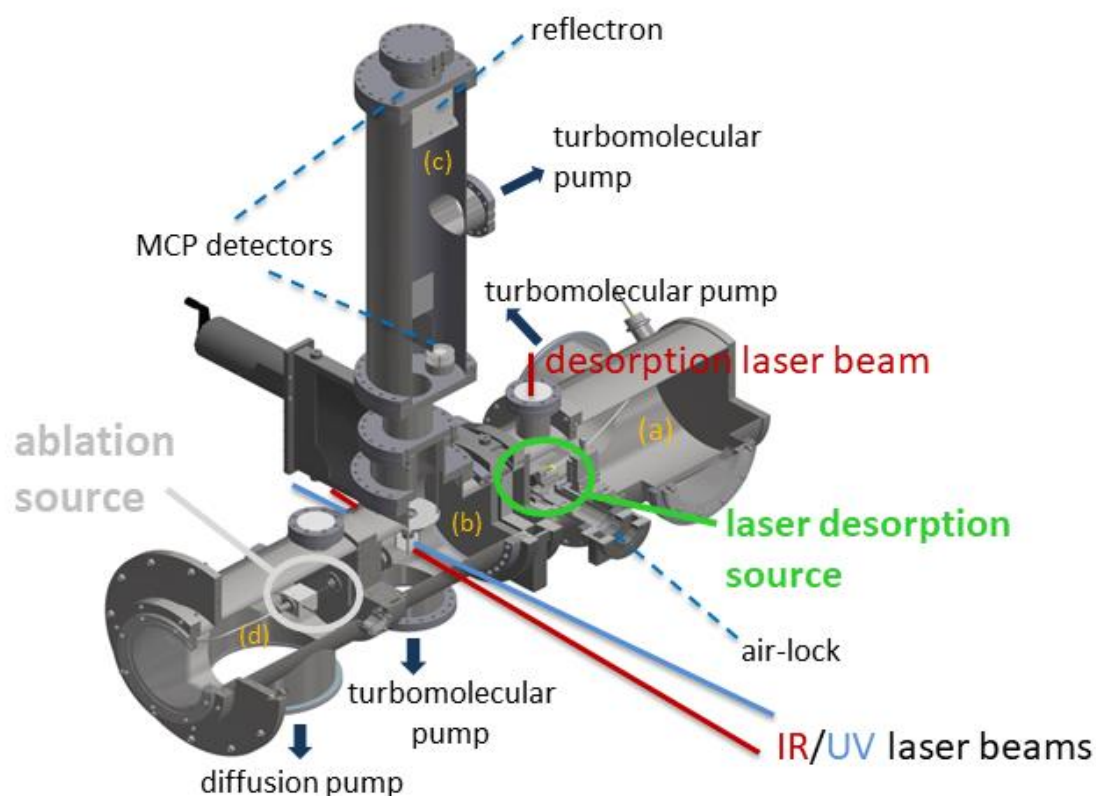


Figure 10 a): Schematic drawing of the molecular beam apparatus (II), with (a) desorption chamber, (b) ionization chamber, (c) flight tube, (d) ablation chamber.

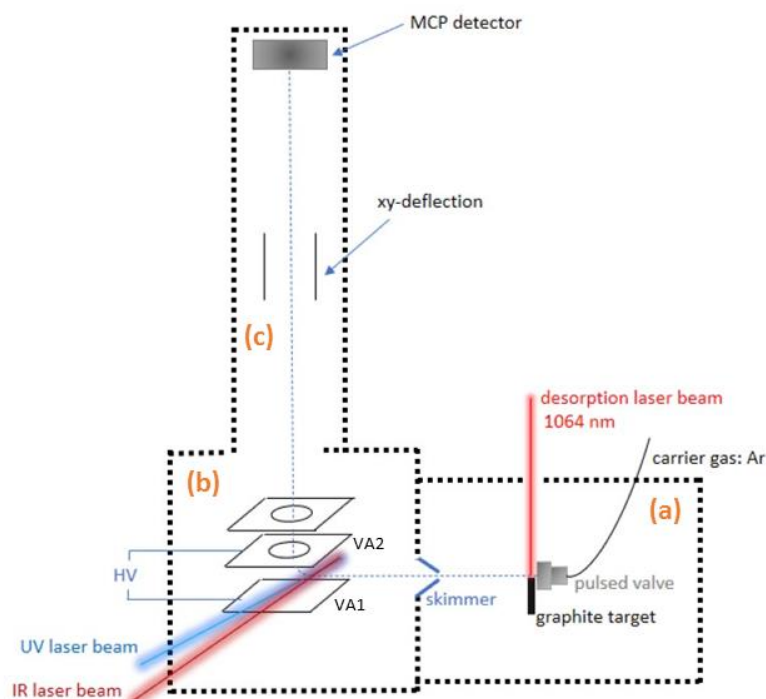


Figure 10 b): Simplified sketch of the apparatus (II), showing the most relevant parts (ablation chamber is omitted), with (a) desorption chamber, (b) ionization chamber, (c) flight tube, (VA1/VA2) acceleration plates of the Wiley-McLaren arrangement.

#### *Differentially pumped vacuum system*

The machine is composed of the laser desorption chamber (a), the ionization chamber (b), the flight tube (c) and the ablation chamber (d). Hereby, chambers (b) and (c) form the time-of-flight (TOF) mass spectrometer. During the laser desorption experiments the ablation (or thermal) source implemented in chamber (d) is not running, but this chamber has nevertheless to be evacuated for technical reasons. The laser desorption chamber (a) is pumped by the combination of a two-stage rotary-vane pump and a roots pump, providing the pre-vacuum required for the operation of the turbomolecular pump (Turbovac 1000, 4140 m<sup>3</sup>/h, Leybold), used to reach a final vacuum of about  $1.2 \cdot 10^{-4}$  mbar with running pulsed valve ( $10^{-6}$  mbar with switched-off pulsed valve). In the standby operation mode, the desorption chamber is separated from the mass spectrometer by a gate valve (Co. VAT). This has the crucial advantage that the source chamber can be vented for maintenance, while the TOF-mass spectrometer with its air sensitive micro channel plate (MCP) detectors remains evacuated. Between the desorption chamber (a) and this gate valve there is a small intermediate volume which is linked to the source chamber *via* a skimmer (aperture of 1 mm, Beam Dynamics) and (when no experiment is running) also *via* a bypass. The intermediate volume can thus be evacuated together with the whole chamber (a). Just before running an experiment, the gate valve is opened, while the bypass between

chamber (a) and the intermediate volume is then closed. Thus, this intermediate volume is virtually part of chamber (b) during measurement operation.

Concerning the ablation chamber (d) the pre-vacuum is generated by a two-stage rotary-vane pump (TRIVAC D65B, 65 m<sup>3</sup>/h, Leybold) combined with a roots pump (WAU 501, 505 m<sup>3</sup>/h, Leybold), while the final vacuum (1·10<sup>-6</sup> mbar) is reached with an oil-diffusion pump (DI 3000, 3000 l/s  $\hat{=}$  10800 m<sup>3</sup>/h, Leybold). The ionization chamber (b) is pumped by a turbomolecular pump (Turbovac 361, 1242 m<sup>3</sup>/h, Leybold) (pressure: 10<sup>-6</sup> mbar), using the same backing pumps as the oil-diffusion pump. The flight-tube is pumped by another turbomolecular pump (Turbovac 361, 1242 m<sup>3</sup>/h, Leybold) to reach a final vacuum of about 2·10<sup>-8</sup> mbar, whereby the pre-vacuum is provided by another two-stage rotary vane pump (TRIVAC D40B, 40 m<sup>3</sup>/h, Leybold).

As the graphite target carrying the investigated sample has to be exchanged at short intervals when using the desorption source, an air lock has been mounted on the side of chamber (a), which allows an exchange of the target while keeping the desorption chamber under high vacuum. The air lock (see figure 14), consisting of a small additional vacuum chamber which is separated from the source chamber (a) by a gate valve, is pumped by a two-stage rotary vane pump (either TRIVAC D8B, 8 m<sup>3</sup>/h, Leybold or TRIVAC D16B, 16.5 m<sup>3</sup>/h, Leybold) to reach a pressure of 10<sup>-3</sup> mbar.

In the following subchapter the laser desorption source, implemented in chamber (a) and generating the seeded molecular beam, is described in detail.

### *Laser desorption source*

The laser desorption source applied in this work was constructed and implemented into the molecular beam apparatus by the former group member Dr. Markus Becherer. This setup is based on the design used in the group of Prof. Dr. Anouk Rijs (now at Vrije Universiteit Amsterdam).<sup>[105]</sup> A detailed view of the laser desorption source used in the Gerhards group is presented in figure 11 below.

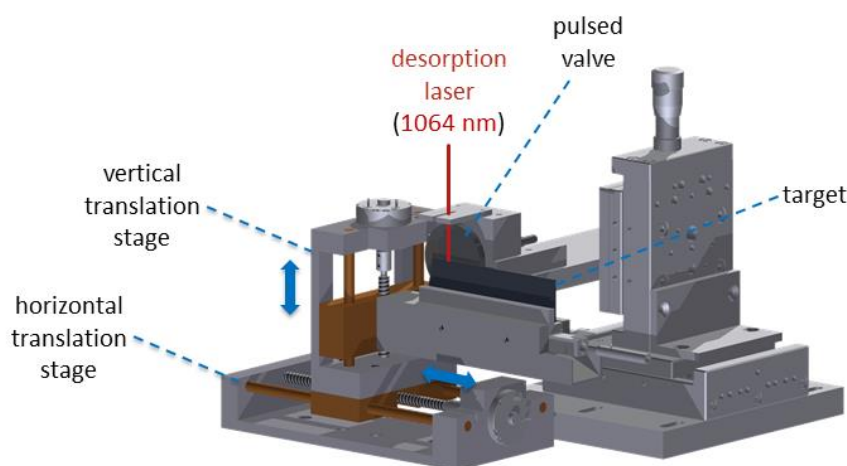


Figure 11: Schematic drawing of the laser desorption source used in the Gerhards group.

The molecular beam is generated by a pulsed valve (General Valve, Series 9, 500  $\mu\text{m}$  orifice), whereby argon (instead of helium) proved to be the most appropriate carrier gas. Backing pressures of 2.2-3.0 bar (relative to lab atmosphere) provided efficient vibrational/rotational cooling during the adiabatic expansion. The opening time of the valve can be adjusted and was systematically maintained at 210-220  $\mu\text{s}$ . In the beginning of this work, the gas load coming out of the valve was further optimized by adjusting its cap. Hereby, the optimized setting, yielding the most intense ion signals, went along with pressures of about  $1.0\text{-}1.2 \cdot 10^{-4}$  mbar in the source chamber with running pulsed valve.

The graphite target (75x24x3 mm) with the investigated compound is mounted in front of the pulsed valve, whereby a mixture, composed of the probed substance and the chosen matrix (soot, graphite powder or active charcoal powder), is put on the narrow target edge with a reduced width of only 1 mm (figure 12). Compared to laser desorption sources using pellets as target<sup>[100,112]</sup>, the setup used here has the advantage that smaller amounts of substance are required.

Targets ready for experiment are obtained by preparing a mixture of a certain amount of the investigated compound and the chosen matrix substance before smoothly pressing it onto the surface of the graphite bar. Hereby, the ratio between the investigated compound and the matrix substance can be adapted individually, whereby a ratio of approximately 1:1 was used for most experiments.

During the present work this handling was crucially optimized. Concretely, the employed amount of probe mixture was enlarged, while the force applied to press the substance onto the graphite target was deliberately kept more moderate. In this way, targets carrying a substantial (clearly visible to the naked eye) and homogenous substance layer were systematically obtained. This was a major step towards an increased ion signal intensity and improved signal stability.

Another crucial aspect is the specific choice of the most appropriate matrix substance. For the first laser desorption experiments with the new setup soot and partly graphite powder were applied as matrix. Graphite-based laser desorption matrices are indeed very commonly used by many groups.<sup>[99,102,106,112,113]</sup> The group of Fernández and Coccinero, however, also applied carbon nanotube matrices for the investigation of specific compounds where the ion signal intensity was rather weak.<sup>[114]</sup> Carbon nanotubes have the advantage that they have an exceptionally large surface at a molecular level<sup>[115]</sup>, which may facilitate the uptake of energy introduced into the matrix by the desorption laser. During this work, the main trigger was to look for another maybe more efficient matrix substance than soot or graphite powder. No experiments using carbon nanotubes were performed, as these materials are known for being hazardous to the lungs and even cancerogenic.<sup>[116]</sup> Furthermore, carbon nanotubes are rather expensive. Another approach was to use active charcoal powder as laser desorption matrix, since it is comparatively cheap and has a very high pore surface area.<sup>[117]</sup> On top of that, charcoal is not associated with any major health issues as it is the case for carbon nanotubes. To the best of my knowledge no studies where active charcoal powder was chosen as laser desorption matrix have been published up to now, but in the present work this “new” matrix substance led to considerably increased ion signal intensities (up to a factor of 3-4) and a substantially ameliorated ion signal stability. This was without any doubt a crucial step towards the first UV- and especially combined IR/UV-spectroscopic experiments with the new setup.

The prepared graphite target (see figures 11 and 12) is put into a target holder which is pushed into a rail to fix the target just in front of the pulsed valve (within 2 mm from the valve cap). During an experiment the height of the graphite target relative to the valve can principally be adapted, as indicated by the vertical blue arrows in figure 11. Hereby, movements are realized by a small DC-motor (2619S024S R 814:1, Faulhaber). An optimal ion signal was commonly obtained when the target surface carrying the probe was placed about 1 mm below the nozzle. This is valid both for investigations on isolated molecules as well as for aggregates (homodimers). The fact that efficient cluster formation

occurred (see subchapter 5.1.1) shows that the expansion conditions were well-adjusted with the described settings, as clustering of molecules in combination with a laser desorption source is generally less evident than with a thermal source (with more efficient adiabatic cooling). The graphite target is moved continuously (as indicated by the horizontal blue arrows in figure 11) during the measurement by a small DC-motor (2619S024S R 814:1 or 2619S024S R 1257:1, Faulhaber), so that the desorption laser (1064 nm, Continuum Minilite, 10 Hz) hits fresh sample with every single shot. As a high translation velocity generally goes along with an improved ion signal stability, the translation motor voltage was generally kept at a value which corresponds to a measurement duration of 30 min before the next target exchange.

For further illustration of the setup, a sketch of the desorption laser beam path is shown in figure 12.

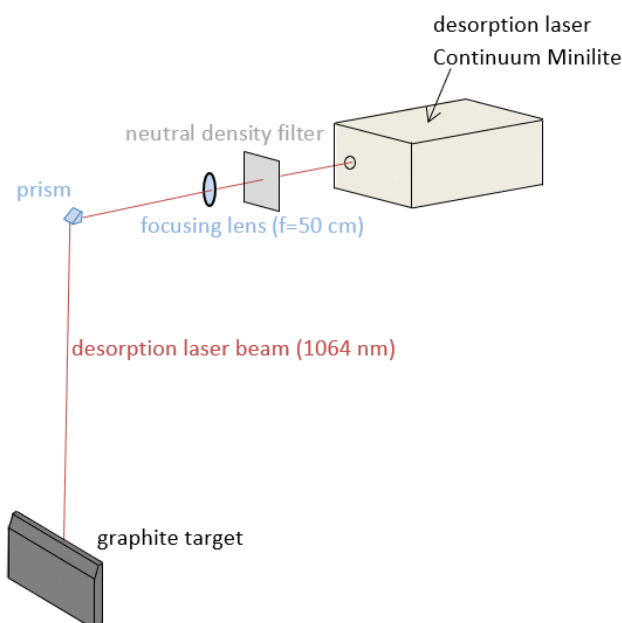


Figure 12: Sketch of the desorption laser beam path.

The desorption laser is mounted onto a framework above the desorption chamber and the desorption laser beam is deflected by 90° by a prism in the way to perpendicularly hit the target on the axis of the molecular beam, so that the desorbed material is carried off by the gas pulse. The laser is mildly focused onto the target surface by a convex CaF<sub>2</sub>-lens (f= 50 cm), using rather moderate desorption laser powers in the range of 1.5-2.5 mJ/pulse (which are thus lower than for laser ablation/vaporization cluster sources (~10 mJ/pulse)<sup>[75]</sup>) to ensure a soft desorption process.

### *Experimental operation*

The seeded expansion is generated by the laser desorption source as described above. After a distance of about 40 mm from the laser desorption source, the molecular beam passes through a skimmer into the ionization chamber, whereby the outer turbulent part of the beam is skimmed off. In the second chamber, the aromatic molecules are ionized *via* an R2PI process and after passing through a field-free drift zone of about 20 mm the center of the Wiley-McLaren arrangement<sup>[118]</sup> is reached, which is composed of three acceleration plates, with high voltage pulses being applied to the two lower plates (VA1 and VA2 in figure 10 b)), while the upper plate is grounded. For all the experiments the same voltage settings were used with VA1: +3850 V and VA2: +3322 V. The two potentials are applied by two fast high voltage switches (HTS 50, Behlke), accelerating the ions into the field-free flight tube, perpendicular to the propagation direction of the molecular beam. With this pulsed setup, the occurrence of a constant background ion signal is thus avoided. In the field-free drift zone, the ions pass between the VXY-deflection plates, with voltages of +210 V or +260 V (when investigating compounds with  $m/z > 500$ ) being applied. This ion optic is required in order to compensate for the horizontal drift component in the propagation direction of the molecular beam remaining after ion extraction. The ions are then mass-resolvedly detected at the micro channel plate (MCP) detector in chevron arrangement. Hereby, the apparatus can be run in the linear time-of-flight mode or alternatively in the reflectron TOF mode, whereby the ions are then detected at the second MCP detector. In this work all experiments were performed in the linear TOF mode, mainly because the efficient ion velocity focusing under reflectron TOF conditions hinders the “reference ion signal correction” approach applied for all combined IR/UV experiments, which is described further down. The MCP detector is supplied with a total voltage of –3780 V, which is split up by a cascade of resistors (VD1 = 44 %, VD2 = 24 %, VD3 = 4 %) and applied to the MCPs. The signal is amplified by a low-noise wideband amplifier (HVA-200M-40-B, 40B, Femto) and visualized with a digital oscilloscope (TDS 520A, Tektronix). All spectra are recorded by LabVIEW-based software programs installed on a computer, interacting with the oscilloscope *via* a GPIB interface.

As already mentioned, the experiments are performed in pulsed operation at a repetition rate of 10 Hz. Hereby, the pulse driver triggering the pulsed valve acts as master trigger. Thus, every pulse sequence starts with the opening of the gas valve, while all the other processes, namely the flashlamps and Q-switches (pockels cells) of the Nd:YAG lasers, the oscilloscope as well as the high voltage switches (acceleration pulses) are triggered at specific time delays *via* two digital delay generators (DG 535, Stanford Research Systems). The optimized timing on the example of the IR/R2PI experiments performed in this work is presented in figure 13.



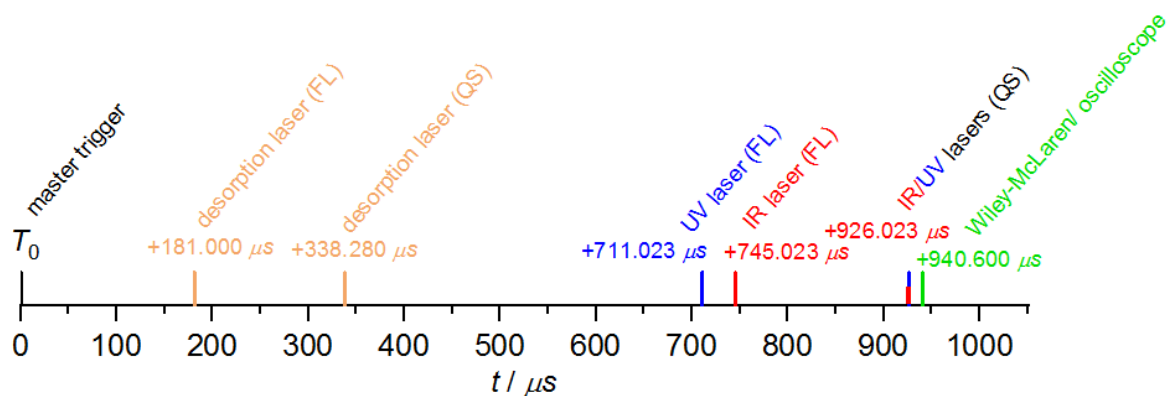


Figure 13: Temporal sequence of all processes on the example of an IR/R2PI experiment. The given time delays indicate the optimized trigger delays relative to the master trigger (opening of the pulsed valve).

It should be noted that, even if the same delay for the IR and UV laser pockels cell triggers is set at the delay generator, both lasers do not cross the molecular beam simultaneously. With the optimized timing, the IR laser reaches the molecular beam about 50 ns prior to the UV laser, as required for an IR/R2PI experiment (see chapter 2.2). For the UV/UV/IR scans exactly the same experimental conditions were maintained, the only difference consisting in the adapted timing of the IR laser (fired about 100 ns later than for IR/R2PI). Regarding the 2C-R2PI investigations, the timing of the two independent UV lasers was also synchronized, so that they simultaneously crossed the molecular beam.

As mentioned above, targets are exchanged *via* an air lock installed on the side of the desorption chamber. On the basis of figure 14, it should be clarified how samples are pulled out or implemented.

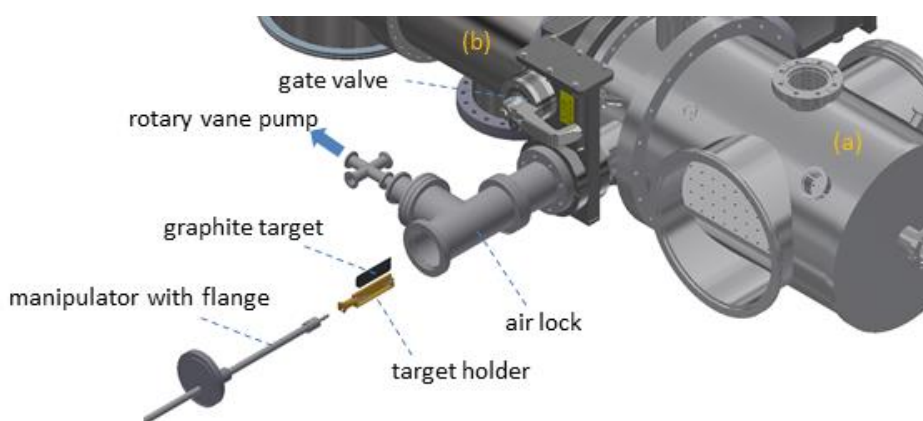


Figure 14: Schematic view of the air lock with its most relevant parts.

When a new target is inserted, the graphite bar is put into the target holder, which is then mounted onto the tip of the so-called “manipulator”. This manipulator is required to implement or remove a target from the desorption chamber (a). The manipulator is provided with a flange, so that it can be

mounted on the T-shaped tube of the air lock, prior to evacuation with the rotary vane pump. After reaching a pressure of about  $1 \cdot 10^{-2}$  mbar, the gate valve (Co. VAT) towards the source chamber can be opened to push the target into the target rail just in front of the pulsed valve. After inserting the target, the manipulator bar is pulled backwards and the gate valve can then be closed again. As soon as the measurement cycle is finished, the target is removed from the apparatus in the same manner.

#### *Reference ion signal correction*

Although the described optimization steps had been realized, the ion signal fluctuations observed in the laser desorption experiments turned out to be too significant to perform combined IR/UV experiments, especially if vibrational modes of rather low oscillator strength were of interest. Up to then, even the experimentally most demanding investigations on neutral molecules/aggregates performed in the Gerhards group were successfully carried out by simply averaging a considerable number of scans. However, these experiments had all been executed in combination with a thermal source, where the signal-to-noise ratio is in general far better than when applying a laser desorption source.<sup>[39,119]</sup> Therefore, a “reference signal correction” method was established in this work, to make the IR/UV spectroscopic techniques accessible in combination with the new laser desorption setup. Within that, the ionizing UV laser beam is redirected after passing through the molecular beam in order to cross the interaction region a second time, as illustrated in figure 15 a).

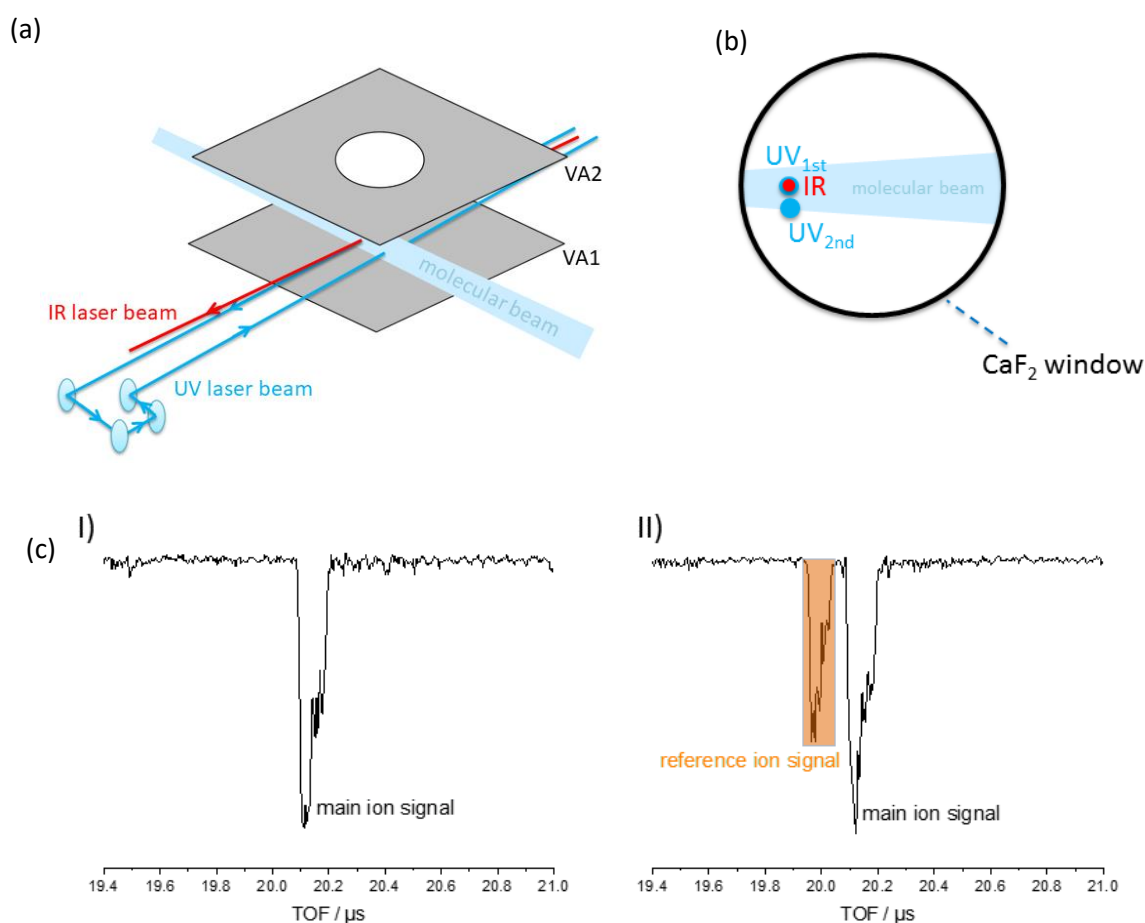


Figure 15: “Reference ion signal correction” with (a) sketch of the UV/IR laser beam paths, crossing the molecular beam between the acceleration plates of the TOF mass spectrometer; (b) side view through the CaF<sub>2</sub>-windows of the ionization chamber with the UV laser beam crossing the molecular beam at two distinct heights (UV<sub>1st</sub> and UV<sub>2nd</sub>); (c) (I): mass spectrum with the UV laser beam passing once through the interaction region (only UV<sub>1st</sub>), (II): mass spectrum with the UV laser passing twice through the interaction region (UV<sub>1st</sub> and UV<sub>2nd</sub>).

In this way, two clearly separated mass signals for exactly the same mass-to-charge ratio ( $m/z$ ) can be obtained as shown in figure 15 (c), provided that the Wiley-McLaren settings are slightly off the ideal mass focusing conditions. Here, it should be noted that an optimal setting of the Wiley-McLaren setup would largely compensate for the initial spatial separation of both ion packets. A further precondition for this “reference signal” approach is that the molecular beam has to be crossed at two distinct heights (difference of  $\sim 5$  mm) relative to the acceleration plates (see figure 15 (b)), because of the perpendicular orientation of the time-of-flight mass spectrometer axis relative to the propagation direction of the molecular beam. Concretely, the bunch of molecules which is ionized at the second passage of the UV laser beam through the interaction region (UV<sub>2nd</sub> in figure 15 (b)) is closer to the repeller plate (VA1 in figure 15 (a)) of the mass spectrometer than particles that are hit at its first

passage (UV<sub>1st</sub>). In consequence, the ion packet of UV<sub>2nd</sub> experiences a stronger electric field and thus a slightly harder acceleration towards the flight tube than ions generated by UV<sub>1st</sub>. Along the field-free drift zone, the ion packet of UV<sub>2nd</sub> can therefore overtake the ions formed by UV<sub>1st</sub>. This explains why the additional “second” mass peak (marked in orange in figure 15 (c)) appears at a shorter time-of-flight than the “main ion signal”.

Assuming that the UV laser beam is ideally overlapped with the molecular beam when it passes for the first time through the interaction region, the molecular beam can only be “grazed” when the UV laser passes a second time. Mainly for this reason, but also due to the inevitably reduced laser power after this long beam path, the “second” ion signal (with shorter time-of-flight) is generally weaker in intensity than the “main ion signal”. Therefore, the IR laser beam is spatially overlapped with the first point of interaction between the UV laser beam and the molecular beam, so that the analyte molecules of the intense “main ion signal” interact with the wavelength-tuned IR laser. At the same time, the “second”, smaller ion signal is only affected by signal fluctuations and is taken as “reference ion signal”. In the IR/R2PI experiments scans on the “main ion signal” are recorded, while parallel measurements are performed on the “reference ion signal”. Finally, the intended reference signal correction is realized by taking the ratio between the “main ion signal” and “reference ion signal” mass traces, which largely eliminates the strong background signal fluctuations. For illustration, two IR/R2PI spectra (for Cs<sup>+</sup>PABA<sup>-</sup>) are depicted in figure 16. For spectrum (a) the “reference ion signal correction” was applied, while spectrum (b) was obtained by (“classical”) simple averaging of exactly the same scans without considering the “reference ion signal” in the evaluation. In (b) the resonance at 3419 cm<sup>-1</sup> hardly comes out, while it is very clearly resolved in (a).

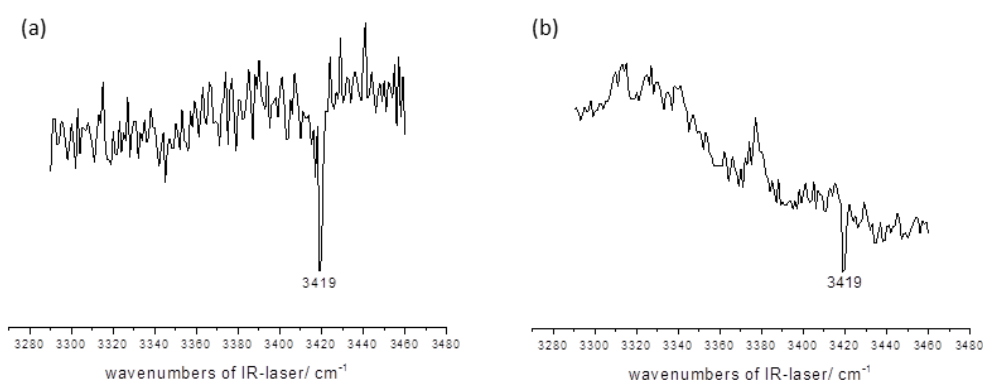


Figure 16: Illustration of the effect of the “reference ion signal correction” approach. Spectrum (a) was obtained by applying the new approach. Spectrum (b) was obtained by simple averaging of exactly the same scans.

The effect of the described “reference ion signal correction” is most notable if the two mass signals are of similar intensity. This could often be realized by intentionally non-optimally overlapping the UV laser beam ( $UV_{1st}$ ) with the molecular beam at the first interaction to obtain two mass peaks of comparable size.

The described “correction method” is similar to the techniques used by the groups of Lee<sup>[52]</sup>, Zwier<sup>[120]</sup>, Kleinermanns<sup>[121]</sup> and Mons<sup>[112]</sup>. Hereby, it should be noted that the molecular beam apparatus used by the Mons group has the advantage that the time-of-flight mass spectrometer is mounted downstream along the propagation axis of the molecular beam. In that case the UV laser beam can be ideally overlapped with the molecular beam for both the first and the second interaction, whereby two separated mass signals for the same  $m/z$  can still be obtained.

It is also worth mentioning that many other groups commonly carry out so-called on/off measurements with the UV laser running at 10 Hz, and the IR laser at 5 Hz (or optionally the UV laser at 20 Hz and the IR laser at 10 Hz) to correct for ion signal fluctuations.<sup>[104,105,107,122]</sup> Within this approach, the IR depletion spectrum is finally obtained by subtracting (or dividing) signals recorded with and without IR laser.

## 4 Theoretical methods

Accurate theoretical predictions are often essential assets to molecular beam spectroscopy, as assignments of specific structural motifs on the sole basis of experimental spectra are rarely possible. Therefore, quantum chemical calculations were performed on all investigated systems, partly by my colleagues Patrick Strebert and Marcel Meta as well as by myself. In the present work mostly geometry optimizations, harmonic vibrational frequency calculations and NBO population analyses were carried out using dispersion corrected DFT, as well as the ADC(2) and CC2 approaches. In the way to further confirm (maybe unexpected) trends obtained within DFT, single point calculations at the DLPNO-CCSD(T) level were additionally performed for some clusters.

In the following, the theoretical methods applied in this work will be briefly introduced, while the energy decomposition approaches are discussed in detail in the PhD thesis of Patrick Strebert as well as in publication 2.

### 4.1 Density Functional Theory (DFT)

Unlike the *ab initio* approaches (such as the Hartree-Fock (HF) method<sup>[123]</sup>), density functional theory does not require the exact wavefunction to describe a molecular system. Concretely, it has been postulated that the ground state properties of a system can be fully described by its spatially varying electron density  $\rho(\vec{r})$ .<sup>[124]</sup> This postulation was finally proven by Hohenberg and Kohn in 1964.<sup>[125]</sup>

In other words, this means that the properties of a compound in its ground state are functionals of the electron density. On that basis, Kohn and Sham<sup>[126]</sup> suggested the following approach for the ground state energy of a system comprising  $N$  paired electrons:

$$E[\rho(\vec{r})] = -\frac{1}{2} \sum_i^N \langle \varphi_i | \nabla^2 | \varphi_i \rangle + \frac{1}{2} \sum_i^N \sum_j^N \iint |\varphi_i(\vec{r}_1)|^2 \frac{1}{r_{12}} |\varphi_j(\vec{r}_2)|^2 d\vec{r}_1 d\vec{r}_2 + E_{XC}[\rho(\vec{r})] - \sum_i^N \int \sum_A^M \frac{Z_A}{r_{iA}} |\varphi_i(\vec{r}_1)|^2 d\vec{r}_1 \quad (1)$$

Herein, the first term describes the kinetic energy of the electrons, the second term represents the Coulomb interaction between the total charge distributions and the last term describes the electron-nucleus attractions. The remaining term  $E_{XC}(\rho)$  represents the exchange correlation energy of the electrons, which is a functional of the electron density.

In equation (1),  $\varphi_i$  represents the Kohn-Sham orbitals, which are in relation to the electron density distribution:

$$\rho(\vec{r}) = \sum_k^N |\varphi_k(\vec{r})|^2 \quad (2)$$

Thus, equation (1) can also be written as:

$$E[\rho(\vec{r})] = -\frac{1}{2} \sum_i^N \langle \varphi_i | \nabla^2 | \varphi_i \rangle + \frac{1}{2} \int \frac{\rho(\vec{r}_1)\rho(\vec{r}_2)}{r_{12}} d\vec{r}_1 d\vec{r}_2 + E_{XC}[\rho(\vec{r})] - \sum_A^M \int \frac{Z_A}{r_{1A}} \rho(\vec{r}_1) d\vec{r}_1 \quad (3)$$

The one-electron Schrödinger equations, also referred to as Kohn-Sham equations, are then obtained by applying the variational principle to  $E[\rho(\vec{r})]$ :

$$\left( \frac{1}{2} \nabla^2 + \left[ \frac{\rho(\vec{r}_2)}{r_{12}} d\vec{r}_2 + V_{XC}(\vec{r}_1) - \sum_A^M \frac{Z_A}{R_{1A}} \right] \right) \varphi_i = \varepsilon_i \varphi_i \quad (4)$$

Hereby  $\varepsilon_i$  stands for the energy of the Kohn-Sham orbital  $i$  and  $V_{XC}$  is the exchange-correlation potential. It can be noted that for an  $N$  electron system,  $N$  one-electron Schrödinger equations have to be solved.

$V_{XC}$  is a functional derivative of the exchange-correlation functional  $E_{XC}[\rho]$ :

$$V_{XC}[\rho] = \frac{\partial E_{XC}[\rho]}{\partial \rho} \quad (5)$$

The exact exchange-correlation functional  $E_{XC}[\rho]$  is not exactly known, so that the Kohn-Sham equations have to be solved *via* iteration. The required approximation of the exchange-correlation term  $E_{XC}[\rho]$  is a major challenge within density functional theory. Therefore, several approaches, like the local density approximation (LDA)<sup>[127]</sup> or the generalized gradient approximation (GGA)<sup>[128]</sup>, have been developed. Regarding the calculation of many molecular properties like geometries, vibrational frequencies and rotational constants so-called hybrid functionals, incorporating a portion of Hartree-Fock exchange energy, yield accurate results for most systems. One of the most common hybrid functionals is the B3LYP functional<sup>[128,129]</sup>, which was also used in this work.

A significant deficiency of DFT is that it cannot properly describe dispersion interactions, although they play a key role in non-covalently bound aggregates and within larger molecules (*e.g.* peptides<sup>[33]</sup>). Therefore, Grimme<sup>[130–132]</sup> and few other groups<sup>[133]</sup> developed different dispersion correction terms, which are subtracted from the conventional DFT energy:

$$E_{dispersion\ corrected\ DFT} = E_{KS-DFT} - E_{disp} \quad (6)$$

whereby  $E_{KS-DFT}$  is the uncorrected DFT energy, while  $E_{disp}$  is the respective correction term which is composed of two and three body terms:

$$E_{disp} = E^{(2)} + E^{(3)} \quad (7)$$

Herein the most important two body term  $E^{(2)}$  is defined as:

$$E_{disp}^{(2)} = -\frac{1}{2} \sum_{AB} \sum_{n=6,8,10,\dots} s_n \frac{C_n^{AB}}{r_{AB}^n} f_{d,n}(r_{AB}) \quad (8)$$

with the scaling factor  $s_n$ , the averaged  $n^{\text{th}}$ -order dispersion coefficient  $C_n^{AB}$  (orders  $n=6, 8, 10, \dots$ ) for an atom pair  $AB$ , the damping function  $f_{d,n}$  (needed to avoid singularities at small interatomic distances between  $A$  and  $B$ ), and  $r_{AB}$  being the internuclear distance.

Within this work, Grimme's D3-correction approach, published in 2010<sup>[131]</sup>, as well as the D3-correction with Becke-Johnson damping<sup>[132]</sup> were used.

The program packages Gaussian09<sup>[134]</sup>, Turbomole<sup>[135]</sup> as well as ORCA<sup>[136]</sup> give the possibility to perform *e.g.* geometry optimizations, harmonic vibrational frequency calculations as well as natural bond orbital (NBO)<sup>[137]</sup> analyses. Harmonic frequencies are generally scaled to account for anharmonicity, whereby either established (mode specific) scaling factors were taken from literature or appropriate factors were determined by performing reference calculations on simple model systems and referring to the corresponding experimental spectra. The specific scaling factors used for the various systems studied within this work are addressed in the respective subchapters.

When molecules or complexes of huge structural flexibility are investigated, local minima on the potential energy surface may be almost iso-energetic. In cases of fine energetic balances between multiple isomers, the zero-point vibrational energy (ZPE) and even the basis set superposition error (BSSE) can sometimes be decisive for the predicted energetic ordering. Therefore, all relative energy values given in this work systematically include the harmonic ZPE.

The basis set superposition error plays a role if two molecules are interacting within an aggregate, for example in a solute-solvent cluster or in dimers. Within a dimer  $AB$ , the basis functions of molecule  $A$  are shared by molecule  $B$  and *vice versa*. In other words, an increased number of basis functions is available for each monomer unit  $A$  or  $B$  (compared to the situation in an isolated monomer), which leads to an artificial stabilization of the aggregate  $AB$ . The described effect is particularly pronounced if small basis sets are used. To account for this artefact, the counterpoise method established by Boys and Bernardi<sup>[138]</sup> can be applied.

Besides the energetic minima on a potential energy surface, the interconversion barriers between distinct minimum structures may be of interest, since estimated isomerization barriers can provide valuable hints on the relative population of various isomers in the molecular beam experiments.



Transition state optimizations can for example be performed by applying the QST3<sup>[139]</sup> method implemented in Gaussian 09. For this, the required initial transition state guesses can for example be generated using the “woelfling” path finder<sup>[140]</sup> algorithm of Turbomole.

For some systems so-called relaxed potential energy surface (PES) scans can be realized, where *e.g.* a specific dihedral angle is varied (scanned) in a stepwise manner. Geometry optimizations are then performed at each fixed angle. This rather simple approach may however not be applicable in case of a more complex isomerization mechanism.

## 4.2 *Ab initio* methods

### 4.2.1 Coupled-Cluster Methods

Within Hartree-Fock (HF) theory, electron-electron interactions (electron correlations) are only considered by assuming that each electron feels all the other electrons in the system as an average charge cloud.<sup>[123]</sup> Different Coupled Cluster approaches, often called post-Hartree-Fock methods, were established to describe the explicit electron correlation.<sup>[141]</sup> One approach is the configuration interaction (CI) method<sup>[142,143]</sup>, where the wavefunction  $\Psi_{CI}$  is a linear combination of the HF ground state Slater determinant and the Slater determinants obtained by exciting electrons from occupied orbitals ( $i, j, k, l, \dots$ ) into non-occupied orbitals ( $a, b, c, d, \dots$ ):

$$\Psi_{CI} = \Phi_0 + \sum_{a,i} c_i^a \Phi_i^a + \sum_{i<j,a<b} c_{ij}^{ab} \Phi_{ij}^{ab} + \sum_{i<j<k,a<b<c} c_{ijk}^{abc} \Phi_{ijk}^{abc} + \dots = \left(1 + \sum_p^n \hat{C}_p\right) \Phi_0 \quad (9)$$

whereby the operator  $\hat{C}_p$  is used to describe the electronic excitations.

A so-called full CI approach, considering all possible configurations of a molecular system, is however computationally very demanding. That is why, the above linear combination is often truncated after the second or third term, so that only single (CIS) or single and double (CISD) excitations are considered.

A significant disadvantage of these two methods is their lack of size-consistency ( $E(A+B) \neq E(A) + E(B)$ , with  $A$  and  $B$  being two non-interacting systems). To overcome this deficiency, the following exponential coupled cluster approach can be applied<sup>[144]</sup>:

$$\Psi_{CC} = e^{\hat{T}} \Psi_0 \quad (10)$$

with the operator  $\hat{T} = \hat{T}_1 + \hat{T}_2 + \hat{T}_3 + \dots$ , which is equivalent to the operator  $\hat{C}_p$  and includes all electronic excitations.

Coupled cluster calculations are commonly performed with only single and double excitations (CCSD, scaling with  $\sim N^6$ , whereby  $N$  is a measure of system size), as the inclusion of triple excitations already requires much higher computational efforts (CCSDT, scaling with  $\sim N^8$ ).<sup>[145]</sup> Therefore, the third term  $\hat{T}_3$  is often treated using perturbation theory, which significantly reduces computational costs (scaling with  $\sim N^7$ ).<sup>[145]</sup> The latter approach, abbreviated with CCSD(T), is often considered as the “gold standard in quantum chemistry”.<sup>[146]</sup> Nevertheless, these variants are still limited to small molecular systems. That is why less expansive approximation methods were developed.

### SCS-CC2

The CC2 approach<sup>[143]</sup> is an approximated CCSD method, in which the double excitation part of the equations has MP2(Møller–Plesset perturbation theory)-like character<sup>[147]</sup>, while only the singles are fully treated *via* the iterative coupled cluster approach. Hereby, the obtained energies are of MP2 quality<sup>[143]</sup>, while computational costs are considerably reduced (scaling  $\sim N^5$  with increasing system size). In this way, also larger systems can be treated, which are difficult to access with higher correlated methods.

The spin-component scaling (SCS) approach, which introduces distinct scaling factors for the same-spin ( $\text{css} = 1/3$ ) and opposite-spin ( $\text{cos} = 6/5$ ) contributions to the correlation energy, is applied to improve the accuracy of the CC2 method.<sup>[148,149]</sup> That approach is ideally suited to compute electronic excitation energies<sup>[149,150]</sup>, besides its good performance regarding geometry optimizations and harmonic frequency calculations.

### DLPNO-CCSD(T)

Despite its huge success, the CCSD(T) method has the huge disadvantage that it is non-affordable for large systems due to a non-linear scaling with system size. By applying the “domain based local pair natural orbital” approaches DLPNO-CCSD and -CCSD(T), developed by Neese and coworkers<sup>[145,151]</sup>, fully linear scaling with system size can be achieved while considering about 99.9% of the total correlation energy<sup>[152]</sup>. This is realized by combining the pair natural orbital (PNO) approach with the concept of domain-based orbitals, whereby terms without any significant contribution are neglected. In other words, it is assumed that the electron correlation is a local phenomenon, with a strong weakening of electron-electron interactions upon increase of the inter-electronic distance.<sup>[153]</sup>

## 4.2.2 Algebraic Diagrammatic Construction (ADC) Methods

The Algebraic Diagrammatic Construction (ADC( $n$ )) approach is a family of excited state methods based on perturbation theory. Hereby, the ADC method of  $n$ -th order is the excited state equivalent of the  $n$ -th order Møller–Plesset (MP $n$ ) perturbation theory for the ground state. The second-order ADC (ADC(2)) method<sup>[154]</sup> can at the same time be considered as an approximation to the CC2 method presented above, neglecting the  $T_1$  amplitudes ( $\hat{T}_1 = 0$ ) and symmetrizing the Jacobian matrix.<sup>[141,155–157]</sup> Geometry optimizations and harmonic frequency calculations performed by using the ADC(2) approach are of CC2 accuracy, which also applies to predictions of electronic excitation energies. However, the mentioned symmetrization of the ADC approach is of crucial importance for physically correct descriptions in proximity of intersections between potential energy surfaces, where CC methods likely fail.<sup>[155–157]</sup>

The strict version of second order ADC (ADC(2)-s), also used in this work, scales with  $N^5$ , while its extended variant ADC(2)-x scales with  $N^6$ .<sup>[157]</sup> Similarly as for the CC2 approach, the accuracy of the ADC(2) method is considerably improved by applying its spin-component scaled variant SCS-ADC(2).<sup>[156]</sup>

## 5 Results and discussion

### 5.1 Laser desorption experiments

The first experiments combining the UV and IR/UV techniques with the newly established laser desorption setup were performed within this work. Crucial apparatus refinements were realized on the basis of these initial measurements, using the compounds *para*-aminobenzoic acid and the cyclic dipeptide cyclo Trp-Tyr. These spectra are discussed in subchapter 5.1.1, together with all relevant experimental details.

After these initial studies, investigations on various isolated contact ion pairs were performed. The results obtained for the monovalent *para*-aminobenzoate alkali ( $M^+PABA^-$ ) ion pairs are discussed in subchapter 5.1.2.2 and in manuscript draft [1]. The spectra recorded for the aggregates formed by complexation of a divalent metal ion ( $Mg^{2+}$ ,  $Ca^{2+}$ ,  $Ba^{2+}$ ) with two *para*-aminobenzoate ligands are presented in subchapter 5.1.2.3. All spectra recorded for the alkali *para*-methoxybenzoate ( $M^+PMBA^-$ ) and alkali benzoate ( $M^+BA^-$ ) ion pairs are discussed in subchapter 5.1.2.4.

In order to make first studies on a larger neutral isolated metal complex in the gas phase, investigations with the OLED relevant complex tris(8-hydroxyquinolato)aluminium ( $Alq_3$ ) were performed. These experiments are presented in subchapter 5.1.2.5.

### 5.1.1 Successful implementation of R2PI- and IR/R2PI experiments

In the following the first R2PI- and especially IR/R2PI spectra recorded with the newly established laser desorption setup are presented.

#### *para*-aminobenzoic acid monomer (PABAH)

In figure 17, the 1C-R2PI spectrum of the *para*-aminobenzoic acid (PABAH) monomer, chosen as reference substance for optimization of the laser desorption setup, is shown.

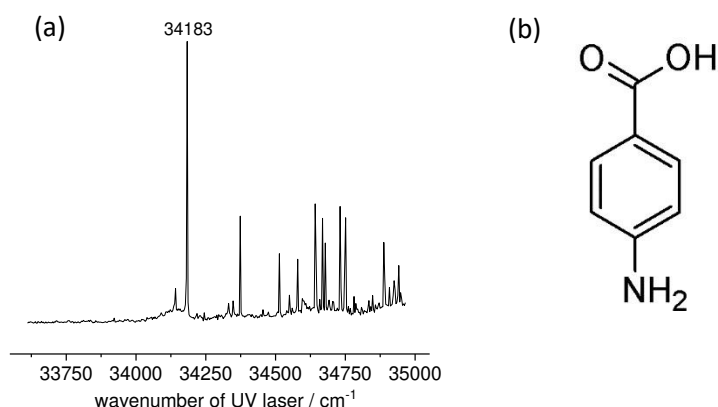


Figure 17: (a) 1C-R2PI spectrum of the *para*-aminobenzoic acid (PABAH) monomer; (b) schematic structure of PABAH.

This is the first R2PI spectrum recorded with the new source, where it turned out that the sharp  $S_1 \leftarrow S_0$  transitions observed by Meijer and de Vries *et al.*<sup>[94]</sup> can only be properly reproduced when argon (2.2 bar relative to lab atmosphere) is used as carrier gas instead of helium. Nowadays, argon is indeed almost exclusively used as carrier gas in combination with laser desorption experiments by many groups (*e.g.* <sup>[104,105,108]</sup>). In the Gerhards group, however, this step was somehow a novelty as up to that point, making use of a thermal source, almost all experiments have been performed in helium or neon as expansion gas, while attempts in argon were generally less successful. To avoid confusion, it should also be noted that all (1C- and 2C-)R2PI experiments presented in this thesis were realized without using any “reference signal correction”, which was only applied for combined IR/UV measurements.

After this achievement, the next step was to measure an IR/R2PI spectrum of PABAH in the way to couple the desorption setup with the combined IR/UV spectroscopic techniques. However, as discussed above within the context of the “reference signal correction” approach, the signal fluctuations due to the desorption source were too significant to record a valuable IR/R2PI spectrum. Finally, the newly established correction approach brought the decisive breakthrough. The obtained spectrum is shown below in figure 18.

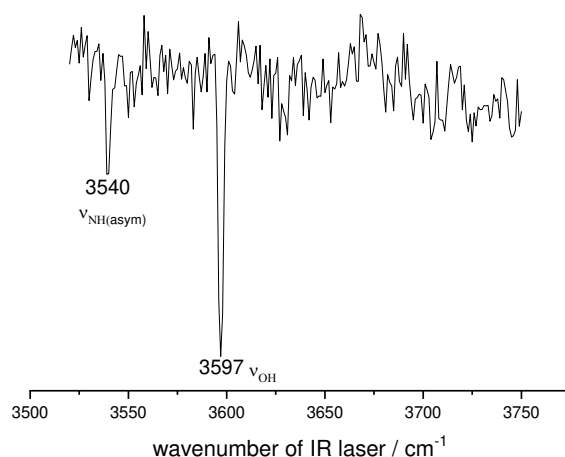


Figure 18: IR/R2PI spectrum of the *para*-aminobenzoic acid (PABAH) monomer in the region of 3520-3750 cm<sup>-1</sup>, measured *via* the  $0_0^0$ -UV transition at 34183 cm<sup>-1</sup>.

The asymmetric NH-stretching band of the amino group as well as the OH-stretching band of the carboxylic acid group are clearly resolved. The symmetric NH-stretching frequency is found at 3446 cm<sup>-1</sup> and was measured later on (see draft [1]).

### The cyclic dipeptide *cyclo Trp-Tyr*

After this, the next step was to investigate a larger molecule. Therefore, the cyclic dipeptide *cyclo Trp-Tyr* (*cyclo-L-tryptophanyl-L-tyrosine*; see figure 19 (b)) was chosen. The obtained IR/R2PI spectrum, measured *via* the R2PI resonance of the indole chromophore at  $35073\text{ cm}^{-1}$ , is depicted in figure 19 (a). The gap in this spectrum between  $3460$  and  $3520\text{ cm}^{-1}$  is due to the spectral gap of the used DFM1/OPA IR laser system (see chapter 3.1.2).

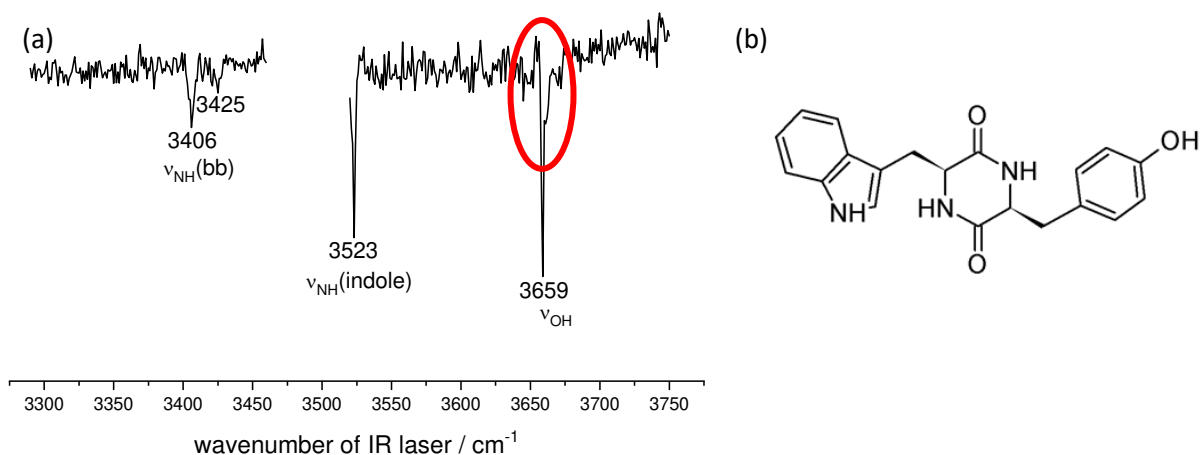


Figure 19: (a) IR/R2PI spectrum of *cyclo Trp-Tyr*, measured *via* the R2PI resonance at  $35073\text{ cm}^{-1}$ , with  $\nu_{\text{NH}}(\text{bb})$ : NH-stretching vibrations of the cyclic backbone; (b) molecular structure of *cyclo Trp-Tyr*.

Within this IR/R2PI spectrum the measured bands, especially the indole NH- and OH-stretching bands, are strikingly sharp, which underlines that the expansion conditions have been successfully optimized. At closer look, the circled region in the spectrum shows that the OH-stretching band is slightly asymmetric on the high-frequency side of the main peak. Therefore, the spectral region between  $3645$  and  $3685\text{ cm}^{-1}$  was scanned at a particularly high resolution (with a  $0.2\text{ cm}^{-1}$  step size), as shown in figure 20.

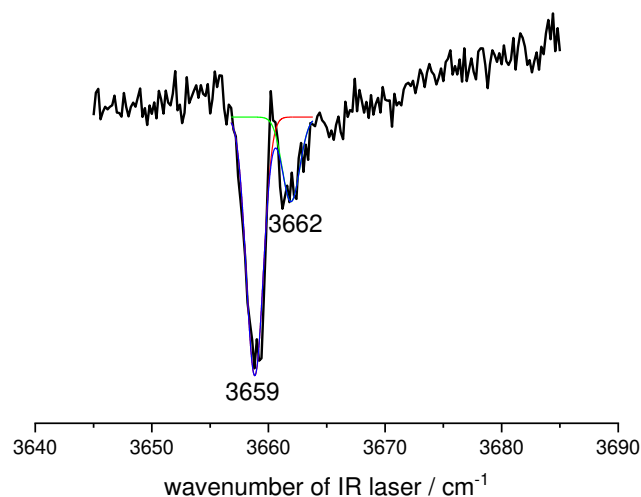


Figure 20: IR/R2PI spectrum of cyclo Trp-Tyr in the region from 3645 to 3685  $\text{cm}^{-1}$  including Gaussian fits, measured *via* the R2PI resonance at 35073  $\text{cm}^{-1}$  and scanned with a step size of 0.2  $\text{cm}^{-1}$ .

The spectrum in figure 20 clearly shows that, besides the strong peak at 3659  $\text{cm}^{-1}$ , there is another albeit smaller feature at 3662  $\text{cm}^{-1}$ , which is likely due to the presence of a second isomer. In figure 21, a comparison between the experimental IR/R2PI spectrum and the harmonically calculated IR spectra for the energetically most relevant geometries (see figure 22), as obtained at the DFT/B3LYP-D3/TZVP level, is depicted.

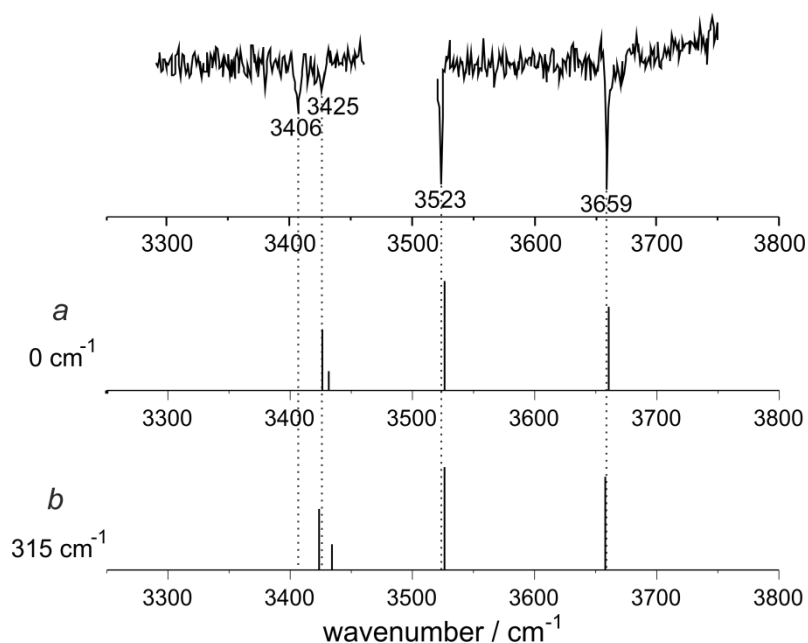


Figure 21: Comparison of the experimental IR/R2PI spectrum of cyclo Trp-Tyr and predicted vibrational frequencies obtained from DFT calculations (B3LYP-D3/TZVP) for the two energetically favored structural motifs *a* and *b*; scaling factors: 0.9608 for free NH-stretching frequencies<sup>[158]</sup>, 0.9593 for OH-stretching frequencies (determined by taking phenol as reference molecule). Also indicated are the relative Gibbs free energies (at 298.15 K) according to DFT.



Regarding the OH-stretching frequency as well as the NH-stretching frequency of the indole substituent, the calculated vibrational frequencies of both isomers *a* and *b* are in perfect accordance with the experimental spectrum. Concerning the spectral region of the stretching vibrations of the backbone NH groups around  $3400\text{ cm}^{-1}$ , however, the splitting of  $19\text{ cm}^{-1}$  between both bands observed in the experiment is in best accordance with the vibrational pattern predicted for isomer *b*. The slight differences regarding the splitting between the backbone NH-stretching frequencies are due to the distinct (although weak)  $\text{NH}\cdots\pi$  interactions.

Even if isomer *b* is, at least according to DFT, not the global minimum structure, it is predicted to be only  $315\text{ cm}^{-1}$  higher in energy, which makes an assignment of structure *b* to the experiment definitely feasible. The discussed geometries *a* and *b* are depicted in figure 22.

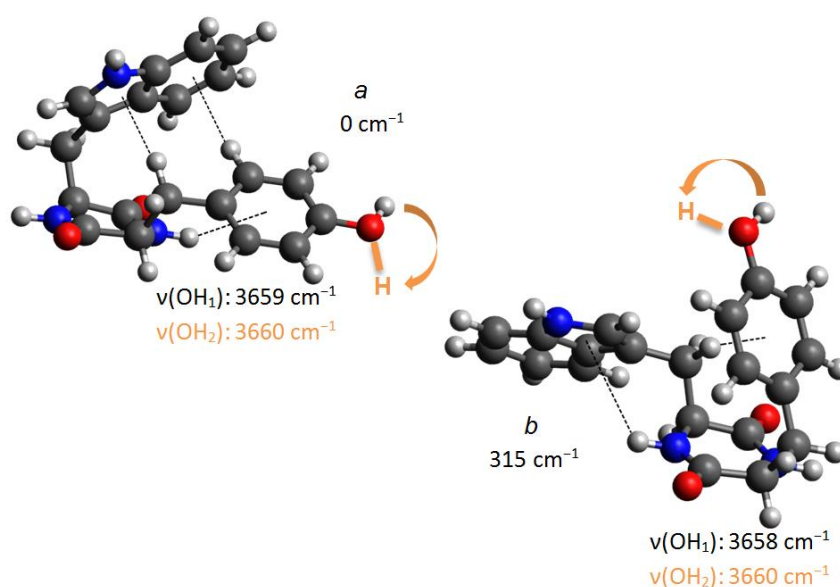


Figure 22: Optimized DFT (B3LYP-D3/TZVP) geometries and relative Gibbs free energies (calculated at 298.15 K) of isomers *a* and *b*. The structures of the corresponding OH-rotamers are indicated in orange, together with the respective OH-stretching frequencies of all rotamers. Scaling factor: 0.9593 (determined by taking phenol as reference molecule).

Both isomers *a* and *b* have in common that one aromatic residue (either Trp or Tyr) is folded over the cyclic peptide backbone, while the other aromatic substituent is turned away from this ring. For structure *a*, the  $\text{CH}_2$  group of Tyr as well as one of its aromatic C-Hs undergo  $\text{CH}\cdots\pi$  interactions with the extended  $\pi$ -system of the indole substituent, which lies above the cyclic backbone. Regarding isomer *b*, the indole substituent points away, while the  $\text{CH}_2$  group of Trp shows a  $\text{CH}\cdots\pi$  interaction with the aromatic ring of the Tyr residue, which is folded over the peptide backbone. Furthermore, weak  $\text{NH}\cdots\pi$  interactions occur between the backbone NH groups and the aromatic residues ( $\text{NH}\cdots\pi(\text{Tyr})$  for structure *a* and  $\text{NH}\cdots\pi(\text{Trp})$  for structure *b*).

Hereby, in particular geometry *b* is extremely similar to the structures that the Zehnacker group assigned for cyclo Tyr-Tyr<sup>[107]</sup> and cyclo Phe-Phe<sup>[159]</sup>. In the performed conformational analysis a multitude of other local minimum structures was found. Most of these isomers were, however, considerably higher in energy. One of these structures (not depicted here) could principally be assigned to the experiment, although it is higher in energy by 617 cm<sup>-1</sup>. Yet, this structure is very similar to the geometry of isomer *b*, since the  $\chi_2$  angle of the Trp residue is the only major structural difference relative to *b*.

Figure 22 also indicates the structures of the respective OH group rotamers of isomers *a* and *b*. Hereby, the geometries of the most stable rotamers are depicted, with the unfavored rotamer being 44 and 216 cm<sup>-1</sup> less stable for motifs *a* and *b*, respectively. Regarding motifs *a* and *b*, the calculated OH-stretching frequencies (see figure 22) predict a slight blue-shift of 1-2 cm<sup>-1</sup> for the OH-stretching frequencies of the less stable rotamers. As the feature at about 3662 cm<sup>-1</sup> in the experimental spectrum is indeed comparatively low in intensity, it seems conceivable to assign this band to an energetically higher rotamer. Concerning the intense NH-stretching band at 3523 cm<sup>-1</sup> no “additional” feature is obtained. However, the indole NH group is completely free for the discussed geometries, so that no considerable NH(indole)-frequency shifts may occur between two OH-rotamers. Regarding the backbone NH-stretching vibrations, the measured bands are so weak in intensity that such small effects as observed for the intense OH-bands may not be experimentally detectable anymore.

Finally, as mentioned above, structure *b* could most likely be assigned to the experiment. Due to an energetic gap of 216 cm<sup>-1</sup> between both OH-rotamers, the relative population of the energetically higher rotamer may be lower, which may explain the relative intensities of the measured OH-bands at 3659 and 3662 cm<sup>-1</sup>. The theoretical Boltzmann distribution predicts a population ratio of 0.35 between both rotamers at 298.15 K, which is a fair temperature to estimate population ratios in molecular beam experiments (*e.g.*<sup>[39,72]</sup>). At the same time, the deconvolution of the experimental spectrum (figure 20) yields a ratio of 0.34. Thus, there is indeed a very good correlation between the experimental and theoretical ratios. For motif *a*, both rotamers are energetically separated by only 44 cm<sup>-1</sup>, so that a more similar contribution of both rotamers would be very likely in that case (theoretical ratio of 0.81), which is however not in accordance with the measured IR/R2PI spectrum. This aspect makes the assignment of structural motif *b* even more conceivable.

Thus, even if the main aim of the investigations on cyclo Trp-Tyr was to extend the newly established combination of laser desorption and IR/UV techniques to a first larger molecule, a structural assignment could be made.

### The *para*-aminobenzoic acid dimer ((PABAH)<sub>2</sub>)

Since nowadays the aggregation behavior between two or even more molecules is often of particular interest in gas phase spectroscopy, a further step was to investigate a molecular aggregate by applying the R2PI and IR/R2PI techniques. Therefore, the homodimer of the previously investigated *para*-aminobenzoic acid ((PABAH)<sub>2</sub>) was studied. The R2PI spectrum of (PABAH)<sub>2</sub> is depicted in figure 23.

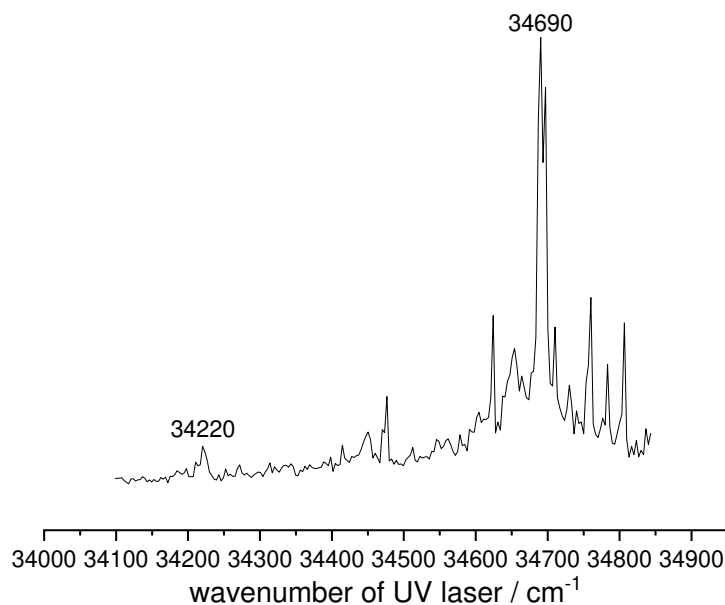


Figure 23: R2PI spectrum of the *para*-aminobenzoic acid dimer (PABA)<sub>2</sub>.

Within this spectrum, the  $0_0^0$  transition is blue-shifted relative to the electronic origin of the PABAH monomer by  $37\text{ cm}^{-1}$ , which is in good agreement with the spectra published by Meijer and de Vries *et al.*<sup>[94]</sup>. The IR/R2PI spectra were recorded *via* the intense R2PI resonance at  $34690\text{ cm}^{-1}$  to obtain a strong enough ion signal for the IR scans. Furthermore, it should be noted that the ion signal intensity of the dimer was significantly improved by increasing the argon backing pressure from 2.2 to 3.0 bar (relative to lab atmosphere). As expected, dimerization primarily occurs under the particularly cold expansion conditions at higher backing pressures. For most experiments on smaller molecules (*e.g.* for the  $M^+PABA^-$  ion pairs; see draft [1]), however, the backing pressure was deliberately maintained at only 2.2 bar to suppress the formation of (undesired) argon containing clusters. Clustering of the investigated molecule with argon frequently leads to crowded UV and IR spectra on lower (often most relevant) mass traces if these argon clusters undergo UV fragmentation upon photoionization.

The IR/R2PI spectrum of (PABAH)<sub>2</sub> is depicted in figure 24, together with its optimized DFT geometry.

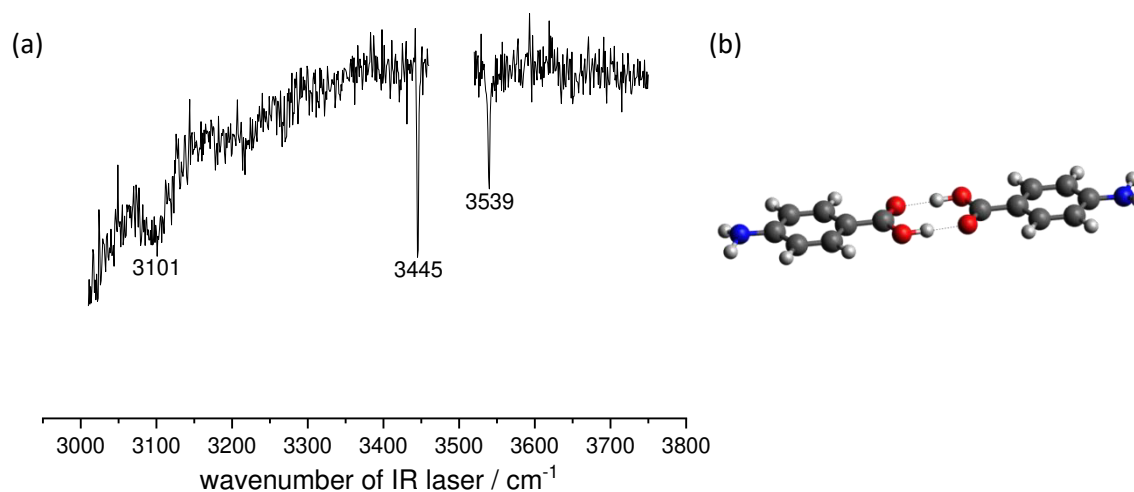


Figure 24: (a) IR/R2PI spectrum of the *para*-aminobenzoic acid dimer (PABAH)<sub>2</sub>, measured *via* the intense R2PI transition at 34690 cm<sup>-1</sup>; (b) Optimized DFT geometry of (PABAH)<sub>2</sub>, calculated at the DFT/B3LYP-D3/TZVP level.

Regarding the NH-stretching region, the spectrum is very similar to the IR spectrum of the PABAH monomer. The symmetric and asymmetric NH-stretching bands were found at 3445 and 3539 cm<sup>-1</sup>, which are thus almost identical to the values found for the PABAH monomer, with 3446 and 3540 cm<sup>-1</sup>. This observation is however not surprising, as the amino groups remain completely free within the expected dimer structure, cleared up by Meijer and de Vries through R2PI experiments supported by specific deuterations.<sup>[94]</sup> A major difference compared to the IR spectrum of the PABAH monomer is the obvious drop of the baseline towards 3000 cm<sup>-1</sup>, which is due to the OH-stretching frequencies of the strongly hydrogen-bonded carboxylic acid OH groups in the dimer structure. In the fluorescence dip IR spectra (FDIR spectra) measured for the dimers of the structurally related compounds anthranilic acid and salicylic acid, the OH-bands are indeed strongly red-shifted and extremely broadened, so that the “true baseline” is only reached at about 2700 cm<sup>-1</sup>.<sup>[58,59]</sup> However, the broad features in that spectral region were of minor relevance within the context of this work. In other words, the IR/R2PI spectrum of (PABAH)<sub>2</sub> was mainly recorded to validate the potential of the new laser desorption setup for further IR/UV investigations on isolated clusters. The shoulder around 3100 cm<sup>-1</sup> may be explained by (aromatic) CH stretching vibration(s).

*Laser desorption with larger organic molecules (of high mass-to-charge ratio (m/z))*

Apart from the spectra discussed above, attempts to investigate larger molecules were also made.

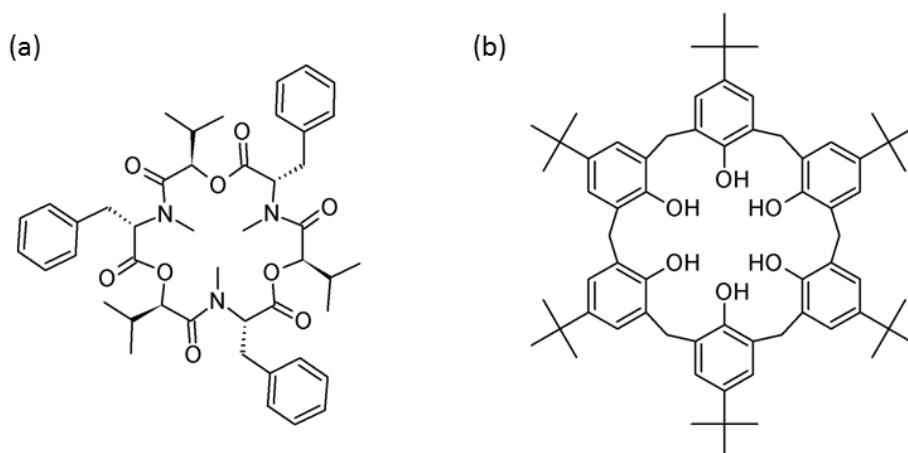


Figure 25: Molecular structures of (a) beauvericin; (b) 4-*tert*-butylcalix[6]arene.

In initial experiments with the cyclic hexadepsipeptide beauvericin (structure (a) in figure 25) the (charged) alkali adducts (with  $\text{Na}^+$ ,  $\text{K}^+$ ) were successfully detected, while the isolated neutral monomer species could not be found. Either the R2PI process for this neutral species was not efficient or there was no major amount of free uncomplexed beauvericin on the target. Since beauvericin is known to be a very efficient ionophore<sup>[160]</sup>, complex formation with the ubiquitous alkali ions  $\text{Na}^+$  or  $\text{K}^+$  is definitely conceivable. As there was only a very small amount of substance available, experimental possibilities were unfortunately very limited for this sample.

Therefore, test measurements with other organic macrocycles from the calixarene family were performed to further refine the experimental parameters. Calixarenes are organic macrocycles formed by hydroxyalkylation of phenol and aldehyde.<sup>[161]</sup> Specifically, 4-*tert*-butylcalix[6]arene, depicted in figure 25 (b), as well as its smaller structural analogue 4-*tert*-butylcalix[4]arene, with only four 4-*tert*-butylphenole monomer units, were investigated. These compounds were both intactly transferred into the gas phase by laser desorption, ionized within an R2PI process and subsequently detected in the mass spectrometer. For these species with comparatively higher  $m/z$  ratio, it turned out that an ion signal can be readily obtained with the same settings as for the “small” PABA species. However, the ion signal intensities were drastically lower for the large macrocycles. Slight improvements of the ion signals were realized by increasing the acceleration voltages up to 4200 V and 3770 V, respectively, as well as by adjusting the voltage applied to the MCP detector to -3964 V. Furthermore, the VXY-deflection voltages were set to +260 V (instead of 210 V) in order to compensate for the comparatively high inertia of heavier compounds.

However, the recorded R2PI and IR/R2PI spectra did not show any convincing features. The absence of any pronounced spectral effects is likely due to the less efficient adiabatic cooling if flexible molecules of this size are investigated. Furthermore, the ion signal intensities were still a limiting factor. In contrast, very impressive ion signal intensities were observed for most compounds of low molecular weight (*e.g.* for  $M^+PABA^-$  ion pairs, see draft [1]). At this point one should also note that a significant decrease of the photoionization efficiency with increasing molecular weight is to be expected, leading to a reduced ion signal size for larger molecules.<sup>[162]</sup> Apart from that, a reduced sensitivity of the time-of-flight mass spectrometer for high molecular weight species (with  $m/z \gg 500$ ) could be another limiting factor. Thus, the limitations of the used experimental setup were probably gradually reached.

Principally, there should still be room for further improvement, which would, however, likely entail greater expenditure. Given the change of the circumstances during the course of the present work, any more extensive remodeling of the laser desorption setup would have been beyond the scope.

## 5.1.2 Investigations on isolated contact ion pairs (CIPs)

### 5.1.2.1 Introduction

After the successful first R2PI and IR/R2PI experiments with the new desorption setup, the focus of this work turned towards investigations of isolated neutral contact ion pairs. Ion pairs are of major relevance in nature, as they *e.g.* play a key role in the self-assembly of charged oligomeric bilayers<sup>[19]</sup>, in ion transport through phospholipid bilayers<sup>[20]</sup> or in pharmacology, where the solubility of charged hydrophilic therapeutics is often regulated by targeted ion pairing<sup>[21,22]</sup>. On top of that, ion pairing is of crucial importance in organic synthesis, *e.g.* in asymmetric ion-pairing catalysis<sup>[23,24]</sup>. Therefore, it may not seem surprising that ion pairs have already been studied extensively, predominantly in various condensed phase experiments.<sup>[25,163,164,165]</sup> Despite this, the characterization of the intrinsic properties of ion pairs through experiments in condensed media is still a huge challenge, because their spectroscopy is evidently influenced by the surrounding medium.<sup>[25]</sup> A major challenge is the aspect that the structure of cation-anion pairs may fluctuate between three different ion pair types, namely the solvent separated ion pairs (SSIP, with intact primary solvation shells around both counterions), solvent shared ion pairs (SIP, with a single solvent layer between cation and anion) and finally the contact ion pairs (CIP, without any solvent molecules separating cation and anion), where no solvent molecules are separating cation and anion.<sup>[25,166,167]</sup> Due to these limitations in condensed media experiments, investigations on isolated contact ion pairs in the gas phase are an ideal tool to explore the intrinsic properties of ion pairs. Nevertheless, gas phase studies on isolated ion pairs are still very scarce, which may be due to the fact that the majority of ion pairs (salts) have a low vapor pressure, so that most of them cannot be transferred into the gas phase by simple heating. A few works on (comparatively volatile) ionic liquids, investigated by using thermal sources (*e.g.* <sup>[168]</sup>), as well as on ion pairs embedded in helium nanodroplets<sup>[169]</sup> have already been published. In 2016, the group of Mons and Gloaguen were the first to transfer isolated contact ion pairs (namely Li<sup>+</sup>⋯phenylacetate, Li<sup>+</sup>⋯benzylacetate as well as Li<sup>+</sup>⋯(4)-phenylbutyrate) into the gas phase by using a laser desorption source.<sup>[15]</sup> In their first publications, they performed UV and combined IR/UV experiments and discussed the high potential of the gained spectra as benchmark values for investigations on ion pairs in solution.<sup>[15,166]</sup> Later on they focused on Stark experiments, where huge resonance shifts were observed in the UV spectra upon substitution of the alkali ion (from Li<sup>+</sup> over Na<sup>+</sup>, K<sup>+</sup>, Rb<sup>+</sup> to Cs<sup>+</sup>) due to the tuned electric field strength of up to about 4 GV · m<sup>-1</sup> reigning within ion pairs.<sup>[14,170]</sup> Here, it should be pointed out that in common capacitor-based experiments, electric field strength of no more than 0.1 GV · m<sup>-1</sup> are reached.<sup>[170,171]</sup> Furthermore, they demonstrated by UV experiments on model ion pairs in a molecular beam, in combination with electric field calculations, that UV based Stark

spectroscopy in the gas phase has a high potential for conformational investigations of biomolecules.<sup>[14]</sup>

These particularly stimulating studies were the motivation to investigate isolated alkali ( $\text{Li}^+$  to  $\text{Cs}^+$ ) *para*-aminobenzoate ion pairs ( $\text{M}^+\text{PABA}^-$ ) within the present work (see draft [1]). Regarding the structure of these systems, the cation is doubly coordinated to the carboxylate group of the *para*-aminobenzoate anion. For the sake of clarity, the calculated geometry of an  $\text{M}^+\text{PABA}^-$  ion pair is exemplarily shown in figure 26 (a).

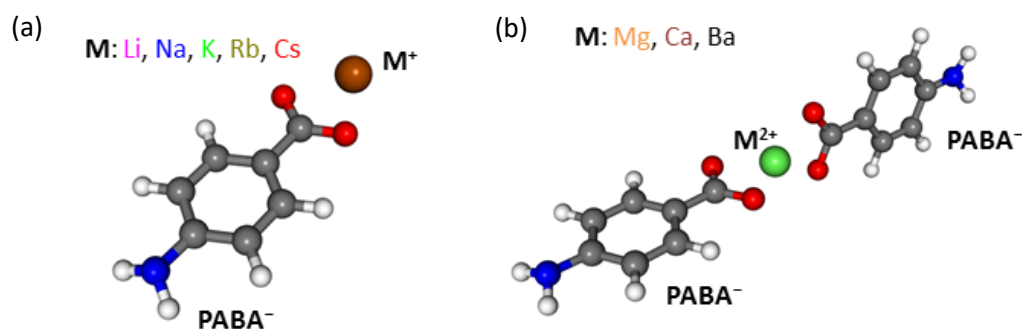


Figure 26: Molecular structures of a)  $\text{M}^+\text{PABA}^-$  ion pairs; b)  $\text{M}^{2+}(\text{PABA}^-)_2$  complexes. Geometries as obtained within DFT optimizations (using B3LYP-D3(BJ)/def2-TZVP).

As the binding motif is the same for all these ion pairs and the anion does not show any major conformational flexibility, trends observed in the (one color- and two color-)R2PI, IR/R2PI as well as UV/UV/IR experiments should be mainly due to electronic Stark effects. Specifically, the spectroscopic behavior of the *para*-aminobenzoate chromophore depends on the size of the coordinating alkali cation, leading to clear trends in both the UV and IR spectra. Regarding the IR/UV experiments, the NH-stretching frequencies of the amino group in *para* position were probed to get insights about the specific influence of the positive charge at this larger distance from the cation. This represents a novel aspect, as in the studies of Mons and Gloaguen the C=O-stretching vibrations of the carboxylate were investigated, whereby the cation is thus directly coordinated to the probed functional group.<sup>[15,166]</sup>

To the best of my knowledge, the ion current curves, recorded in order to estimate the ionization potentials of the different species, are the first ion current curves measured for isolated contact ion pairs. Moreover, the IR spectra recorded for the photoionized complexes (ionic ground state  $\text{D}_0$ ) contribute to the understanding of the studied systems and are the first  $\text{D}_0$  state IR spectra reported for CIPs so far.

Additionally, R2PI spectra were recorded for the structurally related alkali *para*-methoxybenzoate ion pairs as well as for the unsubstituted alkali benzoate ion pairs, yielding further information, especially regarding ion pair photostabilities. On top of that, small metal complexes comprising a divalent metal



center ( $\text{Mg}^{2+}$ ,  $\text{Ca}^{2+}$  and  $\text{Ba}^{2+}$ ) linked to two *para*-aminobenzoate units, as depicted in figure 26 (b), were investigated by R2PI spectroscopy, whereby the measured trends are in line with the observations for the respective monovalent alkali ion pairs.

To give an overview of the ion pairs investigated in this work, all successfully probed systems are highlighted in table 1 below.

Table 1: Overview of the alkali and earth alkaline ion pairs investigated in this work. All successfully probed cation–anion combinations are highlighted using green check marks.

	<i>para</i> -aminobenzoate ( $\text{NH}_2$ substituent)	<i>para</i> -methoxybenzoate (OMe substituent)	benzoate (no substituent)
Li	✓	✓	✓
Na	✓	✓	✓
K	✓	✓	✓
Rb	✓	✓	-
Cs	✓	✓	-
Mg	✓	-	-
Ca	✓	-	-
Ba	✓	-	-

All results are discussed in the following subchapters and partly in manuscript draft [1].

### 5.1.2.2 Isolated alkali/*para*-aminobenzoate contact ion pairs in gas phase: insights into nuclear and electronic structure by laser spectroscopy (see manuscript draft [1])

#### **Preamble:**

All laser desorption experiments were performed by myself. I conducted the DFT- and ADC(2) calculations. The concept was designed by myself, together with Christoph Riehn. The results were analyzed and interpreted by myself. Furthermore, I wrote an initial manuscript. The manuscript was revised by Christoph Riehn, Kirsten Schwing and myself. Christoph Riehn was my supervisor.

This chapter has been prepared as a manuscript draft for publication and is printed in chapter 7; see manuscript draft [1]. To give a short overview, the most important results and discussions are briefly summarized in the following.

#### **Summary:**

This project dealt with the spectroscopic investigation of isolated alkali (Li-Cs) *para*-aminobenzoate ion pairs ( $M^+PABA^-$ ). Within that, the main aim was to probe the structural and electronic behavior of the  $PABA^-$  chromophore in dependence of the size of the coordinating alkali cation (increasing from  $Li^+$  to  $Cs^+$  [172]). Structurally, the alkali cation is doubly-coordinated to the carboxylate group of  $PABA^-$ . The structure of the  $M^+PABA^-$  ion pairs is illustrated in figure 27 (a).

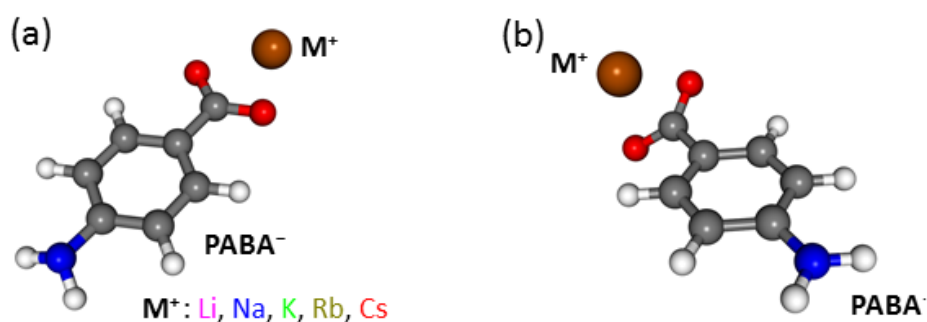


Figure 27: Optimized geometries of an  $M^+PABA^-$  ion pair in the  $S_0$  (a) and  $D_0$  (b) state. Structures as obtained at the DFT/B3LYP-D3(BJ)/def2-TZVP level.

As the binding motif of  $M^+$  to  $PABA^-$  does not change along the row from  $Li^+PABA^-$  to  $Cs^+PABA^-$ , the spectral effects observed in the measured UV and IR/UV experiments should result from electrostatic effects, rather than from geometric changes.

Various spectroscopic techniques (see subchapter 2) were applied to probe both the  $S_0$  and  $D_0$  state, namely 1C-R2PI, 2C-R2PI (ion current curves), IR/R2PI and UV/UV/IR. First of all, 1C-R2PI spectra (see figure 28) were recorded, revealing that the  $M^+PABA^-$  species exhibit well-defined electronic transitions, as already observed for the *para*-aminobenzoic acid monomer (PABAH).

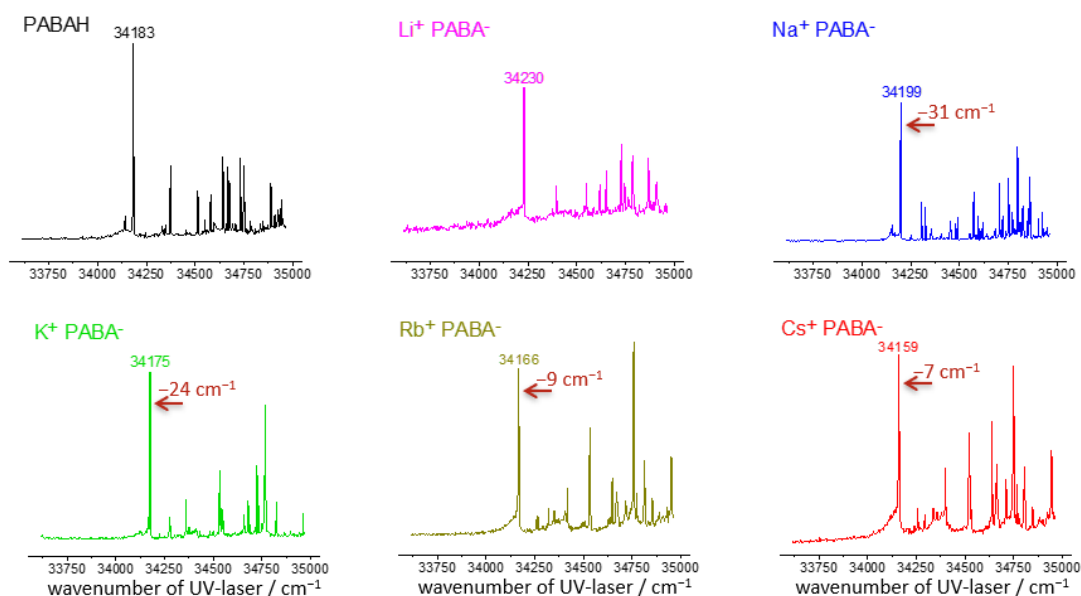


Figure 28: 1C-R2PI spectra of *para*-aminobenzoic acid (PABAH) and its alkali ion pairs  $Li^+PABA^-$ ,  $Na^+PABA^-$ ,  $K^+PABA^-$ ,  $Rb^+PABA^-$  and  $Cs^+PABA^-$  in the spectral range of 33613-34965  $cm^{-1}$ . For the ion pairs the shift of the  $0_0^0$  transition relative to the next smallest cation is given in dark red.

As indicated by the arrows in figure 28, the electronic origin transition ( $S_1 \leftarrow S_0$  transition of  $\pi \rightarrow \pi^*$  character) undergoes a successive red-shift when going from  $Li^+PABA^-$  over  $Na^+PABA^-$ ,  $K^+PABA^-$  and  $Rb^+PABA^-$  towards  $Cs^+PABA^-$ . Hereby, the relative frequency shifts decrease from 31  $cm^{-1}$  between  $Li^+PABA^-$  and  $Na^+PABA^-$  to only 7  $cm^{-1}$  between  $Rb^+PABA^-$  and  $Cs^+PABA^-$ . The pronounced correlation between the electronic origin and the size of the respective alkali ion can be demonstrated by plotting the frequencies of the  $0_0^0$  transition against the inverse radius of the coordinating cation (see figure 29 (a)). The obtained approximately linear dependence is in nice accordance with the Coulomb law.<sup>[173,174]</sup>

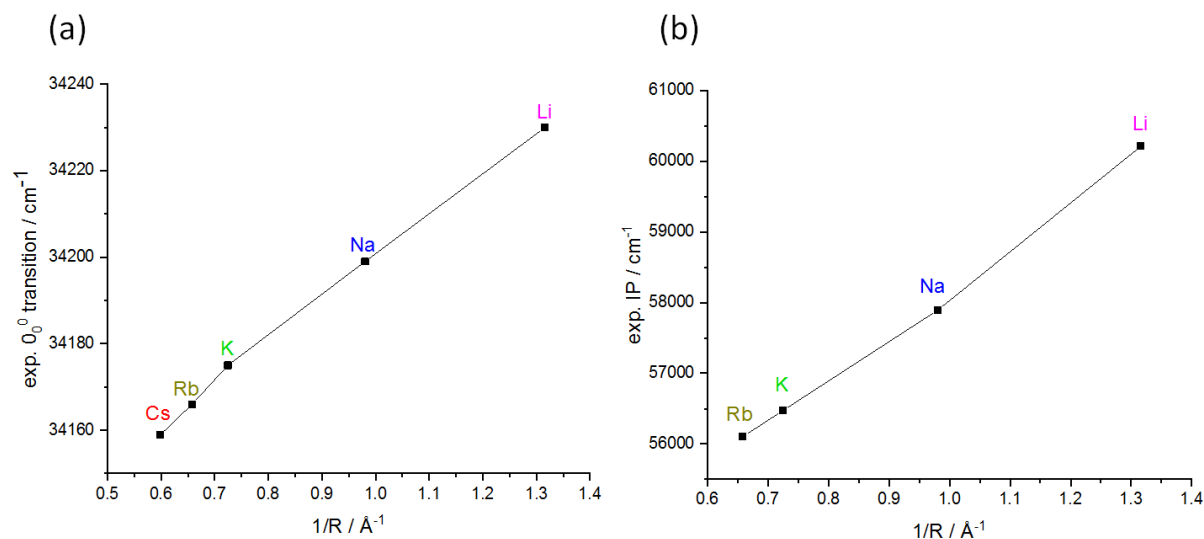


Figure 29: Correlation between (a) the electronic origin transitions and (b) the ionization potentials (IPs) and the inverse radius of the coordinating alkali ion.

The measured spectral shifts are relatively small, with the ion pairs exhibiting UV transitions in the same spectral region as the PABAH monomer. This is also reflected by the adiabatic excitation energies calculated at the SCS-ADC(2)/def2-TZVP level, predicting very similar  $S_1 \leftarrow S_0$  transition frequencies for all considered species.

To estimate the ionization potentials (IPs) of the ion pairs, ion current curves (see figure 30) were recorded by keeping the UV excitation laser frequency-fixed at the respective electronic origin transition while scanning the UV ionization laser.

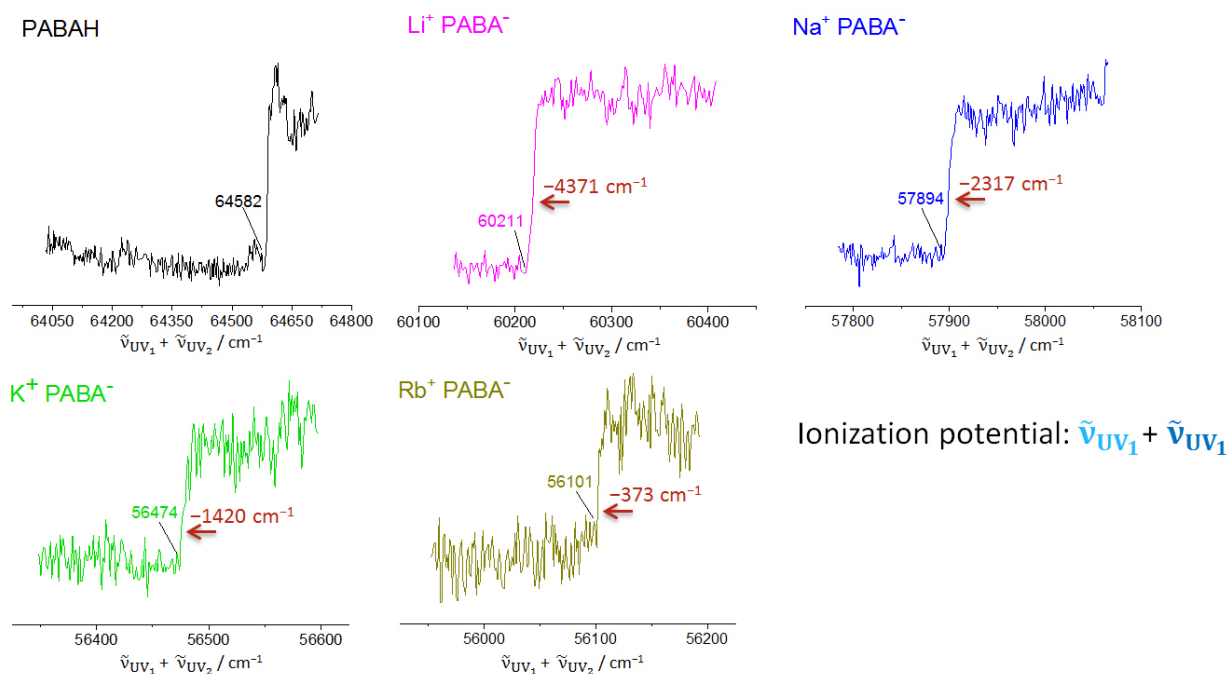


Figure 30: Ion current curves of *para*-aminobenzoic acid (PABAH) and its alkali ion pairs  $\text{Li}^+\text{PABA}^-$ ,  $\text{Na}^+\text{PABA}^-$ ,  $\text{K}^+\text{PABA}^-$ ,  $\text{Rb}^+\text{PABA}^-$ . For each ion pair the ionization laser wavelength was tuned in the region of the respective ionization potential, while the excitation laser was frequency-fixed at the respective  $0_0^0$  transition.

No ion current curve for  $\text{Cs}^+\text{PABA}^-$  is depicted, since no two color (2C) effect could be obtained for this species anymore (2C effect of about 50 % for  $\text{Li}^+\text{PABA}^-$ ; ca. 10 % for  $\text{Rb}^+\text{PABA}^-$ ). The ionization potential undergoes a significant red-shift of in total  $4110\text{ cm}^{-1}$  between  $\text{Li}^+\text{PABA}^-$  and  $\text{Rb}^+\text{PABA}^-$ . The IPs measured for the ion pairs are drastically red-shifted relative to the IP of PABAH (shift by  $4371\text{ cm}^{-1}$  between PABAH and  $\text{Li}^+\text{PABA}^-$ ). This is not surprising, as an electron is photodetached from the anionic PABA<sup>-</sup> chromophore for the  $\text{M}^+\text{PABA}^-$  species. Like shown in figure 29 (b), an almost perfect linear correlation is observed between the (estimated) IPs and the size of the alkali cation.

The frequency shifts measured for the IPs are much stronger than for the  $S_1 \leftarrow S_0$  electronic origins. Thus, the energetic gap between the  $S_1$  and  $D_0$  state decreases significantly from  $\text{Li}^+\text{PABA}^-$  to  $\text{Cs}^+\text{PABA}^-$ . This trend may be explained by consulting the respective binding energies between cation and chromophore in the  $S_0$  and  $D_0$  state. For the  $\text{Li}^+$  species, the binding energy is lowered by  $\Delta BE = 32906\text{ cm}^{-1}$  upon photoionization. If, however,  $\text{Cs}^+$  is bound to the *para*-aminobenzoate, the interaction between  $\text{Cs}^+$  and the carboxylate is throughout weaker, which goes along with a decrease of the binding energy by only  $\Delta BE = 28343\text{ cm}^{-1}$  due to ionization. Focusing on the last-mentioned numbers,

the decline of the  $M^+\cdots PABA^{-/}$  binding energy upon photoionization decreases by  $\Delta(\Delta BE) = 32906 - 28343 = 4563 \text{ cm}^{-1}$  from  $\text{Li}^+PABA^-$  to  $\text{Cs}^+PABA^-$ . Interestingly, the value of  $4563 \text{ cm}^{-1}$  ( $4565 \text{ cm}^{-1}$  when considering  $\text{Li}^+PABA^-$  and  $\text{Rb}^+PABA^-$ ) is indeed close to the experimentally observed decrease of the IP by  $4110 \text{ cm}^{-1}$  between  $\text{Li}^+PABA^-$  and  $\text{Rb}^+PABA^-$ , which supports the suggested interpretation on the basis of  $M^+\cdots PABA^{-/}$  binding energies.

Apart from the described UV experiments, IR spectra were recorded for both the  $S_0$  and  $D_0$  state. Hereby, the focus was put on the NH-stretching frequencies of the amino ( $\text{NH}_2$ ) group. In figure 31, the IR/(1C-)R2PI spectra are depicted, all featuring a sharp transition, which is assigned to the symmetric NH-stretching vibration  $\nu(\text{NH}_{\text{sym}})$ .

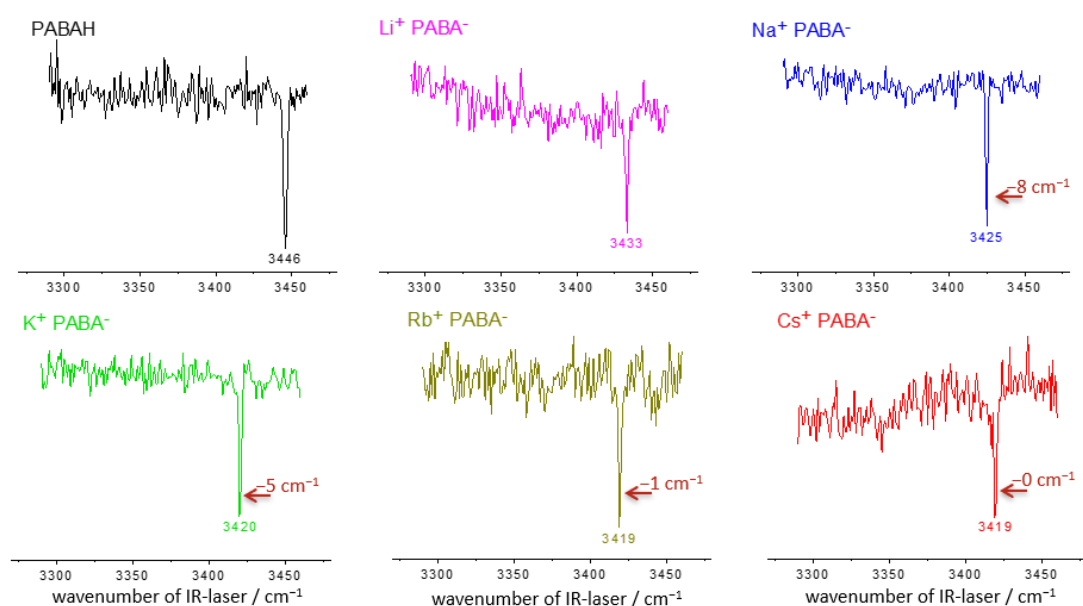


Figure 31: IR/R2PI spectra of the  $\text{Li}^+PABA^-$ ,  $\text{Na}^+PABA^-$ ,  $\text{K}^+PABA^-$ ,  $\text{Rb}^+PABA^-$  and  $\text{Cs}^+PABA^-$  ion pairs ( $S_0$  state) in the spectral region of  $\nu(\text{NH}_{\text{sym}})$ , measured *via* the respective  $O_0^0$  transitions.

As described above for the UV experiments, a red-shift of the symmetric NH-stretching frequency is observed between  $\text{Li}^+PABA^-$  and  $\text{Cs}^+PABA^-$ . Among the  $M^+PABA^-$  series,  $\text{Li}^+PABA^-$  exhibits the highest value of  $3433 \text{ cm}^{-1}$  for  $\nu(\text{NH}_{\text{sym}})$ . This observation can be explained by the strong mesomeric donor (+M) effect of the amino group towards the aromatic ring if a small cation of high positive charge density is coordinated to the  $PABA^-$  chromophore. This +M effect goes along with an increased “s” hybridization character of the N atom and with an enhanced planarization of the amino group (according to DFT calculations). This higher “s” character also leads to a contraction of the N–H bonds (with increased bond strength) and thus to a relatively higher NH-stretching frequency. Within free  $PABA^-$ , however, no “perturbation” by a cationic counterion occurs, leading to a strong pyramidalization of the  $\text{NH}_2$  group, a reduced “s” character and a particularly red-shifted NH-stretching

frequency of  $3382\text{ cm}^{-1}$  according to theory (obtained at DFT/B3LYP-D3(BJ)/def2-TZVP level; scal.: 0.963). With increasing size of the alkali cation the influence of  $M^+$  on  $\text{PABA}^-$  successively decreases, so that the IR frequencies shift towards lower frequencies relative to  $\text{Li}^+\text{PABA}^-$  ( $3433\text{ cm}^{-1}$ ). Accordingly, an almost linear correlation between the symmetric NH-stretching frequency and the respective inverse ionic radius is observed (see draft [1]). Finally, it should be pointed out that the measured vibrational frequencies are in excellent agreement with the values predicted by the harmonic frequency calculations at the DFT/B3LYP-D3(BJ)/def2-TZVP level. The shifts of the asymmetric NH-stretching frequencies  $\nu(\text{NH}_{\text{asym}})$  are not further discussed here. For several ion pairs they fall into the spectral gap of the used IR laser system (see subchapter 3.1.2) and could thus not be detected. However, DFT calculations predict very similar trends for the vibrational shifts of  $\nu(\text{NH}_{\text{sym}})$  and  $\nu(\text{NH}_{\text{asym}})$ .

In addition to the IR/R2PI experiments, IR spectra of the photoionized  $M^+\text{PABA}^-$  ions (in the  $D_0$  state) were also recorded by applying the UV/UV/IR technique. The respective mass traces for the spectral region of the symmetric NH-stretching vibration  $\nu(\text{NH}_{\text{sym}})$  are depicted in figure 32.

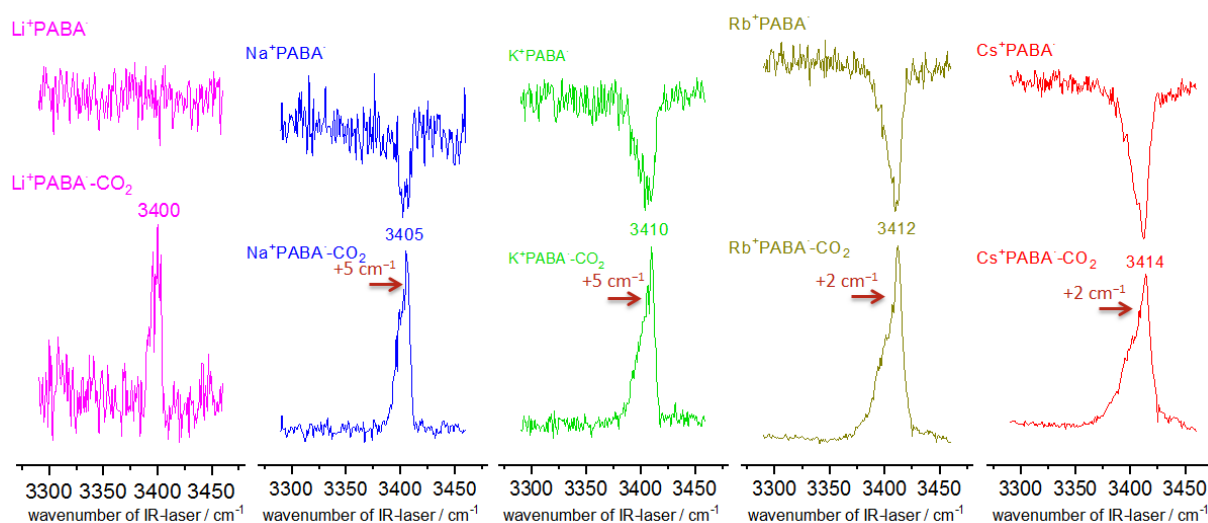


Figure 32: UV/UV/IR spectra of the  $\text{Li}^+\text{PABA}^-$ ,  $\text{Na}^+\text{PABA}^-$ ,  $\text{K}^+\text{PABA}^-$ ,  $\text{Rb}^+\text{PABA}^-$  and  $\text{Cs}^+\text{PABA}^-$  species ( $D_0$  state) in the spectral region of  $\nu(\text{NH}_{\text{sym}})$ , showing the parent ( $M^+\text{PABA}^-$ ) and fragment ( $M^+\text{PABA}^- - \text{CO}_2$ ) mass traces. The initially neutral ion pairs were ionized *via* 1C-R2PI at the respective  $0_0^0$  transitions.

In the UV/UV/IR spectra, the resonance effects could be detected on both the fragment and parent mass traces, with the dissociation channel corresponding to a loss of neutral  $\text{CO}_2$ . Hereby, the IR photodissociation efficiency drastically increased from  $\text{Li}^+\text{PABA}^-$  towards  $\text{Cs}^+\text{PABA}^-$ , which is largely due to the lower stability of ion pairs with larger cations. As the effects observed for  $\text{Li}^+\text{PABA}^-$  were very weak, the resonance effect could only be detected on the fragment mass trace, showing a significantly improved signal-to-noise ratio (due to the zero-background effect, see subchapter 2.6).

According to the DFT geometry optimizations, the doubly-coordinated binding motif observed in the  $S_0$  state is maintained in the  $D_0$  state. Exemplarily, the optimized geometry of an  $M^+PABA^-$  ion pair is depicted in figure 27 (b). For all systems, except  $Li^+PABA^-$ , the carboxylate group is twisted relative to the aromatic ring plane. The latter geometric effect, which is most pronounced for  $M^+PABA^-$  species with larger  $M^+$ , may go along with structural fluctuations (due to a low rotational barrier around the C(aromatic)–C(carboxylate) bond). Therefore, structures that are slightly displaced from the ideal geometry, exhibiting (slightly) distinct NH-stretching frequencies, may contribute to the spectrum. This might be a reason for the band broadening observed in the  $D_0$  state IR spectra. However, it should also be kept in mind that the probed radical species are formed *via* 1C-R2PI, so that the excess energy upon photoionization cannot be specifically adjusted. Particularly high excess energies of up to  $12231\text{ cm}^{-1}$  (for  $Rb^+PABA^-$ ) may lead to the population of low frequency modes, possibly coupling with high frequency vibrations. This is another potential explanation for the broad tail on the low frequency side of the measured IR bands.

At first glance, it may seem surprising that, in contrast to the effects in the  $S_0$  state, a successive blue shift of  $\nu(NH_{sym})$  is observed when going from  $Li^+PABA^-$  towards  $Cs^+PABA^-$ , to gradually approach the value of  $3450\text{ cm}^{-1}$  predicted for free  $PABA^-$ . This trend is perfectly reflected by the predicted harmonic frequencies (at DFT level). Regarding the isolated  $PABA^-$  radical, the frequency of  $3450\text{ cm}^{-1}$  is significantly blue-shifted relative to the respective  $S_0$  state vibrational frequency of  $PABA^-$ . This shift could be readily expected, as the amino group is strongly planarized in the  $D_0$  state, which goes along with an increased “s” hybridization character and thus stronger N–H bonds. Yet, a further effect must play a role: Although the amino group is almost fully planar for all  $M^+PABA^-$  ion pairs, a red-shift of  $\nu(NH_{sym})$  by  $33\text{ cm}^{-1}$  relative to the respective frequency in the  $S_0$  state is measured for  $Li^+PABA^-$ , which is to a minor extent also observed for  $Na^+PABA^-$  (red-shift of  $20\text{ cm}^{-1}$ ) and  $K^+PABA^-$  (red-shift of  $10\text{ cm}^{-1}$ ). Regarding  $Rb^+PABA^-$  and  $Cs^+PABA^-$ , the  $D_0$  state frequencies are closer to the values for  $\nu(NH_{sym})$  in the  $S_0$  state (red-shifts by merely  $7\text{ cm}^{-1}$  and  $5\text{ cm}^{-1}$ , respectively). These effects may be explained by consulting the orbital occupancies, obtained within a natural bond orbital (NBO) analysis, performed at the DFT level. The  $\sigma^*(N-H_1)$  and  $\sigma^*(N-H_2)$  orbital occupancies are given in table 2.



Table 2: Total ( $\alpha + \beta$ ) orbital occupancies obtained for the antibonding  $\sigma^*(\text{N-H}_1)$  and  $\sigma^*(\text{N-H}_2)$  orbitals in the  $D_0$  state. The NBO population analysis was performed at the DFT/B3LYP-D3(BJ)/def2-TZVPP level.

	occ. $\sigma^*$ tot(N-H <sub>1</sub> ), occ. $\sigma^*$ tot(N-H <sub>2</sub> )
<b>Li<sup>+</sup>PABA<sup>-</sup></b>	0.00847/ 0.00847
<b>Na<sup>+</sup>PABA<sup>-</sup></b>	0.00839/ 0.00839
<b>K<sup>+</sup>PABA<sup>-</sup></b>	0.00829/ 0.00829
<b>Rb<sup>+</sup>PABA<sup>-</sup></b>	0.00825/ 0.00825
<b>Cs<sup>+</sup>PABA<sup>-</sup></b>	0.00824/ 0.00824
<b>PABA<sup>-</sup></b>	0.00774/ 0.00777

An increased  $\sigma^*(\text{N-H})$  occupancy should go along with a weakening of the N-H bond. Like mentioned above, the hybridization of the N atom definitely has a crucial influence on the N-H bond strength and frequency. However, as for the  $D_0$  state a very similar hybridization of  $sp^{2.34}$  or  $sp^{2.35}$  is predicted for all  $M^+\text{PABA}^-$  species, the orbital occupancies may become the more decisive factor. Indeed, the  $\sigma^*(\text{N-H})$  population decreases along the row from  $\text{Li}^+\text{PABA}^-$  to  $\text{Cs}^+\text{PABA}^-$ , which is in line with the measured as well as the simulated vibrational frequencies (at DFT level). In other words, the change in hybridization and the electron density transfer to the antibonding orbitals are competing processes, whereby the latter one should be most relevant for the  $M^+\text{PABA}^-$  species in the  $D_0$  state. It can also be noted that in the  $S_0$  state the  $\sigma^*(\text{N-H})$  occupancies are throughout lower and hardly change along the series from  $\text{Li}^+\text{PABA}^-$  to  $\text{Cs}^+\text{PABA}^-$  (see supplementary information of draft [1]).

The described approach has already been applied to interpret the  $\text{NH}_2$  stretching frequencies measured for the structurally related aniline and its radical cation<sup>[175]</sup>, as well as for guanine and its dimer<sup>[176]</sup>. It should be further noted that the vibrational shifts observed in the  $D_0$  state are once again in nice accordance with the Coulomb law (see draft [1]). However, the spectroscopic effects found for the alkali *para*-aminobenzoate ion pairs (especially regarding the  $D_0$  state) may not be explained by assuming a “classical” vibrational Stark effect<sup>[163,164,171]</sup>. Instead, the spectroscopic shifts seem to be caused by electronic effects, which are induced by the electric field of the coordinating alkali cation.

### 5.1.2.3 Metal *para*-aminobenzoate complexes with divalent metal centers ( $Mg^{2+}$ , $Ca^{2+}$ and $Ba^{2+}$ )

With the idea to make a further step towards investigations on neutral isolated metal complexes in the gas phase, complexes of the types  $Mg^{2+}(PABA^-)_2$ ,  $Ca^{2+}(PABA^-)_2$  and  $Ba^{2+}(PABA^-)_2$  were also studied in this work. The compounds  $Mg^{2+}(PABA^-)_2$  and  $Ca^{2+}(PABA^-)_2$  were synthesized by a salt metathesis reaction between  $K^+PABA^-$  and the corresponding chloride salts  $MgCl_2$  and  $CaCl_2$ , respectively.  $Ba^{2+}(PABA^-)_2$  was obtained by simple acid-base reaction between  $Ba(OH)_2$  and *para*-amino benzoic acid.

In the optimized geometries of the complexes, the metal center is coordinated by the two bidentate carboxylate groups of the  $PABA^-$  ligands (see figure 33 (b)). Hereby, the planes of the aromatic rings/carboxylates are twisted with respect to one another by  $\sim 82^\circ$ . Although the ion signals obtained for the  $M^{2+}(PABA^-)_2$  complexes were drastically smaller than for the  $M^+PABA^-$  ion pairs, R2PI spectra could be recorded for the three  $M^{2+}(PABA^-)_2$  compounds, as depicted in figure 33 (a).

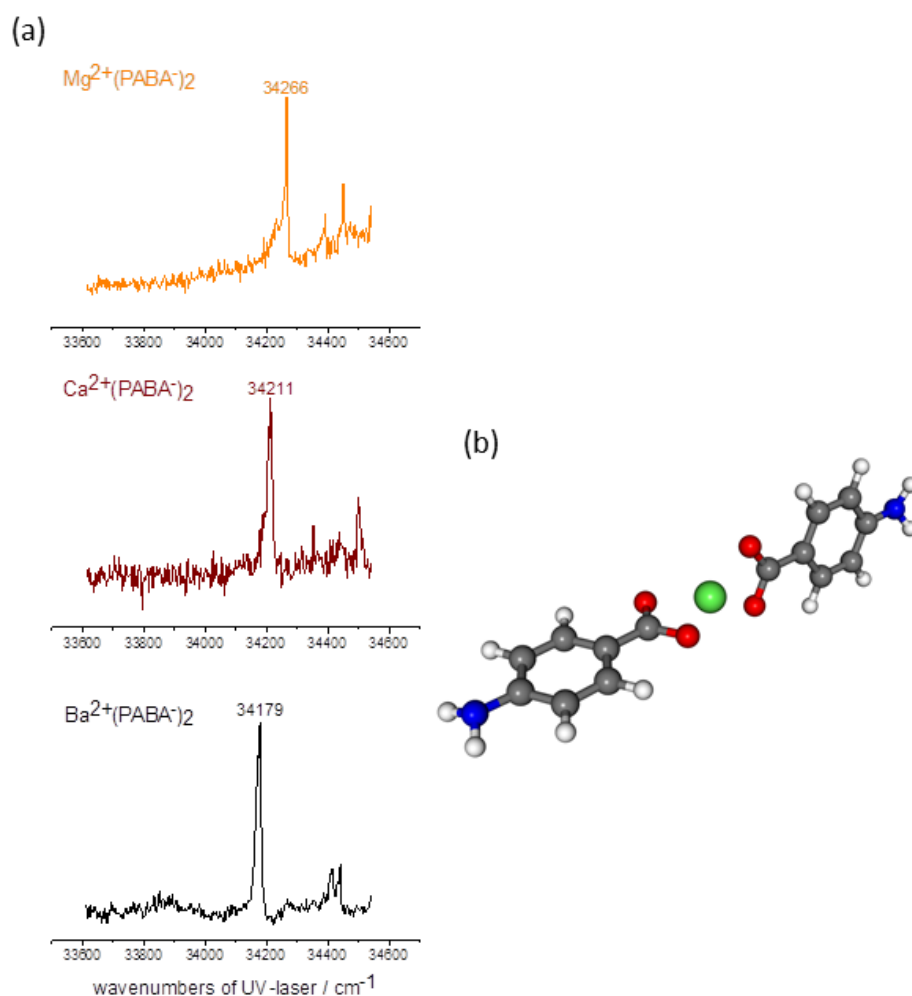


Figure 33: (a) 1C-R2PI spectra of the metal *para*-aminobenzoate complexes  $Mg^{2+}(PABA^-)_2$ ,  $Ca^{2+}(PABA^-)_2$  and  $Ba^{2+}(PABA^-)_2$ ; (b) Optimized geometry of  $Mg^{2+}(PABA^-)_2$  (calculated at the DFT/B3LYP-D3(BJ)/def2-TZVP level).

In the R2PI spectra the electronic origin transition shifts to the red when going from  $\text{Mg}^{2+}(\text{PABA}^-)_2$  over  $\text{Ca}^{2+}(\text{PABA}^-)_2$  to  $\text{Ba}^{2+}(\text{PABA}^-)_2$ . This trend reflects the observations made for the corresponding alkali ion pairs (see draft [1]). For illustration, the correlation between the measured electronic origin transitions and the inverse ion radii is depicted in figure 34.

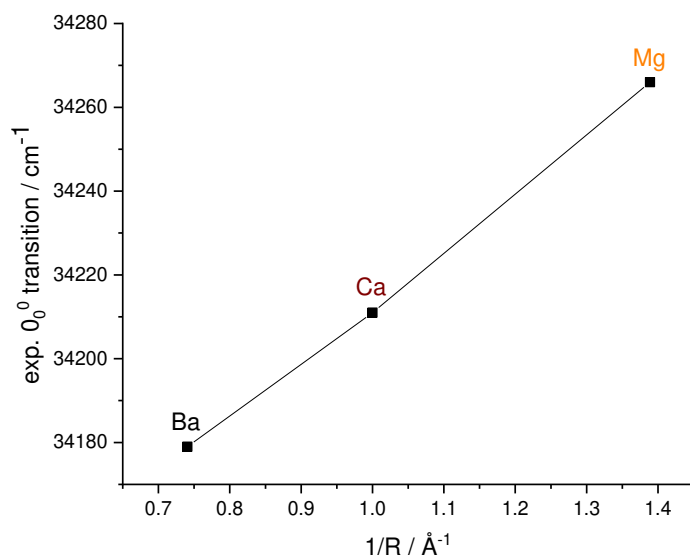


Figure 34: Correlation between the electronic origin transitions of the  $\text{M}^{2+}(\text{PABA}^-)_2$  complexes and the inverse ion radii of the respective earth alkaline ion.

Thus, similar to the  $\text{M}^+\text{PABA}^-$  ion pairs, a linear correlation is obtained. However, it should be noted that the red-shift of  $87 \text{ cm}^{-1}$  between  $\text{Mg}^{2+}(\text{PABA}^-)_2$  and  $\text{Ba}^{2+}(\text{PABA}^-)_2$  is considerably larger than the shift of  $40 \text{ cm}^{-1}$  observed for the alkali row ( $\text{Na}^+\text{PABA}^-$  to  $\text{Cs}^+\text{PABA}^-$ ). Most probably, the divalent earth alkaline ions, exhibiting smaller ion radii ( $0.72 \text{ \AA}$  for  $\text{Mg}^{2+}$  to  $1.35 \text{ \AA}$  for  $\text{Ba}^{2+}$ )<sup>[172]</sup> and thus a comparatively higher positive charge density, have a stronger influence on the spectroscopy of the coordinating  $\text{PABA}^-$  chromophores than the larger monovalent alkali ions (with radii of  $1.02 \text{ \AA}$  for  $\text{Na}^+$  to  $1.67 \text{ \AA}$  for  $\text{Cs}^+$ )<sup>[172]</sup> within the  $\text{M}^+\text{PABA}^-$  species.

Principally, the NH-stretching frequencies of the *para*-aminobenzoate ligands would be perfectly suited for IR/R2PI experiments (as demonstrated in draft [1] for the  $\text{M}^+\text{PABA}^-$  ion pairs). However, no combined IR/UV experiments were performed for the  $\text{M}^{2+}(\text{PABA}^-)_2$  species because of a too low ion signal intensity, ruling out the application of the “reference signal correction” approach.

5.1.2.4 Alkali *para*-methoxybenzoate ( $M^+PMBA^-$ ) and alkali benzoate ( $M^+BA^-$ ) ion pairs*Alkali para-methoxybenzoate ( $M^+PMBA^-$ ) ion pairs*

Prior to the measurements on the respective alkali ion pair species, attempts were made to record an R2PI spectrum of the (still protonated) neutral *para*-methoxybenzoic acid monomer (PMBAH). However, no photoionized molecules could be detected. As for this species the stability of the compound may rather not be a limiting factor, decomposition during either the laser desorption or photoionization process seems improbable. Instead, no ion signal may be observed due to an unsuccessful R2PI process, at least if a resonant ionization *via* 1C-R2PI is pursued. Maybe the ionization potential cannot be surpassed by absorption of two UV excitation photons, so that a UV ionization laser with a shorter wavelength may be required to resonantly ionize PMBAH (*via* a 2C-R2PI process). Nevertheless, 1C-R2PI spectra could be successfully recorded for the respective alkali ion pairs (from  $Li^+$  to  $Cs^+$ ), as presented in figure 35.

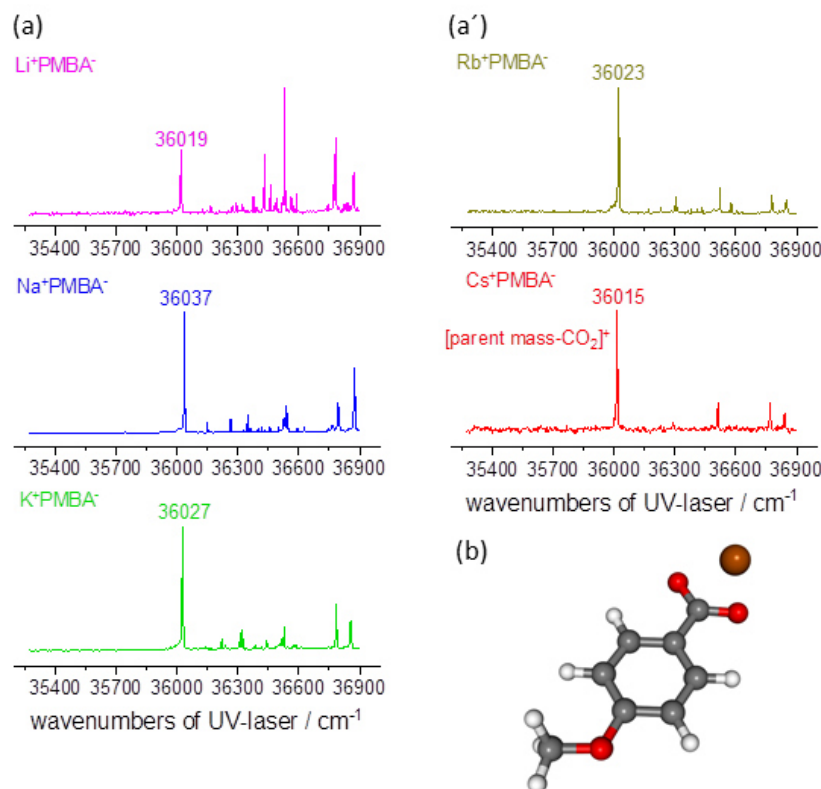


Figure 35: (a) and (a') 1C-R2PI spectra of the alkali *para*-methoxybenzoate ion pairs  $Li^+PMBA^-$ ,  $Na^+PMBA^-$ ,  $K^+PMBA^-$ ,  $Rb^+PMBA^-$  and  $Cs^+PMBA^-$ ; (b) Optimized geometry of  $Na^+PMBA^-$  (calculated at the DFT/B3LYP-D3(BJ)/def2-TZVP level).

Similar to the observations for the  $M^+PABA^-$  ion pairs, sharp electronic transitions are observed in all R2PI spectra shown in figure 35, which are blue-shifted by about  $1850\text{ cm}^{-1}$  relative to the transitions of  $M^+PABA^-$ . As the bands are again very sharp, even small frequency shifts can be unambiguously

detected. A significant difference compared to the experiments with  $M^+PABA^-$  ion pairs is the obviously lower photoionization stability of the  $M^+PMBA^-$  species. Concretely, strong UV photofragmentation effects upon electronic excitation/ionization were readily observed for  $K^+PMBA^-$  and  $Rb^+PMBA^-$ , while the R2PI spectrum of  $Cs^+PMBA^-$  could only be recorded *via* the fragment mass traces, as no ion signal was detected on the parent mass trace for this species. Therefore, the R2PI trace for the [parent mass- $CO_2$ ] $^+$  ion signal, appearing upon UV photodissociation (loss of neutral  $CO_2$ ) within the ionization process of  $Cs^+PMBA^-$ , is depicted in figure 35 (a'). Due to the increasing UV fragmentation yield observed from  $Li^+PMBA^-$  (no fragmentation) to  $Rb^+PMBA^-$  (strong fragmentation), the features detected on the [parent mass- $CO_2$ ] $^+$  trace of the Cs species very likely belong to the parent  $Cs^+PMBA^-$  ion pair species. For further illustration, R2PI traces reflecting the observed photofragmentation pathways are shown in figure 36, on the example of  $Rb^+PMBA^-$ . As this species undergoes strong fragmentation, with the parent ion signal still being detectable,  $Rb^+PMBA^-$  is most convenient for demonstration.

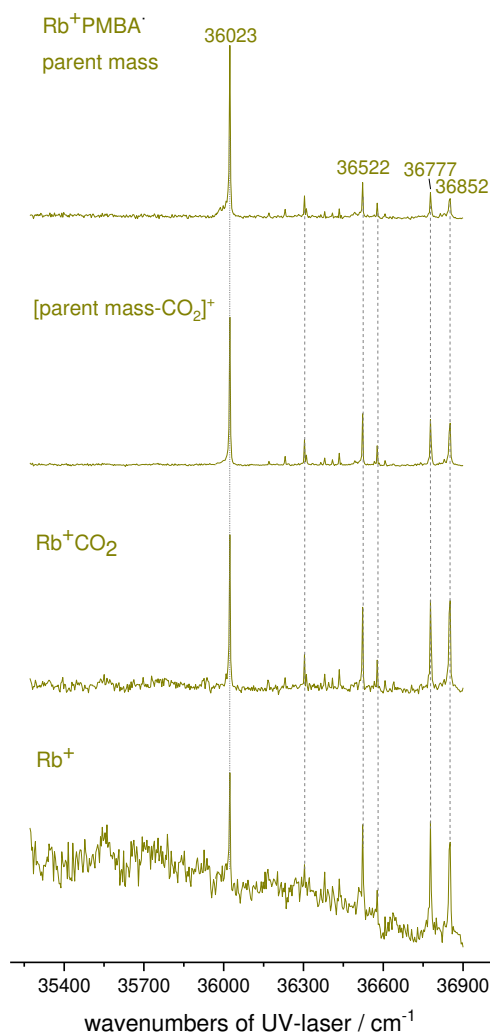


Figure 36: 1C-R2PI spectrum of Rb<sup>+</sup>PMBA<sup>-</sup> (recorded on the Rb<sup>+</sup>PMBA<sup>-</sup> mass trace) together with the fragment mass traces [parent mass-CO<sub>2</sub>]<sup>+</sup>, Rb<sup>+</sup>CO<sub>2</sub> and Rb<sup>+</sup>. The dashed lines should illustrate the photofragmentation channels.

As highlighted by the dashed lines in figure 36, all vibronic transitions observed on the parent Rb<sup>+</sup>PMBA<sup>-</sup> trace are parallelly detected on the respective fragment mass traces [parent mass-CO<sub>2</sub>]<sup>+</sup>, Rb<sup>+</sup>CO<sub>2</sub> and Rb<sup>+</sup>. This fragmentation behavior is very similar to the effects observed by Gloaguen and Mons and coworkers for various alkali-carboxylate ion pairs.<sup>[14]</sup> Compared to the relative peak intensities measured on the parent trace, the transitions at 36777 and 36852 cm<sup>-1</sup> are particularly pronounced on the fragment mass traces, especially for Rb<sup>+</sup> and Rb<sup>+</sup>CO<sub>2</sub>. This effect may be due to an increased photofragmentation yield if a larger amount of energy (higher photon energy) is introduced into the chromophore within the R2PI process. Furthermore, the population of (higher) vibrational modes in the electronically excited state or in the ionic ground state may facilitate photofragmentation.

These effects are in contrast to the observations made for the  $M^+PABA^-$  ion pairs, where no significant UV photofragmentation was observed for the whole series from  $Li^+PABA^-$  to  $Cs^+PABA^-$ . For the  $M^+PABA^-$  species, considerable dissociation effects were merely observed upon resonant vibrational excitation (symmetric NH-stretching mode) of the photoionized species, thus in the  $D_0$  state (see draft [1]). The trends regarding ion pair stability in function of the substituent in the *para*-position (-NH<sub>2</sub>, -OMe or -H) are discussed further down.

Concerning the measured  $0_0^0$  transitions, clear but maybe unexpected frequency shifts were observed. A blue-shift of 18 cm<sup>-1</sup> is observed when going from  $Li^+PMBA^-$  to  $Na^+PMBA^-$ , while a successive red-shift of in total 22 cm<sup>-1</sup> occurs between  $Na^+PMBA^-$  and  $Cs^+PMBA^-$ . Overall, a strong dependance of the  $0_0^0$  frequencies on the size of the respective alkali ions is observed from  $Li^+PMBA^-$  to  $Cs^+PMBA^-$ , as shown in figure 37.

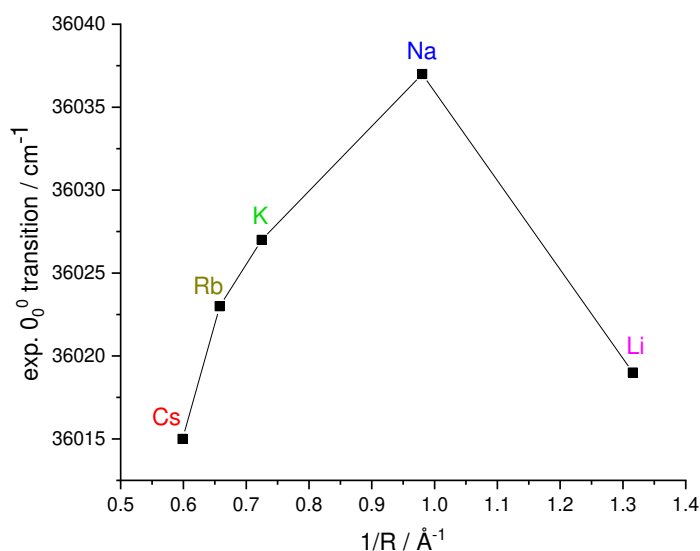


Figure 37: Correlation between the electronic origin ( $0_0^0$ ) transitions of the  $M^+PMBA^-$  ion pairs and the inverse ion radii of the coordinating alkali ions.

The red-shift from  $Na^+PMBA^-$  to  $Cs^+PMBA^-$  is in line with the trends observed for the  $M^+PABA^-$  species, while the value for  $Li^+PMBA^-$  somehow breaks this tendency. The origin of this unexpected effect remains unclear, but major geometric effects may be ruled out, as the same doubly-coordinated structural motif is maintained for the  $S_0$  state geometries of the whole alkali row, according to the performed DFT geometry optimizations. Thus, a deeper interpretation of the measured frequency shifts is challenging. A strong peak at 36530 cm<sup>-1</sup> (+511 cm<sup>-1</sup>) is observed in the R2PI spectrum of  $Li^+PMBA^-$ . In contrast, this transition is much weaker or even absent in the R2PI spectra of  $Na^+PMBA^-$ ,  $K^+PMBA^-$ ,  $Rb^+PMBA^-$  and  $Cs^+PMBA^-$ . This may be an indication of clearly distinct electronic properties for  $Li^+PMBA^-$ , relative to the electronic behavior of the  $PMBA^-$  chromophore in the presence of a larger

alkali counterion. However, the possibility that the intense and also most red-shifted peaks occurring in the measured R2PI spectra may result from transitions to higher vibronic states (and thus, at least for some of the  $M^+PMBA^-$  species, not the  $0_0^0$  transitions) should not be completely excluded. According to the DFT geometry optimizations, the presence of a second isomer (exhibiting a distinct binding motif) in the case of  $Li^+PMBA^-$  is not to be expected.

It should also be noted that geometry optimizations in the electronically excited state, performed at the SCS-ADC(2)/def2-TZVP level, were challenging, since the subsequent harmonic vibrational frequency calculations yielded imaginary frequencies for most  $M^+PMBA^-$  species. Any further interpretation of the R2PI spectra might be realized on the basis of Franck Condon simulations, as performed in several studies in the literature (*e.g.* <sup>[173,177]</sup>).

A structural similarity compared to the  $M^+PABA^-$  ion pairs is that, according to DFT, the plane of the carboxylate group is twisted relative to the aromatic ring plane in the  $D_0$  state, thus after photoionization. Merely for photoionized  $Li^+PMBA^-$ , named  $Li^+PMBA^{\cdot}$  in the following, a second binding motif occurs, with the  $Li^+$  ion being singly-coordinated to only one O atom of the carboxylate group, whereby this isomer is however  $1516\text{ cm}^{-1}$  less stable. The two discussed minimum structures are presented in figure 38 below.

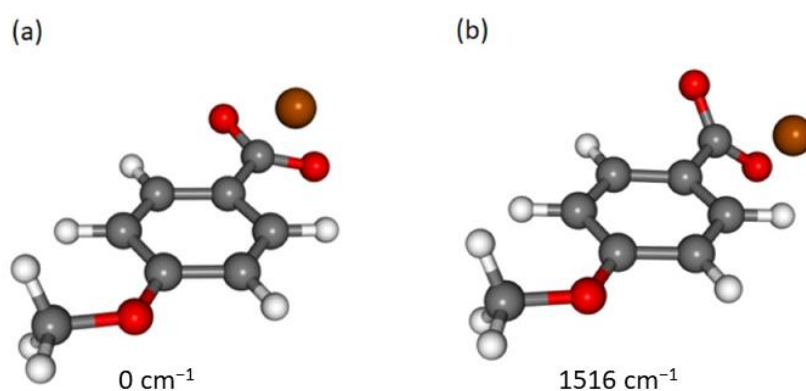


Figure 38: Optimized geometries of both  $Li^+PMBA^{\cdot}$  minimum structures in the  $D_0$  state, together with the corresponding relative energies (including ZPE; calculated at the DFT/B3LYP-D3(BJ)/def2-TZVP level): (a) with doubly coordinated  $Li^+$  ion; (b) with singly coordinated  $Li^+$  ion.

Regarding the singly coordinated arrangement in the  $D_0$  state, a particularly high negative partial charge is localized on the O atom which is linked to the small, highly charged  $Li^+$  ion, as illustrated in table 3.



Table 3: Atomic partial charges for the  $\text{Li}^+\text{PMBA}^-$  ion pairs in the  $D_0$  state, as obtained from an NBO analysis at the DFT/B3LYP-D3(BJ)/def2-TZVP level.

$\text{Li}^+\text{PMBA}^-$	O(1)	O(2)	$\text{M}^+$
<b>doubly coordinated</b>	-0.74110	-0.74175	0.96021
<b>singly coordinated</b>	-0.49276 (free O)	-0.85034 (coord. O)	0.97789

For the  $\text{M}^+\text{PMBA}^-$  species, this binding motif may occur due to the (relative to *e.g.* PABA<sup>-</sup>) reduced mesomeric donor (+M) effect of the methoxy substituent<sup>[178]</sup>, which goes along with an overall lower electron density on the carboxylate group being available for cation stabilization (in the case of PMBA<sup>-</sup>). Therefore, especially the smaller cations of high charge density may favor a singly coordinated motif, with the negative charge being “accumulated” on the coordinating O atom. Indeed, as further discussed below, geometries of this motif were also found for the alkali benzoate ( $\text{M}^+\text{BA}^-$ ) ion pairs, whereby it is even the most stable binding type if  $\text{Li}^+$  is involved. In this line, no minimum structure of this motif could be found for the  $\text{M}^+\text{PABA}^-$  compounds. Finally, singly coordinated structures may likely occur if a small cation of high charge density is linked to a comparatively electron-poor carboxylate group. Regarding  $\text{Li}^+\text{PMBA}^-$ , the presence of the still energetically favored doubly-coordinated motif is to be expected. IR experiments (UV/UV/IR) in the ionic ground state, focusing on the C=O stretching region, would provide a final proof for this statement. However, IR experiments in that spectral region were virtually inaccessible within the context of this work, especially in combination with the laser desorption setup.

To avoid confusion, it should be pointed out that the discussed structural variety may merely occur in the ionic ground state ( $D_0$ ), while only planar geometries with a doubly coordinated  $\text{M}^+$  ion are predicted for the electronic ground state ( $S_0$ ) of all ion pairs considered in this work.

It should also be noted that the orientation of the methoxy group of PMBA<sup>-</sup> (with its  $\text{H}_3\text{C}-\text{O}$  bond always being in the plane of the aromatic ring) has no relevant influence on the energy of the  $\text{M}^+\text{PMBA}^-$  systems.

*Alkali benzoate ( $M^+BA^-$ ) ion pairs*

In the following the 1C-R2PI spectra of the unsubstituted alkali benzoates ( $M^+BA^-$  with  $M^+$ :  $Li^+$ - $K^+$ ) are discussed. Regarding the (unsubstituted) alkali benzoate ion pairs particularly strong (photo)fragmentation effects were observed. Due to this low ion pair stability, merely R2PI spectra for  $Li^+BA^-$ ,  $Na^+BA^-$  and  $K^+BA^-$  could be recorded and are depicted in figure 39.

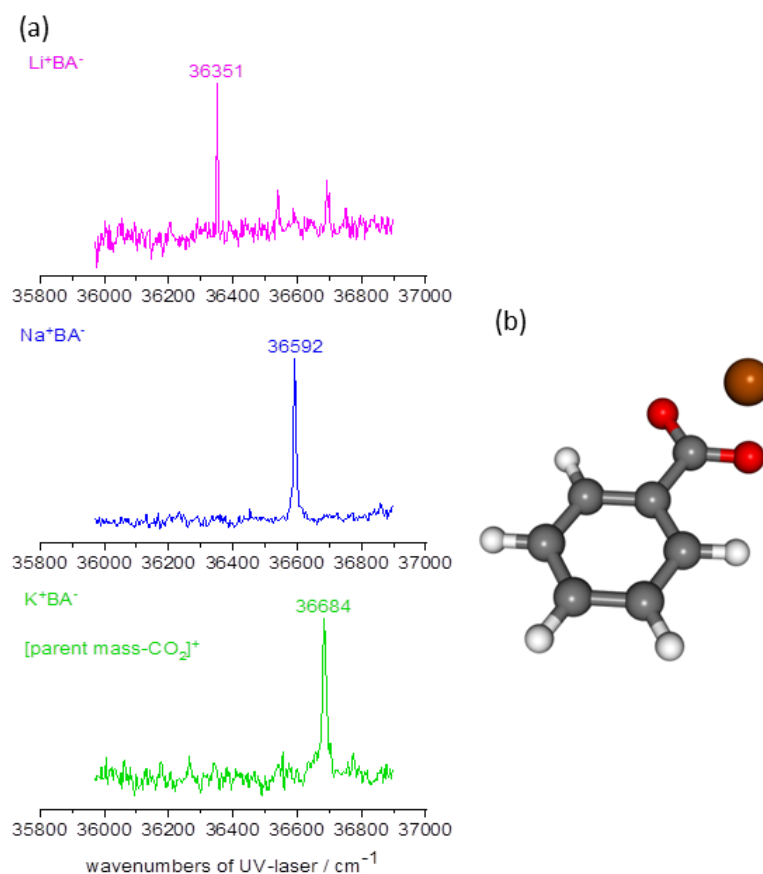


Figure 39: (a) 1C-R2PI spectra of the measured alkali benzoate ion pairs  $Li^+BA^-$ ,  $Na^+BA^-$  and  $K^+BA^-$ ; (b) Optimized geometry of  $Na^+BA^-$  (calculated at the DFT/B3LYP-D3(BJ)/def2-TZVP level).

The photoionization stability of  $K^+BA^-$  is already strongly reduced, so that only a small ion signal of the decarboxylated species was obtained, while the parent mass could not be detected at all. Regarding  $Rb^+BA^-$  and  $Cs^+BA^-$ , not even fragment mass signals could be observed. Thus, it seems rather probable that  $Rb^+BA^-$  and  $Cs^+BA^-$  already undergo fragmentation during the laser desorption process. Concerning the (photo)fragmentation pathways, the dominant fragmentation channel (loss of neutral  $CO_2$ ) already observed for  $M^+PMBA^-$  (and for  $M^+PABA^-$  upon resonant IR excitation) also occurs for  $M^+BA^-$ . The observed trends regarding ion pair (photo)stability are discussed in detail further down.

A clear difference compared to the  $M^+PABA^-$  and  $M^+PMBA^-$  species is the blue shift of the  $O_0^0$  transition observed between  $Li^+BA^-$  and  $K^+BA^-$ , whereby the frequency shifts upon substitution of the alkali

element are also stronger than for the  $M^+PABA^-$  and  $M^+PMBA^-$  ion pairs. Particularly pronounced shifts may be observed here due to the (according to the NBO analysis, see table 3) reduced electron density localization on the carboxylate group if no substituent exhibiting a positive mesomeric (+M) effect is attached to the *para*-position of the aromatic ring. In other words, a higher negative charge density on the carboxylate group may shield the probed chromophore from the positive charge of the cation if an  $-NH_2$  or  $-OMe$  substituent is attached to the ring.

It should also be noted that the benzoic acid monomer (BAH) undergoes intersystem crossing into the triplet manifold upon electronic excitation and that, in contrast to the experiments performed for the  $M^+BA^-$  species, no ionization *via* 1C-R2PI is possible for BAH. Specifically, Meijer *et al.* found the  $S_1 \leftarrow S_0$  origin (into the  $^1(\pi,\pi^*)$  state) at  $35960\text{ cm}^{-1}$  by performing a 2C-R2PI experiment, whereby they used a wavelength of 193 nm for subsequent ionization.<sup>[95]</sup> This also means that the  $0_0^0$  transitions of the  $M^+BA^-$  ion pairs are blue-shifted relative to the resonance of the benzoic acid monomer. Regarding the  $M^+BA^-$  ion pairs, a still considerable (calculated) adiabatic ionization potential of  $59114\text{ cm}^{-1}$  (for  $Cs^+BA^-$ ) to  $67646\text{ cm}^{-1}$  (for  $Li^+BA^-$ ) is obtained within DFT, with a predicted  $T_1 \leftarrow S_0$  gap of merely  $27284\text{ cm}^{-1}$  (for  $Cs^+BA^-$ ) to  $26974\text{ cm}^{-1}$  (for  $Li^+BA^-$ ). Thus, the observed photoionization *via* 1C-R2PI would probably not be possible in the presence of an efficient intersystem crossing process. This statement may be further confirmed by performing a 2C-R2PI experiment, yielding an estimation of the excited state lifetime. However, the ion signal intensity observed for the  $M^+BA^-$  species was very low (compared to *e.g.* investigations on  $M^+PABA^-$  ion pairs), so that a demanding 2C-R2PI experiment, in which the efficient 1C-R2PI process has to be suppressed, would be very challenging.

In figure 40, the correlation between the  $0_0^0$  transitions and the inverse ion radii is given for  $\text{Li}^+\text{BA}^-$ ,  $\text{Na}^+\text{BA}^-$  and  $\text{K}^+\text{BA}^-$ .

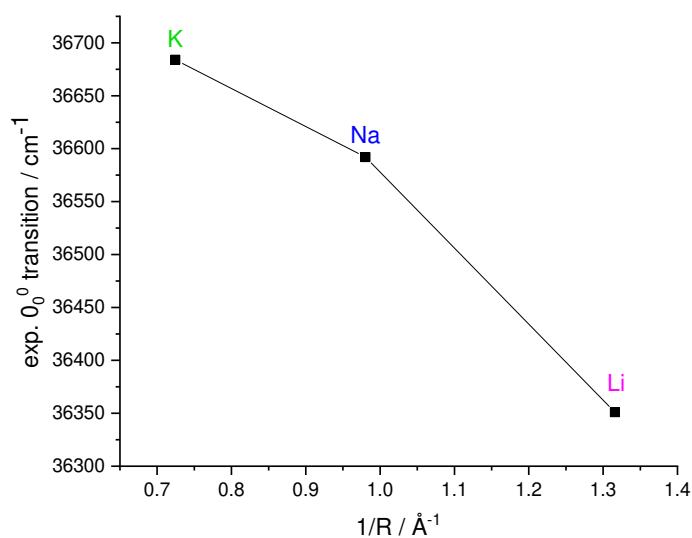


Figure 40: Correlation between the measured electronic origin ( $0_0^0$ ) transitions of the  $\text{M}^+\text{BA}^-$  ion pairs and the inverse ion radii of the coordinating alkali ions.

Once again, a pronounced dependence of the electronic origin transitions on the size of the coordinating alkali cation is observed. As for the  $\text{M}^+\text{PMBA}^-$  ion pairs, excited state geometry optimizations performed at the ADC(2) level revealed to be problematic and may therefore not explain the experimentally observed trends.

Regarding the conformational analysis in the  $D_0$  state, a variety of minimum structures was found, in contrast to  $\text{M}^+\text{PABA}^-$  and  $\text{M}^+\text{PMBA}^-$  (see above and draft [1]). Concretely, fully planarized motifs with doubly-coordinated  $\text{M}^+$ , twisted doubly coordinated structures as well as twisted geometries with  $\text{M}^+$  being singly coordinated to only one O atom of the carboxylate were found (see figure 41).

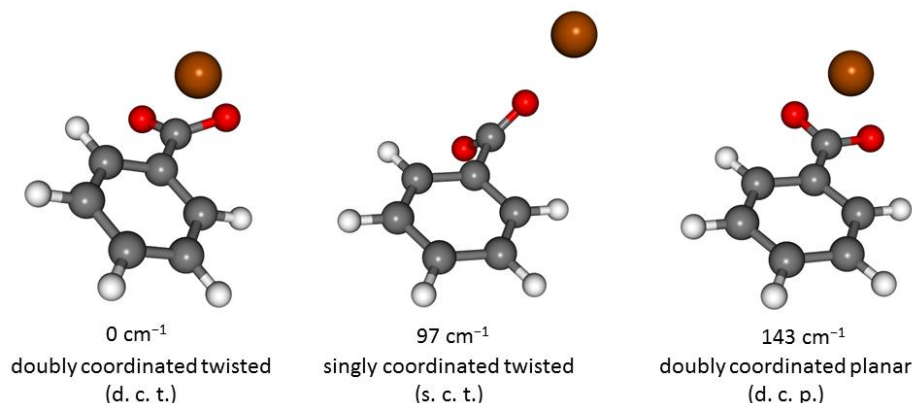


Figure 41: Structural motifs observed for the  $M^+BA^-$  ion pairs in the  $D_0$  state with the corresponding relative energies (including ZPE; calculated at the DFT/B3LYP-D3(BJ)/def2-TZVP level), illustrated on the example of  $K^+BA^-$ : (a) twisted structure with doubly coordinated  $K^+$  ion; (b) twisted structure with singly coordinated  $K^+$  ion; (c) planar structure with doubly coordinated  $K^+$  ion.

The relative energies obtained for all conformers of  $M^+BA^-$  are summarized in table 4.

Table 4: Relative energies for the doubly coordinated twisted (d. c. t.), singly coordinated twisted (s. c. t.) and doubly coordinated planar (d. c. p.) structures of the  $M^+BA^-$  ion pairs in the  $D_0$  state, as obtained at the DFT/B3LYP-D3(BJ)/def2-TZVP level. All values are given in  $\text{cm}^{-1}$ .

	$Li^+BA^-$	$Na^+BA^-$	$K^+BA^-$	$Rb^+BA^-$	$Cs^+BA^-$
d. c. t.	306	0	0	no min.	no min.
s. c. t.	0	145	97	207	255
d. c. p.	1054	706	143	0	0

Here, it is to note that the singly coordinated binding type is the most stable motif in the presence of a small highly-charged  $Li^+$  ion, while this motif is more and more disadvantaged with increasing cation size. The doubly coordinated and twisted type, as also found for the  $M^+PABA^-$  and  $M^+PMBA^-$  species, is advantaged for  $Na^+BA^-$  and  $K^+BA^-$ , while it is less favored for  $Li^+BA^-$  and was not found for  $Rb^+BA^-$  and  $Cs^+BA^-$ . The doubly coordinated fully planar structures, which are similar to the  $S_0$  state geometries, were found for all considered  $M^+BA^-$  species and are the favored motifs for  $Rb^+BA^-$  and  $Cs^+BA^-$ . Finally, the singly coordinated motif is advantaged for ion pairs with small highly charged cations, which is in line with the observations made for  $M^+PMBA^-$ . The presence of the last-mentioned structural motif for all  $M^+BA^-$  ion pairs may be explained by the relatively reduced electron density on the carboxylate group of  $BA^-$  (compared to  $PABA^-$  and  $PMBA^-$ ), due to the absence of any substituent with strong +M effect in *para*-position. The *per se* small electron density is thus “accumulated” on the coordinating O atom to stabilize the positive charge of the respective  $M^+$  cation. In the presence of a larger  $M^+$  cation

with a reduced positive charge density, the doubly coordinated motifs are still energetically advantaged, even in the absence of any substituent with +M effect.

*Comparison of the electronic origin ( $0_0^0$ ) transition frequencies of  $M^+PABA^-$ ,  $M^+PMBA^-$  and  $M^+BA^-$*

The trends observed for the electronic origin ( $0_0^0$ ) transitions of the alkali ion pairs  $M^+PABA^-$ ,  $M^+PMBA^-$  and  $M^+BA^-$  are compared to each other in figure 42 below.

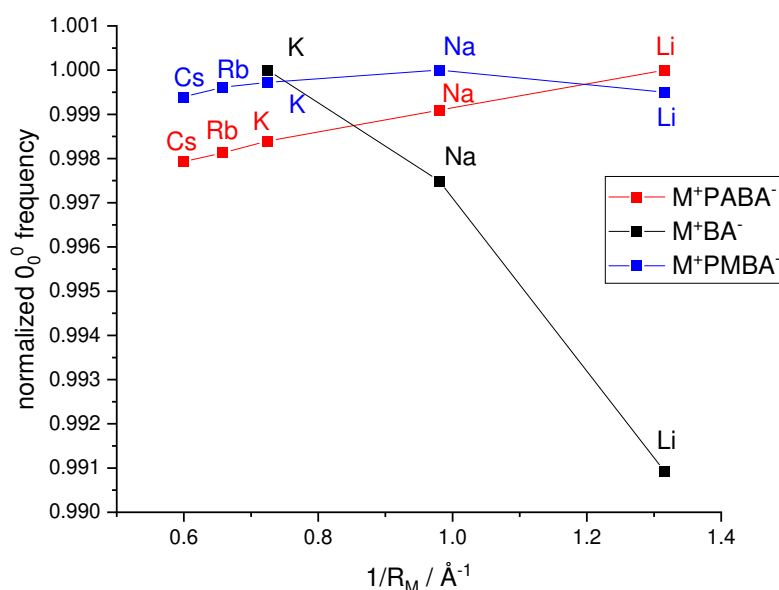


Figure 42: Comparison of the trends observed for the measured electronic origin ( $0_0^0$ ) transitions of the alkali ion pair species  $M^+PABA^-$ ,  $M^+PMBA^-$  and  $M^+BA^-$ . For the sake of clarity, the most blue-shifted transition of each row was normalized to 1.

The plot in figure 42 clearly shows that the shifts of the electronic origin transitions upon substitution of the alkali ion are rather small for the  $M^+PABA^-$  and  $M^+PMBA^-$  ion pairs, while the induced effects are much larger for the  $M^+BA^-$  ion pairs. As mentioned above, the particularly large shifts observed for  $M^+BA^-$  are probably due to the absence of any substituent exhibiting a positive mesomeric (+M) effect in *para*-position.

*(Photo)stability of the investigated ion pairs*

Overall, clear trends are observed regarding the (photo)stability of the studied ion pairs. Concerning the  $M^+PABA^-$  ion pairs a maybe surprisingly high stability was observed, whereby considerable fragmentation effects were merely obtained if a resonant IR laser (symmetric NH-stretching frequency) was irradiated after the R2PI process. As demonstrated, fragmentation effects are already strong for  $M^+PMBA^-$  species with larger alkali metal ions, and are even more pronounced for the  $M^+BA^-$  ion pairs.

The fragmentation pathways, discussed in the paragraphs above, reflect the observations that Mons, Gloaguen and coworkers made for other alkali carboxylate ion pair species<sup>[14]</sup> and can be explained by the respective alkali-carboxylate binding energies, which are summarized in table 5.

Table 5: Alkali-carboxylate binding energies for the  $M^+PABA^-$ ,  $M^+PMBA^-$  and  $M^+BA^-$  ion pairs (including ZPEs), calculated at the DFT/B3LYP-D3(BJ)/def2-TZVP level. All values are given in  $\text{cm}^{-1}$ .

	<b>PABA<sup>-</sup></b>	<b>PMBA<sup>-</sup></b>	<b>BA<sup>-</sup></b>
<b>Li<sup>+</sup></b>	61372	60698	59965
<b>Na<sup>+</sup></b>	52055	51513	50941
<b>K<sup>+</sup></b>	44994	44517	44044
<b>Rb<sup>+</sup></b>	42499	41953	41511
<b>Cs<sup>+</sup></b>	41281	40817	40363

Obviously, the binding energy between the alkali ions and the respective anions systematically decreases with increasing size of the alkali ion. A second observation is the decrease of the binding energy (when considering the same alkali element) from  $PABA^-$  over  $PMBA^-$  to  $BA^-$ . Here, the strength of the positive mesomeric effect (+M) of the substituent in the *para*-position of the benzoate should be the decisive factor. The +M effect of the  $-NH_2$  group of  $PABA^-$  is stronger than the +M effect of the  $-OMe$  group of  $PMBA^-$ .<sup>[178]</sup> Therefore, a slightly stronger negative partial charge is localized on the O atoms of the carboxylate group of  $M^+PABA^-$  ion pairs, compared to the respective species with an OMe substituent. The negative partial charge on the carboxylate is lower if no substituent with +M effect is attached in *para*-position. This is illustrated in table 6, on the basis of the  $Na^+$  ion pairs.

Table 6: Atomic partial charges for the investigated ion pairs in the  $S_0$  state, given for the respective  $\text{Na}^+$  species, as obtained from an NBO analysis at the DFT/B3LYP-D3(BJ)/def2-TZVP level.

	O(1)	O(2)	M <sup>+</sup>
<b>Na<sup>+</sup>PABA<sup>-</sup></b>	-0.81099	-0.81207	0.93571
<b>Na<sup>+</sup>PMBA<sup>-</sup></b>	-0.80825	-0.80825	0.93724
<b>Na<sup>+</sup>BA<sup>-</sup></b>	-0.80255	-0.80239	0.93876

A higher electron density on the carboxylate group goes along with an increased binding energy, due to a strengthening of the electrostatic interaction with the cation. According to literature, the  $\text{M}^+\cdots\text{OOC}$  bond should indeed be dominated by electrostatics.<sup>[179]</sup> Therefore, the binding energies (see table 5) are comparatively high for  $\text{M}^+\text{PABA}^-$  ion pairs, relative to the respective  $\text{M}^+\text{PMBA}^-$  and  $\text{M}^+\text{BA}^-$  species ( $\text{M}^+\text{PABA}^- > \text{M}^+\text{PMBA}^- > \text{M}^+\text{BA}^-$ ). In case of the unsubstituted benzoate, no substituent with a +M substituent is present, so that the binding energy is thus particularly weak for the  $\text{M}^+\text{BA}^-$  species.

#### 5.1.2.5 Investigations on the metal complex tris(8-hydroxyquinolato)aluminium

The newly implemented technique of molecular beam sampling by laser desorption was also successfully applied to the preparation of ligand stabilized metal complexes. In a pilot study, the complex tris(8-hydroxyquinolato)aluminium ( $\text{Alq}_3$ ), presented in figure 43 (a), was selected, which is composed of three anionic bidentate 8-hydroxyquinolate ligands that are coordinated to a trivalent aluminium center. It should also be noted that this complex is commonly used for light-emitting diodes (OLEDs).<sup>[180-183]</sup> These aromatic 8-hydroxyquinolate ligands should be strong UV chromophores, as required for an efficient photoionization of the complex *via* R2PI. In solution (in polar solvents), the UV absorption spectrum exhibits four absorption bands, with a very pronounced feature in the region of 350-450 nm (transition of predominantly  $\pi \rightarrow \pi^*$  character) and an even more dominant band at about 210-280 nm (transition of predominantly  $p \rightarrow \pi^*$  character).<sup>[181,183]</sup> Principally, these intense ligand centered transitions should provide a good basis for R2PI based experiments. The ionization energy of  $\text{Alq}_3$  (as a film surface), determined by applying high-sensitivity photoelectron yield spectroscopy (HS-PYS), is relatively low with 5.7 eV.<sup>[180]</sup> Thus, an efficient ionization *via* one color R2PI may be possible, even when exciting the complex in the spectral region around 400 nm. However, no effect of the UV excitation/ionization laser could be detected when applying a UV laser wavelength between 380 and 405 nm. Yet, an intense ion signal of the intact  $\text{Alq}_3$  complex was found using a much higher UV laser photon energy of 260 nm. Hereby, the same experimental parameters were used as for the



investigations on metal *para*-aminobenzoate systems. The respective mass spectrum of photoionized  $\text{Alq}_3$  and three parallelly detected fragment mass signals is depicted in figure 43 (b).

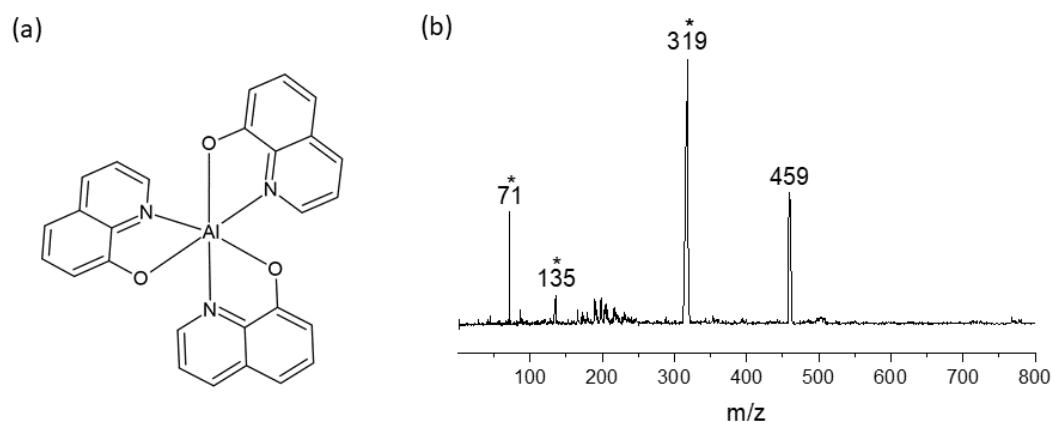


Figure 43: (a) Schematic structure of tris(8-hydroxyquinolino)aluminium ( $\text{Alq}_3$ ); (b) Mass spectrum of  $\text{Alq}_3$  and three fragment mass signals marked with asterisks ( $71 m/z$ ,  $135 m/z$  and  $319 m/z$ ; the noise around  $200 m/z$  is due to artefacts).

The mass spectrum clearly shows the intense mass signal of the intact  $\text{Alq}_3$  complex at  $459 m/z$ . The peaks at  $71 m/z$ ,  $135 m/z$  and  $319 m/z$  could not be assigned to specific species up to know, but the signals at  $135 m/z$  and at  $319 m/z$  likely belong to cationic fragments resulting from fragmentation during the laser desorption process, as their intensity is largely independent from the UV laser radiation. In contrast, the signal at  $71 m/z$  only appears when the UV excitation laser is irradiated.

The R2PI spectra recorded for  $\text{Alq}_3$  did not show any vibronic features, but the ion signal intensity of  $\text{Alq}_3$  clearly decreased towards longer wavelength, when tuning the UV laser between 260 nm and 283.5 nm. Merely the fragment at  $71 m/z$ , which might result from impurities in the used laser desorption matrix or might be due to the (resonant) photoionization of an initially neutral fragment of  $\text{Alq}_3$ , formed within the laser desorption process, exhibited sharp UV transitions in the R2PI scans.

Finally, it can be pointed out that, although the R2PI spectra did not show any resolved electronic transitions, the OLED relevant complex  $\text{Alq}_3$  could be successfully desorbed, photoionized and subsequently detected in the TOF mass spectrometer. In this way, these experiments once more underline the potential of laser desorption setups for investigations on isolated neutral metal complexes in the gas phase.

## 5.2 Non-covalent interactions

### 5.2.1 Introduction

In the second part of this thesis, aromatic ketone–alcohol aggregates were investigated with regard to non-covalent interactions, which play a key role *e.g.* in biochemical processes and in catalysis.<sup>[31,184]</sup> Within that, the main focus was put on the role of London dispersion interactions<sup>[26,27]</sup>, which belong to the attractive long-range van der Waals interactions<sup>[28]</sup>, along with the, also attractive, Debye (induction)<sup>[29]</sup> and the ambivalent Keesom<sup>[30]</sup> forces. However, London dispersion forces have been underestimated for a long time and have therefore often been wrongly neglected. Dispersion forces may be considered as weak, but that is only valid if only one single pair of interacting atoms is considered.<sup>[31]</sup> As the three mentioned forces are all proportional to  $1/r^6$ , with  $r$  being the distance separating two atoms or molecules, these interactions are particularly relevant in larger systems.<sup>[31,32]</sup> A vivid example from nature illustrating the strength of dispersion forces is the adhesion of Gecko spatulae, allowing these animals to climb up even smooth glass walls.<sup>[185]</sup> Beyond that, dispersion forces contribute crucially to the stability of the DNA helix<sup>[186]</sup> and play a decisive role in interactions between proteins<sup>[187]</sup> and other molecules. In a molecular beam study performed in the Gerhards group, the finally assigned folded structure of the linear depsipeptide CyCO-Gly-Lac-NH-PhOMe (cyclohexylcarbonyl-glycine-lactate-2-anisidine) was only retrieved within DFT calculations if Grimme's D3 dispersion correction<sup>[131]</sup> was applied.<sup>[33]</sup>

In organic synthesis, unusual compounds can be stabilized by dispersion forces. For example, hexaphenylethane is unstable due to steric repulsion of the phenyl groups. If, however, *tert*-butyl substituents (also called dispersion energy donors (DEDs)<sup>[31]</sup>) are introduced in all *meta* positions, attractive dispersion forces between both subunits overcome the steric Pauli repulsion to stabilize an exceptionally long C–C-bond.<sup>[188]</sup> Moreover, the all-*meta tert*-butyl substituted triphenylmethane showed a dimerization with a so-called head-to-head arrangement in the condensed phase with an exceptionally short intermolecular CH...H–C distance.<sup>[189]</sup> By applying Raman spectroscopy in molecular beam experiments it could be demonstrated that this unique dimer structure is maintained under isolated gas phase conditions. Regarding the unsubstituted triphenylmethane dimer, however, a so-called tail-to-tail arrangement is formed due to the absence of any *tert*-butyl groups (DEDs) compensating Pauli repulsion.<sup>[34]</sup>

Thus, London dispersion interactions obviously play a decisive role in many systems, so that a deeper understanding as well as an accurate theoretical description of dispersion interactions and their interplay with other non-covalent forces is required.

Investigations on small isolated model aggregates in molecular beams, eliminating any environmental effects, are ideal tools for benchmarking of quantum chemical methods. After the adiabatic expansion and in absence of any kinetic trapping effects, only the lowest energy isomers and vibrational states should be preferentially populated, which facilitates direct comparison with theoretical predictions. For these studies, selected complexes formed between an (aromatic) organic compound and a solvent molecule, exhibiting fine energetic balances between competing binding motifs and sites, are specifically chosen. By investigating multiple aggregates with various dispersion energy donors (*e.g.* by considering alcohols with varying alkyl residues) random error cancellation is ruled out, while subtle deficiencies of the theoretical methods are unveiled.<sup>[36]</sup>

Within this context, extensive studies on aromatic ether–alcohol aggregates have been performed, whereby several spectroscopic methods (FTIR, IR/UV and MW) in molecular beam experiments were applied and combined with various theoretical methods.<sup>[56,68,83,190–192]</sup> Herein, primarily the competition between the distinct binding motifs OH $\cdots$ O(ether) and OH $\cdots$  $\pi$  was investigated. Regarding the structures of diphenylether (DPE)–alcohol aggregates, the OH $\cdots$ O motif is increasingly favored over the OH $\cdots$  $\pi$  arrangement with increasing size of the alcohol alkyl group, throughout the series from water, over methanol, *tert*-butanol to adamantanol. This counterintuitive trend is driven by the interplay between dispersion and deformation energies.<sup>[192]</sup> Partly, these systems were also investigated in the electronically excited state ( $S_1$ ) by applying the UV/IR/UV technique, as well as in the ionic ground state ( $D_0$ ) (using the UV/UV/IR method). In the  $S_1$  state, the binding motifs observed for the respective species in the electronic ground state were generally maintained. Nevertheless, vibrational shifts of the OH-stretching frequencies occurred due to charge transfer processes upon electronic excitation.<sup>[56,83,190]</sup> Concerning the DPE–methanol complex in the  $D_0$  state, however, the OH $\cdots$ O bond observed in the  $S_0$  and  $S_1$  state is broken upon photoionization.<sup>[83]</sup>

Over the last couple of years, the focus has been gradually turned towards the investigation of ketone–solvent balances, that have been launched by the Suhm group, investigating complexes between acetophenone derivatives (with varying alkyl substituents) and several alcohols (with different alkyl residues) by FTIR spectroscopy in a molecular jet in combination with DFT calculations.<sup>[35]</sup> In the following, they performed similar investigations on pinacolone–alcohol aggregates<sup>[36]</sup>, as well as on phenol–halogenated acetophenone clusters<sup>[37]</sup>. Other studies on ketone–solvent complexes include investigations on fenchone–phenol/benzene aggregates.<sup>[193]</sup>

In this work, chromone–methanol aggregates were analyzed by applying IR/UV spectroscopy in a molecular beam experiment. As chromone has a rather high vapor pressure and has a convenient thermal stability, apparatus (I), with its thermal source, could be used.

In this complex, the methanol is hydrogen-bonded to the carbonyl O atom, which has two very similar free electron pairs. In this way, the molecular balance consists of the competition between these two

docking sites, named “*outside pocket*” and “*inside pocket*”. These two isomers are energetically very close to each other, but are stabilized *via* distinct CH $\cdots$ O contacts (1,2-like contact for the *outside* isomer and 1,3-like contact for the *inside* isomer). The possible structural motifs of chromone–alcohol aggregates with the two competing sites are illustrated in figure 44.

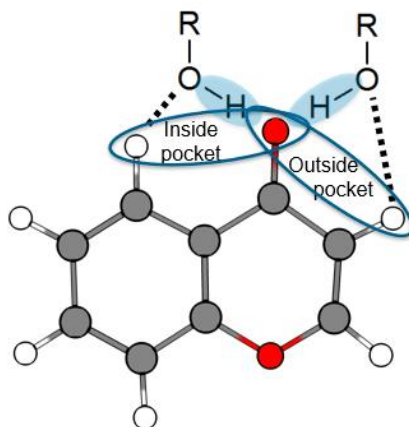


Figure 44: Schematic structure of the chromone–alcohol aggregate, illustrating the two competing “*outside pocket*” and “*inside pocket*” structural motifs.

Regarding the chromone–methanol system, both the electronic ground and excited state were of interest. Most importantly, as already demonstrated in the Gerhards group for the related compound xanthone<sup>[71]</sup>, chromone undergoes intersystem crossing (ISC) into the triplet manifold upon electronic excitation into the  $S_2$  state<sup>[38]</sup>. Similarly, an ISC is also expected for the respective chromone–methanol clusters. To the best of my knowledge, the first UV/IR/UV spectrum of an organic molecule–solvent complex in an electronically excited triplet state is presented here. Moreover, the thus prepared triplet state facilitates the quantum chemical investigations with respect to the energy partitioning. As the  $T_1$  state (in contrast to  $S_1$ ) has ground state character, energy decomposition (LED) approaches like “symmetry-adapted perturbation theory” (SAPT)<sup>[194,195]</sup> and “domain based local pair natural orbital” (DLPNO)-CCSD(T)/LED<sup>[196,197]</sup> can thus be applied. As the “*outside pocket*” and “*inside pocket*” docking sites are structurally very similar to each other, merely a low zero point vibrational energy (ZPVE) difference between both isomers is to be expected.<sup>[35,36]</sup> This is another advantage of this model system compared to previous studies with competing OH $\cdots$ O and OH $\cdots$  $\pi$  binding motifs.

Other nature-related compounds containing carbonyl groups in different environments are protected amino acids, like the protected phenylalanine AcPheOMe. AcPheOMe<sup>[198,199]</sup>, as well as its mono-, di- and trihydrates<sup>[1]</sup>. They have been extensively studied in the Gerhards group by applying IR/R2PI spectroscopy in the amide A and amide I/II regions. As the very polar C- and N-termini are capped, the solvent molecules may only interact with the amino acid residue and with the NH and CO groups of the backbone. Therefore, these protected amino acids are predestined for investigations of peptide

backbone solvations.<sup>[1]</sup> Within this context, the aggregate of the protected tyrosine AcTyr(Me)OMe with methanol was also studied in the present work by applying IR/R2PI spectroscopy (using apparatus (I)). The optimized DFT geometry of isolated AcTyr(Me)OMe is depicted in figure 45.

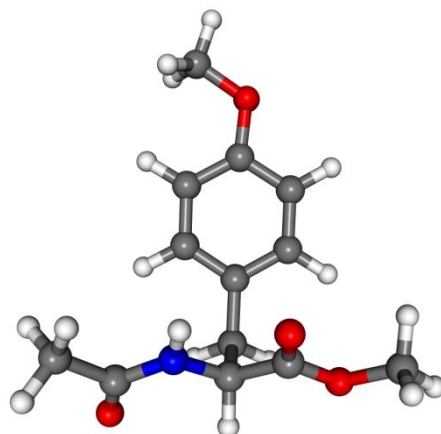


Figure 45: Optimized global minimum geometry of AcTyr(Me)OMe with its stretched ( $\beta_L$ -)backbone conformation, as obtained at the DFT/B3LYP-D3(BJ)/def2-TZVP level.

At first glance, the backbone of AcTyr(Me)OMe shows several potential docking sites for solvent molecules, with one (amide) NH group and two (amide and ester) carbonyl groups. Furthermore, interactions with the  $\pi$ -system and the OMe groups are conceivable. Therefore, a huge variety of possible minimum geometries within the conformational search could readily be expected, whereby IR/R2PI experiments in the region of OH- and NH-stretching vibrations allowed for a preliminary structural assignment.

### 5.2.2 Chromone–methanol cluster in the electronic ground and lowest triplet state: A delicate interplay of non-covalent interactions (see publication [2])

#### **Preamble:**

The combined IR/UV experiments in the molecular beam were performed by Patrick Strebart and myself, assisted by Marcel Meta. Quantum chemical analyses consisting of (TD)DFT-, SAPT- and DLPNO-CCSD(T)/LED calculations were performed by Patrick Strebart and Marcel Meta. The procedure was designed by Fabian Dietrich and Markus Gerhards. An initial manuscript was written by Patrick Strebart and myself. The manuscript was revised by contributions of all coauthors. Markus Gerhards and Christoph Riehn were my supervisors.

This part has already been published in the journal *Physical Chemistry Chemical Physics* (as part of the 2022 PCCP HOT Articles collection) and is reprinted in chapter 7; see publication [2]. To give a short overview, the most important results and discussions are briefly summarized in the following.

### **Summary:**

In this project the chromone–methanol carbonyl balance was probed by applying combined IR/UV spectroscopy in combination with sophisticated quantum chemical investigations (DFT, SAPTO<sup>[194,195]</sup> and DLPNO-CCSD(T)<sup>[196,197]</sup>). The chromone unit provides two very similar carbonyl lone pairs as binding sites for an alcohol molecule, which are stabilized *via* distinct CH $\cdots$ O contacts. Concretely, the two competing structural arrangements, called “*outside*” isomer and “*inside*” isomer, exhibit 1,2-like and 1,3-like CH $\cdots$ O contacts, respectively (see figure 44). Energetically, both isomers are separated by  $\Delta E = 1.8 \text{ kJ}\cdot\text{mol}^{-1}$  in favor of the “*outside*” isomer according to DFT. Consistent with this, the measured IR/R2PI spectrum for the  $S_0$  state reveals a higher population of the more stable “*outside*” isomer in the molecular beam.

As the chromone unit undergoes a fast and efficient intersystem crossing (ISC) into the triplet manifold upon electronic excitation into the  $S_2$  state,<sup>[38]</sup> the studies on (aromatic) molecule–solvent aggregates could for the first time be extended to a cluster in an electronically excited triplet state ( $T_1$  state). In this way, the present study demonstrates that the powerful UV/IR/UV technique can be applied to investigate a neutral cluster in an excited triplet state. Hereby, possibly (vibrationally) “hot” clusters are probed, as the isolated clusters cannot dissipate any energy by collisions after ISC. At the same time, the experiment may, however, be supported by UV-induced cluster fragmentation, *i.e.* evaporative cooling effects, going along with a loss of excess energy and yielding “cooled” triplet state clusters.

For both competing isomers, the measured UV/IR/UV spectrum (in accordance with the DFT harmonic frequency calculations) unveils a blue-shift of the OH-stretching frequencies after electronic excitation and subsequent ISC, indicating a weakening of the hydrogen bonds. The latter trend is further confirmed by binding energy calculations and by the energy decomposition analysis (performed using SAPTO).

In the  $T_1$  state, the clusters keep a strong preference for the OH $\cdots$ O structures observed in the  $S_0$  state. However, a ring puckering, localized on the 4-pyrone ring, occurs in the  $T_1$  state. Concretely, the C atom of the CH moiety adjacent to the ether O atom lies outside the plane of the chromone unit. Hereby, the spin density is localized on the puckered C atom. This geometric distortion leads to a stronger

energetic differentiation between the two competing isomers (with  $\Delta E = 3.2 \text{ kJ}\cdot\text{mol}^{-1}$  (at DFT level)), since the “*outside pocket*” binding site is part of the flexible non-planar 4-pyrone ring. The energy decomposition analysis further reveals that, for both isomers, dispersion forces are similarly dampened by the electronic excitation, while the electrostatic and inductive interactions are strongly modulated depending on the binding site. Finally, distinct electrostatic and induction contributions for both isomers are responsible for the increased  $\Delta E$  rather than dispersion forces.

### 5.2.3 AcTyr(Me)OMe–methanol cluster

Besides the chromone–methanol clusters, the AcTyr(Me)OMe–methanol cluster, formed by aggregation of the protected amino acid AcTyr(Me)OMe (see figure 45) and one methanol molecule, was investigated. Amino acid– or small polypeptide–solvent clusters are, of course, convenient model systems for exploration of non-covalent interactions and also allow to follow the possible structural rearrangement of peptides upon stepwise microsolvation. Hereby, most studies found in literature focus on hydrate clusters (*e.g.* <sup>[1,200,201,202]</sup>), with water being one of the most relevant aggregation partners in nature, while investigations using methanol<sup>[201,202]</sup> as solvent are rather scarce.

AcTyr(Me)OMe corresponds to the amino acid (L)-tyrosine (Tyr) with protected N- and C-termini, as well as a methylated OH group. Due to these protecting groups, an attached methanol molecule may interact with the NH- and CO groups of the “peptide” backbone or with the  $\pi$ -system of the Tyr residue, but not with the polar end groups as it would be the case for unprotected Tyr. Therefore, such protected amino acid (model “peptide”)–solvent aggregates are ideal model systems to investigate peptide backbone solvations. Within this context, the mono- di- and trihydrates of AcPheOMe<sup>[1]</sup>, were investigated in the Gerhards group by applying IR/R2PI spectroscopy. In the present work, the focus was put on the AcTyr(Me)OMe–MeOH cluster, comprising merely one methanol molecule, whereby the aggregation to larger clusters with more than one methanol molecule was suppressed by adapting the vapor pressure of the solvent *via* the temperature of the cooled reservoir.

The R2PI spectrum of AcTyr(Me)OMe features a broad transition around  $36461 \text{ cm}^{-1}$ , which is thus blue-shifted relative to the  $S_1 \leftarrow S_0$  transitions of the various conformers of unprotected Tyr, found between  $35491$  and  $35650 \text{ cm}^{-1}$  <sup>[122]</sup>. However, the UV resonance of AcTyr(Me)OMe does not undergo any clearly visible frequency shifts upon attachment of a methanol (or water) molecule.

Regarding the IR/R2PI experiments, the amide I/II region ( $1400\text{--}1800\text{ cm}^{-1}$ ) was not readily accessible within this work, so that the focus was put on the spectral region of the NH- and OH-stretching vibrations. For the isolated AcTyr(Me)OMe monomer, very similar features as for the structurally related AcPheOMe<sup>[198,199]</sup> were observed in the IR/R2PI spectrum, depicted in figure 46.

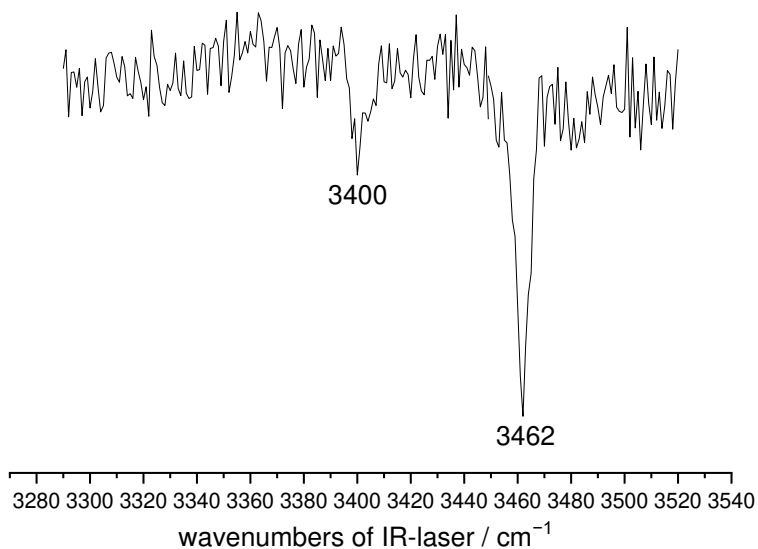


Figure 46: IR/R2PI spectrum of the AcTyr(Me)OMe monomer.

Concretely, a sharp NH-stretching band is observed at  $3462\text{ cm}^{-1}$ , as well as a weaker feature at  $3400\text{ cm}^{-1}$ , which was assigned to the overtone of the C=O stretching vibration of the amide group. Finally, a geometry with a stretched backbone and a so-called C5 interaction<sup>[39,203]</sup> between the NH group and the ester carbonyl group ( $\beta$ -sheet arrangement<sup>[39]</sup>) was found, similar to AcPheOMe<sup>[198,199]</sup>. The orientation of the Tyr(Me) residue relative to the backbone may be further elucidated by probing the amide I/II spectral region.

Geometry optimizations and harmonic vibrational frequency calculations at DFT level were performed by my colleague Patrick Strebert. The energetically most stable structure, with a  $\beta_{\text{L}}(\text{g}+)$  conformation, is depicted in figure 45. At this point, it can also be noted that both methoxy rotamers are almost isoenergetic, both minima being only separated by few wavenumbers.

On that basis the microsolvation of AcTyr(Me)OMe was investigated. The IR/R2PI spectrum of AcTyr(Me)OMe–MeOH, recorded in the spectral region between  $3190$  and  $3750\text{ cm}^{-1}$  *via* the R2PI transition at  $36461\text{ cm}^{-1}$  is depicted in figure 47, together with the calculated stick spectra for selected isomers (A-F). Hereby mode specific scaling factors were applied, with the OH-stretching frequencies being scaled by a factor of  $0.9674$ <sup>[191]</sup>, while all NH-stretching frequencies were scaled by  $0.9597$ . These scaling factors were derived from reference calculations for an isolated MeOH molecule and for the isolated AcTyr(Me)OMe monomer, respectively.



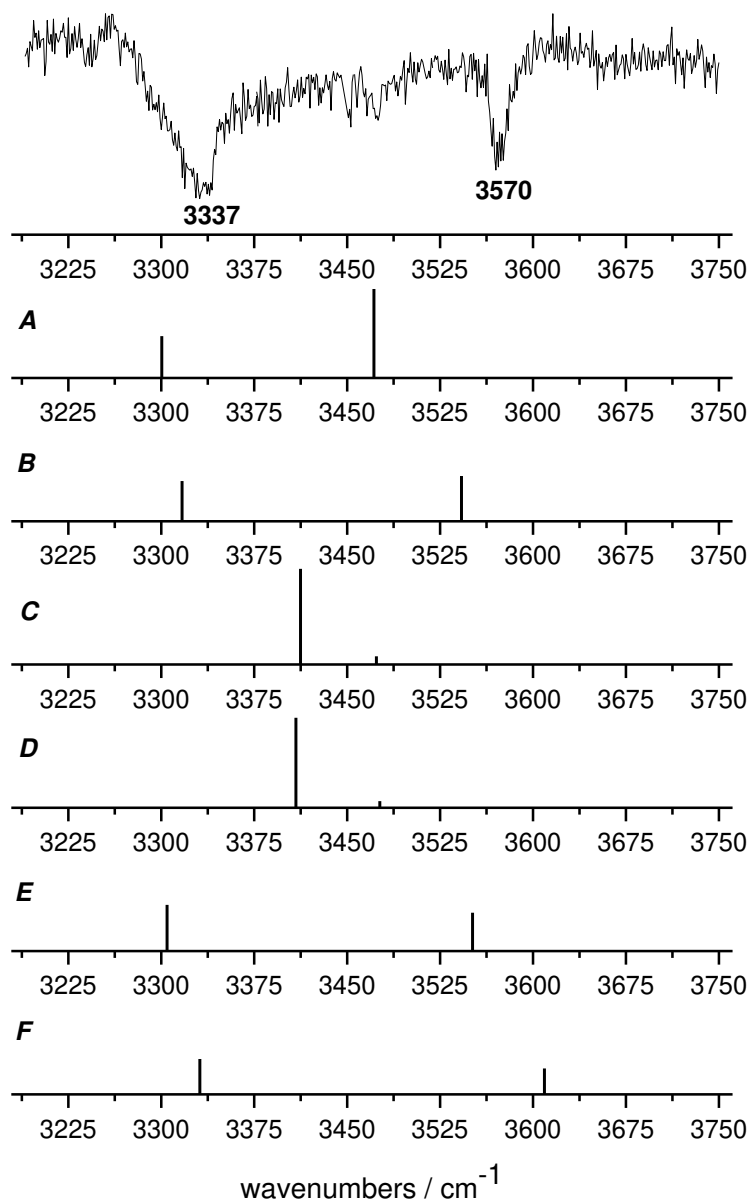


Figure 47: IR/R2PI spectrum of AcTyr(Me)OMe–MeOH, recorded *via* the UV transition at  $36461\text{ cm}^{-1}$ , together with the calculated stick spectra for selected isomers (A-F), as obtained at the DFT/B3LYP-D3(BJ)/def2-TZVP level.

The IR/R2PI spectrum of the AcTyr(Me)OMe–MeOH cluster shows two clearly dominating features at about  $3337\text{ cm}^{-1}$  and at  $3570\text{ cm}^{-1}$ , respectively. The slightly broadened intense band at about  $3337\text{ cm}^{-1}$  should definitely be assigned to a hydrogen-bonded NH (or OH) group, while the somewhat sharper band at  $3570\text{ cm}^{-1}$  likely arises from an OH-stretching frequency of a weakly bound methanol molecule. The two much weaker dips around  $3460\text{ cm}^{-1}$  may be due to the minor contribution of a second isomer or might be caused by UV photofragmentation of larger AcTyr(Me)OMe–(MeOH)<sub>n</sub> or AcTyr(Me)OMe–(MeOH)<sub>n</sub>–(H<sub>2</sub>O)<sub>n</sub> clusters upon ionization. As the two mentioned transitions at 3337

and  $3570\text{ cm}^{-1}$ , respectively, clearly stand out in this IR/R2PI spectrum, this is a first indication for the predominance of one single isomer of AcTyr(Me)OMe–MeOH in the molecular beam.

A selection of the optimized DFT (B3LYP-D3(BJ)/def2-TZVP) geometries is depicted in figure 48. As can be seen in table 7, entropic contributions seem to have a considerable influence on the relative stabilities of the found minimum structures. Therefore, the relative Gibbs free energies ( $\Delta G$ , at 298.15 K) of the distinct isomers are considered in the following.

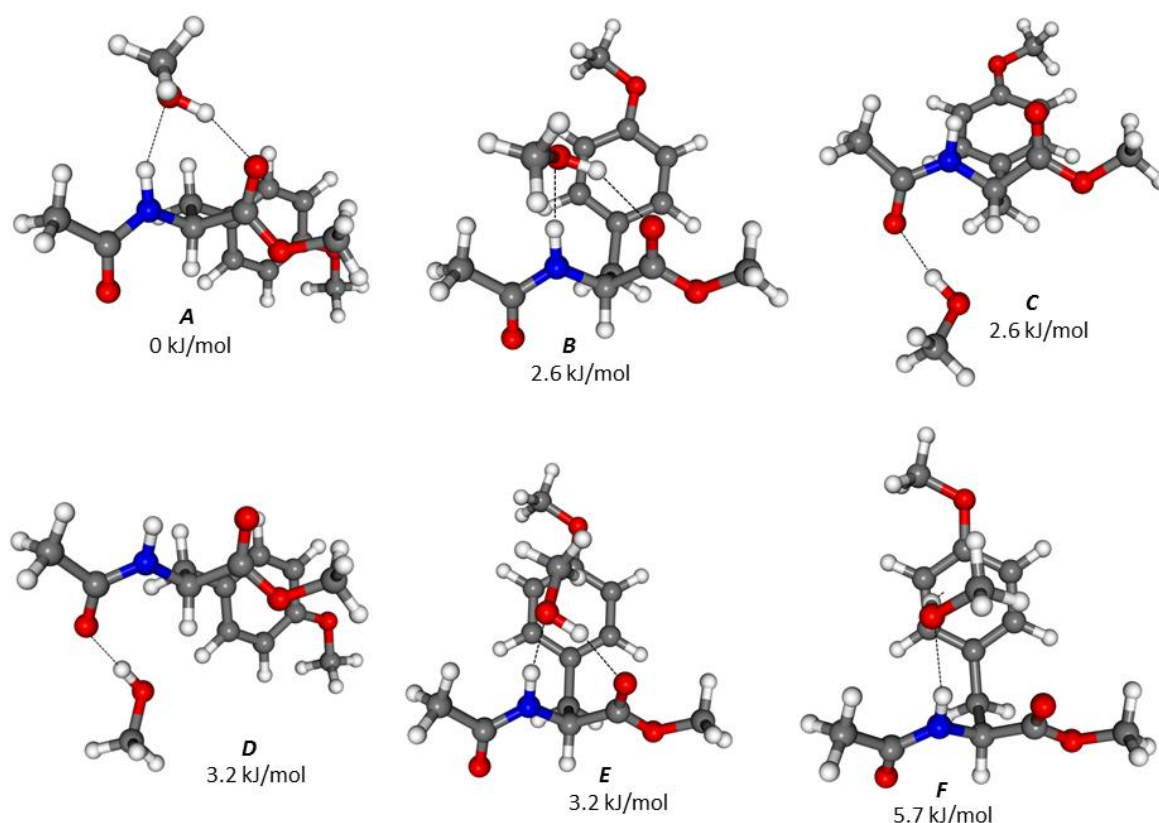


Figure 48: Optimized geometries of the AcTyr(Me)OMe–MeOH clusters, as obtained at the DFT/B3LYP-D3(BJ)/def2-TZVP level, together with the corresponding relative Gibbs free energies (at 298.15 K).

Table 7: Relative Gibbs free energies ( $\Delta G$ ) and relative electronic energy values ( $\Delta E_0$ , including zero-point energy (ZPE) correction) for the considered isomers A-F, as obtained at the DFT/B3LYP-D3(BJ)/def2-TZVP level.

	$\Delta G / \text{kJ}\cdot\text{mol}^{-1}$	$\Delta E_0 / \text{kJ}\cdot\text{mol}^{-1}$
<b>A</b>	0.0	9.1
<b>B</b>	2.6	6.5
<b>C</b>	2.6	8.5
<b>D</b>	3.2	8.2
<b>E</b>	3.2	0.0
<b>F</b>	5.7	3.8

Regarding the global minimum structure (isomer *A*), the methanol molecule is doubly bound to the peptide backbone, with the OH group simultaneously acting as hydrogen bond donor and acceptor. Concretely, the amide NH group is linked to one of the free electron pairs of the O atom of the methanol, while the OH group acts as hydrogen bond donor towards the O atom of the C=O site of the ester. Hereby, the corresponding calculated vibrational frequencies are however only partly in accordance with the measured IR/R2PI spectrum. The predicted NH-stretching frequency may correlate with the broadened band at  $3337\text{ cm}^{-1}$ , but the calculated OH-stretching frequency of about  $3470\text{ cm}^{-1}$  is too low to be assigned to the intense band observed in the experiment at  $3570\text{ cm}^{-1}$ . Thus, the global minimum structure may rather not occur in the experiment.

In contrast, the calculated NH- and OH-stretching frequencies of structure *B*, which is merely  $2.6\text{ kJ/mol}$  higher in energy, principally reflect the measured features. Here, the NH-stretching frequency perfectly fits to the measured band at  $3337\text{ cm}^{-1}$ , while the OH-stretching frequency is significantly blue-shifted relative to isomer *A* to give a much better agreement with the experiment for structure *B*. This effect can be explained by minor distortions within the backbone geometry, which go along with a slightly increased OH $\cdots$ OC distance of  $1.924\text{ \AA}$  (compared to  $1.855\text{ \AA}$  for isomer *A*) and a marginally larger  $\angle\text{C=O}\cdots\text{H}$  angle of  $130.1^\circ$  (relative to  $123.0^\circ$  for isomer *A*). These geometric changes should give rise to a somewhat weakened OH $\cdots$ O=C hydrogen bond in the case of structure *B*, coinciding with its higher OH-stretching frequency. It should also be noted that, within the investigations on the related AcPheOMe–H<sub>2</sub>O aggregate, a feature observed at  $3575\text{ cm}^{-1}$  had been attributed to the hydrogen-bonded OH-stretching vibration of the water molecule that is bridged to the C=O group of the ester. On top of that, a geometry showing the discussed doubly hydrogen-bonded motif was indeed one of the assigned structures for monohydrated AcPheOMe.<sup>[1]</sup>

Regarding isomers *C* and *D*, the methanol molecule is singly hydrogen-bonded to the O atom of the amide group, while the backbone conformation of the lowest energy isomers is basically maintained. For these two structures, the calculated vibrational spectra do not reflect the experimental data. As the solvent molecule is in a sterically free environment it can adopt an optimal orientation for strong hydrogen bonding between the OH group and the lone pair of the carbonyl O atom. This goes along with a particularly red-shifted OH-stretching frequency around  $3410\text{ cm}^{-1}$ , which does not correlate with the IR/R2PI spectrum. It should however be noted that, besides a doubly-bound geometry, a structure of this binding motif had been assigned for AcPheOMe–H<sub>2</sub>O.<sup>[1]</sup>

The IR frequencies predicted for structure *E*, showing the same binding motif and a similar backbone geometry as the most stable structures *A* and *B*, are principally in accordance with the experiment. However, this also means that the orientation of the Tyr(Me) side chain, as well as the orientation of the methanol molecule relative to the residue may not be fully cleared up by IR/R2PI experiments in the OH-/NH-stretching region. Interestingly, isomer *E* is the most stable structure if the pure electronic

energies (including ZPE) are considered, but is disadvantaged by 3.2 kJ/mol if the relative Gibbs free energies are taken into consideration. Within structure *E*, the methyl group of the solvent molecule interacts with the  $\pi$ -system of Tyr(Me), stabilizing the cluster. However, this interaction may be the reason for its higher relative Gibbs free energy, as the CH $\cdots\pi$  contacts go along with a loss of conformational entropy.

Finally, isomers showing an OH $\cdots\pi$  interaction, such as isomer *F*, should be discussed. This structure is 5.7 kJ/mol less stable relative to isomer *A*, but the corresponding vibrational pattern is principally in agreement with the experimental spectrum. Within this geometry, the NH group of the backbone is hydrogen-bonded to an electron lone-pair of the O atom of the methanol molecule, while the OH group interacts with the  $\pi$ -system of Tyr(Me). Surprisingly, OH $\cdots\pi$  interactions did not play a major role within the studies on AcPheOMe, which is however likely due to the fact that, by this time, geometry optimizations were performed without taking dispersion interactions into account (no DFT-D correction). In spite of that, it should also be emphasized that the predicted OH-stretching frequency clearly lies above 3600 cm $^{-1}$ , while the measured band was found at 3570 cm $^{-1}$ . Indeed, as observed for the deeply investigated aromatic ether–methanol aggregates, OH-stretching frequencies are mostly found between 3620 and 3640 cm $^{-1}$  in case of OH $\cdots\pi$  bound structures.<sup>[68,191]</sup> Furthermore, the measured feature is slightly broadened, which is typical for hydrogen-bonded OH groups. Therefore, the discussed band may be assigned to an OH $\cdots$ O bound motif, rather than to an OH $\cdots\pi$  geometry. Finally, the presence of an OH $\cdots\pi$  structure might not be completely excluded, but seems rather unlikely. This statement may be further confirmed through measurements in the spectral region of C=O stretching vibrations (amide I/II region), which was unfortunately not readily accessible within the present work.

Lastly, it remains to mention that other binding motifs, such as structures with the methanol molecule being linked to the C=O site of the ester, as well as geometries with the solvent molecule being hydrogen-bonded to the the O atom of the OMe group of the Tyr(Me) residue are all higher in energy and are therefore not further discussed here.

To conclude, the measured IR/R2PI spectrum with its two pronounced features is a clear indication of the presence of one specific structural type in the molecular beam. Specifically, isomer *B*, in which the methanol molecule is inserted between the NH and ester CO groups should most likely be assigned. Structurally, the stretched backbone geometry of isolated AcTyr(Me)OMe is largely maintained in its methanol aggregate, so that the stretched  $\beta_L$  arrangement is conserved. Regarding binding type and backbone geometry, this structural motif resembles one of the two isomers of monohydrated AcPheOMe.<sup>[1]</sup> As mentioned above, the proposed assignments may be further supported by probing the C=O stretching vibrations, whereby OH $\cdots$ O and OH $\cdots\pi$  bound structures should yield distinct vibrational patterns. From a theoretical point of view, sophisticated local energy decomposition

approaches such as SAPT<sup>[194,195]</sup> and (DLPNO)-CCSD(T)/LED<sup>[196,197]</sup>, demonstrating the contributions of distinct types of intra- and intermolecular (electrostatic, induction, dispersion, repulsive exchange) interactions to the stability of specific structural motifs, may be of interest with regard to this project.

## 5.3 Metal ion–peptide interactions

### 5.3.1 Introduction

Although the conformation of a peptide strongly depends on intrinsic factors such as the amino acid sequence, structure and functionality of peptides are often further influenced by the presence of cofactors (such as solvent (water) molecules or metal cations).<sup>[39–41]</sup> Hereby, it should be mentioned that almost half of all proteins coordinate to metal atoms to form so-called metalloproteins<sup>[41,42]</sup>, which play a decisive role in numerous biochemical reactions (*e.g.* <sup>[42]</sup>). Despite this, the specific role of metallic cofactors is not yet fully understood for many biological processes. Therefore, a so-called bottom up approach, starting with gas phase and quantum chemical investigations on rather small aggregates between isolated amino acids or peptides and other binding partners (*e.g.* metal cations <sup>[15,75]</sup>), can be a constructive first step.<sup>[39,40,42]</sup>

Within this context, structural analyses on the cationic [AlAcTrpOMe]<sup>+</sup> aggregate were performed here. In this system, a monovalent aluminium(I) ion is coordinated to the protected amino acid AcTrpOMe. Structurally, isolated AcTrpOMe forms a stretched backbone conformation, which is very similar to the geometry of AcTyr(Me)OMe depicted in figure 45.<sup>[204]</sup>

In most gas phase studies on ionic metal–amino acid/peptide complexes, the isolated aggregates are commonly generated by using ESI sources in combination with room temperature (*e.g.* <sup>[205–208]</sup>) or cold<sup>[209,210]</sup> ion traps. Alternatively, these experiments can also be realized in a molecular beam experiment by using a cluster source like the combined thermo-ablation source applied in the Gerhards group (implemented in apparatus (II)), already used for the IR/UV investigations of [AlAcPheOMe]<sup>+</sup> and [AlAcPheOMe]<sup>3+</sup>.<sup>[75]</sup> The IR+UV photodissociation spectra of [AlAcTrpOMe]<sup>+</sup>, discussed in draft [3], were recorded by the former group members Dr. Philipp Bialach and Dr. Markus Becherer utilizing the same setup. Most studies on small metalloproteins in the gas phase focused on the biologically relevant alkali and earth alkaline elements like *e.g.* Na<sup>+</sup>, K<sup>+</sup> or Ca<sup>2+</sup> (*e.g.* <sup>[205–210]</sup>). In the Gerhards group aggregates with aluminium cations were investigated, whereby aluminium does however not show any specific biological function. Nevertheless, it should be noted that since the 1970s a link between exposure to aluminium and Alzheimer’s disease has been suspected. In fact, particularly high aluminium concentrations are frequently detected in the brain tissue of Alzheimer patients (*e.g.* <sup>[211]</sup>).

Due to the low stability of monovalent aluminium ions, and aluminium being commonly found in the +3 oxidation state, their biological relevance is of course arguable. This high reactivity may also be a reason for the very limited number of publications about stable Al(I) organometallic complexes.<sup>[212,213]</sup> Aluminium(I) can however be stabilized by complexation with a  $\beta$ -diketiminato (NacNac) ligand. Interestingly, compounds with stable X–H bonds (with X = *e.g.* H, N, O) can be activated by these Al(I)NacNac complexes to form an aluminium hydride species.<sup>[212,214]</sup> Isolated aluminium hydride clusters can also be generated *e.g.* in a pulsed arc cluster ionization source (PACIS), with the formed clusters likely exhibiting terminal Al–H bonds.<sup>[215]</sup> Compared to the Phe residue of AcPheOMe, the heterocyclic indole group of Trp shows a considerably larger  $\pi$ -system and an increased reactivity, which is already apparent from the formation of indole Grignards.<sup>[216]</sup> These aspects should be kept in mind, as the indolic residue of Trp already leads to another homodimer geometry of (AcTrpOMe)<sub>2</sub> relative to (AcPheOMe)<sub>2</sub>. Within (AcTrpOMe)<sub>2</sub>, a hydrogen bond is formed between an indole NH group and a backbone CO group, which cannot be formed in the case of (AcPheOMe)<sub>2</sub>.<sup>[198,199,204]</sup>

In order to simulate the experimental IR+UV spectrum of [AlAcTrpOMe]<sup>+</sup> an extensive conformational search was performed in the present work. Besides the geometry optimizations and harmonic frequency calculations, single point energy calculations were conducted at the DLPNO-CCSD(T) level. Later on, the theoretical studies on the DFT level were extended to aggregates of AcTrpOMe with other monovalent metal ions (Li<sup>+</sup>, Na<sup>+</sup>, K<sup>+</sup>, Rb<sup>+</sup>, Cs<sup>+</sup>, Mg<sup>+</sup>, Ti<sup>+</sup>, Zn<sup>+</sup>, Ag<sup>+</sup>, Ga<sup>+</sup>), in order to reveal the influence of the specific metal ion properties (such as redox properties and ion radii) on the structural behavior and reactivity of the cluster.

### 5.3.2 Theoretical and Spectroscopic Investigations on Monovalent Cationic Metal–AcTrpOMe Clusters in the Gas Phase (see manuscript draft [3])

#### **Preamble:**

The UV- and IR+UV experiments were performed by Philip Bialach and Markus Becherer. I reconducted and complemented initial DFT studies and further extended the studies to clusters with other metal elements apart from aluminium. Additionally, I conducted single point calculations at DLPNO-CCSD(T) level and performed transition state calculations. Markus Gerhards and Kirsten Schwing assisted in interpreting the results. An initial manuscript was written by Kirsten Schwing and myself. The manuscript was revised by Markus Gerhards, Kirsten Schwing and myself. Markus Gerhards was my supervisor.

This chapter has been prepared as a manuscript draft for publication and is printed in chapter 7; see manuscript draft [3]. To give a short overview, the most important results and discussions are briefly summarized in the following.

#### **Summary:**

This project focused on the structural analysis of the cationic  $[\text{AlAcTrpOMe}]^+$  cluster, formed by aggregation between a monovalent aluminium ion ( $\text{Al}^+$ ) and the protected amino-acid AcTrpOMe. Compared to the structurally similar  $[\text{AlAcPheOMe}]^+$ , investigated in a previous study (see <sup>[75]</sup>), the Trp residue of AcTrpOMe with its extended  $\pi$ -system and a potentially reactive NH group may lead to “new” binding motifs. Indeed, the conformational search (at DFT level) performed for  $[\text{AlAcTrpOMe}]^+$  yielded a unique and maybe unexpected structural arrangement, depicted in figure 49 (a). Herein, the aluminium ion is linked to both carbonyl groups of the backbone and is at the same time inserted into the N–H bond of the indole system. This “insertion” could be considered as a kind of oxidative addition of the indole NH group onto aluminium, which thus approaches its most stable +3 oxidation state.

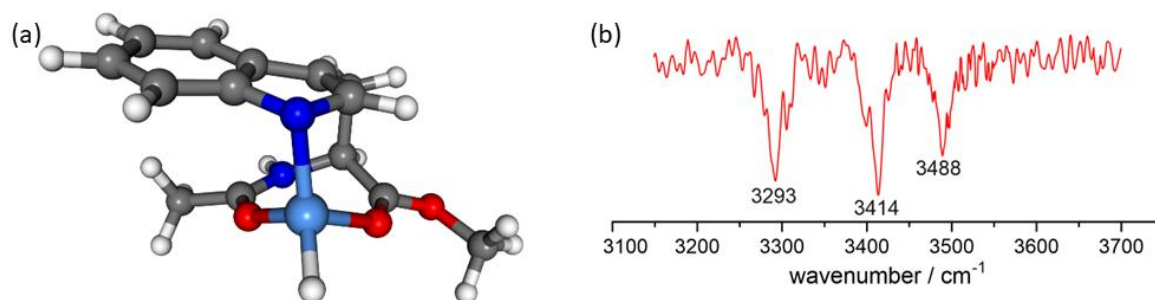


Figure 49: (a) Optimized geometry of the “inserted” minimum structure of  $[\text{AlAcTrpOMe}]^+$  as obtained at the DFT/B3LYP-D3/TZVP level; (b) IR+UV spectrum of  $[\text{AlAcTrpOMe}]^+$ .

Alongside this unique isomer, a multitude of other “intact” minimum structures, with the  $\text{Al}^+$  ion being either coordinated to one or both carbonyl groups of AcTrpOMe, were found. However, the extraordinary “inserted” motif is by far the most stable isomer, being  $1133 \text{ cm}^{-1}$  lower in energy than the most stable “intact” geometry. Even if entropic effects are taken into account, the “inserted” structure is still among the most stable geometries. This finding was further confirmed by single point energy calculations at the DLPNO-CCSD(T) level, according to which this unique motif is  $4786 \text{ cm}^{-1}$  more stable than the energetically most stable structure with intact AcTrpOMe. Harmonic frequency calculations were performed for all minimum structures, which were then compared to the measured IR+UV spectrum (see figure 49 (b)). In the presence of one single isomer of  $[\text{AlAcTrpOMe}]^+$  in the molecular beam, two features would principally be expected in the probed NH-stretching region. However, the experimental spectrum shows three clearly separated bands. Hereby, the occurrence of a Fermi resonance between the first overtone of a C=O stretching mode and the fundamental of an NH-stretching vibration seems very improbable (according to the calculated C=O stretching frequencies).

Finally, the measured spectrum can only be explained by the presence of two isomers. An “intact” structure with  $\text{Al}^+$  being doubly-coordinated to both carbonyl groups can be unambiguously assigned, explaining the two measured features at  $3293 \text{ cm}^{-1}$  (NH-stretching mode of the backbone NH group, undergoing  $\text{NH}\cdots\pi$  interaction) and  $3488 \text{ cm}^{-1}$  (indole NH-stretching frequency). Although exhibiting slightly different backbone conformations, the latter geometry resembles the two structural motifs previously assigned for  $[\text{AlAcPheOMe}]^+$ . Besides, a second isomer must be responsible for the additional feature at  $3414 \text{ cm}^{-1}$ . Here, a geometry in which  $\text{Al}^+$  is coordinated to  $\text{CO}_{\text{Ac}}$  and additionally stabilized by  $\text{Al}^+\cdots\pi$  interactions could in principle be assigned. In that case, the feature at  $3488 \text{ cm}^{-1}$  would result from an overlay of the indolic NH stretching vibrations of two distinct isomers. Alternatively, the discussed “inserted” structure could indeed be assigned as second isomer. In order to elucidate if an “insertion” reaction may occur as isomerization process in the molecular beam, transition state optimizations were performed. As the predicted (lowest) transition state lies



16300  $\text{cm}^{-1}$  higher in energy than the maybe most plausible starting geometry (a geometry with identical backbone conformation as the “inserted” structure and with the indolic NH group placed above the  $\text{Al}^+$  ion), an isomerization in the molecular beam expansion can be ruled out. Nevertheless, an oxidative addition reaction under the harsh plasma conditions of the used thermo-ablation source remains conceivable. A final assignment may be possible on the basis of measurements in the amide I/II region, since the relevant isomers exhibit distinct vibrational patterns in this spectral region.

In addition, the DFT study was extended to other clusters of the type  $[\text{M}(\text{I})\text{AcTrpOMe}]^+$ , with  $\text{M}(\text{I})$ :  $\text{Li}^+$ ,  $\text{Na}^+$ ,  $\text{K}^+$ ,  $\text{Rb}^+$ ,  $\text{Cs}^+$ ,  $\text{Mg}^+$ ,  $\text{Ti}^+$ ,  $\text{Zn}^+$ ,  $\text{Ag}^+$ ,  $\text{Ga}^+$ . In this way, it could be cleared up whether the “inserted” structural motif is only advantaged for  $[\text{AlAcTrpOMe}]^+$  or if it may also occur in presence of other monovalent metal ions. Among this row, an “inserted” structural motif is only favored relative to the competing “intact” structural motifs in presence of  $\text{Ti}^+$  and  $\text{Al}^+$ .

## 6 References

- [1] H. Fricke, K. Schwing, A. Gerlach, C. Unterberg, M. Gerhards, *Phys. Chem. Chem. Phys.* **2010**, *12*, 3511.
- [2] A. Stamm, K. Schwing, M. Gerhards, *The Journal of Chemical Physics* **2014**, *141*, 194304.
- [3] M. Dole, L. L. Mack, R. L. Hines, R. C. Mobley, L. D. Ferguson, M. B. Alice, *The Journal of Chemical Physics* **1968**, *49*, 2240.
- [4] J. B. Fenn, M. Mann, C. K. Meng, S. F. Wong, C. M. Whitehouse, *Science (New York, N.Y.)* **1989**, *246*, 64.
- [5] T. G. Dietz, M. A. Duncan, D. E. Powers, R. E. Smalley, *The Journal of Chemical Physics* **1981**, *74*, 6511.
- [6] C. Berg, T. Schindler, G. Niedner-Schatteburg, V. E. Bondybey, *The Journal of Chemical Physics* **1995**, *102*, 4870.
- [7] N. Morgner, T. Kleinschroth, H.-D. Barth, B. Ludwig, B. Brutschy, *Journal of the American Society for Mass Spectrometry* **2007**, *18*, 1429.
- [8] M. Karas, F. Hillenkamp, *Anal. Chem.* **1988**, *60*, 2299.
- [9] Z. Takáts, J. M. Wiseman, B. Gologan, R. G. Cooks, *Science (New York, N.Y.)* **2004**, *306*, 471.
- [10] R. B. Cody, J. A. Laramée, H. D. Durst, *Anal. Chem.* **2005**, *77*, 2297.
- [11] C. N. McEwen, R. G. McKay, B. S. Larsen, *Anal. Chem.* **2005**, *77*, 7826.
- [12] A. Habib, S. Ninomiya, L. C. Chen, D. T. Usmanov, K. Hiraoka, *Journal of the American Society for Mass Spectrometry* **2014**, *25*, 1177.
- [13] a) T. D. Vaden, S. A. N. Gowers, T. S. J. A. de Boer, J. D. Steill, J. Oomens, L. C. Snoek, *J. Am. Chem. Soc.* **2008**, *130*, 14640; b) A. Abo-Riziq, B. O. Crews, M. P. Callahan, L. Grace, M. S. de Vries, *Angewandte Chemie International Edition* **2006**, *45*, 5166.
- [14] J. Donon, S. Habka, M. Mons, V. Brenner, E. Gloaguen, *Chemical science* **2021**, *12*, 2803.
- [15] S. Habka, V. Brenner, M. Mons, E. Gloaguen, *J. Phys. Chem. Lett.* **2016**, *7*, 1192.
- [16] Y. Schmitt, K. Chevalier, F. Rupp, M. Becherer, A. Grün, A. M. Rijs, F. Walz, F. Breher, R. Diller, M. Gerhards et al., *Phys. Chem. Chem. Phys.* **2014**, *16*, 8332.
- [17] a) A. M. Dow, A. R. Wittrig, H. I. Kenttämä, *European journal of mass spectrometry (Chichester, England)* **2012**, *18*, 77; b) X. Ma, Y. Zhang, H.-R. Lei, H. I. Kenttämä, *MRS Bull.* **2019**, *44*, 372.
- [18] M. Becherer, *IR spectroscopy on metal-ligand clusters in molecular beam experiments and implementation of a laser desorption source*. PhD thesis, **2018**.
- [19] G. J. Taylor, Y. Luo, K. Hong, S. A. Sarles, R. L. Sacci, B. Doughty, C. P. Collier, *Self-Assembly of Charged Oligomeric Bilayers at the Aqueous/Organic Interface Regulated by Ion-Pair Associations*, **2020**.
- [20] Z. Su, J. J. Leitch, S. Sek, J. Lipkowski, *Langmuir : the ACS journal of surfaces and colloids* **2021**, *37*, 9613.
- [21] K. D. Ristoph, R. K. Prud'homme, *Nanoscale advances* **2019**, *1*, 4207.
- [22] R. Wibel, J. D. Friedl, S. Zaichik, A. Bernkop-Schnürch, *European journal of pharmaceuticals and biopharmaceuticals : official journal of Arbeitsgemeinschaft für Pharmazeutische Verfahrenstechnik e.V* **2020**, *151*, 73.
- [23] R. Ning, H. Zhou, S.-X. Nie, Y.-F. Ao, D.-X. Wang, Q.-Q. Wang, *Angewandte Chemie (International ed. in English)* **2020**, *59*, 10894.

- [24] M. Retini, F. Bartoccini, G. Zappia, G. Piersanti, *Eur. J. Org. Chem.* **2021**, 2021, 825.
- [25] Y. Marcus, G. Hefter, *Chemical reviews* **2006**, 106, 4585.
- [26] F. London, *Z. Physik* **1930**, 63, 245.
- [27] R. Eisenschitz, F. London, *Z. Physik* **1930**, 60, 491.
- [28] J. D. van der Waals, *Over de continuïteit van de gas- en vloeistofoestand*, Leiden, **1873**.
- [29] P. Debye, *Nachrichten von der Gesellschaft der Wissenschaften zu Göttingen, Mathematisch-Physikalische Klasse* **1920**, 1920, 55.
- [30] W. H. Keesom, *Koninklijke Nederlandsche Akademie van Wetenschappen Proceedings* **1915**, 18, 636.
- [31] J. P. Wagner, P. R. Schreiner, *Angewandte Chemie International Edition* **2015**, 54, 12274.
- [32] F. L. Leite, C. C. Bueno, A. L. Da Róz, E. C. Ziemath, O. N. Oliveira, *International journal of molecular sciences* **2012**, 13, 12773.
- [33] A. Stamm, D. Bernhard, M. Gerhards, *Phys. Chem. Chem. Phys.* **2016**, 18, 15327.
- [34] D. Maué, P. H. Strebert, D. Bernhard, S. Rösel, P. R. Schreiner, M. Gerhards, *Angewandte Chemie International Edition* **2021**, 60, 11305.
- [35] C. Zimmermann, H. C. Gottschalk, M. A. Suhm, *Phys. Chem. Chem. Phys.* **2020**, 22, 2870.
- [36] C. Zimmermann, T. L. Fischer, M. A. Suhm, *Molecules (Basel, Switzerland)* **2020**, 25.
- [37] C. Zimmermann, M. Lange, M. A. Suhm, *Molecules (Basel, Switzerland)* **2021**, 26.
- [38] T. Itoh, *Journal of Photochemistry and Photobiology A: Chemistry* **2010**, 214, 10.
- [39] E. Gloaguen, M. Mons, K. Schwing, M. Gerhards, *Chemical reviews* **2020**, 120, 12490.
- [40] K. Schwing, M. Gerhards, *International Reviews in Physical Chemistry* **2016**, 35, 569.
- [41] J. Finkelstein, *Nature* **2009**, 460, 813.
- [42] Y. Lu, N. Yeung, N. Sieracki, N. M. Marshall, *Nature* **2009**, 460, 855.
- [43] a) M. S. de Vries, *Topics in current chemistry* **2015**, 364, 271; b) A. M. Rijs, J. Oomens, *Topics in current chemistry* **2015**, 364, 1.
- [44] a) P. M. Johnson, *The Journal of Chemical Physics* **1976**, 64, 4143; b) V. S. Antonov, I. N. Knyazev, V. S. Letokhov, V. M. Matiuk, V. G. Movshev, V. K. Potapov, *Optics letters* **1978**, 3, 37; c) U. Boesl, H. J. Neusser, E. W. Schlag, *Zeitschrift für Naturforschung A* **1978**, 33, 1546; d) L. Zandee, R. B. Bernstein, *The Journal of Chemical Physics* **1979**, 70, 2574; e) V. S. Letokhov, *Laser photoionization spectroscopy*, Academic Press, Orlando, **1987**; f) T. R. Rizzo, Y. D. Park, L. Peteanu, D. H. Levy, *The Journal of Chemical Physics* **1985**, 83, 4819; g) J. R. Cable, M. J. Tubergen, D. H. Levy, *J. Am. Chem. Soc.* **1988**, 110, 7349.
- [45] J. R. Cable, M. J. Tubergen, D. H. Levy, *J. Am. Chem. Soc.* **1989**, 111, 9032.
- [46] G. M. Florio, C. J. Gruenloh, R. C. Quimpo, T. S. Zwier, *The Journal of Chemical Physics* **2000**, 113, 11143.
- [47] a) J. Franck, E. G. Dymond, *Trans. Faraday Soc.* **1926**, 21, 536; b) E. Condon, *Phys. Rev.* **1926**, 28, 1182.
- [48] a) K. Müller-Dethlefs, E. W. Schlag, *Annual review of physical chemistry* **1991**, 42, 109; b) K. Müller-Dethlefs, *Journal of Electron Spectroscopy and Related Phenomena* **1995**, 75, 35; c) K. Müller-Dethlefs, E. W. Schlag, *Angewandte Chemie International Edition* **1998**, 37, 1346; d) G. Reiser, W. Habenicht, K. Müller-Dethlefs, E. W. Schlag, *Chemical Physics Letters* **1988**, 152, 119.
- [49] L. Zhu, P. Johnson, *The Journal of Chemical Physics* **1991**, 94, 5769.
- [50] M. Gerhards, S. Schumm, C. Unterberg, K. Kleinermanns, *Chemical Physics Letters* **1998**, 294, 65.
- [51] M. Gerhards, C. Unterberg, S. Schumm, *The Journal of Chemical Physics* **1999**, 111, 7966.
- [52] R. H. Page, Y. R. Shen, Y. T. Lee, *The Journal of Chemical Physics* **1988**, 88, 4621.

- [53] a) C. Riehn, C. Lahmann, B. Wassermann, B. Brutschy, *Chemical Physics Letters* **1992**, *197*, 443; b) B. Brutschy, *Chemical reviews* **2000**, *100*, 3891; c) M. Gerhards, C. Unterberg, K. Kleinermanns, *Phys. Chem. Chem. Phys.* **2000**, *2*, 5538.
- [54] T. S. Zwier, *Annual review of physical chemistry* **1996**, *47*, 205.
- [55] A. Stamm, M. Weiler, A. Brächer, K. Schwing, M. Gerhards, *Phys. Chem. Chem. Phys.* **2014**, *16*, 21795.
- [56] D. Bernhard, F. Dietrich, M. Fatima, C. Perez, A. Poblitzki, G. Jansen, M. A. Suhm, M. Schnell, M. Gerhards, *Phys. Chem. Chem. Phys.* **2017**, *19*, 18076.
- [57] T. Ebata, A. Fujii, N. Mikami, *International Reviews in Physical Chemistry* **1998**, *17*, 331.
- [58] T. Yahagi, A. Fujii, T. Ebata, N. Mikami, *J. Phys. Chem. A* **2001**, *105*, 10673.
- [59] C. A. Southern, D. H. Levy, J. A. Stearns, G. M. Florio, A. Longarte, T. S. Zwier, *J. Phys. Chem. A* **2004**, *108*, 4599.
- [60] P. Esherick, A. Owyong, J. Plíva, *The Journal of Chemical Physics* **1985**, *83*, 3311.
- [61] P. Esherick, A. Owyong, *Chemical Physics Letters* **1983**, *103*, 235.
- [62] G. V. Hartland, B. F. Henson, V. A. Ventura, R. A. Hertz, P. M. Felker, *J. Opt. Soc. Am. B* **1990**, *7*, 1950.
- [63] P. M. Felker, P. M. Maxton, M. W. Schaeffer, *Chemical reviews* **1994**, *94*, 1787.
- [64] A. Golan, N. Mayorkas, S. Rosenwaks, I. Bar, *The Journal of Chemical Physics* **2009**, *131*, 24305.
- [65] M. Fatima, D. Maué, C. Pérez, D. S. Tikhonov, D. Bernhard, A. Stamm, C. Medcraft, M. Gerhards, M. Schnell, *Phys. Chem. Chem. Phys.* **2020**, *22*, 27966.
- [66] V. A. Shubert, T. S. Zwier, *J. Phys. Chem. A* **2007**, *111*, 13283.
- [67] M. Weiler, K. Bartl, M. Gerhards, *The Journal of Chemical Physics* **2012**, *136*, 114202.
- [68] C. Medcraft, S. Zinn, M. Schnell, A. Poblitzki, J. Altnöder, M. Heger, M. A. Suhm, D. Bernhard, A. Stamm, F. Dietrich et al., *Phys. Chem. Chem. Phys.* **2016**, *18*, 25975.
- [69] A. Stamm, D. Maué, M. Gerhards, *J. Phys. Chem. Lett.* **2018**, *9*, 4360.
- [70] a) P. M. Palmer, Y. Chen, M. R. Topp, *Chemical Physics Letters* **2000**, *318*, 440; b) J. A. Stearns, A. Das, T. S. Zwier, *Phys. Chem. Chem. Phys.* **2004**, *6*, 2605; c) K. Bartl, A. Funk, M. Gerhards, *The Journal of Chemical Physics* **2008**, *129*, 234306; d) K. Bartl, A. Funk, K. Schwing, H. Fricke, G. Kock, H.-D. Martin, M. Gerhards, *Phys. Chem. Chem. Phys.* **2009**, *11*, 1173.
- [71] K. Bartl, A. Funk, M. Gerhards, *Chemphyschem : a European journal of chemical physics and physical chemistry* **2009**, *10*, 1882.
- [72] Y. Loquais, E. Gloaguen, S. Habka, V. Vaquero-Vara, V. Brenner, B. Tardivel, M. Mons, *J. Phys. Chem. A* **2015**, *119*, 5932.
- [73] a) T. Walther, H. Bitto, T. K. Minton, J. Huber, *Chemical Physics Letters* **1994**, *231*, 64; b) T. Ebata, N. Mizuochi, T. Watanabe, N. Mikami, *J. Phys. Chem.* **1996**, *100*, 546; c) B. C. Dian, A. Longarte, T. S. Zwier, *The Journal of Chemical Physics* **2003**, *118*, 2696.
- [74] a) N. C. Polfer, *Chemical Society reviews* **2011**, *40*, 2211; b) J. Roithová, *Chemical Society reviews* **2012**, *41*, 547; c) A. B. Wolk, C. M. Leavitt, E. Garand, M. A. Johnson, *Accounts of chemical research* **2014**, *47*, 202.
- [75] P. M. Bialach, T. C. Martin, M. Gerhards, *Physical chemistry chemical physics : PCCP* **2012**, *14*, 8185.
- [76] P. M. Bialach, M. Braun, A. Lüchow, M. Gerhards, *Phys. Chem. Chem. Phys.* **2009**, *11*, 10403.
- [77] P. M. Bialach, A. Funk, M. Weiler, M. Gerhards, *The Journal of Chemical Physics* **2010**, *133*, 194304.
- [78] A. Fujii, E. Fujimaki, T. Ebata, N. Mikami, *The Journal of Chemical Physics* **2000**, *112*, 6275.

- [79] B. Kwasigroch, T. Khuu, E. H. Perez, J. K. Denton, E. K. Schneider, A. Straßner, M. Theisen, S. V. Kruppa, P. Weis, M. M. Kappes et al., *Chemistry (Weinheim an der Bergstrasse, Germany)* **2021**, *27*, 15136.
- [80] a) T. Omi, H. Shitomi, N. Sekiya, K. Takazawa, M. Fujii, *Chemical Physics Letters* **1996**, *252*, 287; b) S. Ishiuchi, H. Shitomi, K. Takazawa, M. Fujii, *Chemical Physics Letters* **1998**, *283*, 243.
- [81] a) A. Fujii, T. Sawamura, S. Tanabe, T. Ebata, N. Mikami, *Chemical Physics Letters* **1994**, *225*, 104; b) T. Nakanaga, F. Ito, J. Miyawaki, K. Sugawara, H. Takeo, *Chemical Physics Letters* **1996**, *261*, 414; c) T. Nakanaga, K. Kawamata, F. Ito, *Chemical Physics Letters* **1997**, *279*, 309; d) H. Piest, G. von Helden, G. Meijer, *The Journal of Chemical Physics* **1999**, *110*, 2010; e) K. Kleinermanns, C. Janzen, D. Spangenberg, M. Gerhards, *J. Phys. Chem. A* **1999**, *103*, 5232.
- [82] C. Unterberg, A. Jansen, M. Gerhards, *The Journal of Chemical Physics* **2000**, *113*, 7945.
- [83] D. Bernhard, C. Holzer, F. Dietrich, A. Stamm, W. Klopper, M. Gerhards, *Chemphyschem : a European journal of chemical physics and physical chemistry* **2017**, *18*, 3634.
- [84] M. Gerhards, *Optics Communications* **2004**, *241*, 493.
- [85] W. Demtröder, *Laserspektroskopie 2*, Springer Berlin Heidelberg, Berlin, Heidelberg, **2013**.
- [86] a) D. Dutta, M. Becherer, D. Bellaire, F. Dietrich, M. Gerhards, G. Lefkidis, W. Hübner, *Phys. Rev. B* **2018**, *97*; b) W. Jin, M. Becherer, D. Bellaire, G. Lefkidis, M. Gerhards, W. Hübner, *Phys. Rev. B* **2014**, *89*.
- [87] J. Grotemeyer, U. Boesl, K. Walter, E. W. Schlag, *J. Am. Chem. Soc.* **1986**, *108*, 4233.
- [88] J. Grotemeyer, U. Boesl, K. Walter, E. W. Schlag, *Org. Mass Spectrom.* **1986**, *21*, 645.
- [89] H. v. Weysenhoff, H. L. Selzle, E. W. Schlag, *Zeitschrift für Naturforschung A* **1985**, *40*, 674.
- [90] C. H. Becker, K. T. Gillen, *Anal. Chem.* **1984**, *56*, 1671.
- [91] R. J. Cotter, *Anal. Chem.* **1980**, *52*, 1767.
- [92] F. Engelke, J. H. Hahn, W. Henke, R. N. Zare, *Anal. Chem.* **1987**, *59*, 909.
- [93] G. Meijer, M. S. de Vries, H. E. Hunziker, H. R. Wendt, *Appl. Phys. B* **1990**, *51*, 395.
- [94] G. Meijer, M. S. de Vries, H. E. Hunziker, H. R. Wendt, *The Journal of Chemical Physics* **1990**, *92*, 7625.
- [95] G. Meijer, M. S. de Vries, H. E. Hunziker, H. R. Wendt, *J. Phys. Chem.* **1990**, *94*, 4394.
- [96] J. R. Cable, M. J. Tubergen, D. H. Levy, *J. Am. Chem. Soc.* **1987**, *109*, 6198.
- [97] a) M. S. de Vries, H. E. Hunziker, *Journal of Photochemistry and Photobiology A: Chemistry* **1997**, *106*, 31; b) E. Nir, L. Grace, B. Brauer, M. S. de Vries, *J. Am. Chem. Soc.* **1999**, *121*, 4896.
- [98] E. Nir, H. E. Hunziker, M. S. de Vries, *Anal. Chem.* **1999**, *71*, 1674.
- [99] R. Cohen, B. Brauer, E. Nir, L. Grace, M. S. de Vries, *J. Phys. Chem. A* **2000**, *104*, 6351.
- [100] F. Piuze, I. Dimicoli, M. Mons, B. Tardivel, Q. Zhao, *Chemical Physics Letters* **2000**, *320*, 282.
- [101] H. Mitsuda, M. Miyazaki, I. B. Nielsen, P. Çarçabal, C. Dedonder, C. Jouvet, S. Ishiuchi, M. Fujii, *J. Phys. Chem. Lett.* **2010**, *1*, 1130.
- [102] I. Hünig, K. A. Seefeld, K. Kleinermanns, *Chemical Physics Letters* **2003**, *369*, 173.
- [103] a) T. Uhlemann, S. Seidel, C. W. Müller, *Physical chemistry chemical physics : PCCP* **2017**, *19*, 14625; b) M. Taherkhani, M. Riese, M. BenYezzar, K. Müller-Dethlefs, *Review of Scientific Instruments* **2010**, *81*, 63101.
- [104] I. Usabiaga, J. González, P. F. Arnáiz, I. León, E. J. Cocinero, J. A. Fernández, *Physical chemistry chemical physics : PCCP* **2016**, *18*, 12457.
- [105] S. Bakels, S. B. A. Porskamp, A. M. Rijs, *Angewandte Chemie (International ed. in English)* **2019**, *58*, 10537.
- [106] N. Teschmit, K. Długociński, D. Gusa, I. Rubinsky, D. A. Horke, J. Küpper, *The Journal of Chemical Physics* **2017**, *147*, 144204.

- [107] F. BenNasr, A. Pérez-Mellor, I. Alata, V. Lepere, N.-E. Jaïdane, A. Zehnacker, *Faraday discussions* **2018**, *212*, 399.
- [108] K. N. Blodgett, G. Jang, S. Kim, M. K. Kim, S. H. Choi, T. S. Zwier, *J. Phys. Chem. A* **2020**, *124*, 5856.
- [109] A. Insausti, E. R. Alonso, B. Tercero, J. I. Santos, C. Calabrese, N. Vogt, F. Corzana, J. Demaison, J. Cernicharo, E. J. Cocinero, *The journal of physical chemistry letters* **2021**, *12*, 1352.
- [110] R. J. Levis, *Annual review of physical chemistry* **1994**, *45*, 483.
- [111] a) P. Voumard, R. Zenobi, *The Journal of Chemical Physics* **1995**, *103*, 6795; b) Y. Li, R. T. McIver, J. C. Hemminger, *The Journal of Chemical Physics* **1990**, *93*, 4719; c) R. Zenobi, J. H. Hahn, R. N. Zare, *Chemical Physics Letters* **1988**, *150*, 361; d) R. N. Zare, R. D. Levine, *Chemical Physics Letters* **1987**, *136*, 593; e) R. B. Hall, *J. Phys. Chem.* **1987**, *91*, 1007.
- [112] E. Gloaguen, H. Valdes, F. Pagliarulo, R. Pollet, B. Tardivel, P. Hobza, F. Piuze, M. Mons, *The journal of physical chemistry. A* **2010**, *114*, 2973.
- [113] a) W. Chin, J.-P. Dognon, C. Canuel, F. Piuze, I. Dimicoli, M. Mons, I. Compagnon, G. von Helden, G. Meijer, *The Journal of Chemical Physics* **2005**, *122*, 54317; b) E. J. Cocinero, P. Carçabal, T. D. Vaden, J. P. Simons, B. G. Davis, *Nature* **2011**, *469*, 76.
- [114] M. Carini, M. P. Ruiz, I. Usabiaga, J. A. Fernández, E. J. Cocinero, M. Melle-Franco, I. Diez-Perez, A. Mateo-Alonso, *Nature communications* **2017**, *8*, 15195.
- [115] M. Pumera, *Chemical record (New York, N.Y.)* **2009**, *9*, 211.
- [116] a) M. A. Saleemi, M. Hosseini Fouladi, P. V. C. Yong, K. Chinna, N. K. Palanisamy, E. H. Wong, *Chemical research in toxicology* **2021**, *34*, 24; b) A. P. Francis, T. Devasena, *Toxicology and industrial health* **2018**, *34*, 200.
- [117] a) Z.-Y. Li, M. S. Akhtar, D.-H. Kwak, O.-B. Yang, *Applied Surface Science* **2017**, *404*, 88; b) F. Malekian, H. GHAFOURIAN, K. ZARE, A. A. SHARIF, Y. ZAMANI, *J. Mex. Chem. Soc.* **2019**, *63*.
- [118] W. C. Wiley, I. H. McLaren, *Review of Scientific Instruments* **1955**, *26*, 1150.
- [119] A. Camiruaga, I. Usabiaga, C. Calabrese, I. Lamas, F. J. Basterretxea, J. A. Fernández, *Chemistry (Weinheim an der Bergstrasse, Germany)* **2022**, *28*, e202103636.
- [120] R. N. Pribble, T. S. Zwier, *Science (New York, N.Y.)* **1994**, *265*, 75.
- [121] T. Häber, K. Seefeld, K. Kleinermanns, *J. Phys. Chem. A* **2007**, *111*, 3038.
- [122] Y. Shimoazono, K. Yamada, S. Ishiuchi, K. Tsukiyama, M. Fujii, *Phys. Chem. Chem. Phys.* **2013**, *15*, 5163.
- [123] P. Echenique, J. L. Alonso, *Molecular Physics* **2007**, *105*, 3057.
- [124] a) L. H. Thomas, *Math. Proc. Camb. Phil. Soc.* **1927**, *23*, 542; b) E. Fermi, *Z. Physik* **1928**, *48*, 73.
- [125] P. Hohenberg, W. Kohn, *Phys. Rev.* **1964**, *136*, B864-B871.
- [126] W. Kohn, L. J. Sham, *Phys. Rev.* **1965**, *140*, A1133-A1138.
- [127] W. Kohn, A. D. Becke, R. G. Parr, *J. Phys. Chem.* **1996**, *100*, 12974.
- [128] Lee, Yang, Parr, *Physical review. B, Condensed matter* **1988**, *37*, 785.
- [129] a) Becke, *Physical review. A, General physics* **1988**, *38*, 3098; b) A. D. Becke, *The Journal of Chemical Physics* **1993**, *98*, 5648.
- [130] S. Grimme, *WIREs Comput Mol Sci* **2011**, *1*, 211.
- [131] S. Grimme, J. Antony, S. Ehrlich, H. Krieg, *The Journal of Chemical Physics* **2010**, *132*, 154104.
- [132] S. Grimme, S. Ehrlich, L. Goerigk, *Journal of computational chemistry* **2011**, *32*, 1456.
- [133] a) C. Corminboeuf, *Accounts of chemical research* **2014**, *47*, 3217; b) A. Tkatchenko, L. Romaner, O. T. Hofmann, E. Zojer, C. Ambrosch-Draxl, M. Scheffler, *MRS Bull.* **2010**, *35*, 435; c) J. Klimeš, A. Michaelides, *The Journal of Chemical Physics* **2012**, *137*, 120901.



- [134] M. J. Frisch, G. W. Trucks, H. B. Schlegel, G. E. Scuseria, M. A. Robb, J. R. Cheeseman, G. Scalmani, V. Barone, B. Mennucci, G. A. Petersson, H. Nakatsuji, M. Caricato, X. Li, H. P. Hratchian, A. F. Izmaylov, J. Bloino, G. Zheng, J. L. Sonnenberg, M. Hada, M. Ehara, K. Toyota, R. Fukuda, J. Hasegawa, M. Ishida, T. Nakajima, Y. Honda, O. Kitao, H. Nakai, T. Vreven, J. A. Montgomery Jr., J. E. Peralta, F. Ogliaro, M. J. Bearpark, J. Heyd, E. N. Brothers, K. N. Kudin, V. N. Staroverov, R. Kobayashi, J. Normand, K. Raghavachari, A. P. Rendell, J. C. Burant, S. S. Iyengar, J. Tomasi, M. Cossi, N. Rega, N. J. Millam, M. Klene, J. E. Knox, J. B. Cross, V. Bakken, C. Adamo, J. Jaramillo, R. Gomperts, R. E. Stratmann, O. Yazyev, A. J. Austin, R. Cammi, C. Pomelli, J. W. Ochterski, R. L. Martin, K. Morokuma, V. G. Zakrzewski, G. A. Voth, P. Salvador, J. J. Dannenberg, S. Dapprich, A. D. Daniels, Ö. Farkas, J. B. Foresman, J. V. Ortiz, J. Cioslowski and D. J. Fox, *Gaussian 09, Revision D.01, Gaussian, Inc, Wallingford, CT, USA* **2009**.
- [135] R. Ahlrichs, M. Bär, M. Häser, H. Horn, C. Kölmel, *Chemical Physics Letters* **1989**, *162*, 165.
- [136] F. Neese, *WIREs Comput Mol Sci* **2012**, *2*, 73.
- [137] A. E. Reed, L. A. Curtiss, F. Weinhold, *Chemical reviews* **1988**, *88*, 899.
- [138] S. F. Boys, F. Bernardi, *Molecular Physics* **1970**, *19*, 553.
- [139] C. Peng, H. Bernhard Schlegel, *Isr. J. Chem.* **1993**, *33*, 449.
- [140] P. Plessow, *Journal of chemical theory and computation* **2013**, *9*, 1305.
- [141] R. Izsák, *WIREs Comput Mol Sci* **2020**, *10*.
- [142] B. Roos, *Chemical Physics Letters* **1972**, *15*, 153.
- [143] O. Christiansen, H. Koch, P. Jørgensen, *Chemical Physics Letters* **1995**, *243*, 409.
- [144] a) R. J. Bartlett, M. Musiał, *Rev. Mod. Phys.* **2007**, *79*, 291; b) K. B. Lipkowitz, D. B. Boyd (Eds.) *Reviews in Computational Chemistry*, John Wiley & Sons, Inc, Hoboken, NJ, USA, **2000**.
- [145] C. Riplinger, F. Neese, *The Journal of Chemical Physics* **2013**, *138*, 34106.
- [146] I. Prigogine, S. A. Rice (Eds.) *Advances in Chemical Physics. Vol. 125*, John Wiley & Sons, Inc, Hoboken, USA, **2003**.
- [147] C. Møller, M. S. Plesset, *Phys. Rev.* **1934**, *46*, 618.
- [148] S. Grimme, L. Goerigk, R. F. Fink, *WIREs Comput Mol Sci* **2012**, *2*, 886.
- [149] A. Hellweg, S. A. Grün, C. Hättig, *Phys. Chem. Chem. Phys.* **2008**, *10*, 4119.
- [150] a) N. O. C. Winter, N. K. Graf, S. Leutwyler, C. Hättig, *Phys. Chem. Chem. Phys.* **2013**, *15*, 6623; b) A. Tajti, P. G. Szalay, *Journal of chemical theory and computation* **2019**, *15*, 5523.
- [151] a) C. Riplinger, B. Sandhoefer, A. Hansen, F. Neese, *The Journal of Chemical Physics* **2013**, *139*, 134101; b) M. Saitow, U. Becker, C. Riplinger, E. F. Valeev, F. Neese, *The Journal of Chemical Physics* **2017**, *146*, 164105; c) Y. Guo, C. Riplinger, U. Becker, D. G. Liakos, Y. Minenkov, L. Cavallo, F. Neese, *The Journal of Chemical Physics* **2018**, *148*, 11101; d) D. G. Liakos, Y. Guo, F. Neese, *J. Phys. Chem. A* **2020**, *124*, 90.
- [152] C. Riplinger, P. Pinski, U. Becker, E. F. Valeev, F. Neese, *The Journal of Chemical Physics* **2016**, *144*, 24109.
- [153] S. Mallick, B. Roy, P. Kumar, *Computational and Theoretical Chemistry* **2020**, *1187*, 112934.
- [154] a) J. Schirmer, *Physical review. A, General physics* **1982**, *26*, 2395; b) A. B. Trofimov, J. Schirmer, *J. Phys. B: At. Mol. Opt. Phys.* **1995**, *28*, 2299.
- [155] C. Hättig in *Advances in Quantum Chemistry*, Elsevier, **2005**, pp. 37–60.
- [156] A. Tajti, L. Tulipán, P. G. Szalay, *Journal of chemical theory and computation* **2020**, *16*, 468.
- [157] D. Tuna, D. Lefrancois, Ł. Wolański, S. Gozem, I. Schapiro, T. Andruniów, A. Dreuw, M. Olivucci, *Journal of chemical theory and computation* **2015**, *11*, 5758.
- [158] A. Stamm, D. Maué, A. Schaly, S. Schlicher, J. Bartl, S. Kubik, M. Gerhards, *Phys. Chem. Chem. Phys.* **2017**, *19*, 10718.

- [159] A. Pérez-Mellor, I. Alata, V. Lepere, A. Zehnacker, *Journal of Molecular Spectroscopy* **2018**, *349*, 71.
- [160] a) A. D'Amato, R. Volpe, M. C. Vaccaro, S. Terracciano, I. Bruno, M. Tosolini, C. Tedesco, G. Pierri, P. Tecilla, C. Costabile et al., *The Journal of organic chemistry* **2017**, *82*, 8848; b) Q. Wu, J. Patocka, E. Nepovimova, K. Kuca, *Frontiers in pharmacology* **2018**, *9*, 1338.
- [161] *Calixarenes*, Royal Society of Chemistry, Cambridge, **2008**.
- [162] E. W. Schlag, J. Grotemeyer, R. D. Levine, *Chemical Physics Letters* **1992**, *190*, 521.
- [163] J. Hack, D. C. Grills, J. R. Miller, T. Mani, *The journal of physical chemistry. B* **2016**, *120*, 1149.
- [164] T. Mani, D. C. Grills, J. R. Miller, *Journal of the American Chemical Society* **2015**, *137*, 1136.
- [165] a) W. W. Rudolph, D. Fischer, G. Irmer, *Dalton transactions (Cambridge, England : 2003)* **2014**, *43*, 3174; b) J. Kahlen, L. Salimi, M. Sulpizi, C. Peter, D. Donadio, *The journal of physical chemistry. B* **2014**, *118*, 3960.
- [166] S. Habka, T. Very, J. Donon, V. Vaquero-Vara, B. Tardivel, F. Charnay-Pouget, M. Mons, D. J. Aitken, V. Brenner, E. Gloaguen, *Physical chemistry chemical physics : PCCP* **2019**, *21*, 12798.
- [167] a) J. Smiatek, A. Heuer, M. Winter, *Batteries* **2018**, *4*, 62; b) O. Nordness, J. F. Brennecke, *Chemical reviews* **2020**, *120*, 12873.
- [168] a) D. Strasser, F. Goulay, M. S. Kelkar, E. J. Maginn, S. R. Leone, *The journal of physical chemistry. A* **2007**, *111*, 3191; b) R. Cooper, A. M. Zolot, J. A. Boatz, D. P. Sporleder, J. A. Stearns, *The journal of physical chemistry. A* **2013**, *117*, 12419; c) R. S. Booth, C. J. Annesley, *J. Phys. Chem. A* **2020**, *124*, 9683.
- [169] a) K. Hanke, M. Kaufmann, G. Schwaab, M. Havenith, C. T. Wolke, O. Gorlova, M. A. Johnson, B. P. Kar, W. Sander, E. Sanchez-Garcia, *Physical chemistry chemical physics : PCCP* **2015**, *17*, 8518; b) E. I. Obi, C. M. Leavitt, P. L. Raston, C. P. Moradi, S. D. Flynn, G. L. Vaghjiani, J. A. Boatz, S. D. Chambreau, G. E. Doublerly, *The journal of physical chemistry. A* **2013**, *117*, 9047; c) J. Tandy, C. Feng, A. Boatwright, G. Sarma, A. M. Sadoon, A. Shirley, N. D. N. Rodrigues, E. M. Cunningham, S. Yang, A. M. Ellis, *The Journal of Chemical Physics* **2016**, *144*, 121103.
- [170] J. Donon, S. Habka, V. Vaquero-Vara, V. Brenner, M. Mons, E. Gloaguen, *The journal of physical chemistry letters* **2019**, *10*, 7458.
- [171] S. D. Fried, S. G. Boxer, *Accounts of chemical research* **2015**, *48*, 998.
- [172] R. D. Shannon, *Acta Cryst A* **1976**, *32*, 751.
- [173] D. Müller, P. Nieto, M. Miyazaki, O. Dopfer, *Faraday discussions* **2019**, *217*, 256.
- [174] P. Nieto, D. Müller, A. Sheldrick, A. Günther, M. Miyazaki, O. Dopfer, *Phys. Chem. Chem. Phys.* **2018**, *20*, 22148.
- [175] P. M. Wojciechowski, W. Zierkiewicz, D. Michalska, P. Hobza, *The Journal of Chemical Physics* **2003**, *118*, 10900.
- [176] P. Hobza, V. Špirko, *Phys. Chem. Chem. Phys.* **2003**, *5*, 1290.
- [177] N. Helle, T. Raeker, J. Grotemeyer, *Phys. Chem. Chem. Phys.* **2022**, *24*, 2412.
- [178] R. W. Taft, S. Ehrenson, I. C. Lewis, R. E. Glick, *J. Am. Chem. Soc.* **1959**, *81*, 5352.
- [179] C. Mayeux, P. Burk, J.-F. Gal, I. Leito, L. Massi, *J. Phys. Chem. A* **2020**, *124*, 4390.
- [180] H. Kinjo, H. Lim, T. Sato, Y. Noguchi, Y. Nakayama, H. Ishii, *Appl. Phys. Express* **2016**, *9*, 21601.
- [181] T. Hoshi, K. Kumagai, K. Inoue, S. Enomoto, Y. Nobe, M. Kobayashi, *Journal of Luminescence* **2008**, *128*, 1353.
- [182] C. W. Tang, S. A. VanSlyke, *Appl. Phys. Lett.* **1987**, *51*, 913.
- [183] B. Derkowska-Zielinska, *Optics letters* **2017**, *42*, 567.
- [184] a) J. Cerný, P. Hobza, *Phys. Chem. Chem. Phys.* **2007**, *9*, 5291; b) J.-M. Lehn, *Angewandte Chemie International Edition* **1988**, *27*, 89; c) E. A. Meyer, R. K. Castellano, F. Diederich,



- Angewandte Chemie International Edition* **2003**, *42*, 1210; d) K. Müller-Dethlefs, P. Hobza, *Chemical reviews* **2000**, *100*, 143; e) M. A. Strauss, H. A. Wegner, *Angewandte Chemie International Edition* **2019**, *58*, 18552.
- [185] K. Autumn, M. Sitti, Y. A. Liang, A. M. Peattie, W. R. Hansen, S. Sponberg, T. W. Kenny, R. Fearing, J. N. Israelachvili, R. J. Full, *Proceedings of the National Academy of Sciences of the United States of America* **2002**, *99*, 12252.
- [186] S. Hanlon, *Biochemical and Biophysical Research Communications* **1966**, *23*, 861.
- [187] C. M. Roth, B. L. Neal, A. M. Lenhoff, *Biophysical Journal* **1996**, *70*, 977.
- [188] a) P. R. Schreiner, L. V. Chernish, P. A. Gunchenko, E. Y. Tikhonchuk, H. Hausmann, M. Serafin, S. Schlecht, J. E. P. Dahl, R. M. K. Carlson, A. A. Fokin, *Nature* **2011**, *477*, 308; b) A. A. Fokin, L. V. Chernish, P. A. Gunchenko, E. Y. Tikhonchuk, H. Hausmann, M. Serafin, J. E. P. Dahl, R. M. K. Carlson, P. R. Schreiner, *J. Am. Chem. Soc.* **2012**, *134*, 13641.
- [189] S. Rösel, H. Quanz, C. Logemann, J. Becker, E. Mossou, L. Cañadillas-Delgado, E. Caldeweyher, S. Grimme, P. R. Schreiner, *J. Am. Chem. Soc.* **2017**, *139*, 7428.
- [190] D. Bernhard, F. Dietrich, M. Fatima, C. Pérez, H. C. Gottschalk, A. Wuttke, R. A. Mata, M. A. Suhm, M. Schnell, M. Gerhards, *Beilstein journal of organic chemistry* **2018**, *14*, 1642.
- [191] D. Bernhard, M. Fatima, A. Poblitzki, A. L. Steber, C. Pérez, M. A. Suhm, M. Schnell, M. Gerhards, *Phys. Chem. Chem. Phys.* **2019**, *21*, 16032.
- [192] F. Dietrich, D. Bernhard, M. Fatima, C. Pérez, M. Schnell, M. Gerhards, *Angewandte Chemie International Edition* **2018**, *57*, 9534.
- [193] E. Burevschi, E. R. Alonso, M. E. Sanz, *Chemistry (Weinheim an der Bergstrasse, Germany)* **2020**, *26*, 11327.
- [194] E. G. Hohenstein, C. D. Sherrill, *The Journal of Chemical Physics* **2010**, *132*, 184111.
- [195] E. G. Hohenstein, R. M. Parrish, C. D. Sherrill, J. M. Turney, H. F. Schaefer, *The Journal of Chemical Physics* **2011**, *135*, 174107.
- [196] W. B. Schneider, G. Bistoni, M. Sparta, M. Saitow, C. Riplinger, A. A. Auer, F. Neese, *Journal of chemical theory and computation* **2016**, *12*, 4778.
- [197] A. Altun, F. Neese, G. Bistoni, *Journal of chemical theory and computation* **2019**, *15*, 215.
- [198] M. Gerhards, C. Unterberg, *Phys. Chem. Chem. Phys.* **2002**, *4*, 1760.
- [199] M. Gerhards, C. Unterberg, A. Gerlach, *Phys. Chem. Chem. Phys.* **2002**, *4*, 5563.
- [200] a) H. Fricke, A. Gerlach, C. Unterberg, P. Rzepecki, T. Schrader, M. Gerhards, *Phys. Chem. Chem. Phys.* **2004**, *6*, 4636; b) P. S. Walsh, R. Kusaka, E. G. Buchanan, W. H. James, B. F. Fisher, S. H. Gellman, T. S. Zwier, *J. Phys. Chem. A* **2013**, *117*, 12350; c) H. S. Biswal, Y. Loquais, B. Tardivel, E. Gloaguen, M. Mons, *J. Am. Chem. Soc.* **2011**, *133*, 3931; d) K. Schwing, C. Reyheller, A. Schaly, S. Kubik, M. Gerhards, *Chemphyschem : a European journal of chemical physics and physical chemistry* **2011**, *12*, 1981.
- [201] M. N. Blom, I. Compagnon, N. C. Polfer, G. von Helden, G. Meijer, S. Suhai, B. Paizs, J. Oomens, *J. Phys. Chem. A* **2007**, *111*, 7309.
- [202] H. Zhu, M. Blom, I. Compagnon, A. M. Rijs, S. Roy, G. von Helden, B. Schmidt, *Phys. Chem. Chem. Phys.* **2010**, *12*, 3415.
- [203] V. R. Mundlapati, Z. Imani, V. C. D'mello, V. Brenner, E. Gloaguen, J.-P. Baltaze, S. Robin, M. Mons, D. J. Aitken, *Chemical science* **2021**, *12*, 14826.
- [204] A. Gerlach, C. Unterberg, H. Fricke, M. Gerhards \*, *Molecular Physics* **2005**, *103*, 1521.
- [205] N. C. Polfer, J. Oomens, R. C. Dunbar, *Phys. Chem. Chem. Phys.* **2006**, *8*, 2744.
- [206] N. C. Polfer, J. Oomens, D. T. Moore, G. von Helden, G. Meijer, R. C. Dunbar, *J. Am. Chem. Soc.* **2006**, *128*, 517.

- [207] G. C. Boles, R. L. Hightower, R. A. Coates, C. P. McNary, G. Berden, J. Oomens, P. B. Armentrout, *The journal of physical chemistry. B* **2018**, *122*, 3836.
- [208] A. Kamariotis, O. V. Boyarkin, S. R. Mercier, R. D. Beck, M. F. Bush, E. R. Williams, T. R. Rizzo, *J. Am. Chem. Soc.* **2006**, *128*, 905.
- [209] S. Ishiuchi, Y. Sasaki, J. M. Lisy, M. Fujii, *Phys. Chem. Chem. Phys.* **2019**, *21*, 561.
- [210] E. Sato, K. Hirata, J. M. Lisy, S. Ishiuchi, M. Fujii, *J. Phys. Chem. Lett.* **2021**, *12*, 1754.
- [211] a) D. R. Crapper, S. S. Krishnan, A. J. Dalton, *Science (New York, N.Y.)* **1973**, *180*, 511; b) K. A. Jellinger, *International review of neurobiology* **2013**, *110*, 1; c) V. Rondeau, *Reviews on environmental health* **2002**, *17*, 107.
- [212] C. Cui, H. W. Roesky, H.-G. Schmidt, M. Noltemeyer, H. Hao, F. Cimpoesu, *Angewandte Chemie International Edition* **2000**, *39*, 4274.
- [213] a) C. Dohmeier, D. Loos, H. Schnöckel, *Angewandte Chemie International Edition* **1996**, *35*, 129; b) S. Nagendran, H. W. Roesky, *Organometallics* **2008**, *27*, 457.
- [214] T. Chu, I. Korobkov, G. I. Nikonov, *J. Am. Chem. Soc.* **2014**, *136*, 9195.
- [215] a) X. Zhang, L. Wang, G. R. Montone, A. F. Gill, G. Ganteför, B. Eichhorn, A. K. Kandalam, K. H. Bowen, *Phys. Chem. Chem. Phys.* **2017**, *19*, 15541; b) P. J. Roach, A. C. Reber, W. H. Woodward, S. N. Khanna, A. W. Castleman, *Proceedings of the National Academy of Sciences of the United States of America* **2007**, *104*, 14565; c) J. Vanbuel, P. Ferrari, E. Janssens, *Advances in Physics: X* **2020**, *5*, 1754132.
- [216] a) S. Lakhdar, M. Westermaier, F. Terrier, R. Goumont, T. Boubaker, A. R. Ofial, H. Mayr, *The Journal of organic chemistry* **2006**, *71*, 9088; b) R. A. Heacock, S. Kašpárek in *Advances in Heterocyclic Chemistry*, Elsevier, **1969**, pp. 43–112.

## 7 Publications and manuscript drafts

### 7.1 Manuscript draft [1]

#### Isolated alkali/para-aminobenzoate contact ion pairs in gas phase: insights into nuclear and electronic structure by laser spectroscopy

Pol Boden<sup>a</sup>, Markus Gerhards<sup>†a</sup>, Christoph Riehn<sup>a\*</sup>

<sup>a</sup>Fachbereich Chemie & State Research Center OPTIMAS, TU Kaiserslautern, Erwin-Schrödinger-Str. 52, D-67663 Kaiserslautern, Germany.

#### Abstract

Isolated neutral alkali *para*-aminobenzoate contact ion pairs were investigated by applying combined IR/UV spectroscopy in a molecular beam experiment in combination with quantum chemical calculations (at the DFT and ADC(2) levels). As all species exhibit clearly defined electronic and vibrational transitions, even small spectroscopic effects, induced by a substitution of the alkali cation (*e.g.* Li<sup>+</sup> to Na<sup>+</sup>), could be followed. Significant electronic shifts were observed for the S<sub>1</sub> ← S<sub>0</sub> transitions and especially for the ionization potentials (IPs), exhibiting a strong red-shift from Li<sup>+</sup> towards Cs<sup>+</sup>. Similarly, a spectral shift (red-shift from Li<sup>+</sup> to Cs<sup>+</sup>) of the symmetric NH-stretching vibration as function of the alkali element (in the S<sub>0</sub> state) was observed in the ground state IR experiments. Additionally, IR photodissociation spectra of the photoionized adducts (D<sub>0</sub> state) were also recorded, revealing an opposite trend (blue-shift from Li<sup>+</sup> to Cs<sup>+</sup>) relative to the observations in the S<sub>0</sub> state.

#### Introduction

Ion pairs are ubiquitous in nature and play a crucial role in many biological systems, such as in the self-assembly of charged oligomeric bilayers<sup>[1]</sup>, in ion transport through phospholipid bilayers<sup>[2]</sup>, in pharmacology, where the solubility of charged hydrophilic therapeutics is often controlled by specific ion pairing<sup>[3]</sup>, stabilization and tertiary structure determination of peptides or proteins by salt bridges<sup>[4–6]</sup> or in organic synthesis, in particular for asymmetric ion-pairing catalysis<sup>[7]</sup>. Therefore, it seems obvious that ion pairs have already been studied in depth, predominantly in various condensed phase experiments.<sup>[8–10,11]</sup> Three distinct types of ion pairs are generally distinguished in solution, with cation-anion-aggregates constantly fluctuating between three different types, namely the solvent separated ion pairs (SSIPs, with intact primary solvation shells around both counterions), solvent shared ion pairs (SIPs, with a single solvent layer between cation and anion) and finally the contact ion pairs (CIP)

without any solvent molecules separating cation and anion.<sup>[8,12,13]</sup> Nevertheless, the characterization of the intrinsic properties of ion pairs is still challenging since in condensed phase media the spectroscopic properties of cation-anion-pairs are influenced by the surrounding medium<sup>[8]</sup>, strongly depending on the type of ion pair (see above) and its (specific) interaction with the solvent.

Due to the limitations in condensed media, spectroscopy on isolated ion pairs in the gas phase should be a powerful tool for an in-depth exploration of their intrinsic properties of ion pairs. However, only few studies on neutral isolated ion pairs in the gas phase have been published up to now. One reason for these studies being rather scarce is the aspect that, apart from a few ionic liquids that are vaporizable by using a thermal source<sup>[14,15]</sup>, neutral ion pairs cannot be easily transferred into the gas phase by a simple heating process<sup>[14,15]</sup>. Alternatively, other groups studied cold neutral ion pairs by embedding their samples in helium nanodroplets<sup>[16]</sup>. Related to these experiments are also ion trap studies targeted towards zwitterionic structures of amino acids and small peptides identified by salt bridges formed with alkali metal cations.<sup>[5,6]</sup> However, as emphasized, these investigations relate to overall ionic systems, but contribute as well as studies on neutral systems to the comprehensive topic of metal ion-bioorganic molecule interactions. These studies are often carried out on molecular model systems and detailed by vibronic spectroscopy under metal cation size variation, *e.g.*, in the group of alkalis  $\text{Li}^+ - \text{Cs}^+$ , in order to elucidate deduced structural and functional modulations.<sup>[17,18]</sup>

In 2016, the group of Mons, Gloaguen and coworkers transferred neutral, isolated contact ion pairs for the first time into the gas phase by using a laser desorption source.<sup>[12]</sup>

Subsequently, they have extended their studies in this field.<sup>[19–21]</sup> In their first publication they investigated isolated  $\text{Li}^+\cdots$ phenylacetate and related derivatives in a molecular beam by UV and combined IR/UV-spectroscopy and demonstrated the high potential of such gas phase spectroscopic data as benchmark values for investigations in solution.<sup>[12,19]</sup>

Another aspect of these studies lies in their interpretation as electric Stark experiments on isolated neutral ion pairs.<sup>[21,20]</sup> Hereby, a UV chromophore (phenyl substituent), acting as electric field probe, was intramolecularly immersed into a strong electric field of ca.  $0.2\text{--}4 \text{ GV} \cdot \text{m}^{-1}$ , reigning in the proximity of a carboxylate-alkali ion pair which was covalently linked to the phenyl chromophore. Thus, particularly high electric field strengths are achieved within isolated contact ion pairs, as field strength of no more than  $0.1 \text{ GV} \cdot \text{m}^{-1}$  are reached in common capacitor-based experiments.<sup>[20,22]</sup> Within isolated ion pairs considerable electronic and vibrational spectroscopic effects are induced by these strong fields and detected experimentally.<sup>[21,20]</sup>

Finally, UV experiments in the gas phase in combination with conformer-dependent electric field calculations have been shown to have a high potential for conformational investigations on biomolecules.<sup>[21]</sup> In other words, the spectral features of a UV chromophore, being influenced by the surrounding electric fields (environment-induced electronic Stark effects (EI-ESE)), yield information

on the environment of this chromophore and thus on the structure of the studied biomolecule. In such experiments even small electronic shifts of merely a few wavenumbers can be rationalized.<sup>[21]</sup>

These particularly stimulating and pioneering studies on neutral contact ion pairs by applying UV and combined IR/UV spectroscopy in molecular beam experiments are triggering further investigations in this still juvenile field.

Here, we studied isolated ion pairs of the alkali salts (from Li<sup>+</sup> to Cs<sup>+</sup>) of *para*-aminobenzoate (PABA<sup>-</sup>) in UV and IR/UV experiments in a molecular beam using a laser desorption source. Structurally, the cation is coordinated to the deprotonated carboxylate group of the *para*-aminobenzoate anion (see Figure 2). Upon photoionization, one electron is removed from the  $\pi$ -system of the PABA<sup>-</sup> chromophore, while the binding motif remains unchanged. As only structures of the mentioned binding motif are expected and PABA<sup>-</sup> is geometrically a rather simple molecule without major conformational variations, the spectral shifts observed in the UV- and IR/UV-experiments upon variation of the alkali cation (Li<sup>+</sup> to Cs<sup>+</sup>) should be mainly induced by electronic Stark effects rather than strongly differing structural motifs. Nevertheless, *para*-aminobenzoic acid (PABAH) is a unique system, due to its push-pull character, with the amino-group acting as electron density donor (mesomeric donor (+M) effect) and the carboxylate anion withdrawing electron density from the aromatic ring (mesomeric acceptor (-M) effect).

A series of publications on gas phase studies of PABAH have been published, where the spectroscopic properties of its monomer were investigated by applying the resonant-two-photon ionization method (R2PI)-<sup>[23,24]</sup>, two-color-R2PI<sup>[24]</sup>, IR/VUV-<sup>[25]</sup> as well as zero-electron-kinetic energy (ZEKE)-techniques<sup>[23]</sup>. The electric dipole moments within an isolated PABAH molecule in its ground and excited states were determined by applying rotationally resolved electronic spectroscopy<sup>[26]</sup> and electric deflection measurements<sup>[27]</sup>. In addition, the spectroscopic features as well as the geometry of the PABAH-dimer were characterized by R2PI-spectroscopy<sup>[24]</sup>.

While isolated *para*-aminobenzoic acid and its dimer have thus been investigated in detail, this is not the case for the alkali ion pairs of PABA<sup>-</sup> that are in the focus here. In order to gain a deeper understanding of the intrinsic effects reigning within these ion pairs, various spectroscopic techniques were applied. Besides the 1-color-R2PI spectroscopy, also the ionization potentials of the respective ion pairs were analyzed within a 2-color-R2PI experiment, revealing pronounced electronic effects. To the best of our knowledge, no ion yield curves of isolated contact ion pairs have been reported up to now. As the amino group within PABA<sup>-</sup> is an ideal probe for vibrational spectroscopy, combined IR/UV experiments were also performed, focusing on the relative frequency shifts of the symmetric NH<sub>2</sub> stretching band in dependence of the coordinating alkali cation, both in the electronic and ionic ground state (S<sub>0</sub> and D<sub>0</sub>). We have chosen the NH<sub>2</sub> group as a vibrational probe which is localized in the *para*

position relative to the coordination site (carboxylate group) of the respective alkali cation. Interestingly, the NH modes show a spectral response due to the alkali cation substitution although the vibrational probe is not directly linked to the cation under variation. It should be further noted that no IR-spectroscopic studies on photoionized ion pairs ( $D_0$  state) have been published up to now. However, the comparison of the spectral trends observed in the  $S_0$ - and  $D_0$ -IR spectra may significantly contribute to the understanding of the studied systems.

The spectroscopic results, and in particular the frequency shifts observed upon substitution of the alkali cation ( $Li^+$ - $Cs^+$ ), are discussed in combination with computational predictions obtained from geometry optimizations and harmonic frequency calculations as well as natural bond orbital analysis at density functional theory (DFT) and at SCS-ADC(2)/def2-TZVP level.

### Experimental methods

Isolated neutral ion pairs were prepared in a molecular beam using a laser desorption apparatus, based on the setup developed in the group of A. Rijs<sup>[28]</sup>. The investigated substance was mixed with activated charcoal powder (VWR) in a ratio of approximately 1:1. A thin layer of this sample mixture was applied on the edge of a graphite target which was mounted in front of a pulsed valve (General Valve, 500  $\mu$ m, 10 Hz), about 1 mm below the nozzle. The probe mixture was laser-desorbed by the fundamental of a Nd:YAG laser (Continuum Minilite, 10 Hz, 1064 nm), which was mildly focused onto the target surface by a 50 cm lens, using a laser power of 1.5-2.5 mJ/pulse. The target was translated continuously during the experiments, so that the continuously fresh material could be desorbed. For efficient adiabatic cooling argon was used as a carrier gas at a backing pressure of 3.2 bar. After passing through a skimmer into the second vacuum chamber, the molecular beam was crossed by the UV (and IR) laser(s) in the interaction region of a time of flight (TOF) mass spectrometer, oriented perpendicular to the propagation direction of the molecular beam and operated in the linear-TOF mode.

In order to considerably improve the signal-to-noise ratio in combined IR/UV experiments, a reference-signal correction method was applied, which is quite similar to the approaches used by the groups of Mons<sup>[29]</sup> and Kleinermanns<sup>[30]</sup>. After passing through the interaction region the excitation and ionization UV laser beam (about 1.0 mJ/pulse, unfocused) was redirected through the molecular beam, so that it ionized a second bunch of molecules. As mentioned, the molecular beam propagated perpendicularly to the axis of the flight-tube. For this reason, the UV laser had to cross the molecular beam at two slightly different heights, so that, combined with slightly defocused Wiley-McLaren conditions, two clearly separated mass peaks of the same  $m/z$  are obtained. The IR laser beam was spatially overlapped with the UV laser beam in the first interaction region of the UV laser with the molecular beam. In this way, one of the two ion signals detected was influenced by the wavelength-

tuned IR laser (about 8 mJ/pulse, unfocused) while the second mass peak remained untouched by the IR laser radiation. Thus, this second ion signal, which was only underlying the unavoidable signal intensity fluctuations, could be used as “reference ion signal”. The IR spectra were then obtained by taking the intensity ratio between the ion signal which is affected by the IR beam and the reference ion signal. At this point, it should still be noted that this powerful approach is however limited to combined IR/UV investigations based on a 1-color-R2PI process.

The IR laser was fired about 50 ns prior to the UV laser for IR/R2PI experiments in the  $S_0$  state and about 50 ns after the UV laser if the  $D_0$  state was probed (UV/UV/IR scans). Ion yield curves were obtained within 2C-R2PI-experiments. For this, the wavelength of the excitation laser was set to the  $0_0^0$ -R2PI-resonance of the investigated molecule while the wavelength of the second ionizing UV laser, which was temporally and spatially overlapped with the excitation laser pulse, was tuned. In order to suppress the efficient 1C-R2PI process, the pulse energy of the excitation laser had to be reduced to about 50  $\mu$ J/pulse (unfocused), while the ionization laser had a much higher fluence of 1.0-1.5 mJ/pulse (unfocused).

The required UV laser radiation was obtained by BBO frequency-doubling the output of a dye laser (Sirah, PrecisionScan), pumped by the second harmonic (532 nm) of a Nd:YAG laser (Innolas, Spitlight 1000 or Spitlight 1000.2). For most of the 2C-R2PI experiments radiation in the visible or near UV region was required for ionization, so that the simple output of the dye laser, then pumped by the third harmonic (355 nm) of the Nd:YAG laser, was used. IR radiation was obtained by difference-frequency mixing (DFM) of the fundamental (1064 nm) of a seeded Nd:YAG laser (Pro 230, Spectra Physics) with the output of the dye laser pumped by the second harmonic (532 nm) of the same Nd:YAG laser. The obtained IR radiation was amplified by using an optical parametric amplification (OPA) process in a further  $\text{LiNbO}_3$  crystal using the DFM output and again the fundamental (1064 nm) of the Nd:YAG laser. The spectral window of 3290-3750  $\text{cm}^{-1}$  (except for the 3460 – 3520  $\text{cm}^{-1}$  region due to crystal water absorption) was recorded with the described tunable IR laser.

*Para*-aminobenzoic (PABAH) was purchased from Alfa Aesar and used without further purification. The alkali ( $\text{Li}^+$ - $\text{Cs}^+$ ) *para*-aminobenzoate salts were obtained by reaction of an excess of the corresponding hydroxydes (MOH, M:  $\text{Li}^+$ - $\text{Cs}^+$ ) with PABAH at room temperature using methanol as solvent. After evaporation of the solvent the samples for the laser desorption experiments were prepared as described above.

### Computational approaches

Input structures were generated manually with Avogadro<sup>[31]</sup> and preoptimized by applying the implemented UFF (Universal Force Field)<sup>[32]</sup>. Geometry optimizations as well as harmonic frequency



calculations for both the  $S_0$  and  $D_0$  electronic state were performed at the DFT level, using the B3LYP functional<sup>[33]</sup> including the D3 dispersion correction<sup>[34]</sup> with Becke-Johnson (BJ) damping<sup>[35]</sup> in combination with the basis set def2-TZVP (def2-ecp for Rb and Cs)<sup>[36]</sup> (identical auxiliary basis sets for the RI approximation). Within that, geometry optimizations were carried out using the Berny algorithm from Gaussian 09<sup>[37]</sup>, while energies and gradients were calculated with Turbomole 7.5<sup>[38]</sup>. The obtained harmonic DFT-based frequencies were scaled by 0.963 to account for anharmonic effects. To further understand the measured and calculated trends, a natural bond orbital (NBO) analysis<sup>[39]</sup> was performed using the NBO module<sup>[40]</sup> from Gaussian 09, at the DFT/B3LYP-D3(BJ)/def2-TZVPP<sup>[36]</sup> level. In this approach, the wavefunction of the molecular system is transformed in a way to obtain an optimized “Lewis-like” bonding pattern of the molecular system, composed of localized one-center “core” (c) or “lone pair” (n) NBOs and two-center “bond” ( $\sigma$ ,  $\pi$ ) NBOs with a maximum-occupancy character, complemented by the low-occupancy antibonding orbitals ( $\sigma^*$ ,  $\pi^*$ ) and the (negligibly occupied) extra-valence “Rydberg-type” (Ry) NBOs. Generally, (“Lewis orbital”-type) bonding NBOs have occupation numbers around two electrons, while antibonding (“non-Lewis”-type) orbitals have occupations close to zero. Weak populations of antibonding orbitals are effects of delocalization and resonance stabilization or may be induced by non-covalent interactions such as hydrogen bonding.<sup>[41]</sup> An NBO analysis is thus a convenient tool to describe even very small electronic effects within a compound, which may then explain observed structural features (*e.g.* bond lengths) and spectroscopic observations (*e.g.* vibrational frequencies).<sup>[42,43]</sup>

Additionally, geometry optimizations were performed at the SCS-(ADC(2)-s) level<sup>[44]</sup>, implemented in Turbomole, for the electronic ground state as well as for the first excited singlet state. This latter approach of CC2-like accuracy is well known for its accurate prediction of electronic excitation energies (with typical errors of 0.1-0.2 eV for ADC(2))<sup>[45]. [46]</sup> Hereby, the basis set def2-TZVP (def2-ecp for Rb and Cs)<sup>[47]</sup> was applied, choosing the corresponding auxiliary Coulomb fitting basis set (cbas) def2-TZVP-cbas<sup>[48]</sup> required by the ricc2 module for the RI approximation. The obtained geometries were confirmed to be minimum structures by performing harmonic frequency calculations with the NumForce script of Turbomole, using the option “-central”. The respective harmonic frequencies were scaled by 0.969.

To yield an estimation about the enantiomerization barriers between different isomers, relaxed Potential Energy Surface (PES) scans were performed for the relevant dihedral angle at the DFT/B3LYP-D3(BJ)/def2-TZVP level, using Gaussian 09.



## Results and discussion

### Electronic spectra and ionization potentials (1C-R2PI and 2C-R2PI methods)

One-color R2PI spectra of *para*-aminobenzoic acid (“protonated” neutral monomer, named PABAH in the following) and of all possible alkali cation *para*-aminobenzoate contact ion pairs ( $M^+PABA^-$ , with  $M$ :  $Li^+$ - $Cs^+$ ) (Figure 1), were recorded in the range of  $33613$ - $34965$   $cm^{-1}$ , yielding their vibrationless  $0_0^0$  (electronic origin) transitions as well as higher vibronic transitions in dependence of the coordinating alkali cation.

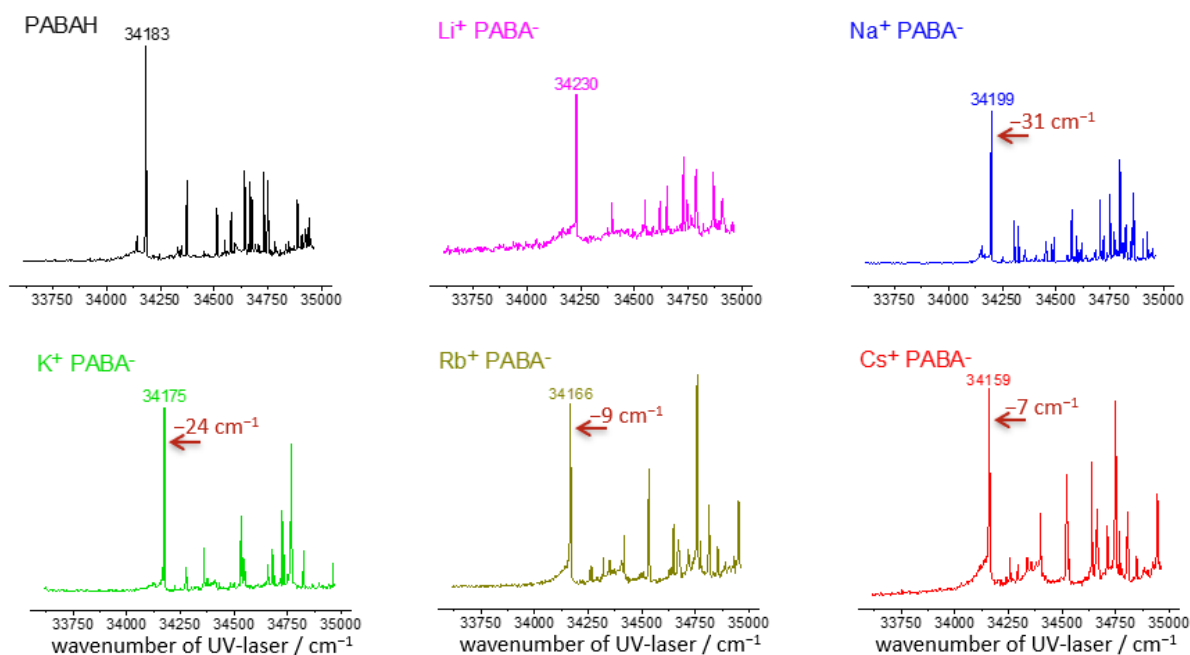


Figure 1: 1C-R2PI spectra of *para*-aminobenzoic acid (PABAH) and its alkali ion pairs  $Li^+PABA^-$ ,  $Na^+PABA^-$ ,  $K^+PABA^-$ ,  $Rb^+PABA^-$  and  $Cs^+PABA^-$  in the spectral range of  $33613$ - $34965$   $cm^{-1}$ . For the ion pairs the shift of the  $0_0^0$  transition relative to the next smallest cation is given by the horizontal arrow (in dark red).

In all spectra a pronounced electronic origin transition is observed, followed by a series of blue-shifted peaks resulting most probably from the excitation of low-frequency vibrational modes in the first excited singlet state ( $S_1$ ). The observed vibronic pattern changes upon substitution of the alkali cation, but here we focus on the values of the respective electronic origin transitions. DFT studies revealed the presence of only one single structural motif ( $M^+$  equally coordinated to both oxygens of the  $COO^-$  group, see Figure 2) and thus suggest a single isomer for all investigated ion pairs. As the measured resonances are sharp, even small relative frequency shifts upon exchange of the alkali cation are clearly detected.

For the PABAH monomer the  $0_0^0$  resonance was obtained at  $34183\text{ cm}^{-1}$ , which is in good agreement with the value of  $34173\pm 2\text{ cm}^{-1}$  published by Wendt and coworkers<sup>[24]</sup>. Although the R2PI spectrum of the PABAH monomer cannot be considered as an ideal reference for the R2PI resonances of the  $M^+PABA^-$  ion pairs, the *para*-aminobenzoate anion ( $PABA^-$ ) chromophore within these pairs, shows UV transitions in a close by spectral region. More precisely, the most blue-shifted  $0_0^0$  transition (with respect to PABAH) was obtained for  $Li^+PABA^-$  at  $34230\text{ cm}^{-1}$ , with a successive red-shift being observed in the order  $Na^+PABA^-$  ( $34199\text{ cm}^{-1}$ ),  $K^+PABA^-$  ( $34175\text{ cm}^{-1}$ ),  $Rb^+PABA^-$  ( $34166\text{ cm}^{-1}$ ) and  $Cs^+PABA^-$  ( $34159\text{ cm}^{-1}$ ). Thus, a relative UV resonance shift of  $31\text{ cm}^{-1}$  is measured between  $Li^+PABA^-$  and  $Na^+PABA^-$ , which successively decreases to only  $7\text{ cm}^{-1}$  between  $Rb^+PABA^-$  and  $Cs^+PABA^-$ .

These shifts of the electronic origins are ascribed to the influence of the electric field of the alkali cations  $M^+$  ( $M^+$ :  $Li^+$ - $Cs^+$ ) which are coordinated to the  $PABA^-$  chromophore. The charge of these  $M^+$  ions is partially screened by the  $COO^-$  group but its electric field still influences the UV chromophore's transitions in dependence of the inverse ionic radius ( $1/R_M$ ) according to Coulombs law.<sup>[17,18]</sup> As  $PABA^-$  is an electron-rich anionic system, with the  $\pi$ -electron density being delocalized not only over the aromatic ring but also the carboxylate and amino groups, the cation will strongly polarize the electron density distribution on the chromophore and thus influence its electronic transitions. This effect is differently pronounced for the different cations, with clear trends being seen for the optimized  $M^+PABA^-$  geometries as well as for the N atom hybridizations (amino group) and the atomic partial charges (see Tables S2 and S4) predicted by the NBO analysis. The N atom of the amino group has a comparatively high "s" character, which increases from  $Cs^+$  ( $sp^{2.84}$ ) to  $Li^+$  ( $sp^{2.75}$ ) and entails planarization (Table 1 and Figure 2). In parallel, the C-N- and the C(ring)-C(carboxylate)-bond lengths successively decrease from  $Cs^+PABA^-$  to  $Li^+PABA^-$ .

Table 1: Geometry parameters (obtained at DFT/B3LYP-D3(BJ)/def2-TZVP) and N atom hybridization, as obtained from an NBO analysis (performed at the DFT/B3LYP-D3(BJ)/def2-TZVPP level) for the  $M^+PABA^-$  ion pairs in the  $S_0$  state.

	$\angle H_1-N-H_2$ ; $C'-C_p-C'' / ^\circ$	N-C <sub>p</sub> / Å	C(Carboxylat)- C(aromat) / Å	N atom hybridization (NBO)	$M^+\cdots M_{ring}$ / Å	N-H <sub>1</sub> , N-H <sub>2</sub> / Å
$Li^+PABA^-$	34.0	1.387	1.482	$sp^{2.75}$	4.978	1.007, 1.007
$Na^+PABA^-$	36.4	1.391	1.484	$sp^{2.80}$	5.375	1.008, 1.007
$K^+PABA^-$	37.6	1.394	1.501	$sp^{2.83}$	5.754	1.008, 1.008
$Rb^+PABA^-$	38.2	1.395	1.504	$sp^{2.83}$	5.932	1.008, 1.008
$Cs^+PABA^-$	38.0	1.395	1.503	$sp^{2.84}$	6.059	1.008, 1.008
$PABA^-$	46.0	1.418	1.546	$sp^{3.07}$	-	1.011, 1.011

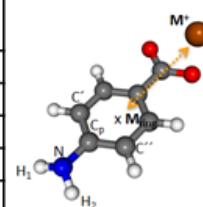


Figure 2: Optimized geometry of an  $M^+PABA^-$  ion pair in the  $S_0$  state illustrating the  $\angle H_1-N-H_2$ ;  $C'-C_p-C''$  angle and the  $M^+\cdots M_{ring}$  distance.

Thus, a significant +M effect of the amino group with respect to the aromatic ring and the carboxylate group is present for  $\text{Li}^+\text{PABA}^-$ , leading to a pronounced flattening of the amino group, while a less pronounced +M effect occurs for ion pairs containing larger cations, *e.g.*,  $\text{Cs}^+\text{PABA}^-$ . As reported above, the strongest blue-shift for the UV  $0_0^0$  transition is observed for the smallest coordinating cation with the highest positive charge density. As given in Table 1, the distance  $\text{M}^+\cdots\text{M}_{\text{ring}}$  declines with decreasing cation size. This means that for  $\text{Li}^+\text{PABA}^-$  the coordinating cation has not only a particularly high positive charge density ( $R_{\text{Li}^+} = 0.76 \text{ \AA}^{[49]}$ ), but is also geometrically significantly closer to the UV chromophore ( $\text{Li}^+\cdots\text{M}_{\text{ring}}$ :  $4.978 \text{ \AA}$  (DFT)). In contrast, for  $\text{Cs}^+\text{PABA}^-$ , featuring a much larger cation size ( $R_{\text{Cs}^+} = 1.67 \text{ \AA}^{[49]}$ ), a low positive charge density and a considerably larger distance between  $\text{Cs}^+$  and the  $\text{PABA}^-$  anion ( $\text{Cs}^+\cdots\text{M}_{\text{ring}}$ :  $6.059 \text{ \AA}$  (DFT)), the cation's Coulomb potential at the UV chromophore and its impact on the frequency of the electronic origin transition should be considerably weaker. Indeed, there is an approximately linear correlation between the  $0_0^0$  transition frequencies and the inverse ion radius  $1/R_{\text{M}}^{[17,18]}$  of the alkali cations (Figure 4).

Remarkably, the described findings are in contrast to the observations reported by Gloaguen *et al.*<sup>[21,20]</sup> In their studies, the "perturbation" of the probed (neutral) UV chromophore, immersed into the electric field reigning in proximity of a cation...anion dipole (and higher-order multipoles), is strengthened with increasing cation size. Regarding the  $\text{M}^+\text{PABA}^-$  ion pairs investigated in our study, however, not a dipole, but the electric field of the alkali cation is responsible for the observed spectroscopic effects. Here, the strongest influence on the chromophore ( $\text{PABA}^-$ ) occurs for ion pairs with smaller cations.

Although clear trends were observed in the 1C-R2PI experiments, the absolute spectral shifts of the measured  $0_0^0$  transitions are rather small (in the few to few tens of  $\text{cm}^{-1}$  regime). Given these experimental results, and considering the accuracy of common *ab initio* quantum chemical computational methods for electronic transitions to lie at  $0.1 - 0.4 \text{ eV}^{[45]}$  it seems not feasible to complement the data with quantum chemical calculations.

However, we have found that there is some accordance with the  $S_1 \leftarrow S_0$  adiabatic excitation energies obtained at the SCS-ADC(2)/def2-TZVP level. This method predicts very similar electronic transition energies for the considered  $\text{M}^+\text{PABA}^-$  series and for the PABAH monomer. The minor shifts observed in the 1C-R2PI spectra may not be reflected by the SCS-ADC(2) calculations due to the still limited accuracy of computed electronic excitation energies.<sup>[45]</sup> However, a particularly low excitation energy of merely  $23304 \text{ cm}^{-1}$  is predicted for the isolated  $\text{PABA}^-$  anion, which may be in line with the measured red-shift from  $\text{Li}^+\text{PABA}^-$  to  $\text{Cs}^+\text{PABA}^-$ . In Table 2 all obtained adiabatic excitation energies for the  $S_1 \leftarrow S_0$  transitions are summarized.

Table 2: Adiabatic excitation energies and zero-point energy (ZPE)-corrected adiabatic excitation energies calculated at the SCS-ADC(2)/def2-TZVP level. All values are given in  $\text{cm}^{-1}$ .

	Li <sup>+</sup> PABA <sup>-</sup>	Na <sup>+</sup> PABA <sup>-</sup>	K <sup>+</sup> PABA <sup>-</sup>	Rb <sup>+</sup> PABA <sup>-</sup>	Cs <sup>+</sup> PABA <sup>-</sup>	PABAH	PABA <sup>-</sup>
$E_{S_1 \leftarrow S_0}, ad.$	36421	36420	36424	36422	36414	36359	24394
$E_{S_1 \leftarrow S_0}, ad., ZPE$	35072	35092	35098	35082	35077	34914	23304

The difference densities based on natural transition orbitals (NTOs) (see Figure S1) show that the  $S_1 \leftarrow S_0$  transitions of all considered species are of  $\pi \rightarrow \pi^*$  character, which is in agreement with the trend that the experimental as well as the calculated excitation energies are very similar. Regarding the  $S_1$  state ion pair geometries obtained from the SCS-ADC(2) approach, the amino group is further planarized compared to the  $S_0$  state structures, in parallel with a shortening of the C–N bond length. This is illustrated in Tables S1-S2, on the basis of the corresponding geometry parameters and the predicted atomic partial charges for both the  $S_0$  and  $S_1$  state structures.

For comparison, the investigation of isolated PABA<sup>-</sup>, “unperturbed” by a coordinating  $M^+$  cation, should be considered as a reference case. For this system theory readily predicts a (compared to the corresponding ion pairs) particularly strong pyramidalization of the amino group and a considerably reduced “s” character of the N atom hybridization ( $sp^{3.07}$ ) (see Table 1). Furthermore, a particularly low excitation energy of only  $23304 \text{ cm}^{-1}$  is predicted for the isolated PABA<sup>-</sup> anion (Table 2), which is in general in line with the measured red-shift from Li<sup>+</sup>PABA<sup>-</sup> to Cs<sup>+</sup>PABA<sup>-</sup>, but does not agree with its extrapolated value for  $1/R_M \rightarrow 0$  (see below).

In parallel to the 1C-R2PI spectra also 2C-R2PI ion yield curves (Figure 3), were recorded to probe the dependence of the ionization potentials (IPs) on the coordinating alkali cation ( $\text{Li}^+$ - $\text{Cs}^+$ ). For this, the excitation laser was frequency-fixed at the respective  $0_0^0$  transition obtained from the 1C-R2PI spectrum while the wavelength of the ionization laser was scanned under field-free conditions.

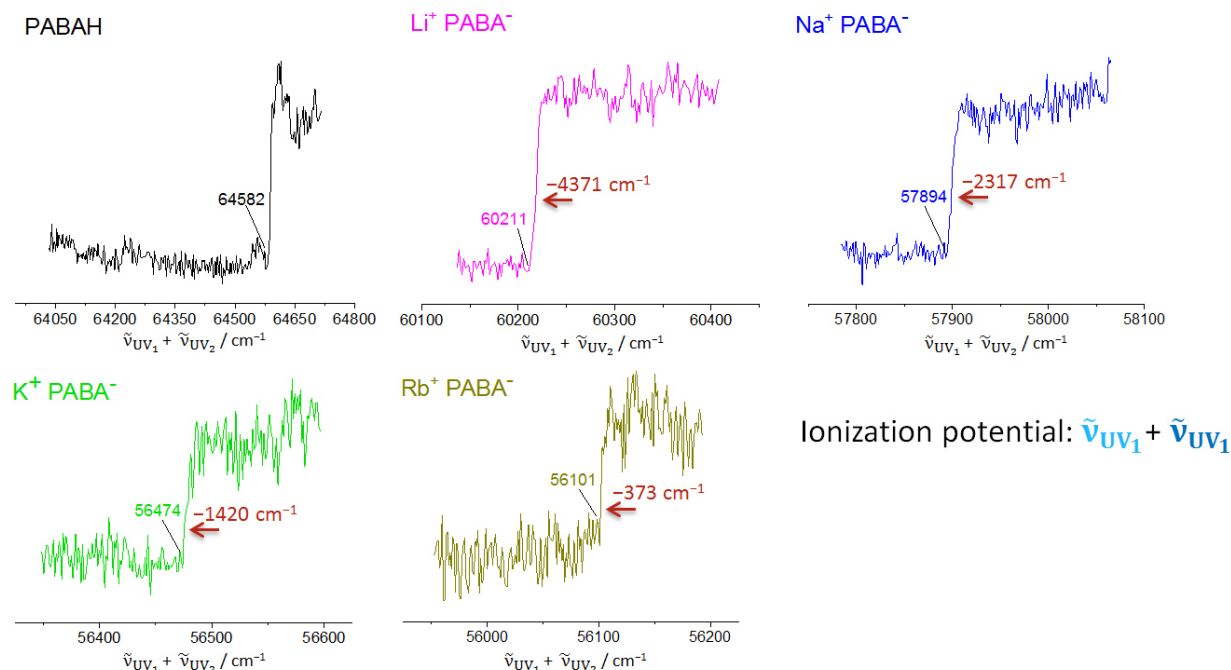


Figure 3: Ion yield curves of *para*-aminobenzoic acid (PABAH) and related alkali ion pairs  $\text{Li}^+\text{PABA}^-$ ,  $\text{Na}^+\text{PABA}^-$ ,  $\text{K}^+\text{PABA}^-$ ,  $\text{Rb}^+\text{PABA}^-$ . For each ion pair the ionization laser wavelength was tuned in the region of the respective ionization potential, while the excitation laser was frequency-fixed at the respective  $0_0^0$  transition. The relative shifts of IPs are given in dark red.

All the recorded spectra show a region where a sharp increase in ion signal intensity (two color effect) is observed. At these steps the according ionization potential (IP) is reached, so that an estimation of their values can thus be obtained. Unfortunately, the experimental determination of the IP was not feasible for  $\text{Cs}^+\text{PABA}^-$ , as no two color effect could be observed for this system. We noticed that the two color effect is strongest for the PABAH monomer and  $\text{Li}^+\text{PABA}^-$  (increase of base ion signal by 50 %), while its efficiency successively decreases into the low percent region for the case of  $\text{Rb}^+\text{PABA}^-$ . An explanation for this observation could be the increasing structural reorganization between the  $S_0/S_1$  and  $D_0$  geometries from  $\text{Na}^+\text{PABA}^-$  to  $\text{Cs}^+\text{PABA}^-$ , which is discussed in detail below. In fact, large structural changes of this type often lead to weak Franck-Condon activities in 2C-R2PI experiments.<sup>[50]</sup> The IP of the PABAH monomer obtained here amounts to:  $64582 \text{ cm}^{-1}$ , in good agreement to the published data of  $64507 \pm 8 \text{ cm}^{-1}$ <sup>[24]</sup>. The small difference may result from the different experimental approaches, as in the experiment of Meijer *et al.*<sup>[24]</sup> the IP was determined in dependence of the electric field strength, with the value at zero electric field only obtained by extrapolation.

In comparing the IPs of the investigated series, a pronounced shift of  $-4371\text{ cm}^{-1}$  (relative to the IP of PABAH) is observed for  $\text{Li}^+\text{PABA}^-$ , where the latter is the  $\text{M}^+\text{PABA}^-$  ion pair with the highest ionization potential. This impressive shift may be less surprising, considering that an electron is detached from the anionic  $\text{PABA}^-$  chromophore within the ion pair. The IP values decrease further in the order of  $\text{Li}^+\text{PABA}^-$ ,  $\text{Na}^+\text{PABA}^-$ ,  $\text{K}^+\text{PABA}^-$  and  $\text{Rb}^+\text{PABA}^-$ . Regarding the IPs, the frequency shifts induced by exchange of the alkali cation are distinctly stronger than for the  $0_0^0$  resonances. As the electronic excitation energies are very similar for all the ion pairs, the shifts of the IPs are mainly provoked by a decrease of the energetic gap between  $S_1$  and  $D_0$ .

The adiabatic ionization potentials determined at DFT level by quantum chemical calculations, predicting a decrease of the IP from  $62451\text{ cm}^{-1}$  to  $53405\text{ cm}^{-1}$  from  $\text{Li}^+\text{PABA}^-$  to  $\text{Cs}^+\text{PABA}^-$ , are in perfect agreement with the experimental trend, yet the experimental values are underestimated by about  $2000\text{ cm}^{-1}$  by theory. The large shifts observed for the IPs demonstrate the high electric field strength reigning within isolated contact ion pairs<sup>[20,21,19,12]</sup>, *e.g.*, compared to the lowering of the IP by an external field which was obtained for PABA by only  $18\text{ cm}^{-1}$  at  $100\text{ V/cm}$ .<sup>[24]</sup> However, it seems challenging to determine the specific electric field strength influencing the IP of an  $\text{M}^+\text{PABA}^-$  ion pair without experimental value for the electron detachment energy of isolated  $\text{PABA}^-$ . Still, the correlation between the measured spectroscopic shifts and the size of the coordinating alkali cation can be discussed. For this, the experimentally determined IPs are plotted against the inverse radius of the coordinating alkali ion<sup>[17,49,18]</sup> (Figure 4). Here, an almost perfect linear correlation is obtained. Thus, the ionization potentials of the compounds are influenced by the electric field strength which itself depends according to Coulombs law on the distance to the field-inducing charge, *i.e.*, the size of the related alkali cation.

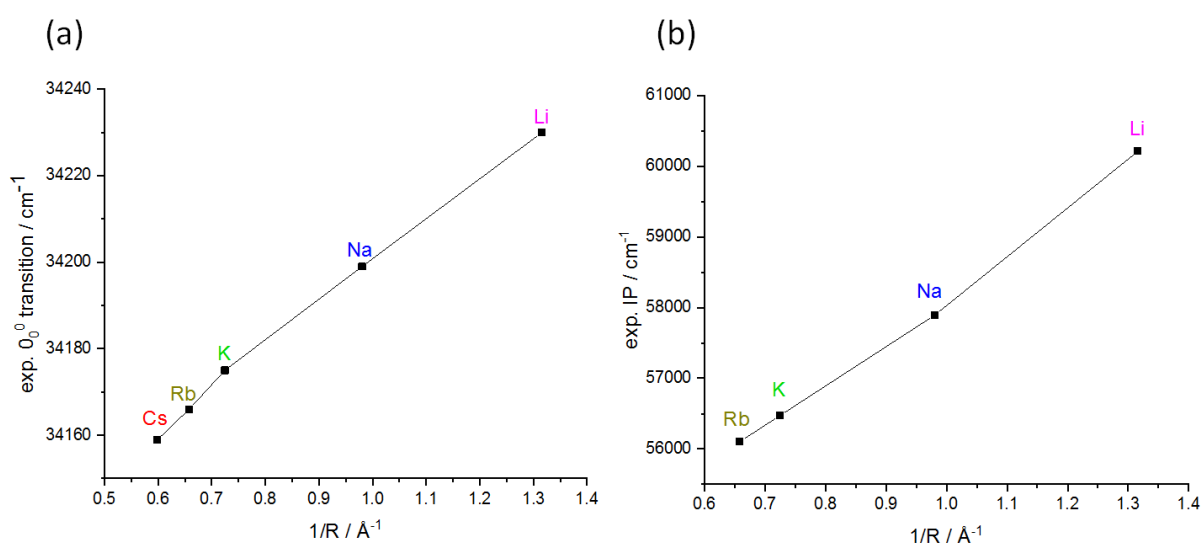


Figure 4: Plots of (a) the R2PI origin transitions and (b) the ionization potentials (IPs) against the inverse radius of the coordinating alkali ion.

As discussed above, the interaction between the cation  $M^+$  and the  $PABA^-$  chromophore is particularly strong if a small and highly charged cation is linked to the carboxylate group, and it weakens towards larger alkali ion size (see binding energies in Table S3 (a),(b)). Here, we investigate the energetics of the metal cation-chromophore interaction further by quantum chemical calculations. Due to the weakening with increasing metal ion size of the  $M^+ \cdots PABA^-$  interaction, the calculated binding energy ( $M^+ \cdots PABA^- \rightarrow M^+ + PABA^-$ ) decreases from  $61372 \text{ cm}^{-1}$  for  $Li^+PABA^-$  to  $41281 \text{ cm}^{-1}$  for  $Cs^+PABA^-$ , which corresponds to 67 % of the value for  $Li^+PABA^-$ . Note that these values are also similar to the ones for the IPs.

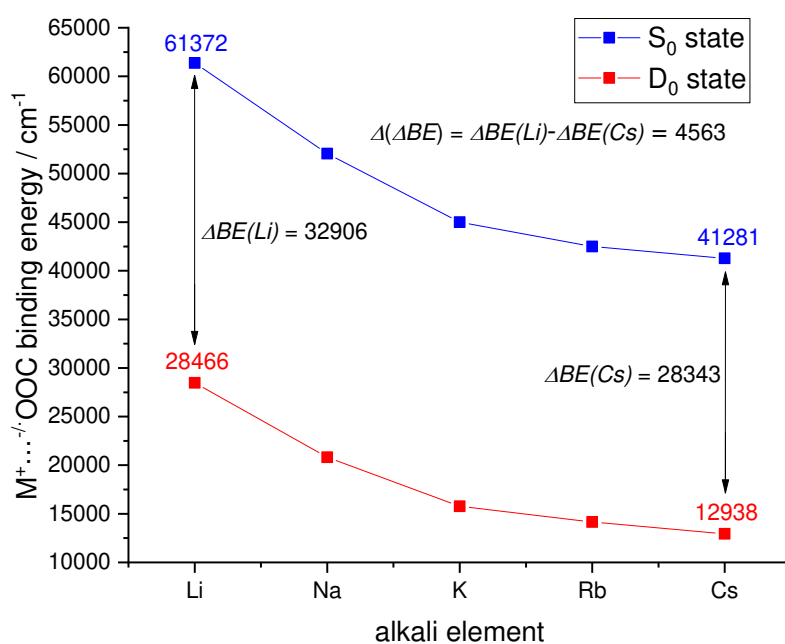


Figure 5: Binding energies between the alkali cation ( $M^+$ :  $Li^+$ - $Cs^+$ ) and the carboxylate ( $COO^-/-$ ) of  $PABA^-/-$  in the  $S_0$  and  $D_0$  state, calculated at the DFT/B3LYP-D3(BJ)/def2-TZVP level. For  $Li^+PABA^-/-$  the binding energy between cation and chromophore decreases by  $20091 \text{ cm}^{-1}$  upon photoionization, while this decline is much less pronounced for  $Cs^+PABA^-/-$  with  $15528 \text{ cm}^{-1}$ . Thus, the decline of the binding energy upon photoionization decreases by  $4563 \text{ cm}^{-1}$  between  $Li^+PABA^-$  and  $Cs^+PABA^-$ .

Additionally, in the ionic ground state  $D_0$ , the binding energy ( $M^+ \cdots PABA^- \rightarrow M^+ + PABA^-$ ) decreases from  $28466 \text{ cm}^{-1}$  ( $Li^+PABA^-$ ) to  $12938 \text{ cm}^{-1}$  for  $Cs^+PABA^-$ , thus to only 46 % of the value for  $Li^+PABA^-$ . Both calculated trends of binding energies are illustrated in Figure 5 and will be discussed in the following under consideration of molecular structures of the different ion pairs.

In accordance with the energetic effects, the  $M^+ \cdots M_{ring}$  distance increases from  $4.978 \text{ \AA}$  for  $Li^+PABA^-$  to  $6.059 \text{ \AA}$  for  $Cs^+PABA^-$ , while this trend is slightly more pronounced in the  $D_0$  state, with  $Li^+ \cdots M_{ring}$ :  $5.035 \text{ \AA}$  and  $Cs^+ \cdots M_{ring}$ :  $6.218 \text{ \AA}$ . These effects are also mirrored by the NBO partial charges (given in Table S2

(a) and S4), as the negative charge on the O atoms of the carboxylate group considerably decreases from  $\text{Li}^+\text{PABA}^-$  to  $\text{Cs}^+\text{PABA}^-$  in the  $D_0$  state. At the same time, this trend is much less pronounced for the anionic chromophore of the  $\text{M}^+\text{PABA}^-$  species in the  $S_0$  state. A considerable decrease of the (negative) charge on the carboxylate group and an increase of the distance separating cation and anion lead to weakening of the electrostatic interaction between  $\text{M}^+$  and  $\text{PABA}^-$  and thus to a lower binding energy. Regarding absolute values, the binding energy between  $\text{Li}^+$  and  $\text{PABA}^-$  decreases by  $32906 \text{ cm}^{-1}$  upon photoionization, while this effect is less pronounced for the  $\text{Cs}^+$  species with  $28343 \text{ cm}^{-1}$ . Thus, the decrease of the binding energy between cation and chromophore upon detachment of an electron ( $\Delta BE$ ) declines by  $4563 \text{ cm}^{-1}$  from  $\text{Li}^+\text{PABA}^-$  to  $\text{Cs}^+\text{PABA}^-$ . This can be explained by the particularly strong attractive electrostatic interaction between a small and highly charged cation (*e.g.*  $\text{Li}^+$ ) and the anion, which weakens towards systems with larger cations. In the  $D_0$  state, however, the size of the cation is (regarding absolute binding energy values) less decisive for the stability of the ion pair, as the chromophore is in a neutral radical state. For this reason, the energetic gap between the respective  $S_0$  and  $D_0$  state species should decrease along the series from  $\text{Li}^+\text{PABA}^-$  to  $\text{Cs}^+\text{PABA}^-$ , which is confirmed by both the experimental and calculated IPs (see Figure S2). It should be noted that the value of  $4563 \text{ cm}^{-1}$  is indeed similar to the calculated decrease of the IP by  $5357 \text{ cm}^{-1}$  between  $\text{Li}^+\text{PABA}^-$  and  $\text{Cs}^+\text{PABA}^-$ , which is once more in line with the experimentally determined shift of the IP by  $4110 \text{ cm}^{-1}$  between  $\text{Li}^+\text{PABA}^-$  and  $\text{Rb}^+\text{PABA}^-$ . Finally, the decrease of the IP towards ion pairs with heavier alkali ions should be due to the varying cation chromophore interactions, which crucially depend on both the size of the coordinating  $\text{M}^+$  ion and the electronic state of the  $\text{PABA}^-$  chromophore. To further confirm these statements regarding IPs, single point calculations were performed for the isolated  $\text{PABA}^-$  chromophores, whereby the alkali cations were replaced with simple positive point charges (see Figure S3 and discussion in the SI). After all, the observed spectroscopic shifts are in nice accordance with the Coulomb law<sup>[17,18]</sup>, which underlines that they clearly arise from dominating electrostatic interactions.

### **Infrared spectra of neutral and ionic ground states (IR/R2PI and UV/UV/IR spectroscopy)**

IR spectra of the molecular beam isolated  $\text{M}^+\text{PABA}^-$  ion pairs in the electronic ( $S_0$ ) and ionic ground state ( $D_0$ ) were recorded in the NH stretching region by IR/UV laser experiments (see Figures 6 and 7). As the intensity of the asymmetric  $\text{NH}_2$  stretching bands predicted by DFT is comparatively low (and these bands are likely positioned in the spectral gap of the used IR laser system), we focused on probing the frequency of the symmetric  $\text{NH}_2$  stretching mode. Furthermore, it should be noted that the calculated frequencies of both the symmetric and asymmetric NH stretching frequencies show a



similar behavior upon alkali cation substitution (see Table S5-S6). All IR spectra depicted in the following feature an intense band around  $3400\text{ cm}^{-1}$  which is unambiguously assigned to the symmetric  $\text{NH}_2$  stretching vibration. It is pointed out that there is an excellent correlation between all measured IR spectra and the NH stretching frequencies predicted by the DFT (and SCS-ADC(2)/def2-TZVP) calculations (see Figures S4 and S5).

First, we focus on the investigation of the ground state vibrations of the ion pairs obtained by IR/R2PI depletion spectroscopy. The IR/R2PI spectra for the  $S_0$  state, in the spectral range from  $3290\text{ cm}^{-1}$  to  $3460\text{ cm}^{-1}$ , are depicted in Figure 6, while the scans in the region above  $3520\text{ cm}^{-1}$  are shown in Figure S6.

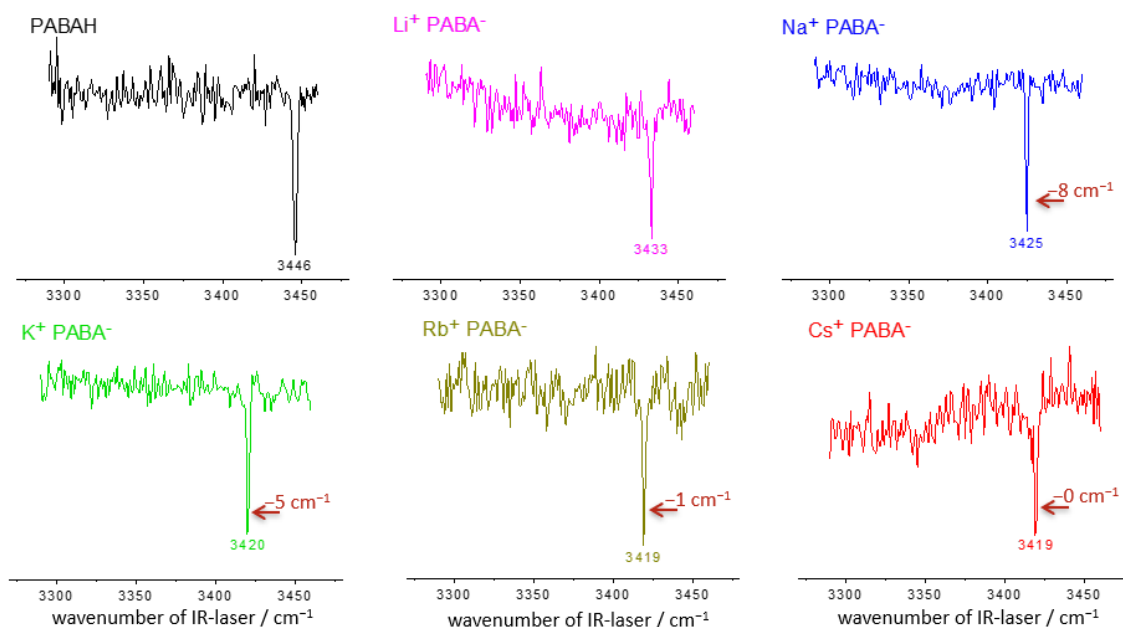


Figure 6: IR/R2PI spectra of the  $\text{Li}^+\text{PABA}^-$ ,  $\text{Na}^+\text{PABA}^-$ ,  $\text{K}^+\text{PABA}^-$ ,  $\text{Rb}^+\text{PABA}^-$  and  $\text{Cs}^+\text{PABA}^-$  ion pairs ( $S_0$  state) in the spectral region of the symmetric NH stretching band, measured *via* the respective  $0_0^0$  transitions. For the ion pairs the relative vibrational shifts are given in dark red.

Similar to the results of the 1C-/2C-R2PI experiments, the variation of the alkali cations leads to a spectral shift of the symmetric NH stretching vibration of the ion pairs. This is at first glance maybe surprising, considering the long distance (of ca.  $8\text{ \AA}$ ) between metal ion center and  $\text{NH}_2$  substituent, but comprehensible in view of the discussed conjugation of carboxylate and amino group *via* the aromatic ring. Thus, the NH stretch represents a sensitive, remote IR probe for the alkali metal binding on the carboxylate site, which will be elaborated on in the following. The highest frequency band (largest blue-shift with respect to the calculated value for PABA) is obtained for  $\text{Li}^+\text{PABA}^-$ , with  $3433\text{ cm}^{-1}$ , and a successive red-shift is observed in the order of  $\text{Na}^+\text{PABA}^-$ ,  $\text{K}^+\text{PABA}^-$ ,  $\text{Rb}^+\text{PABA}^-$  and  $\text{Cs}^+\text{PABA}^-$ . Since the structural motif is maintained when the alkali metal is exchanged, the observed

frequency shifts can readily be assigned to a vibrational Stark effect. An NBO analysis (see Tables 1, S2 (a) and S4 (a)) was performed to further analyze these frequency shifts. As described above, the optimized  $S_0$  geometries show a successively increasing planarization of the amino group from  $\text{Cs}^+\text{PABA}^-$  to  $\text{Li}^+\text{PABA}^-$ , due to the pronounced shift of electron density towards the carboxylate group when a small counterion of high positive charge density is coordinated to  $\text{PABA}^-$ . This electronic effect is further reflected by the N–H- and C–N-bond lengths and N atom hybridizations given in Table 1, as well as by the atomic partial charges obtained *via* NBO analysis (Table S2 (a) and S4 (a)). Generally, an increased “s” hybridization character and thus an enhanced planarization leads to a contraction of the N–H-bonds and consequently to higher  $\text{NH}_2$  stretching frequencies.<sup>[42,43]</sup> In this way, the highest NH stretching frequency is expected for  $\text{Li}^+\text{PABA}^-$ , in full accordance with the experiment. For isolated  $\text{PABA}^-$ , as a theoretical reference system, no cation is withdrawing electron density from the amino group, which explains the reduced amount of “s” character of the N atom ( $\text{sp}^{3.07}$ ) and the predicted strongly red-shifted symmetric NH stretching frequency of  $3382\text{ cm}^{-1}$  ( $3446\text{ cm}^{-1}$  for  $\text{PABAH}$ ). From  $\text{Li}^+\text{PABA}^-$  to  $\text{Cs}^+\text{PABA}^-$  the influence on the NH frequency by the respective counterion successively decreases, with a change in the direction of the frequency predicted for free  $\text{PABA}^-$ . This again leads to a correlation between the NH stretching frequencies and the inverse ion radius of the alkali cation (see Figure 10).

As the electronic and structural properties of  $\text{M}^+\text{PABA}^-$  observed in the electronic ground state have now been illustrated, the intriguing question remains how these features behave upon photoionization. In the ionic ground state  $D_0$ , the alkali cation  $\text{M}^+$  is coordinated to a neutral (dehydrogenated) radical  $\text{PABA}^\cdot$ . The initially neutral ion pairs can be photoionized within a 1C-R2PI process without showing detectable UV fragmentation. This observed high stability of the  $\text{M}^+\text{PABA}^\cdot$  ions is a suitable basis for IR experiments on these ionic species. The IR spectra in the NH stretching region for this ionic ground state ( $D_0$ ) have been recorded by employing the UV/UV/IR method (*e.g.* <sup>[51]</sup>) (Figure 7, spectra for the region above  $3520\text{ cm}^{-1}$  are depicted in Figure S7). The spectra have been recorded for both the parent and fragment mass channels, as an IR photodissociation channel was observed and assigned to a loss of neutral  $\text{CO}_2$  (decarboxylation)<sup>[52]</sup>. For the ionized  $\text{PABAH}^+$  monomer no IR induced fragmentation was observed, which points towards a significantly higher energy barrier of decarboxylation with the carboxylate group in its protonated form.

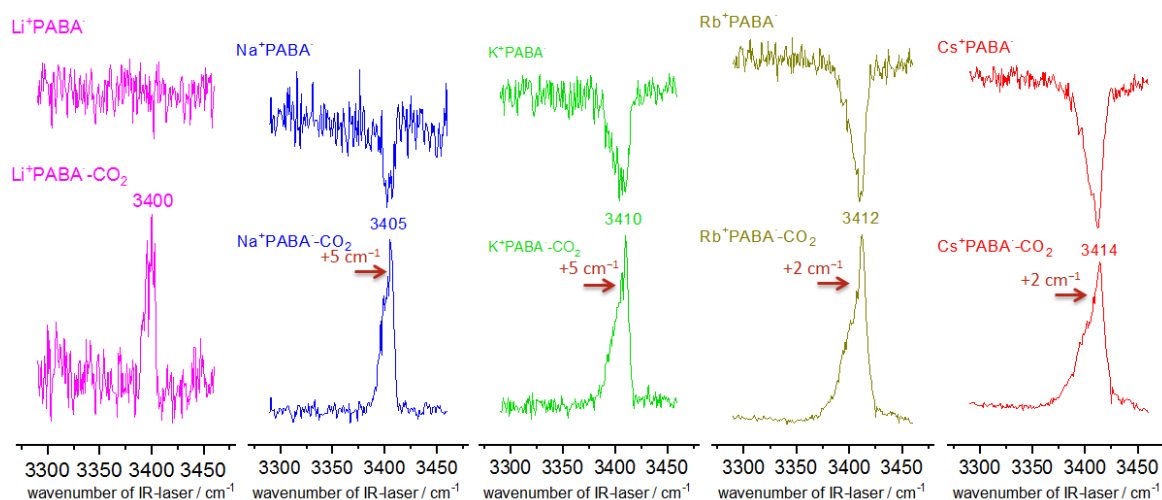


Figure 7: UV/UV/IR spectra of the  $\text{Li}^+\text{PABA}^-$ ,  $\text{Na}^+\text{PABA}^-$ ,  $\text{K}^+\text{PABA}^-$ ,  $\text{Rb}^+\text{PABA}^-$  and  $\text{Cs}^+\text{PABA}^-$  species ( $D_0$  state) in the spectral region of the symmetric NH stretching band, showing the parent ( $\text{M}^+\text{PABA}^-$ ) and fragment ( $\text{M}^+\text{PABA}^- \text{CO}_2$ ) mass traces. The initially neutral ion pairs were ionized *via* 1C-R2PI at the respective  $0_0^0$  transitions. For the ion pairs the relative vibrational shifts are given in dark red.

In order to elucidate the structures of the ions  $\text{M}^+\text{PABA}^- \text{CO}_2$  produced by IR photodissociation we performed quantum-chemical geometry optimization at the UDFT level. In the resulting geometries of the  $\text{K}^+\text{PABA}^- \text{CO}_2$ ,  $\text{Rb}^+\text{PABA}^- \text{CO}_2$  and  $\text{Cs}^+\text{PABA}^- \text{CO}_2$  fragments, the alkali cation is coordinated to the  $\pi$ -system of neutral decarboxylated (and dehydrogenated)  $\text{PABA}^-$  (see Figure S8). Similarly, DFT studies on  $\text{Na}^+$ /phenyl radical ( $\text{C}_6\text{H}_5$ ) and  $\text{K}^+$ /phenyl radical ( $\text{C}_6\text{H}_5$ ) complexes revealed that  $\pi$ -coordination is the only feasible structural motif for these systems.<sup>[53]</sup> Regarding  $\text{Li}^+\text{PABA}^- \text{CO}_2$  and  $\text{Na}^+\text{PABA}^- \text{CO}_2$ , however, a second minimum structure was found, where  $\text{M}^+$  is linked to the bare C-atom of the radical ( $\sigma$ -complex), which is energetically favored by  $2750 \text{ cm}^{-1}$  for  $\text{Li}^+\text{PABA}^- \text{CO}_2$  and disfavored by  $336 \text{ cm}^{-1}$  for  $\text{Na}^+\text{PABA}^- \text{CO}_2$ , relative to the respective  $\pi$ -bound species. Generally, a  $\sigma$ -complex is preferably formed in combination with small cations of high charge density, while larger cations rather coordinate to the  $\pi$ -system. All  $\text{M}^+\text{PABA}^- \text{CO}_2$  geometries are presented in Figure S8.

No IR depletion was observed on the parent mass trace of  $\text{Li}^+\text{PABA}^-$ , *i.e.*, the IR photodissociation effect is particularly weak for this species and cannot be discerned from the “ionization background”. However, the ion signal detected on the fragment mass trace ( $\text{Li}^+\text{PABA}^- \text{CO}_2$ ) is only stemming from the IR laser photodissociation process, so that the signal-to-noise ratio in this “gain” spectrum is comparably higher and an IR spectrum for  $\text{Li}^+\text{PABA}^-$  could be obtained in this way. Comparing all UV/UV/IR spectra, it is observed that the intensity of the resulting IR depletion increases from  $\text{Li}^+\text{PABA}^-$  to  $\text{Cs}^+\text{PABA}^-$ , with an estimated 40 % for the latter. This trend also parallels the improved signal-to-noise ratio observed in the spectra of the heavier alkali metal ion pairs. Indeed, the oscillator strength

of the symmetric NH stretching mode increases (see Table S7) from  $\text{Li}^+\text{PABA}^-$  towards  $\text{Cs}^+\text{PABA}^-$  according to theory. However, other aspects, which will be discussed in the following in more detail, are of even larger importance here.

First, the excess energy introduced into the ion pairs within the 1C-R2PI process increases from  $\text{Li}^+\text{PABA}^-$  to  $\text{Cs}^+\text{PABA}^-$ , due to the impressive lowering of the ionization potentials from  $\text{Li}^+\text{PABA}^-$  to  $\text{Cs}^+\text{PABA}^-$  accompanied by only small shifts observed for the respective  $S_1 \leftarrow S_0$  transitions (see above). We estimate that the excess energy in the  $D_0$  state increases from  $8249 \text{ cm}^{-1}$  to  $12231 \text{ cm}^{-1}$  from  $\text{Li}^+\text{PABA}^-$  to  $\text{Rb}^+\text{PABA}^-$  (Table 3) using the experimental results. Since the photoionization of  $\text{M}^+\text{PABA}^-$  takes place in the cold part of the molecular beam, no major dissipation of excess energy through inelastic collisions should occur for the ionized species. A high excess energy upon photoionization, *i.e.*, high internal energy of the ions, likely supports the IR photodissociation process which may further explain the described trend for the detected IR band intensities. Thus, the increase of the excess energy from  $\text{Li}^+\text{PABA}^-$  to  $\text{Cs}^+\text{PABA}^-$  could also be an explanation for the parallel increase in spectral broadening with a tail on the lower frequency side of the IR band. Namely, for a “warm” molecule the population of low frequency vibrational levels can lead to vibrational coupling between low and high frequency modes.<sup>[54]</sup> Comparingly, a strong broadening of  $\text{C}\equiv\text{N}$  stretching bands was observed for mononitrile-functionalized aryl anion radicals in solution, that were caused by structural fluctuations.<sup>[55]</sup> Such effects are also conceivable for the ion pairs investigated in this work, because of the structural changes described in the following (see also Table 3).

Table 3: Excess energies upon photoionization, and dihedral angles illustrating carboxylate distortion in the  $D_0$  state for the  $\text{Li}^+\text{PABA}^-$ ,  $\text{Na}^+\text{PABA}^-$ ,  $\text{K}^+\text{PABA}^-$ ,  $\text{Rb}^+\text{PABA}^-$  and  $\text{Cs}^+\text{PABA}^-$  species. All energy values were obtained at the DFT/B3LYP-D3(BJ)/def2-TZVP level.

ion pair	excess energy / $\text{cm}^{-1}$	dihedral angle ( $\alpha, \beta, \gamma, \delta$ ) / $^\circ$
$\text{Li}^+\text{PABA}^-$	8249	0.1
$\text{Na}^+\text{PABA}^-$	10504	25.1
$\text{K}^+\text{PABA}^-$	11876	37.7
$\text{Rb}^+\text{PABA}^-$	12231	36.6
$\text{Cs}^+\text{PABA}^-$	–	36.9

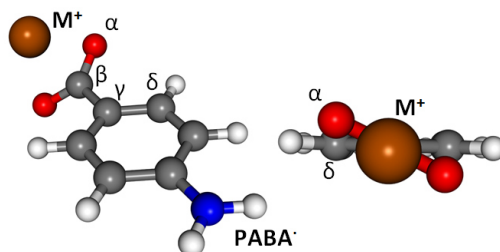


Figure 8: Optimized geometry of  $\text{M}^+\text{PABA}^-$  ions in the  $D_0$  state showing the carboxylate distortion, as obtained at the DFT/B3LYP-D3(BJ)/def2-TZVP level.

The optimized  $D_0$  geometries exhibit a torsion of the carboxylate group relative to the plane of the aromatic ring, in particular for the ion pairs with the larger alkali cations ( $\text{M}^+$ :  $\text{Na}^+$ - $\text{Cs}^+$ ), (Figure 8 and Table 3). This structural change could be considered as a sort of preliminary stage towards decarboxylation, as the loss of planarity prevents the  $\pi$ -conjugation involving the carboxylate group.

Evidently, this means that two isoenergetic (and probably ratiometric) enantiomers are formed, which, however, cannot be detected separately in the UV/UV/IR experiments as they exhibit identical NH stretching frequencies. An estimation of the interconversion barrier between both enantiomers was obtained by running a relaxed PES scan for the dihedral angle  $\angle(\alpha, \beta, \gamma, \delta)$ , yielding values between 0.9 (Na<sup>+</sup>PABA<sup>-</sup>) and 6.2 kJ/mol (Cs<sup>+</sup>PABA<sup>-</sup>).

We will discuss in the following the spectral positions of the NH stretching bands obtained from the UV/UV/IR experiments as observed for the D<sub>0</sub> ionic states of the ion pairs. The band positions are on average moderately red-shifted from the positions in the S<sub>0</sub> ground state. Moreover, it is clearly revealed (Fig. 7) that the symmetric NH stretching frequency blue-shifts from Li<sup>+</sup>PABA<sup>-</sup> to Cs<sup>+</sup>PABA<sup>-</sup>, which is in contrast to the observations for the S<sub>0</sub> state IR spectra. These opposite trends are perfectly reflected by the frequencies predicted by the DFT simulations (Tables S5 and S7).

The vibrational and structural effects induced when PABA<sup>-</sup> (reference system in the S<sub>0</sub> state) is photoionized to form PABA<sup>-</sup> (reference system in the D<sub>0</sub> state) could be considered to elucidate in general the IR spectra in the D<sub>0</sub> state. As evoked, the vibrational bands of PABA<sup>-</sup> cannot be probed in our experiment, but the DFT calculations predict a strong shift of the symmetric NH stretching frequency from 3376 cm<sup>-1</sup> for PABA<sup>-</sup> to 3450 cm<sup>-1</sup> for PABA<sup>-</sup> (see Figures S4, S9 and Tables S5, S7). This pronounced vibrational shift is in line with the considerably increased “s” hybridization character of the N atom in the D<sub>0</sub> state (sp<sup>2.59</sup>), compared to the sp<sup>3.07</sup> hybridization in the S<sub>0</sub> state (see Tables 1 and 4). However, this calculated spectral behavior of the reference system cannot explain the observed experimental trend for the ion pairs.

Hence, another effect has to come into play for rationalizing the shifts obtained for the NH stretching frequencies of the M<sup>+</sup>PABA<sup>-</sup> species. The results of the DFT calculations suggest that the amino group is almost completely planarized in the D<sub>0</sub> state for all the investigated ion pairs, with an N atom hybridization of sp<sup>2.34</sup> or sp<sup>2.35</sup>, respectively. However, the symmetric NH stretching frequency undergoes a clear red-shift upon photoionization, especially for Li<sup>+</sup>PABA<sup>-</sup> (-33 cm<sup>-1</sup>, exp.), Na<sup>+</sup>PABA<sup>-</sup> (-20 cm<sup>-1</sup>, exp.) and to a minor extent also for K<sup>+</sup>PABA<sup>-</sup> (-10 cm<sup>-1</sup>, exp.), while the bands of Rb<sup>+</sup>PABA<sup>-</sup> and Cs<sup>+</sup>PABA<sup>-</sup> only shift by -7 cm<sup>-1</sup> and -5 cm<sup>-1</sup>, respectively. For Rb<sup>+</sup>PABA<sup>-</sup> and Cs<sup>+</sup>PABA<sup>-</sup>, the harmonic DFT frequency calculations even predict a slight blue-shift of about +3 cm<sup>-1</sup> relative to the NH stretches in the S<sub>0</sub> state (see Figures S4, S9 and Tables S7, S9). The red-shifts observed and calculated for Li<sup>+</sup>PABA<sup>-</sup>, Na<sup>+</sup>PABA<sup>-</sup> and K<sup>+</sup>PABA<sup>-</sup> are also reflected in the increase of the N-H bond lengths (Tables 1 and 4). In order to understand this trend, the orbital occupancies obtained from the NBO analysis were considered. This approach was already applied to reveal vibrational shifts observed for the S<sub>0</sub> and D<sub>0</sub> states of the structurally related aniline<sup>[43]</sup> as well as to explain the spectroscopy of guanine and its dimer<sup>[42]</sup>.

Table 4: Geometry parameters and N atom hybridization for the  $M^+PABA^-$  species in the  $D_0$  state. Geometry optimizations were performed at the DFT/B3LYP-D3(BJ)/def2-TZVP level, while NBO calculations were carried out using DFT/B3LYP-D3(BJ)/def2-TZVPP.

	$\angle H_1-N-H_2 ; C'-C_p-C'' / ^\circ$	N-C <sub>p</sub> / Å	C(Carboxylat)-C(aromat) / Å	N atom hybridisation (NBO)	M <sup>+</sup> ...M <sub>ring</sub> / Å	N-H <sub>1</sub> , N-H <sub>2</sub> / Å
Li <sup>+</sup> PABA <sup>-</sup>	0.5	1.330	1.507	sp <sup>2.35</sup>	5.035	1.011, 1.011
Na <sup>+</sup> PABA <sup>-</sup>	0.6	1.332	1.504	sp <sup>2.35</sup>	5.434	1.010, 1.010
K <sup>+</sup> PABA <sup>-</sup>	0.5	1.335	1.500	sp <sup>2.35</sup>	5.856	1.009, 1.009
Rb <sup>+</sup> PABA <sup>-</sup>	0.5	1.336	1.499	sp <sup>2.35</sup>	6.053	1.009, 1.009
Cs <sup>+</sup> PABA <sup>-</sup>	0.6	1.337	1.497	sp <sup>2.35</sup>	6.218	1.008, 1.008
PABA <sup>-</sup>	27.0	1.374	1.456	sp <sup>2.59</sup>	-	1.006, 1.006

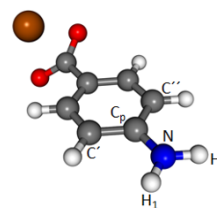


Figure 9: Optimized geometry of an  $M^+PABA^-$  ion in the  $D_0$  state illustrating the angle  $\angle H_1-N-H_2 ; C'-C_p-C''$ .

Within this orbital population analysis, the focus was put on the occupancy of the antibonding  $\sigma^*(N-H_1)$  and  $\sigma^*(N-H_2)$  orbitals. The values obtained for the total orbital populations, determined by summing up both  $\alpha$ - and  $\beta$ -spin occupancies, are given in Table 5.

Table 5: Total ( $\alpha + \beta$ ) orbital occupancies obtained for the antibonding  $\sigma^*(N-H_1)$  and  $\sigma^*(N-H_2)$  orbitals in the  $D_0$  state. The NBO population analysis was performed at the DFT/B3LYP-D3(BJ)/def2-TZVPP level.

	occ. $\sigma^* \text{tot}(N-H_1)$ , occ. $\sigma^* \text{tot}(N-H_2)$
Li <sup>+</sup> PABA <sup>-</sup>	0.00847/ 0.00847
Na <sup>+</sup> PABA <sup>-</sup>	0.00839/ 0.00839
K <sup>+</sup> PABA <sup>-</sup>	0.00829/ 0.00829
Rb <sup>+</sup> PABA <sup>-</sup>	0.00825/ 0.00825
Cs <sup>+</sup> PABA <sup>-</sup>	0.00824/ 0.00824
PABA <sup>-</sup>	0.00774/ 0.00777

Regarding the  $\sigma^*(N-H)$  occupancies a clear trend with an increasing  $\sigma^*(N-H)$  orbital population from Cs<sup>+</sup>PABA<sup>-</sup> to Li<sup>+</sup>PABA<sup>-</sup> is obtained. A “high” occupancy of an antibonding  $\sigma^*(N-H)$  orbital is paralleled with a weakening of the N-H bond and thus with a red-shift of the NH stretching frequency. Keeping in mind that for all  $M^+PABA^-$  ions an almost full planarization of the amino group (see dihedral angles in Table 4) is observed, leading to a blue-shift of the NH stretching frequency, the comparatively high population of the  $\sigma^*(N-H)$ s seems to be decisive, especially in the cases of Li<sup>+</sup>PABA<sup>-</sup> and Na<sup>+</sup>PABA<sup>-</sup>. However, it should also be mentioned that the change in hybridization of the N atom between  $S_0$  and  $D_0$  is less pronounced in the case of Li<sup>+</sup>PABA<sup>-</sup> ( $sp^{2.75} \rightarrow sp^{2.35}$ ) than for ions with a larger cation (for Cs<sup>+</sup>PABA<sup>-</sup>:  $sp^{2.84} \rightarrow sp^{2.35}$ ). Regarding Rb<sup>+</sup>PABA<sup>-</sup> and Cs<sup>+</sup>PABA<sup>-</sup> lower  $\sigma^*(N-H)$  populations and a (compared to Li<sup>+</sup>PABA<sup>-</sup>) relatively strong change in hybridization upon photoionization lead to minor shifts of the NH frequencies upon photoionization. In absence of any  $M^+$  cation (thus for the PABA<sup>-</sup> reference system) the  $\sigma^*(N-H)$ s are only weakly populated which is in accordance with the very high calculated symmetric NH stretching frequency ( $3450 \text{ cm}^{-1}$ ). The described electronic effects are also

reflected by the atomic partial charges and spin densities obtained in the NBO analysis (Tables S4 and S8).

Finally, the NH stretching frequencies in the  $D_0$  state are controlled by a fine interplay between the hybridization character of the N atom of the amino group and the occupancy of the antibonding  $\sigma^*(\text{N-H})$  orbitals. In the  $S_0$  state, the  $\sigma^*(\text{N-H})$  occupancies are considerably lower and almost equal in the order of  $\text{Li}^+\text{PABA}^-$  to  $\text{Cs}^+\text{PABA}^-$  (Table S9). Therefore, it is conceivable that the NH stretching frequencies of the  $\text{M}^+\text{PABA}^-$  ion pairs in the  $S_0$  state mainly depend on the hybridization character of the amino group. Only for the  $\text{PABA}^-$  reference species the  $\sigma^*(\text{N-H})$  population is slightly higher, which is in line with the particularly red-shifted symmetric NH stretching frequency ( $3376\text{ cm}^{-1}$ ) predicted by DFT in this specific case.

Thus, for the  $D_0$  state, there is a correlation between the measured symmetric NH stretching frequencies and the inverse radius of the coordinating alkali ion (Figure 10).

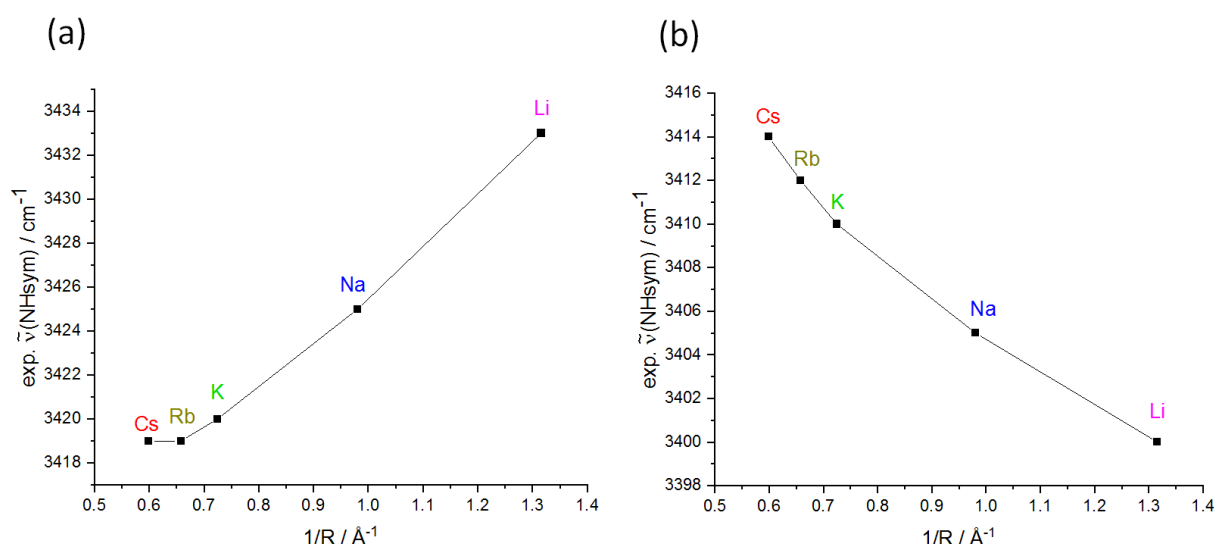


Figure 10: Correlation between the symmetric NH stretching frequencies and the inverse radius of the coordinating alkali ion: a) for the  $S_0$  state; b) for the  $D_0$  state.

This correlation between the NH stretching frequencies (for both the  $S_0$  and  $D_0$  state) and the inverse radius of the coordinating alkali ion is again in accordance with the Coulomb law<sup>[17,18]</sup>. However, the IR spectra recorded for the  $S_0$  and  $D_0$  state interestingly demonstrate that the observed vibrational effects cannot be described by applying the “classical” Stark relationship. Concretely, the blue-shift from  $\text{Li}^+\text{PABA}^-$  to  $\text{Cs}^+\text{PABA}^-$  in the  $D_0$  state and the red-shift between  $\text{Li}^+\text{PABA}^-$  and  $\text{Cs}^+\text{PABA}^-$  observed in the  $S_0$  state clearly show that the classical vibrational Stark approach may not be applicable here. According to the common Stark relationship<sup>[56]</sup>, similar trends for the vibrational frequencies would be obtained in the  $S_0$  and  $D_0$  state IR experiments, since the intrinsic orientation of the electric field relative to the

NH dipoles in the  $S_0$  state is approximately retained in the ionic state. The observed “inversed” trends would thus only be expected in case of a large structural rearrangement (*e.g.* through a change of the binding motif of  $M^+$ ) upon photoionization<sup>[10,9]</sup>, which can however be excluded according to the conformational search performed within DFT. Structures with the  $M^+$  ion being linked to only one O atom of the carboxylate, as well as  $M^+\cdots\pi$ -bound geometries turned out to be no minimum structures or are energetically too high to be further considered.

Finally, the vibrational frequency shifts are not provoked by pure electrostatic effects, but rather by the electronic effects induced through the Coulomb potential of the respective alkali ion. Thus, the spectral trends should rather be explained by considering a “nonclassical” vibrational Stark effect approach.

## Conclusion

In the present work, spectroscopic studies on isolated alkali *para*-aminobenzoate contact ion pairs in a molecular beam are presented. As salts generally have a low vapor pressure and cannot be transferred into the gas phase by simple heating, laser desorption sources like the one used in this study are ideal tools for this purpose.

The focus for this investigation is put on the influence of the type of the alkali cation (by considering  $Li^+$ ,  $Na^+$ ,  $K^+$ ,  $Rb^+$  and  $Cs^+$ ) on the electronic and structural properties of the  $PABA^{-/}$  chromophore. Concerning the cation $\cdots$ anion binding motif, the metal ion is evenly coordinated to both oxygen atoms of the carboxylate group for all studied ion pairs. This means that the observed spectral trends should be mainly due to the change in electric field strength induced by cation substitution. Electronic and vibrational spectra of  $S_0$  and  $D_0$  were obtained by applying 1C/2C-R2PI- and combined IR/UV-laser spectroscopy, respectively. All series of experimental spectra yield clear trends, whereby a deeper understanding of the observed effects is achieved in combination with DFT (B3LYP-D3(BJ)/def2-TZVP(P)) and partly SCS-ADC(2)/def2-TZVP calculations.

Particularly strong electronic effects were observed in the 2C-R2PI spectra (ion yield curves), providing clear estimations regarding ionization potentials, which exhibit impressive red-shifts of up to thousands of wavenumbers upon alkali metal substitution, showing a shift of  $4110\text{ cm}^{-1}$  from  $Li^+$  to  $Cs^+$ . Here, it should also be noted that we present the first ion current curves measured for isolated ion pairs.

Furthermore, IR spectra in the electronic ground state ( $S_0$  state), by applying the IR/R2PI technique, and in the ionic ground state ( $D_0$  state), by using the UV/UV/IR method, were recorded in the NH stretching region, focusing on the relative shifts of the symmetric NH stretching frequency in



dependence of the alkali cation. Hereby, the vibrational probe is thus not directly linked to the alkali ion, but is localized in *para* position relative to the carboxylate group. Thus, the influence of the tuned electric field strength on the NH stretching frequencies can be followed at this larger distance from the cation. Interestingly, opposite trends are observed in the  $S_0$  and  $D_0$  state, which are in perfect accordance with the vibrational frequencies predicted by the DFT calculations. However, a red-shift of the symmetric NH stretching frequency from  $\text{Li}^+\text{PABA}^-$  to  $\text{Cs}^+\text{PABA}^-$  is observed in the  $S_0$  state, while a blue-shift of the same vibrational mode is detected from  $\text{Li}^+\text{PABA}^-$  to  $\text{Cs}^+\text{PABA}^-$  in the  $D_0$  state. It is concluded that the observed effects may not be explained by a “classical” Stark effect approach. Specifically, the obtained effects are rather due to a fine interplay between the hybridization state of the N atom at the amino group and the occupancy of the antibonding  $\sigma^*(\text{NH})$ -orbitals.

Overall, there is a correlation between the relative spectral shifts along the row of alkali ion pairs and the inverse radius of the respective alkali ion. The impact of the Coulomb potential of the cation on the spectroscopic features of the *para*-aminobenzoate chromophore is most pronounced if a small cation with a high charge density is coordinated to it. Thus, the “perturbation” is stronger in the case of  $\text{Li}^+$  than for ion pairs with larger metal cations, like  $\text{Cs}^+$ , and longer metal...chromophore distances. Finally, the size of the coordinating cation is most decisive for the vibronic spectroscopy of the  $\text{PABA}^-$  chromophore.

The presented investigation adds a unique perspective to the electronic and vibrational spectroscopic study of contact ion pairs in gas phase. Furthermore, new possibilities are opened up for the elucidation of ion-radical interaction by molecular beam spectroscopy as well as for the dynamical studies of reactive decarboxylation pathways.

## References

- [1] G. J. Taylor, Y. Luo, K. Hong, S. A. Sarles, R. L. Sacci, B. Doughty, C. P. Collier, *Self-Assembly of Charged Oligomeric Bilayers at the Aqueous/Organic Interface Regulated by Ion-Pair Associations*, **2020**.
- [2] Z. Su, J. J. Leitch, S. Sek, J. Lipkowski, *Langmuir : the ACS journal of surfaces and colloids* **2021**, *37*, 9613.
- [3] a) K. D. Ristroph, R. K. Prud'homme, *Nanoscale advances* **2019**, *1*, 4207; b) R. Wibel, J. D. Friedl, S. Zaichik, A. Bernkop-Schnürch, *European journal of pharmaceutics and biopharmaceutics : official journal of Arbeitsgemeinschaft fur Pharmazeutische Verfahrenstechnik e.V* **2020**, *151*, 73.
- [4] H. R. Bosshard, D. N. Marti, I. Jelesarov, *Journal of molecular recognition : JMR* **2004**, *17*, 1.
- [5] J. S. Prell, M. Demireva, J. Oomens, E. R. Williams, *J. Am. Chem. Soc.* **2009**, *131*, 1232.
- [6] N. C. Polfer, J. Oomens, *Mass spectrometry reviews* **2009**, *28*, 468.
- [7] a) R. Ning, H. Zhou, S.-X. Nie, Y.-F. Ao, D.-X. Wang, Q.-Q. Wang, *Angewandte Chemie (International ed. in English)* **2020**, *59*, 10894; b) M. Retini, F. Bartocchini, G. Zappia, G. Piersanti, *Eur. J. Org. Chem.* **2021**, *2021*, 825.

- [8] Y. Marcus, G. Hefter, *Chemical reviews* **2006**, *106*, 4585.
- [9] J. Hack, D. C. Grills, J. R. Miller, T. Mani, *The journal of physical chemistry. B* **2016**, *120*, 1149.
- [10] T. Mani, D. C. Grills, J. R. Miller, *Journal of the American Chemical Society* **2015**, *137*, 1136.
- [11] a) W. W. Rudolph, D. Fischer, G. Irmer, *Dalton transactions (Cambridge, England : 2003)* **2014**, *43*, 3174; b) J. Kahlen, L. Salimi, M. Sulpizi, C. Peter, D. Donadio, *The journal of physical chemistry. B* **2014**, *118*, 3960.
- [12] S. Habka, V. Brenner, M. Mons, E. Gloaguen, *The journal of physical chemistry letters* **2016**, *7*, 1192.
- [13] a) J. Smiatek, A. Heuer, M. Winter, *Batteries* **2018**, *4*, 62; b) O. Nordness, J. F. Brennecke, *Chemical reviews* **2020**, *120*, 12873.
- [14] D. Strasser, F. Goulay, M. S. Kelkar, E. J. Maginn, S. R. Leone, *The journal of physical chemistry. A* **2007**, *111*, 3191.
- [15] K. Hanke, M. Kaufmann, G. Schwaab, M. Havenith, C. T. Wolke, O. Gorlova, M. A. Johnson, B. P. Kar, W. Sander, E. Sanchez-Garcia, *Physical chemistry chemical physics : PCCP* **2015**, *17*, 8518.
- [16] a) R. Cooper, A. M. Zolot, J. A. Boatz, D. P. Sporleder, J. A. Stearns, *The journal of physical chemistry. A* **2013**, *117*, 12419; b) E. I. Obi, C. M. Leavitt, P. L. Raston, C. P. Moradi, S. D. Flynn, G. L. Vaghjiani, J. A. Boatz, S. D. Chambreau, G. E. Douberty, *The journal of physical chemistry. A* **2013**, *117*, 9047; c) J. Tandy, C. Feng, A. Boatwright, G. Sarma, A. M. Sadoon, A. Shirley, N. D. N. Rodrigues, E. M. Cunningham, S. Yang, A. M. Ellis, *The Journal of chemical physics* **2016**, *144*, 121103.
- [17] D. Müller, P. Nieto, M. Miyazaki, O. Dopfer, *Faraday discussions* **2019**, *217*, 256.
- [18] P. Nieto, D. Müller, A. Sheldrick, A. Günther, M. Miyazaki, O. Dopfer, *Phys. Chem. Chem. Phys.* **2018**, *20*, 22148.
- [19] S. Habka, T. Very, J. Donon, V. Vaquero-Vara, B. Tardivel, F. Charnay-Pouget, M. Mons, D. J. Aitken, V. Brenner, E. Gloaguen, *Physical chemistry chemical physics : PCCP* **2019**, *21*, 12798.
- [20] J. Donon, S. Habka, V. Vaquero-Vara, V. Brenner, M. Mons, E. Gloaguen, *The journal of physical chemistry letters* **2019**, *10*, 7458.
- [21] J. Donon, S. Habka, M. Mons, V. Brenner, E. Gloaguen, *Chemical science* **2021**, *12*, 2803.
- [22] S. D. Fried, S. G. Boxer, *Accounts of chemical research* **2015**, *48*, 998.
- [23] Y. He, C. Wu, W. Kong, *The Journal of chemical physics* **2004**, *121*, 3533.
- [24] G. Meijer, M. S. de Vries, H. E. Hunziker, H. R. Wendt, *The Journal of chemical physics* **1990**, *92*, 7625.
- [25] M. Putter, G. von Helden, G. Meijer, *Chemical Physics Letters* **1996**, *258*, 118.
- [26] D. M. Mitchell, P. J. Morgan, D. W. Pratt, *The journal of physical chemistry. A* **2008**, *112*, 12597.
- [27] I. Compagnon, R. Antoine, D. Rayane, M. Broyer, P. Dugourd, *J. Phys. Chem. A* **2003**, *107*, 3036.
- [28] S. Bakels, S. B. A. Porskamp, A. M. Rijs, *Angew. Chem.* **2019**, *131*, 10647.
- [29] E. Gloaguen, H. Valdes, F. Pagliarulo, R. Pollet, B. Tardivel, P. Hobza, F. Piuze, M. Mons, *The journal of physical chemistry. A* **2010**, *114*, 2973.
- [30] T. Häber, K. Seefeld, K. Kleinermanns, *The journal of physical chemistry. A* **2007**, *111*, 3038.
- [31] M. D. Hanwell, D. E. Curtis, D. C. Lonie, T. Vandermeersch, E. Zurek, G. R. Hutchison, *Journal of cheminformatics* **2012**, *4*, 17.
- [32] A. K. Rappe, C. J. Casewit, K. S. Colwell, W. A. Goddard, W. M. Skiff, *J. Am. Chem. Soc.* **1992**, *114*, 10024.
- [33] a) Becke, *Phys. Rev. A* **1988**, *38*, 3098; b) A. D. Becke, *The Journal of chemical physics* **1993**, *98*, 5648; c) Lee, Yang, Parr, *Physical review. B, Condensed matter* **1988**, *37*, 785.
- [34] S. Grimme, J. Antony, S. Ehrlich, H. Krieg, *The Journal of chemical physics* **2010**, *132*, 154104.

- [35] S. Grimme, S. Ehrlich, L. Goerigk, *Journal of computational chemistry* **2011**, *32*, 1456.
- [36] F. Weigend, R. Ahlrichs, *Phys. Chem. Chem. Phys.* **2005**, *7*, 3297.
- [37] M. J. Frisch, G. W. Trucks, H. B. Schlegel, G. E. Scuseria, M. A. Robb, J. R. Cheeseman, G. Scalmani, V. Barone, B. Mennucci, G. A. Petersson, H. Nakatsuji, M. Caricato, X. Li, H. P. Hratchian, A. F. Izmaylov, J. Bloino, G. Zheng, J. L. Sonnenberg, M. Hada, M. Ehara, K. Toyota, R. Fukuda, J. Hasegawa, M. Ishida, T. Nakajima, Y. Honda, O. Kitao, H. Nakai, T. Vreven, J. A. Montgomery Jr., J. E. Peralta, F. Ogliaro, M. J. Bearpark, J. Heyd, E. N. Brothers, K. N. Kudin, V. N. Staroverov, R. Kobayashi, J. Normand, K. Raghavachari, A. P. Rendell, J. C. Burant, S. S. Iyengar, J. Tomasi, M. Cossi, N. Rega, N. J. Millam, M. Klene, J. E. Knox, J. B. Cross, V. Bakken, C. Adamo, J. Jaramillo, R. Gomperts, R. E. Stratmann, O. Yazyev, A. J. Austin, R. Cammi, C. Pomelli, J. W. Ochterski, R. L. Martin, K. Morokuma, V. G. Zakrzewski, G. A. Voth, P. Salvador, J. J. Dannenberg, S. Dapprich, A. D. Daniels, Ö. Farkas, J. B. Foresman, J. V. Ortiz, J. Cioslowski and D. J. Fox, *Gaussian 09, Revision D.01*, Gaussian, Inc, Wallingford, CT, USA **2009**.
- [38] R. Ahlrichs, M. Bär, M. Häser, H. Horn, C. Kölmel, *Chemical Physics Letters* **1989**, *162*, 165.
- [39] A. E. Reed, L. A. Curtiss, F. Weinhold, *Chemical reviews* **1988**, *88*, 899.
- [40] E. D. Glendening, J. K. Badenhoop, A. E. Reed, J. E. Carpenter, J. A. Bohmann, C. M. Morales, F. Weinhold, *NBO 5.9*, Theoretical Chemistry Institute, University of Wisconsin, Madison, WI, **2009**.
- [41] V. Brenner, E. Gloaguen, M. Mons, *Phys. Chem. Chem. Phys.* **2019**, *21*, 24601.
- [42] P. Hobza, V. Špirko, *Phys. Chem. Chem. Phys.* **2003**, *5*, 1290.
- [43] P. M. Wojciechowski, W. Zierkiewicz, D. Michalska, P. Hobza, *The Journal of chemical physics* **2003**, *118*, 10900.
- [44] a) J. Schirmer, *Phys. Rev. A* **1982**, *26*, 2395; b) A. B. Trofimov, J. Schirmer, *J. Phys. B: At. Mol. Opt. Phys.* **1995**, *28*, 2299.
- [45] P.-F. Loos, A. Scemama, D. Jacquemin, *The journal of physical chemistry letters* **2020**, *11*, 2374.
- [46] a) A. Tajti, L. Tulipán, P. G. Szalay, *Journal of chemical theory and computation* **2020**, *16*, 468; b) C. Hättig in *Advances in Quantum Chemistry*, Elsevier, **2005**, S. 37–60.
- [47] A. Hesselmann, G. Jansen, M. Schütz, *The Journal of chemical physics* **2005**, *122*, 14103.
- [48] C. Hättig, A. Köhn, K. Hald, *The Journal of chemical physics* **2002**, *116*, 5401.
- [49] R. D. Shannon, *Acta Cryst A* **1976**, *32*, 751.
- [50] a) J. Franck, E. G. Dymond, *Trans. Faraday Soc.* **1926**, *21*, 536; b) E. Condon, *Phys. Rev.* **1926**, *28*, 1182.
- [51] A. Fujii, T. Sawamura, S. Tanabe, T. Ebata, N. Mikami, *Chemical Physics Letters* **1994**, *225*, 104.
- [52] R. A. J. O'Hair, N. J. Rijs, *Accounts of chemical research* **2015**, *48*, 329.
- [53] S. Petrie, *International Journal of Mass Spectrometry* **2003**, *227*, 33.
- [54] C. Unterberg, A. Jansen, M. Gerhards, *The Journal of chemical physics* **2000**, *113*, 7945.
- [55] T. Mani, D. C. Grills, M. D. Newton, J. R. Miller, *Journal of the American Chemical Society* **2015**, *137*, 10979.
- [56] S. G. Boxer, *The journal of physical chemistry. B* **2009**, *113*, 2972.

## Electronic Supplementary Information

### Isolated alkali para aminobenzoate ion pairs in the gas phase:

### Clear insights into structural and electronic effects

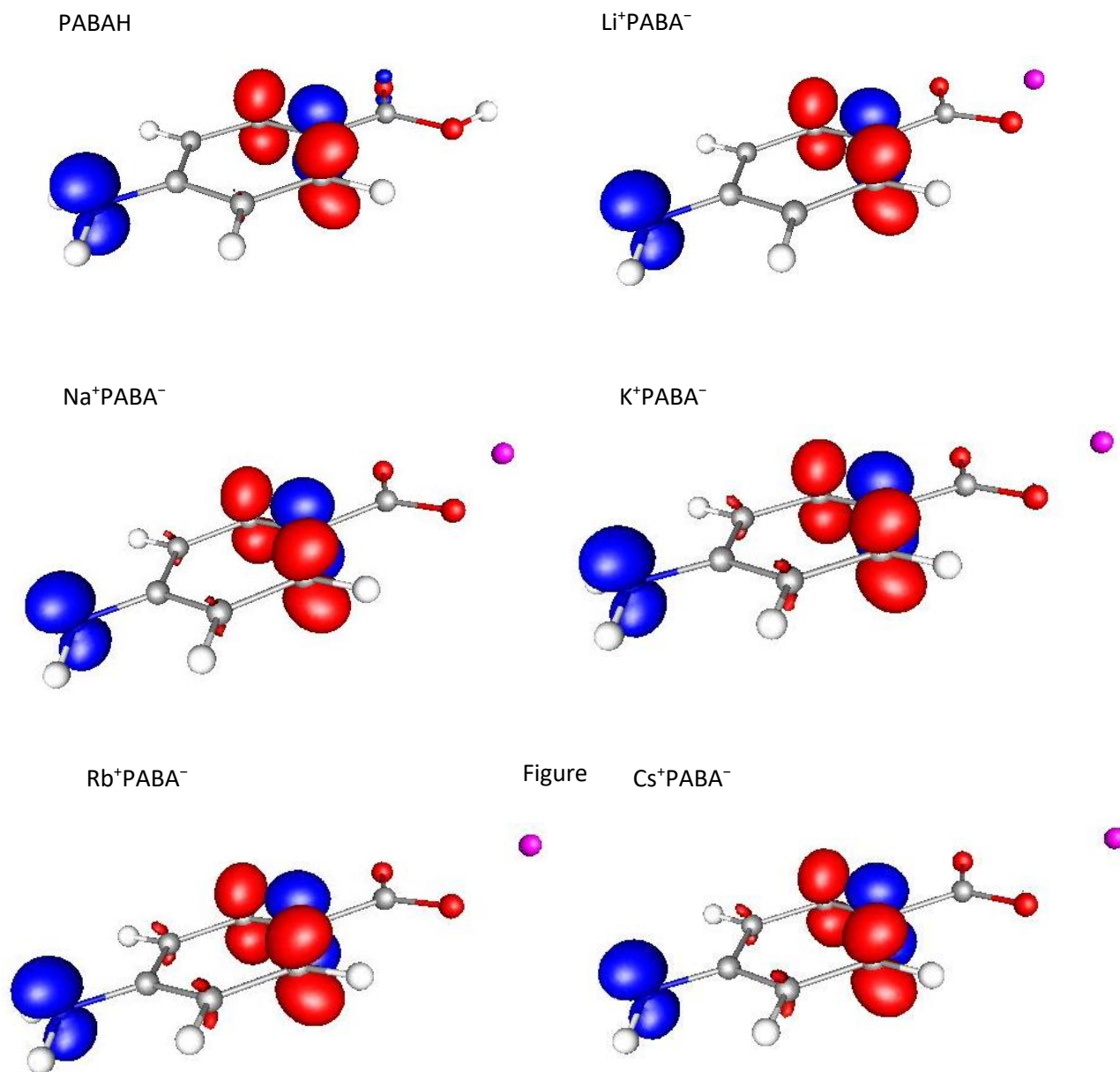
Pol Boden<sup>a</sup>, Christoph Riehn<sup>a\*</sup>

<sup>a</sup>Fachbereich Chemie & State Research Center OPTIMAS, TU Kaiserslautern, Erwin-Schrödinger-Str. 52, D-67663 Kaiserslautern, Germany.

## Content

A) Difference densities based on natural transition orbitals .....	133
B) Geometry parameters and atomic partial charges according to ADC(2) calculations .....	134
C) Cation-anion binding energies according to DFT calculations .....	135
D) Atomic partial charges according to DFT calculations .....	136
E) Experimental and calculated ionization potentials (IPs) .....	137
F) Discussion on the basis of a simplified single point charge model .....	138
G) Measured and predicted NH stretching frequencies for the S <sub>0</sub> state .....	139
H) IR/R2PI spectra .....	141
I) UV/UV/IR spectra .....	142
J) Optimized (DFT) geometries for the detected photofragments .....	143
K) Measured and predicted NH stretching frequencies for the D <sub>0</sub> state .....	144
L) Total spin densities in the D <sub>0</sub> state (DFT) .....	145
M) Orbital occupancies in the S <sub>0</sub> state according to the NBO analysis (DFT) .....	145

## A) Difference densities based on natural transition orbitals



S1: Difference densities for the  $S_1 \leftarrow S_0$  electronic transitions of the PABAH monomer and the  $M^+PABA^-$  alkali ion pairs on the basis of natural transition orbitals (NTOs), as obtained at the SCS-ADC(2)/def2-TZVP level.

## B) Geometry parameters and atomic partial charges according to ADC(2) calculations

Table S1: Geometry parameters in the  $S_0$  and  $S_1$  state, as obtained at the SCS-ADC(2)/def2-TZVP level. The nomenclature proposed in the main manuscript (see figure 2) is applied.

	$S_0$ state				$S_1$ state			
	$\angle \text{H1-N-H2}$ ; $\text{C}'\text{-Cp-C}''$ / $^\circ$	$\text{N-C}_p$ / Å	$\text{C(Carboxylat)-}$ $\text{C(aromat)} / \text{Å}$	$\text{M}^+ \dots \text{M}_{\text{ring}}$ / Å	$\angle \text{H1-N-H2}$ ; $\text{C}'\text{-Cp-C}''$ / $^\circ$	$\text{N-C}_p$ / Å	$\text{C(Carboxylat)-}$ $\text{C(aromat)} / \text{Å}$	$\text{M}^+ \dots \text{M}_{\text{ring}}$ / Å
<b>Li<sup>+</sup>PABA<sup>-</sup></b>	41.4	1.399	1.490	5.003	22.5	1.366	1.486	5.004
<b>Na<sup>+</sup>PABA<sup>-</sup></b>	42.5	1.402	1.500	5.386	24.1	1.368	1.495	5.385
<b>K<sup>+</sup>PABA<sup>-</sup></b>	43.5	1.405	1.506	5.773	25.4	1.369	1.501	5.771
<b>Rb<sup>+</sup>PABA<sup>-</sup></b>	43.6	1.406	1.508	5.940	25.9	1.369	1.502	5.937
<b>Cs<sup>+</sup>PABA<sup>-</sup></b>	43.7	1.406	1.508	6.072	25.8	1.369	1.502	6.074
<b>PABA<sup>-</sup></b>	49.8	1.425	1.546	-	_*	1.451	1.398	-
<b>PABAH</b>	38.5	1.392	1.479	-	17.8	1.362	1.476	-

\*: twisted  $\text{NH}_2$  group in the  $\text{PABA}^-$  geometry

Table S2 (a), (b): Atomic partial charges as obtained from the natural population analysis (NPA) for the (a) ground ( $S_0$ ) and (b) excited ( $S_1$ ) state, performed at the SCS-ADC(2)/def2-TZVP level.

(a)  $S_0$  state

	<b>N</b>	<b>O(1)</b>	<b>O(2)</b>	<b>M<sup>+</sup></b>
<b>Li<sup>+</sup>PABA<sup>-</sup></b>	-0.776	-0.809	-0.809	0.941
<b>Na<sup>+</sup>PABA<sup>-</sup></b>	-0.779	-0.801	-0.801	0.949
<b>K<sup>+</sup>PABA<sup>-</sup></b>	-0.781	-0.801	-0.801	0.969
<b>Rb<sup>+</sup>PABA<sup>-</sup></b>	-0.782	-0.800	-0.800	0.973
<b>Cs<sup>+</sup>PABA<sup>-</sup></b>	-0.782	-0.800	-0.800	0.972
<b>PABA<sup>-</sup></b>	-0.794	-0.744	-0.744	-
<b>PABAH</b>	-0.771	-0.672	-0.564	-

(b)  $S_1$  state

	<b>N</b>	<b>O(1)</b>	<b>O(2)</b>	<b>M<sup>+</sup></b>
<b>Li<sup>+</sup>PABA<sup>-</sup></b>	-0.678	-0.802	-0.802	0.941
<b>Na<sup>+</sup>PABA<sup>-</sup></b>	-0.684	-0.793	-0.793	0.948
<b>K<sup>+</sup>PABA<sup>-</sup></b>	-0.688	-0.792	-0.792	0.967
<b>Rb<sup>+</sup>PABA<sup>-</sup></b>	-0.689	-0.791	-0.791	0.971
<b>Cs<sup>+</sup>PABA<sup>-</sup></b>	-0.689	-0.791	-0.791	0.971
<b>PABA<sup>-</sup></b>	-0.798	-0.458	-0.458	-
<b>PABAH</b>	-0.664	-0.668	-0.552	-

### C) Cation⋯anion binding energies according to DFT calculations

Table S3 (a), (b): Calculated cation⋯anion binding energies for the  $M^+PABA^{-/}$  ion pairs in the (a) ground ( $S_0$ ) and (b) ionic ground ( $D_0$ ) state, obtained at the DFT/B3LYP-D3(BJ)/def2-TZVP level.

#### (a) $S_0$ state

	$M^+⋯PABA^-$ binding energy / $cm^{-1}$
$Li^+PABA^-$	61372
$Na^+PABA^-$	52055
$K^+PABA^-$	44994
$Rb^+PABA^-$	42499
$Cs^+PABA^-$	41281

#### (b) $D_0$ state

	$M^+⋯PABA^-$ binding energy / $cm^{-1}$
$Li^+PABA^-$	28466
$Na^+PABA^-$	20811
$K^+PABA^-$	15780
$Rb^+PABA^-$	14158
$Cs^+PABA^-$	12938

### D) Atomic partial charges according to DFT calculations

Table S4 (a), (b): Atomic partial charges as obtained from the natural bond orbital (NBO) analysis for the (a) electronic ( $S_0$ ) and (b) ionic ( $D_0$ ) ground state, performed at the DFT/B3LYP-D3(BJ)/def2-TZVPP level.

(a)  $S_0$  state

	N	O(1)	O(2)	M <sup>+</sup>
Li <sup>+</sup> PABA <sup>-</sup>	-0.766	-0.826	-0.826	0.941
Na <sup>+</sup> PABA <sup>-</sup>	-0.771	-0.811	-0.812	0.936
K <sup>+</sup> PABA <sup>-</sup>	-0.774	-0.812	-0.812	0.956
Rb <sup>+</sup> PABA <sup>-</sup>	-0.775	-0.811	-0.810	0.950
Cs <sup>+</sup> PABA <sup>-</sup>	-0.774	-0.811	-0.811	0.956
PABA <sup>-</sup>	-0.793	-0.754	-0.754	-
PABAH	-0.759	-0.676	-0.595	-

(b)  $D_0$  state

	N	O(1)	O(2)	M <sup>+</sup>
Li <sup>+</sup> PABA <sup>·</sup>	-0.567	-0.753	-0.753	0.959
Na <sup>+</sup> PABA <sup>·</sup>	-0.586	-0.725	-0.725	0.965
K <sup>+</sup> PABA <sup>·</sup>	-0.603	-0.698	-0.699	0.980
Rb <sup>+</sup> PABA <sup>·</sup>	-0.610	-0.687	-0.687	0.983
Cs <sup>+</sup> PABA <sup>·</sup>	-0.613	-0.682	-0.682	0.983
PABA <sup>·</sup>	-0.377	0.076	0.076	-
PABAH <sup>·</sup>	-0.552	-0.645	-0.502	-



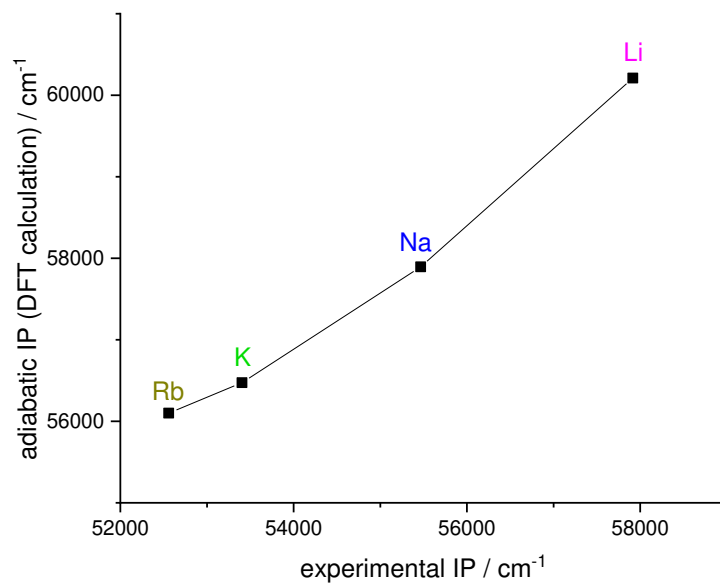
**E) Experimental and calculated ionization potentials (IPs)**

Figure S2: Correlation between the (ZPE-corrected) adiabatic ionization potentials obtained at the DFT/B3LYP-D3(BJ)/def2-TZVP level and the ionization potentials determined within the 2C-R2PI experiments.

## F) Discussion on the basis of a simplified single point charge model

Single point calculations were performed for the isolated  $\text{PABA}^{-/}$  chromophores, whereby the alkali cation was replaced with a simple positive point charge. This was realized by using the “Charge” option of Gaussian 09. The SCF energies obtained herein are plotted in figure S3 for both the  $S_0$  and  $D_0$  states ( $\text{PABA}^-$  and  $\text{PABA}^{\cdot}$ ).

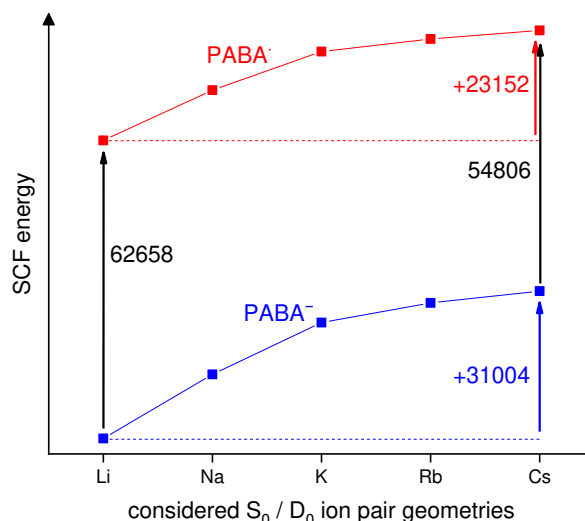


Figure S3: Single point SCF energies obtained for the  $\text{PABA}^-$  and  $\text{PABA}^{\cdot}$  species in the presence of a positive point charge, replacing the respective alkali ion. Hereby, the optimized (DFT) ion pair geometries were considered. All indicated energy values and the considered geometries were obtained at the DFT/B3LYP-D3(BJ)/def2-TZVP level.

As the optimized ion pair geometries were considered, the distance between the point charge and the carboxylate of  $\text{PABA}^-$  successively increases from the  $\text{Li}^+$ - to the  $\text{Cs}^+$ -species, provoking a destabilization of  $\text{PABA}^-$  by  $31004 \text{ cm}^{-1}$  along the series. For  $\text{PABA}^{\cdot}$  a similar trend is observed, which is however less pronounced (with  $23152 \text{ cm}^{-1}$ ) due to the absence of a negative charge to be stabilized by a cationic counterion. Owing to these electrostatic effects, the energetic gap separating both curves in figure S3 decreases from  $62658 \text{ cm}^{-1}$  for the  $\text{Li}^+$  geometries to  $54806 \text{ cm}^{-1}$  for the  $\text{Cs}^+$  geometries. Other effects such as the energetic differences caused by varying  $\text{PABA}^{-/}$  geometries along the considered row (from the  $\text{Li}^+$  to  $\text{Cs}^+$  geometries) play a minor role, as they lead to energetic shifts of merely about  $1000\text{-}1500 \text{ cm}^{-1}$ . Thus, the (almost) pure electrostatic effect, illustrated by the described simplified approach, should further explain the red-shift observed for the IPs along the series from the  $\text{Li}^+$ - to the  $\text{Cs}^+$ -species, whereby the size of the coordinating cation plays a crucial role.

### G) Measured and predicted NH stretching frequencies for the $S_0$ state

Table S5: Experimental ( $\nu(\text{NH}_{\text{sym}}\text{exp.})$  and  $\nu(\text{NH}_{\text{asym}}\text{exp.})$ ) as well as calculated ( $\nu(\text{NH}_{\text{sym}}\text{theo.})$  and  $\nu(\text{NH}_{\text{asym}}\text{theo.})$ , scaled by 0.963) symmetric and asymmetric NH stretching frequencies for the electronic ground state ( $S_0$ ), as obtained at the DFT/B3LYP-D3(BJ)/def2-TZVP level. The predicted IR intensities (Int.) are also given.

	$\nu(\text{NH}_{\text{sym}}\text{exp.}) / \text{cm}^{-1}$	$\nu(\text{NH}_{\text{sym}}\text{theo.}) / \text{cm}^{-1}$	Int. / $\text{km}\cdot\text{mol}^{-1}$	$\nu(\text{NH}_{\text{asym}}\text{exp.}) / \text{cm}^{-1}$	$\nu(\text{NH}_{\text{asym}}\text{theo.}) / \text{cm}^{-1}$	Int. / $\text{km}\cdot\text{mol}^{-1}$
PABAH	3446	3441	50	3540	3540	23
PABA <sup>-</sup>	-	3382	0	-	3461	2
Li <sup>+</sup> PABA <sup>-</sup>	3433	3433	32	3522	3522	17
Na <sup>+</sup> PABA <sup>-</sup>	3425	3425	23	-	3513	14
K <sup>+</sup> PABA <sup>-</sup>	3420	3421	18	-	3507	13
Rb <sup>+</sup> PABA <sup>-</sup>	3419	3419	17	-	3505	12
Cs <sup>+</sup> PABA <sup>-</sup>	3419	3420	18	-	3506	12

Table S6: Experimental ( $\nu(\text{NH}_{\text{sym}}\text{exp.})$  and  $\nu(\text{NH}_{\text{asym}}\text{exp.})$ ) as well as calculated ( $\nu(\text{NH}_{\text{sym}}\text{theo.})$  and  $\nu(\text{NH}_{\text{asym}}\text{theo.})$ , scaled by 0.969) symmetric and asymmetric NH stretching frequencies for the electronic ground state ( $S_0$ ), as obtained at the SCS-ADC(2)/def2-TZVP level. The predicted IR intensities (Int.) are also given.

	$\nu(\text{NH}_{\text{sym}}\text{exp.}) / \text{cm}^{-1}$	$\nu(\text{NH}_{\text{sym}}\text{theo.}) / \text{cm}^{-1}$	Int. / $\text{km}\cdot\text{mol}^{-1}$	$\nu(\text{NH}_{\text{asym}}\text{exp.}) / \text{cm}^{-1}$	$\nu(\text{NH}_{\text{asym}}\text{theo.}) / \text{cm}^{-1}$	Int. / $\text{km}\cdot\text{mol}^{-1}$
PABAH	3446	3443	40	3540	3547	22
PABA <sup>-</sup>	-	3394	0	-	3489	4
Li <sup>+</sup> PABA <sup>-</sup>	3433	3433	25	3522	3535	16
Na <sup>+</sup> PABA <sup>-</sup>	3425	3429	19	-	3529	14
K <sup>+</sup> PABA <sup>-</sup>	3420	3425	15	-	3525	13
Rb <sup>+</sup> PABA <sup>-</sup>	3419	3424	14	-	3524	12
Cs <sup>+</sup> PABA <sup>-</sup>	3419	3424	14	-	3523	12

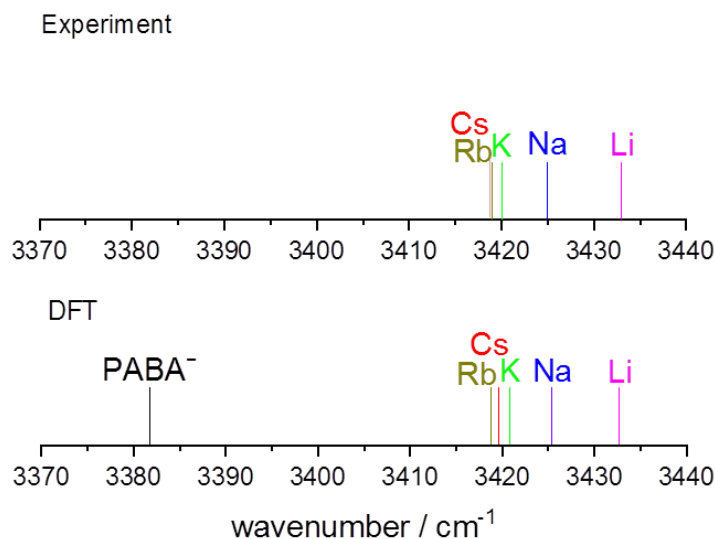


Figure S4: Comparison between the measured symmetric NH stretching frequencies (IR/R2PI experiments) and the values predicted by DFT calculations (DFT/B3LYP-D3(BJ)/def2-TZVP; scal.: 0.963) for the electronic ground state ( $S_0$ ). Please note that the depicted sticks do not represent the predicted or measured IR intensities.

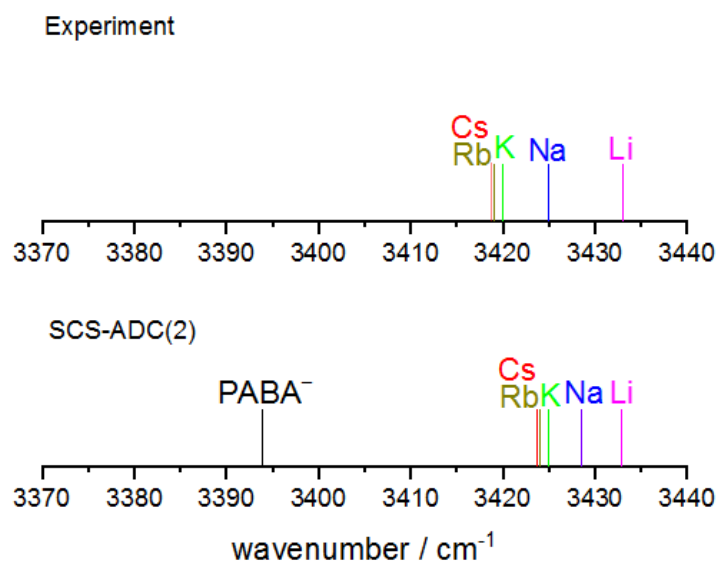


Figure S5: Comparison between the measured symmetric NH stretching frequencies (IR/R2PI experiments) and the values predicted by SCS-ADC(2)/def2-TZVP calculations (scal.: 0.969) for the electronic ground state ( $S_0$ ). Please note that the depicted sticks do not represent the predicted or measured IR intensities.

### Remark on the calculated NH stretching frequencies in the $S_0$ state

As we opted for the SCS-ADC(2) approach in order to calculate adiabatic excitation energies, geometry optimizations as well as (numerical) harmonic frequency calculations were also performed at this level. Thus, it was guaranteed that the obtained geometries are indeed minimum structures, so that the excitation energies could be deduced on the basis of these structures.

The NH stretching frequencies obtained at the SCS-ADC(2)/def2-TZVP level yield the same trend as the experimental IR spectra and the DFT predictions. But interestingly, the experimental trends observed for the symmetric NH stretching frequencies in the  $S_0$  state are better reflected by DFT than by the computationally more expansive SCS-ADC(2) calculations.

### H) IR/R2PI spectra

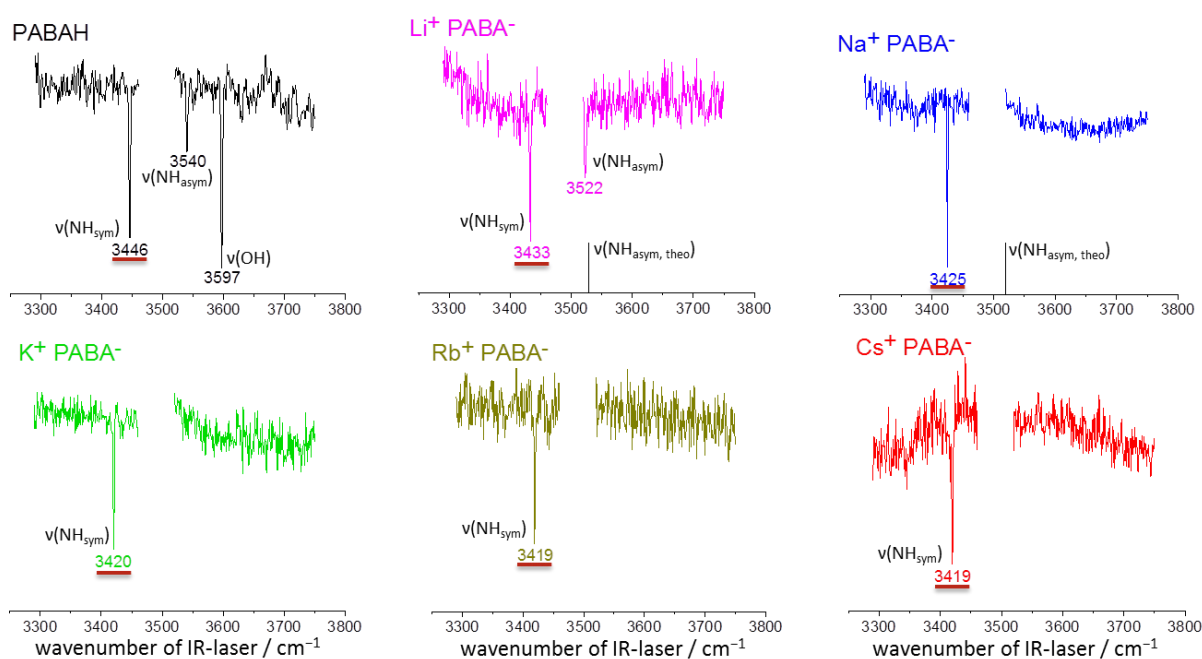


Figure S6: IR/R2PI spectra for the para aminobenzoic acid monomer (PABAH) and its alkali ion pairs  $M^+PABA^-$ , measured *via* the respective  $0_0^0$  transitions. The stick spectra added for  $Li^+PABA^-$  and  $Na^+PABA^-$  illustrate that the asymmetric NH stretching frequency  $\nu(NH_{asym})$  is to be expected in the spectral gap of the applied DFM1/OPA laser system ( $3460\text{--}3520\text{ cm}^{-1}$ ) for  $Na^+PABA^-$  (and all ion pairs with larger alkali ions).

## I) UV/UV/IR spectra

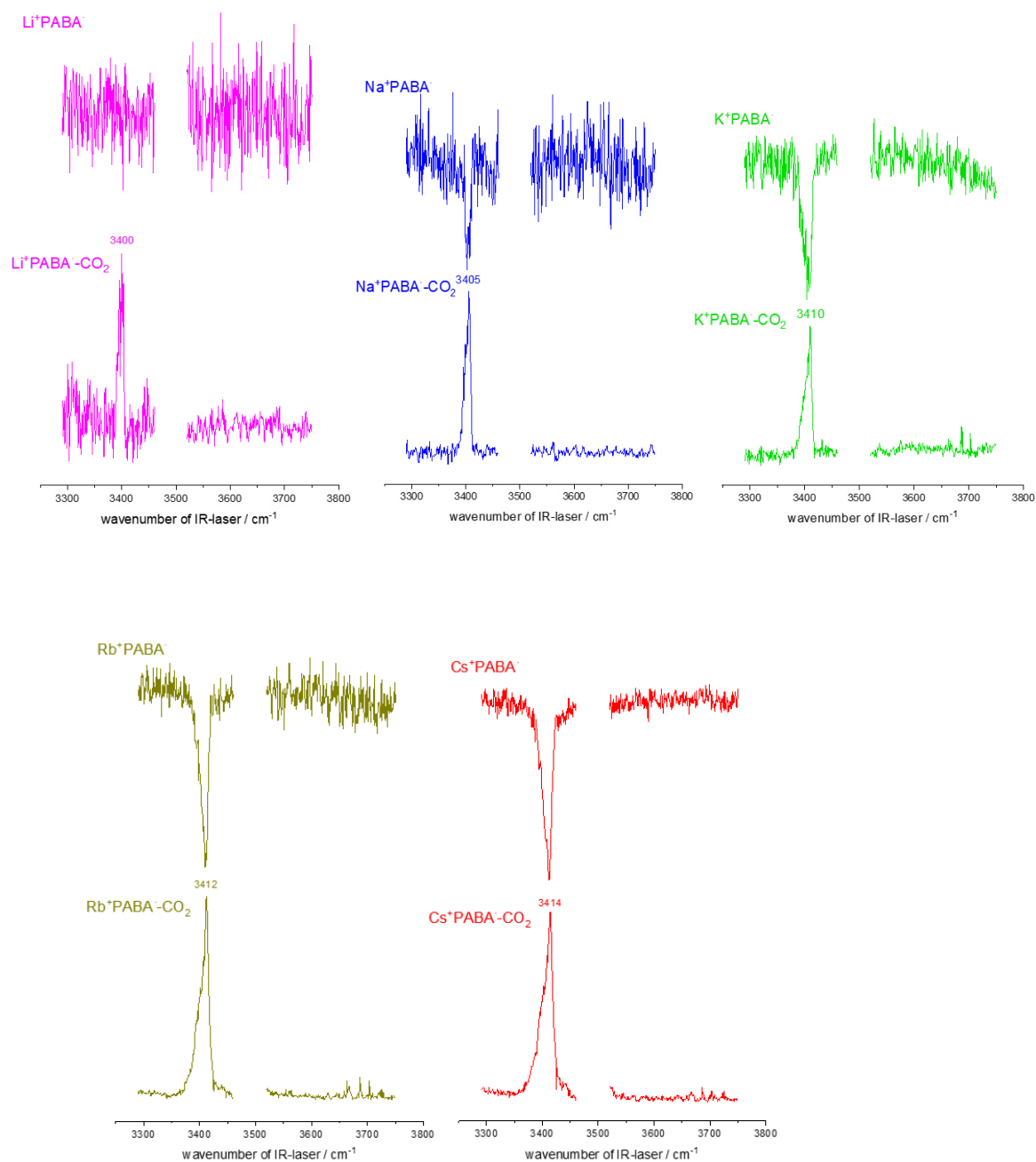
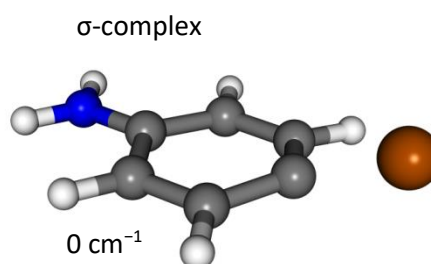
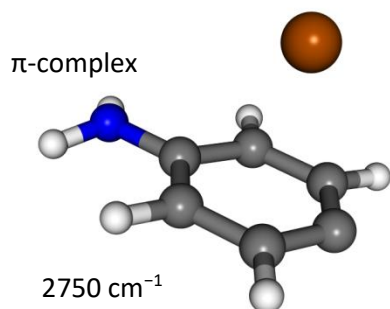


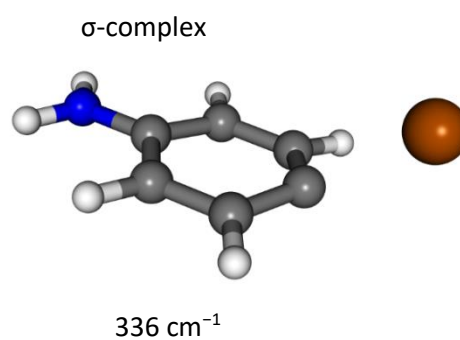
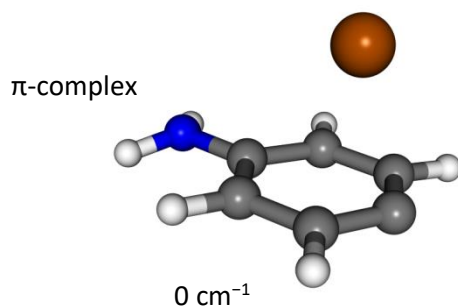
Figure S7: UV/UV/IR spectra for the  $M^+PABA^-$  ions, measured *via* the respective  $0_0^0$  transitions. It should be noted that the minor peaks on the fragment mass traces  $K^+PABA^-CO_2$ ,  $Rb^+PABA^-CO_2$  and  $Cs^+PABA^-CO_2$  around  $3700\text{ cm}^{-1}$  result from non-resonant IR-photodissociation due to intensity peaks of the IR laser power in that spectral region. The asymmetric NH stretching bands may be found in the spectral gap of the applied DFM1/OPA laser system or do not lead to efficient IR fragmentation.

### J) Optimized (DFT) geometries for the detected photofragments

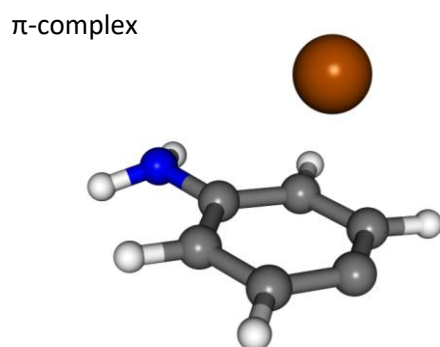
Li<sup>+</sup>PABA<sup>-</sup>-CO<sub>2</sub>



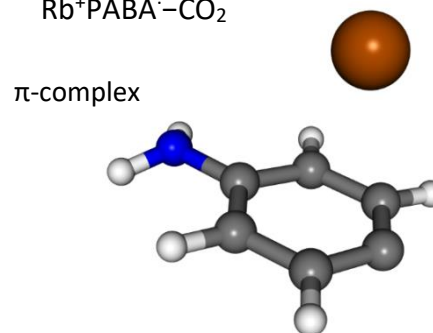
Na<sup>+</sup>PABA<sup>-</sup>-CO<sub>2</sub>



K<sup>+</sup>PABA<sup>-</sup>-CO<sub>2</sub>



Rb<sup>+</sup>PABA<sup>-</sup>-CO<sub>2</sub>



Cs<sup>+</sup>PABA<sup>-</sup>-CO<sub>2</sub>

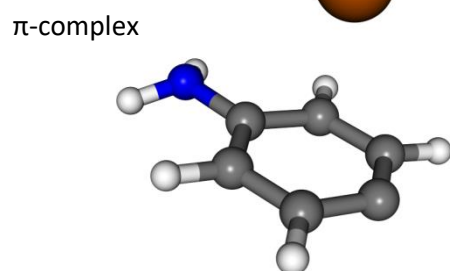


Figure S8: Optimized DFT (B3LYP-D3(BJ)/def2-TZVP) geometries for the M<sup>+</sup>PABA<sup>-</sup>-CO<sub>2</sub> fragments formed by IR photodissociation.

### K) Measured and predicted NH stretching frequencies for the D<sub>0</sub> state

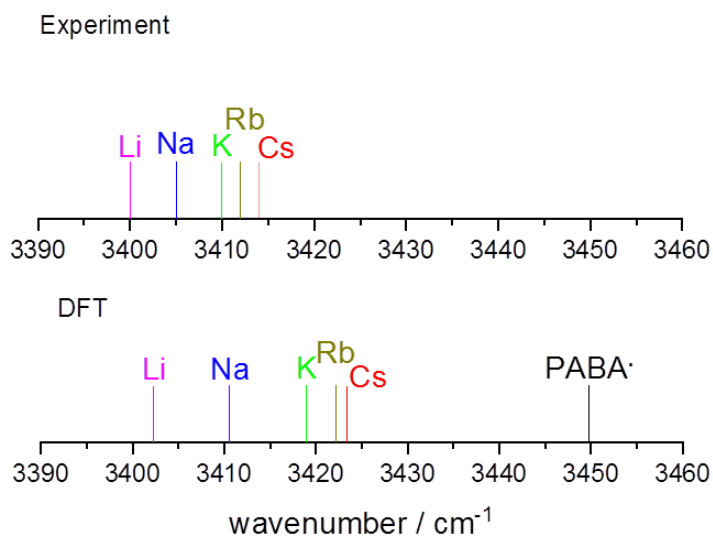


Figure S9: Comparison between the measured symmetric NH stretching frequencies (UV/UV/IR experiments) and the values predicted by DFT calculation (DFT/B3LYP-D3(BJ)/def2-TZVP; scal.: 0.963) for the electronic ground state (D<sub>0</sub>). Please note that the depicted sticks do not represent the predicted or measured IR intensities.

Table S7: Experimental ( $\nu(\text{NH}_{\text{symexp.}})$  and  $\nu(\text{NH}_{\text{asymexp.}})$ ) as well as calculated ( $\nu(\text{NH}_{\text{symtheo.}})$  and  $\nu(\text{NH}_{\text{asymtheo.}})$ , scaled by 0.963) symmetric and asymmetric NH stretching frequencies for the ionic ground state (D<sub>0</sub>). Frequency calculations were performed at the DFT/B3LYP-D3(BJ)/def2-TZVP level. The predicted IR intensities (Int.) are also given.

	$\nu(\text{NH}_{\text{symexp.}}) / \text{cm}^{-1}$	$\nu(\text{NH}_{\text{symtheo.}}) / \text{cm}^{-1}$	Int. / $\text{km}\cdot\text{mol}^{-1}$	$\nu(\text{NH}_{\text{asymexp.}}) / \text{cm}^{-1}$	$\nu(\text{NH}_{\text{asymtheo.}}) / \text{cm}^{-1}$	Int. / $\text{km}\cdot\text{mol}^{-1}$
PABAH <sup>+</sup>	-	3393	322	-	3499	95
PABA <sup>•</sup>	-	3450	68	-	3551	28
Li <sup>+</sup> PABA <sup>•</sup>	3400	3402	298	-	3509	88
Na <sup>+</sup> PABA <sup>•</sup>	3405	3411	294	-	3519	85
K <sup>+</sup> PABA <sup>•</sup>	3410	3419	474	-	3529	78
Rb <sup>+</sup> PABA <sup>•</sup>	3412	3422	499	-	3532	76
Cs <sup>+</sup> PABA <sup>•</sup>	3414	3423	522	-	3534	75



### L) Total spin densities in the D<sub>0</sub> state (DFT)

Table S8: Total spin densities on the N and O atoms, as obtained from the natural bond orbital (NBO) analysis, performed at the DFT/B3LYP-D3(BJ)/def2-TZVPP level.

	N atom spin density	O <sub>1</sub> , O <sub>2</sub> spin density
PABAH <sup>+</sup>	-0.00092	0.52928, 0.52916
PABA <sup>-</sup>	0.33058	0.00181, 0.07906
Li <sup>+</sup> PABA <sup>-</sup>	0.31696	0.03044, 0.03044
Na <sup>+</sup> PABA <sup>-</sup>	0.29084	0.05871, 0.05995
K <sup>+</sup> PABA <sup>-</sup>	0.26559	0.09405, 0.09163
Rb <sup>+</sup> PABA <sup>-</sup>	0.25590	0.10706, 0.10692
Cs <sup>+</sup> PABA <sup>-</sup>	0.25175	0.11262, 0.11305


### M) Orbital occupancies in the S<sub>0</sub> state according to the NBO analysis (DFT)

Table S9: Orbital occupancies obtained for the antibonding  $\sigma^*(\text{N-H}_1)$  and  $\sigma^*(\text{N-H}_2)$  orbitals in the S<sub>0</sub> state. The NBO population analysis was performed at the DFT/B3LYP-D3(BJ)/def2-TZVPP level.

	occ. $\sigma^*$ tot(N-H <sub>1</sub> ), occ. $\sigma^*$ tot(N-H <sub>2</sub> )
PABAH	0.00776/0.00777
PABA <sup>-</sup>	0.00791/ 0.00791
Li <sup>+</sup> PABA <sup>-</sup>	0.00778/ 0.00778
Na <sup>+</sup> PABA <sup>-</sup>	0.00774/ 0.00776
K <sup>+</sup> PABA <sup>-</sup>	0.00774/ 0.00774
Rb <sup>+</sup> PABA <sup>-</sup>	0.00775/0.00771
Cs <sup>+</sup> PABA <sup>-</sup>	0.00773/ 0.00775

## 7.2 Publication [2]

**Reprint License****Chromone-methanol clusters in the electronic ground and lowest triplet state: a delicate interplay of non-covalent interactions**

P. Boden, P. H. Strebert, M. Meta, F. Dietrich, C. Riehn and M. Gerhards, *Phys. Chem. Chem. Phys.*, 2022, **24**, 15208 DOI: 10.1039/D2CP01341J 

To request permission to reproduce material from this article, please go to the [Copyright Clearance Center request page](#).

If you are an author contributing to an RSC publication, you do not need to request permission provided correct acknowledgement is given.

If you are the author of this article, you do not need to request permission to reproduce figures and diagrams provided correct acknowledgement is given. If you want to reproduce the whole article in a third-party publication (excluding your thesis/dissertation for which permission is not required) please go to the [Copyright Clearance Center request page](#).

Read more about [how to correctly acknowledge RSC content](#).


 Cite this: *Phys. Chem. Chem. Phys.*,  
2022, 24, 15208

# Chromone–methanol clusters in the electronic ground and lowest triplet state: a delicate interplay of non-covalent interactions†

 Pol Boden,<sup>‡a</sup> Patrick H. Strebert,<sup>‡a</sup> Marcel Meta,<sup>a</sup> Fabian Dietrich,<sup>§\*ab</sup>  
Christoph Riehn,<sup>§\*a</sup> and Markus Gerhards,<sup>§a</sup>

Chromone offers two energetically almost equivalent docking sites for alcohol molecules, in which the hydroxyl group is hydrogen bonded to one of the free electron pairs of the carbonyl O atom. Here, the delicate balance between these two competing arrangements is studied by combining IR/R2PI and UV/IR/UV spectroscopy in a molecular beam supported by quantum-chemical calculations. Most interestingly, chromone undergoes an efficient intersystem crossing into the triplet manifold upon electronic excitation, so that the studies on aromatic molecule–solvent complexes are for the first time extended to such a cluster in a triplet state. As the lowest triplet state ( $T_1$ ) is of ground state character, powerful energy decomposition approaches such as symmetry-adapted perturbation theory (SAPT) and local energy decomposition using the domain-based local pair natural orbital coupled–cluster method (DLPNO–CCSD(T)/LED) are applied. From the theoretical analysis we infer for the  $T_1$  state a loss of planarity (puckering) of the 4-pyrone ring of the chromone unit, which considerably affects the interplay between different types of non-covalent interactions at the two possible binding sites.

 Received 21st March 2022,  
Accepted 11th May 2022

DOI: 10.1039/d2cp01341j

[rsc.li/pccp](https://rsc.li/pccp)

## Introduction

The role of dispersion interactions in chemistry has been underestimated for a long time. However, they have meanwhile turned out to play an important role in understanding the binding behavior of molecules, which is of fundamental importance for, *e.g.*, (bio)chemical processes and catalysis.<sup>1</sup> The so-called “London dispersion” appears as an attractive potential between non-polar molecules or molecular parts and is balanced by Pauli repulsion at short distances. Due to the nature of London dispersion being cumulative and nearly pairwise additive with respect to the size of the molecule, the importance of this interaction for large molecules cannot be understated. For medium-sized molecules, especially molecular clusters, they also represent a key factor to determine structural preferences. Thus, it is imperative to investigate dispersion-bound systems for developing and enhancing theoretical models, which can then be applied to more complex systems. A promising path

is the investigation of molecular clusters, which represent balances for exploration of the different binding motifs and sites for small solvent molecules. For this purpose, so-called “solvation balances” were extensively studied on complexes between aromatic ether molecules (diphenyl ether, phenyl vinyl ether, different furans) and various alcohols,<sup>2–8</sup> combining several spectroscopic methods (FTIR, IR/UV, MW) in molecular beam experiments. Furthermore, studies of the carbonyl solvation balances have been launched by the Suhm group.<sup>9</sup> They investigated aggregates between acetophenone derivatives (with varying alkyl substituents) and various alcohols (with different alkyl residues) by FTIR spectroscopy in molecular jet experiments combined with DFT-based theoretical studies.<sup>10</sup> In the same context, they also analyzed pinacolone–alcohol clusters,<sup>11</sup> as well as phenol–halogenated acetophenone complexes.<sup>12</sup> Other work on ketone–solvent complexes<sup>13</sup> in the gas phase comprises studies on complexes between camphor and various H-bond donor molecules<sup>14</sup> and investigations of fenchone–solvent aggregates<sup>15</sup> (phenol/benzene *vs.* water/ethanol).

All these studies are focused on molecular aggregates in the electronic ground state ( $S_0$ ). In contrast, the studies of dispersion interactions in electronically excited states are scarce.<sup>16</sup> Fabrizio *et al.*<sup>17</sup> show the importance of dispersion for photochemical processes in molecular switches in a computational study. Further theoretical studies on excited state properties are limited to small clusters, *e.g.* ethene–argon or formaldehyde–methane.<sup>18</sup> In that

<sup>a</sup> *Fachbereich Chemie & State Research Center OPTIMAS, TU Kaiserslautern, Erwin-Schrödinger-Str. 52, D-67663 Kaiserslautern, Germany*
<sup>b</sup> *Núcleo Milenio MultiMat & Departamento de Ciencias Físicas, Universidad de La Frontera, Temuco, Chile. E-mail: fabian.dietrich@ufrontera.cl*
<sup>†</sup> Electronic supplementary information (ESI) available. See DOI: <https://doi.org/10.1039/d2cp01341j>
<sup>‡</sup> P. B. and P. H. S. contributed equally to this work.

<sup>§</sup> In memoriam of Markus Gerhards, who passed away 28.12.2020.

context, a cross-reference should be given to exciplexes, although only weakly-bound in the ground state and often dominated by charge transfer interactions in the excited state, are related to this topic.<sup>19</sup> The aforementioned investigations on diphenyl ether (DPE) with methanol<sup>8,20</sup> and *tert*-butanol<sup>2</sup> have also been applied towards the excited state (here  $S_1$ ). However, a quantification of the dispersion or other interactions was not possible, since the established energy decomposition methods are yet limited to studies on electronic ground states, while their application to electronically excited-states is still under development.

Extending the investigation of microsolvated ketones to electronically excited states, we here study aggregates between chromone, *i.e.*, 1,4-benzopyrone (an isomer of coumarin), and methanol both in the electronic ground state ( $S_0$ ) as well as in the lowest triplet state ( $T_1$ ). Similar to the structurally related xanthone,<sup>21</sup> chromone undergoes a fast and efficient intersystem crossing into the triplet manifold<sup>22</sup> after electronic excitation, which may thus also be expected for the chromone–methanol aggregates. The advantage (for theoretical studies) of investigating the  $T_1$  state (in contrast to  $S_1/S_2$ ) lies in its ground state, *i.e.*, lowest energy triplet state, character giving the opportunity to apply powerful energy decomposition analysis approaches, like SAPT<sup>23,24</sup> (symmetry-adapted perturbation theory) and DLPNO-CCSD(T)/LED<sup>25–27</sup> (local energy decomposition domain-based local pair natural orbital coupled-cluster method).

In the chromone–MeOH complexes produced in our molecular beam experiments, the chromone unit acts as a UV chromophore within the complex providing the possibility for two-photon ionization, a prerequisite for the applied R2PI (resonant two-photon ionization) and IR/R2PI (infrared/resonant two-photon ionization) spectroscopy. The electronically excited state is accessible by the related UV(excitation)/IR/UV(ionization) technique, which has been used in our group for the investigation of (among others) xanthone<sup>21</sup>( $T_1$ ), 3-hydroxychromone<sup>28</sup> ( $S_1$ ) and DPE–solvent clusters ( $S_1$ ).<sup>2,5,6,8,20</sup>

Within the chromone–MeOH complexes, the decisive structural element is given by the two free electron pairs of the carbonyl group, which exhibit distinct stabilization by a fine interplay between electrostatic H-bond interactions (mainly due to coordination of the OH group to a carbonyl O lone pair) and dispersion interactions (including C–H...O contacts involving the OH group of methanol and the C–H groups of the chromone unit). For illustration, the relevant binding sites, which will be named “inside pocket” and “outside pocket” in the following, are sketched in Fig. 1. The main goals of our investigation are now: is it possible to assign a preference for one of the binding sites by spectroscopy and quantum chemical calculations and does this preference change upon electronic excitation?

The choice of chromone also eliminates a theoretical challenge: due to very similar docking sites on the chromone unit, similar ZPVE (zero point vibrational energy) values can be expected for both binding sites, resulting in nearly complete error cancellation for the ZPVE. This aspect is a major difference compared to previous studies<sup>2–6,8,20</sup> which elucidate the subtle energetic balances between isomers of the distinct binding motifs OH...O and OH... $\pi$ .

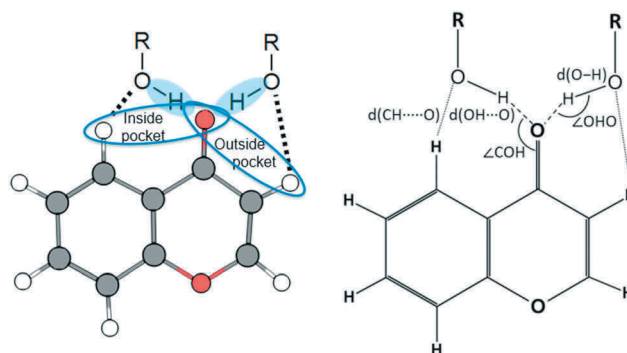


Fig. 1 Left: Schematic depiction of the chromone–solvent cluster with the “inside” and “outside” pocket, stabilized by secondary C–H...O contacts. Right: Lewis structure of the chromone–solvent cluster with selected geometry parameters.

Finally, our studies on the competition between electrostatic, induction and dispersion interactions, combining molecular beam experiments and quantum theory, are for the first time extended to aromatic molecule–solvent complexes in an electronically excited triplet state. The major quest is to compare the importance of these interactions in different electronic states with regards to relative isomer stabilities and the structural consequences for hydrogen-bonded aggregates.

## Experimental methods

The experimental setup for IR/UV experiments is described in detail elsewhere,<sup>29</sup> thus only a brief description is given here. All experiments were carried out in a molecular beam apparatus consisting of a differentially pumped linear time-of-flight (TOF) mass spectrometer with a pulsed valve (General Valve Iota One, 500  $\mu\text{m}$  orifice) for skimmed jet expansion. Chromone was purchased from Sigma-Aldrich (99%) and used without further purification. Methanol (Merck, 99.9%) was supplied *via* a cooled reservoir ( $-16\text{ }^\circ\text{C}$ ) and co-expanded with chromone (heated up to  $35\text{ }^\circ\text{C}$ ) using neon as carrier gas (3.0 bar).

For the two-color R2PI, IR/R2PI and UV/IR/UV experiments up to three tunable nanosecond laser systems are used: two independent UV laser systems and one IR laser system. The UV laser radiation is generated by second-harmonic generation in a BBO crystal using the output of a dye laser (Sirah, Precision-Scan) pumped by the second or third harmonic ( $\lambda = 532, 355\text{ nm}$ ) of a Nd:YAG laser (Spotlight 1000 or 1000.2, Innolas). IR radiation in the region of  $3130\text{--}3750\text{ cm}^{-1}$  is generated with a LiNbO<sub>3</sub> crystal by difference frequency mixing (DFM) of the fundamental ( $\lambda = 1064\text{ nm}$ ) of a seeded Nd:YAG laser (Pro 230, Spectra Physics) and the output of the dye laser pumped by the second harmonic ( $\lambda = 532\text{ nm}$ ) of the same Nd:YAG laser. The obtained IR radiation is amplified by using an optical parametric amplification (OPA) process in a further LiNbO<sub>3</sub> crystal using the DFM output and again the fundamental ( $\lambda = 1064\text{ nm}$ ) of the Nd:YAG laser.

The two-color R2PI spectra were recorded using two unfocused UV lasers. For all experiments, the UV ionization laser

( $\approx 0.3$  mJ pulse $^{-1}$ ) is fired 70 ns after the UV excitation laser ( $\approx 1$  mJ pulse $^{-1}$ ). For the IR/R2PI spectra, the tuned IR laser ( $\approx 8$  mJ pulse $^{-1}$ ) is fired 50 ns prior to the UV excitation laser, whereas for the UV/IR/UV spectra the IR laser is fired 20 ns after the UV excitation laser to avoid temporal overlap of the laser pulses.

## Computational methods

For the theoretical approach, starting geometries for chromone–methanol clusters were obtained using the CREST algorithm<sup>30</sup> by the Grimme group. Calculations of the ground state and electronically excited states were performed using (TD)DFT. We choose the CAM-B3LYP<sup>31</sup> as functional, def2-TZVP<sup>32–34</sup> as basis set and used Grimme's D3 correction<sup>35</sup> with Becke–Johnson damping<sup>36</sup> to account for dispersion interaction. Geometry optimizations were carried out using the Bery algorithm in Gaussian 16<sup>37</sup> and calculating energies and gradients with Turbomole 7.5.<sup>38</sup> A subsequent harmonic frequency calculation was used to check for imaginary frequencies confirming a minimum structure. Harmonic frequencies for excited state geometries were computed using the NumForce script with the option “–central”. All harmonic frequencies were corrected with a scaling factor of 0.95.<sup>39</sup>

Relaxed scans of the potential energy surface in the electronic ground state and excited triplet state were performed to estimate the isomerization barrier between the “inside” and “outside” structure by variation of the COH angle.

Energy decomposition calculations were performed using the SAPT0<sup>23,40</sup> method implemented in Psi4<sup>41</sup> using the basis set jun-cc-pVDZ.<sup>24</sup> A second approach used the DLPNO-CCSD(T)/LED<sup>25–27,42</sup> method implemented in Orca 5.0.0.<sup>43</sup> As basis set def2-TZVP<sup>32–34</sup> was chosen, furthermore the “TightPNO” option was selected.

## Results and discussion

### Theoretical results

Chromone provides multiple possible binding sites for interactions with solvent molecules, namely the carbonyl oxygen, the ether oxygen and the  $\pi$ -system of the aromatic moiety. We thus distinguish between OH $\cdots$ O(carbonyl), OH $\cdots$ O(ether) and OH $\cdots\pi$  structures. As expected from chemical intuition, coordination to the polar carbonyl group, exhibiting a relatively large dipole moment, is energetically preferred over coordination to the ether group or the aromatic  $\pi$ -system. This is confirmed by geometry optimizations using CAM-B3LYP-D3(BJ)/def2-TZVP predicting two nearly isoenergetic OH $\cdots$ O(carbonyl) structures for the chromone–methanol cluster as shown in Fig. 2, omitting the corresponding enantiomers obtained by using the chromone plane as a mirror plane. All other structures show significantly higher relative energies (OH $\cdots$ O(ether),  $\Delta E > 19.6$  kJ mol $^{-1}$ ; OH $\cdots\pi$ ,  $\Delta E > 20.1$  kJ mol $^{-1}$ , see Fig. S7, ESI†). Furthermore, as demonstrated in the experimental results section, only the OH stretching frequencies predicted for the carbonyl-bound

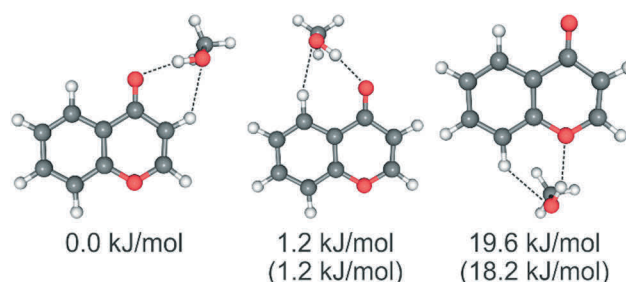


Fig. 2 Optimized structures for the chromone–methanol cluster in the  $S_0$  state with the respective relative electronic energies and zero-point corrected energies (in brackets), as obtained at the DFT/CAM-B3LYP-D3(BJ)/def2-TZVP level.

structures correlate with the experimental IR spectrum. Thus, further discussions are limited to the two OH $\cdots$ O(carbonyl) isomers. As mentioned before, we will refer to these two motifs as the “inside” and “outside” isomers. The main difference between both structures lies in their additional stabilization *via* different CH $\cdots$ O contacts. We observe an 1,2-like contact for the outside isomer and an 1,3-like contact for the inside isomer, leading to different binding angles (especially  $\angle$  CO $\cdots$ H and  $\angle$  CH $\cdots$ O) for the docking solvent molecule.

We can distinguish both structures by their different calculated OH stretching vibrational frequencies which are 3421 cm $^{-1}$  for the outside isomer and 3467 cm $^{-1}$  for the inside isomer (scaled by 0.95<sup>39</sup>). This difference is also visible in the corresponding geometric parameters (Table 1) with an OH $\cdots$ O distance of 1.838 Å for the favored outside isomer and 1.842 Å for the inside isomer. For ether coordination, the OH $\cdots$ O distance is considerably larger with 2.054 Å, indicating a weaker hydrogen bond and thus less stabilization of the cluster resulting in a higher energy. Comparing the COH and OHO angles between the two most favorable isomers yields further insight regarding the energetic ordering (see Table 1). The outside (inside) isomer exhibits a COH angle of 113° (135°) and an OHO angle of 165° (166°), the latter deviating considerably from a linear arrangement. The 1,3-contact for the inside isomer leads to this sub-optimal COH angle, with a greater difference to a probably ideal COH angle of 120° than for the outside isomer, which could be a further reason for the energetic preference of the latter. We also calculated the isomerization barrier with a relaxed potential energy surface (PES) scan for the COH angle with values between

Table 1 Selected geometry parameters for the chromone–methanol cluster in different electronic states, with the  $T_1$  state treated at UDFT/CAM-B3LYP-D3(BJ)/def2-TZVP level

	Ground state $S_0$		Excited state $T_1$		Difference( $S_0, T_1$ )/%	
	Inside	Outside	Inside	Outside	Inside	Outside
$d(\text{C}=\text{O})/\text{\AA}$	1.222	1.224	1.252	1.255	+2.5	+2.5
$d(\text{OH}\cdots\text{O})/\text{\AA}$	1.842	1.838	1.886	1.869	+2.4	+1.7
$d(\text{OH})/\text{\AA}$	0.972	0.974	0.969	0.972	–0.3	–0.2
$\angle(\text{CO}\cdots\text{H})^\circ$	135.0	112.8	134.5	112.1	–0.4	–0.6
$\angle(\text{OH}\cdots\text{O})^\circ$	167.2	164.6	166.0	160.7	–0.7	–2.4
$d(\text{CH}\cdots\text{O})/\text{\AA}$	2.291	2.425	2.316	2.315	+1.1	–4.5
$\angle(\text{CH}\cdots\text{O})^\circ$	162.4	129.1	159.3	132.6	–1.9	+2.7



110° and 230° resulting in a barrier of 11.5 kJ mol<sup>-1</sup> for the electronic ground state (Fig. S18, ESI†).

Furthermore, calculations of excited state properties were carried out using TDA-TDDFT/CAM-B3LYP-D3(BJ)/def2-TZVP. The two lowest singlet and triplet excited states were investigated (see ESI†), with a special focus on the T<sub>1</sub> state, exploiting its “ground state nature” by applying an UDFT/CAM-B3LYP-D3(BJ)/def2-TZVP approach, which provides more reliable results than the TD-DFT method with respect to the obtained geometry (see Table S1, ESI†).

The optimized geometries of the chromone–methanol cluster in the T<sub>1</sub> state keep a strong preference for the OH...O(carbonyl) structures, while the other motifs remain disfavored (Fig. 3). The Δ*E* between the inside and outside isomer increases from 1.2 kJ mol<sup>-1</sup> (S<sub>0</sub>) to 3.2 kJ mol<sup>-1</sup> (T<sub>1</sub>).

The main geometric parameters are listed in Table 1 and emphasize that the general geometry is retained, except for the elongation of the hydrogen bond and the carbonyl bond in the T<sub>1</sub> state. This is caused by the loss of planarity (puckering) of the chromone framework in the triplet state leading to a double minimum potential for both motifs, with a barrier of 1.4 kJ mol<sup>-1</sup> (outside) and 1.2 kJ mol<sup>-1</sup> (inside), respectively (Fig. S21–S22, ESI†). Structurally, the C atom of the CH moiety adjacent to the ether O atom lies outside the plane of the chromone unit (Fig. 4).

For both the inside and outside structures, the puckered C atom is displaced by around 0.3 Å relative to its position in the respective ground state geometry. Consequently, the dihedral angle formed by O(ether)–C(puckered)–C–C(carbonyl) changes from 0° in the S<sub>0</sub> state to around 20° in the T<sub>1</sub> state. For clarity, we limit the discussion to the slightly more stable “down” geometries (see Fig. S16, S17 and Tables S1, S2, ESI†). The isomerization barrier between the inside and outside isomers in the T<sub>1</sub> state is determined to 13.5 kJ mol<sup>-1</sup> by a relaxed scan (Fig. S19 and S20, ESI†), similar to the ground state barrier.

The Δ*E* values are compared to other DFT methods, SAPT0 and DLPNO-CCSD(T), as given in Table 2. All methods predict a larger dispersion interaction for the inside isomer. The value obtained from the D3(BJ) dispersion correction used in DFT yields a good approximation compared to the assumably “correct” energy decomposition approaches.

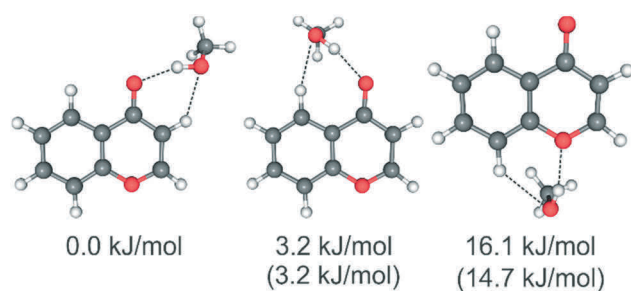


Fig. 3 Optimized structures for the chromone–methanol cluster in the T<sub>1</sub> state with the respective relative electronic energies and zero-point corrected energies (in brackets), as obtained at the UDFT/CAM-B3LYP-D3(BJ)/def2-TZVP level.

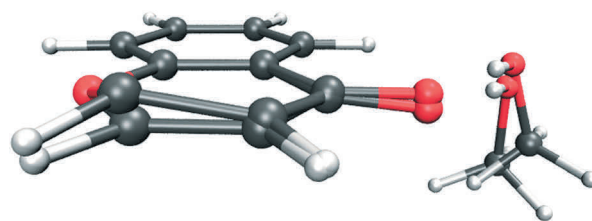


Fig. 4 Overlay of the ground state (S<sub>0</sub>) and puckered excited triplet state (T<sub>1</sub>) geometry for the inside (“down”) isomer. The puckering of the carbon atom is clearly visible. Structures obtained at (U)DFT/CAM-B3LYP-D3(BJ)/def2-TZVP level.

Table 2 Relative energies and dispersion energies for the chromone–methanol cluster in the S<sub>0</sub> state, as obtained by various theoretical methods

Method	<i>E</i> (in)– <i>E</i> (out)	Δ <i>E</i> <sub>disp</sub>
CAM-B3LYP/def2-TZVP	1.8	—
CAM-B3LYP-D3(BJ)/def2-TZVP	1.2	–1.1
PBE0-D3(BJ)/def2-TZVP	1.5	–1.2
SAPT0/jun-cc-pVDZ	0.6	–1.3
DLPNO-CCSD(T)/def2-TZVP	1.5	–0.8

As mentioned above, the goal of this study is to investigate the delicate balance between the inside and outside isomers. In order to gain insight into the relevant interactions leading to the energetic ordering of the isomers, energy decomposition calculations were performed to quantify the dispersion and other interactions. The energy values obtained by the SAPT0 calculations are shown in Table 3 (similar analysis for DLPNO-CCSD(T)/LED can be found in Table S4, ESI†). The strongest interaction, as expected for a hydrogen-bonded cluster, is the electrostatic interaction, showing a clear preference for the outside isomer, confirming the hypothesis of its stronger hydrogen-bond. The induction and dispersion interactions are significantly weaker for both isomers. It is important to note that the induction energy does not differ significantly between both motifs, while the dispersion interaction is stronger for the inside isomer, somewhat compensating for the weaker hydrogen bond. This can be rationalized by the shorter center-of-mass distances between the chromone and methanol moieties: 4.76 (inside) and 5.36 Å (outside). The larger dispersion energy in the SAPT approach leads to a reduced Δ*E* of 0.6 kJ mol<sup>-1</sup> in comparison to the (dispersion-corrected) DFT value of 1.2 kJ mol<sup>-1</sup>. Analyzing the energetics for the T<sub>1</sub> state reveals that the strongest interaction is here the repulsive exchange interaction, with the attractive electrostatic contribution being slightly weaker, while induction and dispersion interactions are significantly weaker.

If we compare these values with the ones for the electronic ground state, it is revealed that the electrostatic interaction decreases by 14 kJ mol<sup>-1</sup> (inside) and 10 kJ mol<sup>-1</sup> (outside), while the induction interaction is reduced by 5 kJ mol<sup>-1</sup> (inside) and 3 kJ mol<sup>-1</sup> (outside). At the same time, the repulsive exchange is also decreased by 7 kJ mol<sup>-1</sup> (inside) and 2 kJ mol<sup>-1</sup> (outside). The dispersion interaction is only slightly weaker in the triplet state, reduced by *ca.* 1.2 kJ mol<sup>-1</sup> for both isomers.

**Table 3** Results of energy decomposition analysis by SAPT0/jun-cc-pVDZ. The raw values for each interaction for the respective electronic state and isomer (col. 2–5), the energy difference between the inside and outside isomer for each interaction (col. 6 and 7), the change in  $\Delta E$  going from the  $S_0$  to  $T_1$  state (col. 8), giving insight which interactions influence the change in  $\Delta E$ , and the modulation (col. 9 and 10) of each interaction in the  $T_1$  state expressed in their relative strength compared to the  $S_0$  state. All values are given in  $\text{kJ mol}^{-1}$ , except col. 9 and 10. Positive values in col. 6–8 refer to stabilization of the outside structure relative to the inside isomer, in col. 9,10 a lower value indicates a weaker interaction in the  $T_1$  state compared to the corresponding value in the  $S_0$  state. A detailed overview of each contribution can be found in the ESI (Table S3)

	Inside isomer ( $S_0$ )	Outside isomer ( $S_0$ )	Inside isomer ( $T_1$ )	Outside isomer ( $T_1$ )	$\Delta E$ ( $S_0$ )	$\Delta E$ ( $T_1$ )	$\Delta\Delta E$ ( $S_0, T_1$ )	$E$ ( $T_1, \text{in}$ )/ $E$ ( $S_0, \text{in}$ )	$E$ ( $T_1, \text{out}$ )/ $E$ ( $S_0, \text{out}$ )
Electrostatics	-57.9	-60.4	-43.5	-50.8	2.5	7.3	4.8	<b>0.75</b>	<b>0.84</b>
Exchange	57.5	58.7	50.4	56.5	-1.2	-6.1	-4.8	0.88	0.96
Induction	-18.2	-18.9	-13.5	-16.0	0.6	2.4	1.8	<b>0.74</b>	<b>0.85</b>
Dispersion	-16.4	-15.2	-15.2	-14.0	-1.3	-1.2	0.0	0.93	0.92
$E_{\text{tot}}/\text{kJ mol}^{-1}$	-35.1	-35.7	-21.8	-24.2	<b>0.6</b>	<b>2.4</b>	<b>1.8</b>	0.62	0.68

Consequently, the interplay of electrostatics, induction and exchange is responsible for the increased  $\Delta E$  for the two discussed isomers in the triplet state, while London dispersion does not influence the carbonyl balance. The observed trend is consistent with the increased  $\text{C}=\text{O}$  and  $\text{O}\cdots\text{HO}$  bond distances in the  $T_1$  state, suggesting weaker hydrogen bonding and resulting in overall smaller interaction energies (see Table S5, ESI<sup>†</sup>). At this point, we propose to analyze the relative instead of the absolute energy differences between the  $S_0$  and  $T_1$  states, unraveling further insights on the interplay of the different interaction terms (Table 3, last two columns). We observe an interesting behavior for the electrostatic and induction terms. Comparing the  $T_1$  values in relation to the  $S_0$  values, we can state that both interactions drop to around 75% for the inside motif, while only dropping to 85% for the outside motif.

This is not a simple geometric effect, since the dispersion energy decreases similarly for both structures to around 92% of its original value. A possible explanation for the energy reduction of the outside structure could be the fact that the distortion of the chromone framework and the spin density is localized strongly onto the 4-pyrone ring, including the bond responsible for the  $\text{CH}\cdots\text{O}$  contact (see Fig. S15, ESI<sup>†</sup>). Thus, for the outside isomer, both the electronic and geometric structure of the ring can better adapt to the situation in the triplet state, leading to an improved interaction between the methanol and the chromone. This is also manifested by the lowering of the  $\text{CH}\cdots\text{O}$  distance by 4.5% for the outside motif, while it is increased for the inside motif.

## Experimental results

### R2PI experiments

As mentioned in the introduction, fast ISC is observed for isolated chromone<sup>22</sup> and for the structurally related xanthone,<sup>21</sup> thus similar behavior is expected for chromone-methanol aggregates. The R2PI spectra are obtained *via* a two-color R2PI process, scanning the UV excitation laser and keeping the UV ionization laser frequency-fixed. By varying the time delay between the ns-UV excitation pulse and ns-UV ionization laser pulse the fast (sub-ns) generation of a long-lived excited state (probably a triplet state populated by ISC) could be confirmed: at a delay of 23  $\mu\text{s}$  a strong ion signal of the chromone-methanol clusters is still

present. In the molecular beam expansion not only clusters comprising one single methanol molecule are observed, but at the same time a multitude of higher clusters comprising several (up to 10–15 methanol molecules) are also obtained. As discussed further down, this strong aggregation behavior has some experimental disadvantages, but allows us to estimate a possible excited state lifetime dependence on the cluster size. However, at least for time delays of up to 23  $\mu\text{s}$  between the excitation and ionization laser pulses, the mass signal distribution (and thus cluster size distribution) in the recorded mass spectra is largely unchanged (see Fig. S2, ESI<sup>†</sup>). This means that all observed cluster sizes should have similar excited state lifetimes. We conclude that most probably an ISC into a triplet state with long lifetime takes place for the chromone-methanol clusters, which is in accordance with the studies of Itoh,<sup>22</sup> who reported gas vapor UV and emission spectra for chromone, and also in line with prior studies on xanthone<sup>21</sup> performed in our group. Finally, we chose a time delay of 70 ns for our experiments to minimize the required spatial shift of the lasers due to the velocity of the molecular beam while still avoiding temporal overlap of the laser pulses.

The R2PI spectrum of chromone, recorded with the UV ionization laser set to a frequency of 46 838  $\text{cm}^{-1}$  exhibits a strong band at 33 896  $\text{cm}^{-1}$  (see Fig. S1, ESI<sup>†</sup>). We assign this band to the  $S_0 \rightarrow S_2$  transition in correspondence to gas vapor UV spectra from literature<sup>22</sup> (33 880  $\text{cm}^{-1}$ ). It should be pointed out that a UV photoexcitation into the  $S_1$  state (prior to ionization) was not possible due to the weak absorption cross section of the  $S_0 \rightarrow S_1$  transition.<sup>22</sup> This was further confirmed by TD-DFT calculations (see Fig. S10, ESI<sup>†</sup>) and is again in accordance with the studies on xanthone.<sup>21</sup> In the accordingly obtained R2PI spectra of chromone with one or more methanol molecules, a strong shift of the  $S_0 \rightarrow S_2$  transition down to 33 292  $\text{cm}^{-1}$  (chromone-methanol (1:1) cluster) is observed, corresponding to a red-shift of 604  $\text{cm}^{-1}$  relative to the value for chromone, which increases with further addition of methanol molecules (see Fig. S1, ESI<sup>†</sup>).

### IR/UV experiments in the electronic ground state

The IR/R2PI spectra were recorded in the IR frequency range from 3130  $\text{cm}^{-1}$  to 3750  $\text{cm}^{-1}$ , with the UV excitation laser frequency set to 33 292  $\text{cm}^{-1}$  and the UV ionization laser frequency-fixed at 46 838  $\text{cm}^{-1}$ . We observe multiple overlapping bands

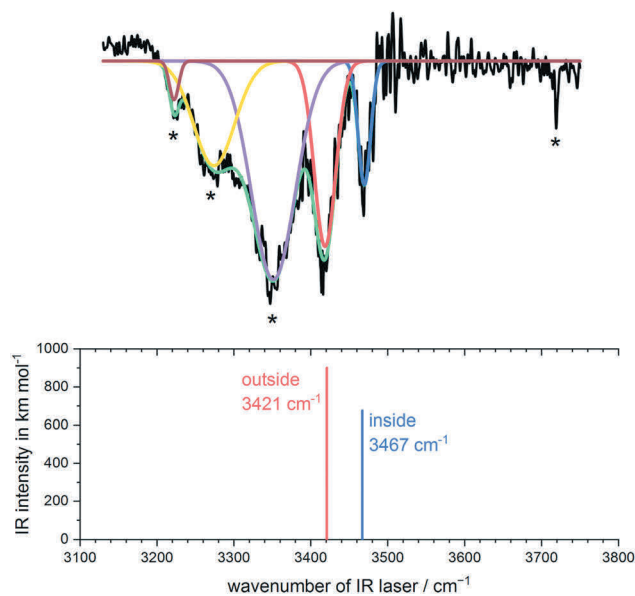


Fig. 5 Experimental and theoretical IR spectra for the chromone–methanol cluster in the  $S_0$  state. Bands marked with asterisks result from UV fragmentation of higher chromone–methanol(–water) clusters. A convolution of five Gaussians (green) is fitted to the spectrum. The red and blue Gaussians were assigned to the outside and inside isomers, respectively. Calculated OH stretching frequencies were obtained at CAM-B3LYP-D3(BJ)/def2-TZVP level and scaled by 0.95.

indicating that more than one species contributes to the IR spectrum of the chromone–MeOH cluster (Fig. 5). By comparing this IR spectrum with the spectra obtained at higher mass traces (see Fig. S3, ESI†) corresponding to clusters with two and more methanol (as well as water) molecules, several features marked with asterisks in the IR spectrum of chromone–methanol are assigned to IR transitions of higher clusters (with more than one methanol molecule) or chromone–methanol–water clusters (feature at  $3719\text{ cm}^{-1}$ ), appearing in the IR spectrum of chromone–methanol due to UV photofragmentation of the respective larger clusters.

Typically, larger alcohol clusters show strong, anharmonic and thus particularly red-shifted OH stretching frequencies, while features around  $3720\text{ cm}^{-1}$  (free OH stretching vibration of  $\text{H}_2\text{O}$ ) are a hint on the formation of water clusters in the molecular beam expansion which are difficult to avoid for hygroscopic substances. The neutral chromone–methanol complexes are expected to undergo intersystem crossing into the triplet-manifold upon UV photoexcitation, resulting in a large amount of excess energy. This could explain why the discussed photofragmentation effects could not be suppressed in usual ways, like keeping the excess energy in the excitation and ionization step moderate or by varying the expansion conditions. Since the investigated aggregates are probed in the cold, collision-free part of the molecular beam, isolated vibrationally hot triplet state clusters formed upon intersystem crossing cannot undergo vibrational relaxation by colliding with the expansion gas (neon). Therefore, we assume that the chromone–solvent clusters (especially the probably more labile larger clusters)

tend to dissipate energy by evaporative cooling,<sup>44</sup> specifically detachment of solvent molecules. We calculate the energy difference between the  $T_1$  and  $S_2$  state to be around  $160\text{ kJ mol}^{-1}$  (see Fig. S10, ESI†), which would require evaporation of multiple methanol molecules for (partial) cooling. This may explain the strong photofragmentation effects observed in the IR/R2PI spectra, since the IR laser is applied temporally prior to the first UV laser and thus before the discussed fragmentation process. Nevertheless, the IR spectrum depicted in Fig. 5 shows two intense features at  $3419$  and  $3470\text{ cm}^{-1}$  that can be assigned with high confidence to two distinct isomers of the chromone–methanol cluster. Indeed, these two bands are in excellent agreement with the OH stretching frequencies predicted by quantum-chemical calculations (CAM-B3LYP-D3(BJ)/def2-TZVP level) for the two energetically favored structures, namely the “outside pocket” ( $3421\text{ cm}^{-1}$ ) and “inside pocket” ( $3467\text{ cm}^{-1}$ ) isomers. This strongly supports the formation of both  $\text{OH}\cdots\text{O}$  bound isomers in the molecular beam expansion, moreover because the  $\text{OH}\cdots\text{O}(\text{ether})$  and  $\text{OH}\cdots\pi$  structures would exhibit resonances at higher wavenumbers (see Fig. S7, ESI†), closer to the value for free methanol<sup>45</sup> at  $3686\text{ cm}^{-1}$ . Thus, the presence of both (expected) isomers is highly suggested by the experimental results presented above, whereby isomerizations between both arrangements seem unlikely due to a high interconversion barrier between both local minima. As mentioned in the theoretical results, this barrier was calculated by a relaxed potential energy surface scan (PES) and estimated to be around  $11.5\text{ kJ mol}^{-1}$ , a value that makes isomerization during the molecular beam expansion unlikely. Nevertheless, the small energetic difference between both isomers also supports the direct population of both isomers within the adiabatic expansion.

However, even if the inside and outside isomers are both observed in the experiment, both minima may not be populated in equal amounts in the molecular beam. Although quantitative assignments based on our IR/UV experiments are difficult, a tentative estimation should be possible in the specific case treated here, since similar UV oscillator strengths are expected for both isomers in question (see predictions of TDDFT in the ESI†). Likewise, the predicted intensities of the respective OH stretching modes are in the same order of magnitude. Thus, it can be claimed that, without indicating any precise value concerning the isomeric ratio between the outside and inside structures, the outside isomer IR-band is clearly more pronounced than the inside isomer band, so that the outside isomer population should predominate in the molecular beam (compared to the inside isomer contribution). This observation is perfectly in accordance with the relative energies of the competing minimum structures (see theoretical results section, further analysis in Fig. S6, ESI†).

#### IR/UV experiments in the electronically excited state ( $T_1$ )

The IR spectrum of chromone–methanol in its electronically excited triplet state ( $T_1$ ), depicted in Fig. 6, was obtained by applying the UV/IR/UV technique. Compared to the ground state IR spectrum discussed above, the UV/IR/UV spectrum shows significantly changed characteristics. First of all, it is



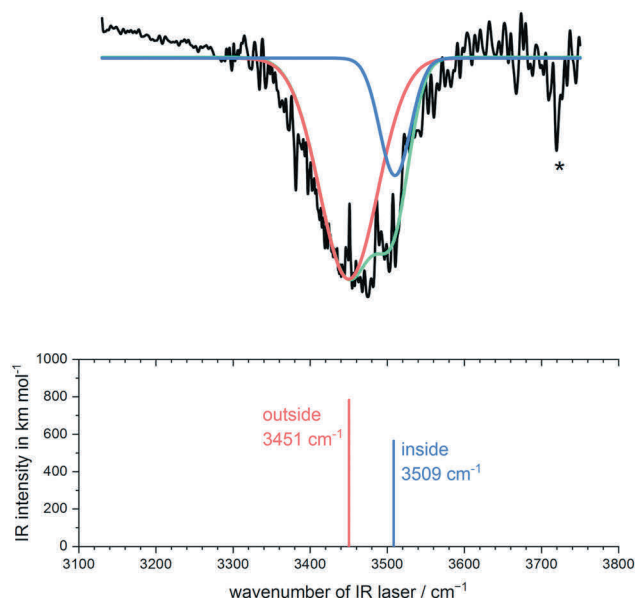


Fig. 6 Experimental and theoretical spectra for the chromone–methanol cluster in the  $T_1$  state. A convolution of two Gaussians (green), representing the outside (red) and inside (blue) isomer peaks, is fitted to the spectrum. Calculated OH stretching frequencies were obtained at CAM-B3LYP-D3(BJ)/def2-TZVP level and scaled by 0.95.

almost free of any features which are caused by UV photofragmentation of larger chromone–methanol clusters. There is one sharp feature at  $3720\text{ cm}^{-1}$ , marked with an asterisk, which is again due to UV photofragmentation of chromone–methanol–water clusters, but any further effects related to higher clusters are not observed. This strengthens the hypothesis that strong UV fragmentation of (especially larger) chromone–methanol clusters occurs after intersystem crossing. Since the ISC process can be expected to take place on a ps timescale, the IR laser (fired about 50 ns after the UV excitation laser) is thus irradiating the sample after the ISC and most probably also after the evaporative cooling takes place. Thus, this could present a plausible explanation for the absence of any major features resulting from larger clusters in the UV/IR/UV spectrum of chromone–methanol.

Finally, we observe a strong and structured band from  $3330\text{ cm}^{-1}$  to  $3600\text{ cm}^{-1}$  that can be deconvoluted into two Gaussians with peak maxima at  $3451\text{ cm}^{-1}$  and  $3510\text{ cm}^{-1}$ , which are in excellent agreement with the predicted calculated values of  $3451\text{ cm}^{-1}$  (outside) and  $3508\text{ cm}^{-1}$  (inside), respectively. At this point it should also be noted that the spikes in the measured band around  $3450$  and  $3510\text{ cm}^{-1}$  are caused by dips in the IR laser power curve (see Fig. S5, ESI† for comparison). Thus, both structural motifs assigned for the ground state ( $S_0$ ) are retained in the  $T_1$  state. As discussed in the theoretical results section, the optimized geometries of the  $T_1$  state isomers are similar compared to those observed for the respective ground state structures. However, the  $\text{OH}\cdots\text{O}$  hydrogen bonds (and  $\text{C}=\text{O}$  bonds) are slightly elongated for both motifs and thus weakened compared to the  $S_0$  state geometries (see Table 1), which explains the blue-shift of the measured as well as the calculated OH

stretching frequencies relative to the ground state OH vibrations and is in line with the calculated lower binding energies (see Table S5, ESI†).

The discussed cluster fragmentation effects upon UV photoexcitation imply that any assumptions regarding isomerization between outside and inside motifs upon ISC into the triplet manifold should be handled carefully. Specifically, the population of both the inside and outside minima may not only be influenced by isomerization processes between both motifs, but also by fragmentation of larger clusters onto the chromone–methanol mass trace prior to IR probing. This means that chromone–methanol clusters initially formed during the adiabatic expansion and kept intact upon ISC, as well as chromone–methanol aggregates generated by UV fragmentation of larger clusters may both contribute to the depicted UV/IR/UV spectrum. Thus, the population ratio between the outside and inside minima in the  $T_1$  state can have different origins. Nevertheless, the outside isomer seems to be again clearly more populated than the inside isomer motif (see deconvolution in Fig. 6).

Another remarkable aspect is that compared to the ground state IR spectrum, the OH stretching bands observed in the UV/IR/UV spectrum are rather broad. As already mentioned, the clusters in the triplet-manifold cannot dissipate any energy by collisions or other interaction with the environment. Thus, it is quite probable that also (vibrationally) hot clusters are probed in the UV/IR/UV experiment. This assumption may explain the large width of the bands observed in the  $T_1$  state spectrum.

An additional rationalization for the broadening of the OH stretching bands (especially for the outside isomer) could be inferred from the fact that, as described in the theoretical results section, the chromone unit in the chromone–methanol cluster forms a puckered 4-pyrone ring when reaching the  $T_1$  state. Consequently, this effect leads to the occurrence of two distinct local minima per binding motif, separated by a very low interconversion barrier (see Fig. S21 and S22, ESI†). The larger binding energy of the outside isomer could lead to the detection of clusters which are structurally and energetically more displaced from the minimum structure. Hereby, a somewhat distorted structure may exhibit a slightly distinct OH stretching frequency (compared to the minimum geometry), leading to a broadening of the measured IR band. In contrast to this, the inside isomer, exhibiting a lower binding energy, might be more likely to undergo fragmentation upon ISC if its structure is slightly off its minimum geometry. For this reason, such hot inside clusters may not contribute to the measured IR spectrum. It should be further noted that the influence of the puckering effect on the cluster stability should be relatively more pronounced for the outside isomer due to the spatial proximity of the puckered 4-pyrone ring and the methanol molecule.

Another reason for the distinct broadness of the two Gaussian peaks could be that the outside isomer, with its red-shifted OH stretching mode (relative to the inside isomer), exhibits a comparatively broad potential well, leading to a relatively increased bandwidth. However, a clear explanation for the observed different broadening of the bands in the triplet-state

is difficult to give, so that the aspects discussed above should be merely considered as possible hypotheses.

## Conclusions

We present the first results for IR/UV spectroscopic investigations of molecular clusters in the triplet state in general as well as an analysis of the interplay of non-covalent interactions over multiple electronic states. Slightly different cluster structures (inside/outside pocket binding) for chromone-methanol have been identified by quantum-chemical calculations and IR/UV laser spectroscopic investigations. The presented results provide a case study for the influence of London dispersion interaction in excited states, serving as a stepping stone for further analysis in other molecular cluster systems. For chromone-methanol, the balance is mainly influenced by electrostatic, induction and exchange interaction. It was shown that, although collisional cooling in the cold part of the molecular beam can be ruled out, meaningful UV/IR/UV measurements in the  $T_1$  state on molecular clusters are possible and may be supported by the loss of excess energy after ISC *via* cluster fragmentation effects, *i.e.* evaporative cooling. We observe a significant blue-shift of the OH stretching band (relative to the respective value for the cluster in its electronic ground state) upon electronic excitation, indicating a weakening of the hydrogen bond. This is indeed confirmed by binding energy calculations and energy decomposition analysis (SAPT0).

Furthermore, the electronic excitation leads to a ring puckering of the 4-pyrone unit with the spin density mostly localized on the puckered carbon atom (see Fig. S15, ESI<sup>†</sup>). This leads to a stronger differentiation between the two binding motifs since the outside pocket is part of this flexible non-planar 4-pyrone ring. Consequently, the energy difference between both motifs increases upon electronic excitation. The energy decomposition analysis reveals that the strength of the dispersion interaction is only dampened slightly by the change in electronic and geometric structure, whereas electrostatic, exchange and induction are strongly modulated depending on the binding site. Finally, not the dispersion interaction leads to the increase in  $\Delta E$ , but stronger electrostatic and induction interaction is the deciding factor on this delicate carbonyl scale.

## Author contributions

Pol Boden: investigation, writing: draft, review and editing; Patrick Horst Strebart: investigation, writing: draft, review and editing, formal analysis and visualization; Marcel Meta: formal analysis and visualization; Fabian Dietrich: conceptualization, writing: review and editing; Christoph Riehn: supervision, writing: review and editing; Markus Gerhards: conceptualization, funding acquisition, resources, supervision.

## Conflicts of interest

There are no conflicts to declare.

## Acknowledgements

The authors thank the German Research Foundation (DFG) for financial support in the context of the Priority Programme SPP 1807 (Ge 961/9-2, Control of London dispersion interactions in molecular chemistry). The authors thank the State Research Center OPTIMAS for financial support. The authors want to thank Dr Kirsten Schwing for fruitful discussion. This work is part of the PhD theses of P. B. and P. H. S.

## Notes and references

- (a) J. Cerný and P. Hobza, *Phys. Chem. Chem. Phys.*, 2007, **9**, 5291–5303; (b) J.-M. Lehn, *Angew. Chem., Int. Ed. Engl.*, 1988, **27**, 89–112; (c) E. A. Meyer, R. K. Castellano and F. Diederich, *Angew. Chem., Int. Ed.*, 2003, **42**, 1210–1250; (d) K. Müller-Dethlefs and P. Hobza, *Chem. Rev.*, 2000, **100**, 143–168; (e) J. P. Wagner and P. R. Schreiner, *Angew. Chem., Int. Ed.*, 2015, **54**, 12274–12296; (f) I. K. Mati and S. L. Cockroft, *Chem. Soc. Rev.*, 2010, **39**, 4195–4205.
- D. Bernhard, F. Dietrich, M. Fatima, C. Pérez, A. Poblitzki, G. Jansen, M. A. Suhm, M. Schnell and M. Gerhards, *Phys. Chem. Chem. Phys.*, 2017, **19**, 18076–18088.
- D. Bernhard, M. Fatima, A. Poblitzki, A. L. Steber, C. Pérez, M. A. Suhm, M. Schnell and M. Gerhards, *Phys. Chem. Chem. Phys.*, 2019, **21**, 16032–16046.
- D. Bernhard, F. Dietrich, M. Fatima, C. Pérez, H. C. Gottschalk, A. Wuttke, R. A. Mata, M. A. Suhm, M. Schnell and M. Gerhards, *Beilstein, J. Org. Chem.*, 2018, **14**, 1642–1654.
- F. Dietrich, D. Bernhard, M. Fatima, C. Pérez, M. Schnell and M. Gerhards, *Angew. Chem., Int. Ed.*, 2018, **57**, 9534–9537.
- M. Fatima, D. Maué, C. Pérez, D. S. Tikhonov, D. Bernhard, A. Stamm, C. Medcraft, M. Gerhards and M. Schnell, *Phys. Chem. Chem. Phys.*, 2020, **22**, 27966–27978.
- H. C. Gottschalk, A. Poblitzki, M. Fatima, D. A. Obenchain, C. Pérez, J. Antony, A. A. Auer, L. Baptista, D. M. Benoit, G. Bistoni, F. Bohle, R. Dahmani, D. Firaha, S. Grimme, A. Hansen, M. E. Harding, M. Hochlaf, C. Holzer, G. Jansen, W. Klopfer, W. A. Kopp, M. Krasowska, L. C. Kröger, K. Leonhard, M. Mogren Al-Mogren, H. Mouhib, F. Neese, M. N. Pereira, M. Prakash, I. S. Ulusoy, R. A. Mata, M. A. Suhm and M. Schnell, *J. Chem. Phys.*, 2020, **152**, 164303.
- C. Medcraft, S. Zinn, M. Schnell, A. Poblitzki, J. Altnöder, M. Heger, M. A. Suhm, D. Bernhard, A. Stamm, F. Dietrich and M. Gerhards, *Phys. Chem. Chem. Phys.*, 2016, **18**, 25975–25983.
- A. Poblitzki, H. C. Gottschalk and M. A. Suhm, *J. Phys. Chem. Lett.*, 2017, **8**, 5656–5665.
- C. Zimmermann, H. C. Gottschalk and M. A. Suhm, *Phys. Chem. Chem. Phys.*, 2020, **22**, 2870–2877.
- C. Zimmermann, T. L. Fischer and M. A. Suhm, *Molecules*, 2020, **25**, 5095.
- C. Zimmermann, M. Lange and M. A. Suhm, *Molecules*, 2021, **26**, 4883.
- S. Blanco, A. Macario and J. C. López, *Phys. Chem. Chem. Phys.*, 2019, **21**, 20566–20570.

- 14 P. Banerjee, P. Pandey and B. Bandyopadhyay, *Spectrochim. Acta, Part A*, 2019, **209**, 186–195.
- 15 E. Burevschi, E. R. Alonso and M. E. Sanz, *Chemistry*, 2020, **26**, 11327–11333.
- 16 (a) Y. Ikabata and H. Nakai, *J. Chem. Phys.*, 2012, **137**, 124106; (b) X. Feng, A. Otero-de-la-Roza and E. R. Johnson, *Can. J. Chem.*, 2018, **96**, 730–737; (c) V. Barone, M. Biczysko and M. Pavone, *Chem. Phys.*, 2008, **346**, 247–256.
- 17 A. Fabrizio and C. Corminboeuf, *J. Phys. Chem. Lett.*, 2018, **9**, 464–470.
- 18 E. A. Briggs and N. A. Besley, *Phys. Chem. Chem. Phys.*, 2014, **16**, 14455–14462.
- 19 (a) Q. Ge, Y. Mao and M. Head-Gordon, *J. Chem. Phys.*, 2018, **148**, 64105; (b) R. A. Krueger and G. Blanquart, *J. Phys. Chem. A*, 2019, **123**, 1796–1806; (c) A. Diaz-Andres and D. Casanova, *J. Phys. Chem. Lett.*, 2021, **12**, 7400–7408.
- 20 D. Bernhard, C. Holzer, F. Dietrich, A. Stamm, W. Klopper and M. Gerhards, *ChemPhysChem*, 2017, **18**, 3634–3641.
- 21 K. Bartl, A. Funk and M. Gerhards, *ChemPhysChem*, 2009, **10**, 1882–1886.
- 22 T. Itoh, *J. Photochem. Photobiol., A*, 2010, **214**, 10–15.
- 23 E. G. Hohenstein, R. M. Parrish, C. D. Sherrill, J. M. Turney and H. F. Schaefer, *J. Chem. Phys.*, 2011, **135**, 174107.
- 24 T. M. Parker, L. A. Burns, R. M. Parrish, A. G. Ryno and C. D. Sherrill, *J. Chem. Phys.*, 2014, **140**, 94106.
- 25 A. Altun, R. Izsák and G. Bistoni, *Int. J. Quantum Chem.*, 2021, **121**, 919.
- 26 A. Altun, F. Neese and G. Bistoni, *Beilstein J. Org. Chem.*, 2018, **14**, 919–929.
- 27 A. Altun, M. Saitow, F. Neese and G. Bistoni, *J. Chem. Theory Comput.*, 2019, **15**, 1616–1632.
- 28 A. Stamm, M. Weiler, A. Brächer, K. Schwing and M. Gerhards, *Phys. Chem. Chem. Phys.*, 2014, **16**, 21795–21803.
- 29 (a) M. Gerhards and C. Unterberg, *Phys. Chem. Chem. Phys.*, 2002, **4**, 1760–1765; (b) C. Unterberg, A. Jansen and M. Gerhards, *J. Chem. Phys.*, 2000, **113**, 7945.
- 30 S. Grimme, *J. Chem. Theory Comput.*, 2019, **15**, 2847–2862.
- 31 (a) M. A.-L. Marques, M. J.-T. Oliveira and T. Burnus, *Comput. Phys. Commun.*, 2012, **183**, 2272–2281; (b) S. Lehtola, C. Steigemann, M. J.-T. Oliveira and M. A.-L. Marques, *SoftwareX*, 2018, **7**, 1–5; (c) T. Yanai, D. P. Tew and N. C. Handy, *Chem. Phys. Lett.*, 2004, **393**, 51–57.
- 32 F. Weigend and R. Ahlrichs, *Phys. Chem. Chem. Phys.*, 2005, **7**, 3297–3305.
- 33 F. Weigend, *J. Comput. Chem.*, 2008, **29**, 167–175.
- 34 A. Hellweg, C. Hättig, S. Höfener and W. Klopper, *Theor. Chem. Acc.*, 2007, **117**, 587–597.
- 35 S. Grimme, J. Antony, S. Ehrlich and H. Krieg, *J. Chem. Phys.*, 2010, **132**, 154104.
- 36 S. Grimme, S. Ehrlich and L. Goerigk, *J. Comput. Chem.*, 2011, **32**, 1456–1465.
- 37 M. J. Frisch, G. W. Trucks, H. B. Schlegel, G. E. Scuseria, M. A. Robb, J. R. Cheeseman, G. Scalmani, V. Barone, G. A. Petersson, H. Nakatsuji, X. Li, M. Caricato, A. V. Marenich, J. Bloino, B. G. Janesko, R. Gomperts, B. Mennucci, H. P. Hratchian, J. V. Ortiz, A. F. Izmaylov, J. L. Sonnenberg, D. Williams-Young, F. Ding, F. Lipparini, F. Egidi, J. Goings, B. Peng, A. Petrone, T. Henderson, D. Ranasinghe, V. G. Zakrzewski, J. Gao, N. Rega, G. Zheng, W. Liang, M. Hada, M. Ehara, K. Toyota, R. Fukuda, J. Hasegawa, M. Ishida, T. Nakajima, Y. Honda, O. Kitao, H. Nakai, T. Vreven, K. Throssell, J. A. Montgomery, Jr., J. E. Peralta, F. Ogliaro, M. J. Bearpark, J. J. Heyd, E. N. Brothers, K. N. Kudin, V. N. Staroverov, T. A. Keith, R. Kobayashi, J. Normand, K. Raghavachari, A. P. Rendell, J. C. Burant, S. S. Iyengar, J. Tomasi, M. Cossi, J. M. Millam, M. Klene, C. Adamo, R. Cammi, J. W. Ochterski, R. L. Martin, K. Morokuma, O. Farkas, J. B. Foresman and D. J. Fox, *Gaussian 16*, Gaussian, Inc., Wallingford, CT, USA, 2016.
- 38 TURBOMOLE V7.5 2020. a development of University of Karlsruhe and Forschungszentrum Karlsruhe GmbH, 1989-2007, TURBOMOLE GmbH, since 2007.
- 39 D. O. Kashinski, G. M. Chase, R. G. Nelson, O. E. Di Nallo, A. N. Scales, D. L. VanderLey and E. F.-C. Byrd, *J. Phys. Chem. A*, 2017, **121**, 2265–2273.
- 40 E. G. Hohenstein and C. D. Sherrill, *J. Chem. Phys.*, 2010, **132**, 184111.
- 41 R. M. Parrish, L. A. Burns, D. G.-A. Smith, A. C. Simmonett, A. E. DePrince, E. G. Hohenstein, U. Bozkaya, A. Y. Sokolov, R. Di Remigio, R. M. Richard, J. F. Gonthier, A. M. James, H. R. McAlexander, A. Kumar, M. Saitow, X. Wang, B. P. Pritchard, P. Verma, H. F. Schaefer, K. Patkowski, R. A. King, E. F. Valeev, F. A. Evangelista, J. M. Turney, T. D. Crawford and C. D. Sherrill, *J. Chem. Theory Comput.*, 2017, **13**, 3185–3197.
- 42 (a) W. B. Schneider, G. Bistoni, M. Sparta, M. Saitow, C. Riplinger, A. A. Auer and F. Neese, *J. Chem. Theory Comput.*, 2016, **12**, 4778–4792; (b) G. Bistoni, *Wiley Interdiscip. Rev.: Comput. Mol. Sci.*, 2020, **10**, 1.
- 43 (a) F. Neese, *Wiley Interdiscip. Rev.: Comput. Mol. Sci.*, 2017, **8**, 33; (b) F. Neese, *Wiley Interdiscip. Rev.: Comput. Mol. Sci.*, 2011, **2**, 73–78.
- 44 C. E. Klots, *J. Chem. Phys.*, 1985, **83**, 5854–5860.
- 45 F. Kollipost, K. Papendorf, Y.-F. Lee, Y.-P. Lee and M. A. Suhm, *Phys. Chem. Chem. Phys.*, 2014, **16**, 15948–15956.

## Electronic Supplementary Information

### Chromone-methanol cluster in the electronic ground and lowest triplet state: A delicate interplay of non-covalent interactions

Pol Boden<sup>a</sup>, Patrick H. Streb<sup>a</sup>, Marcel Meta<sup>a</sup>, Fabian Dietrich<sup>a,b</sup>, Christoph Riehn<sup>a\*</sup>, Markus Gerhards<sup>†a</sup>

<sup>a</sup>Fachbereich Chemie & State Research Center OPTIMAS, TU Kaiserslautern, Erwin-Schrödinger-Str. 52, D-67663 Kaiserslautern, Germany.

<sup>b</sup>Núcleo Milenio MultiMat & Departamento de Ciencias Físicas, Universidad de La Frontera, Temuco, Chile.

#### Contents

Experimental results.....	2
R2PI experiments on chromone and chromone-methanol clusters.....	2
IR/UV experiments on chromone-methanol .....	4
IR/R2PI experiments on higher clusters.....	8
Theoretical results.....	10
Further analysis of the excited states for chromone-methanol .....	10
Further analysis of the T <sub>1</sub> state .....	13
Binding and deformation energies.....	18
Barriers for isomer interconversion.....	18
References.....	21

## Experimental results

### R2PI experiments on chromone and chromone-methanol clusters

R2PI spectra were measured for chromone and the chromone-(MeOH)<sub>n</sub> clusters, based on previous experiments on chromone.<sup>1</sup> Since chromone as well as the structurally related xanthone<sup>2</sup> both undergo intersystem crossing (ISC) into the triplet manifold upon electronic excitation, an ISC is also expected for the chromone-(MeOH)<sub>n</sub> clusters. In the R2PI experiments, even at a delay of 23  $\mu$ s between the excitation and ionization laser pulses, a strong ion signal was observed for the chromone-(MeOH)<sub>n</sub> aggregates, which makes an ISC plausible. For successful ionization, a two-color process was required with the excitation laser scanned between 32522  $\text{cm}^{-1}$  and 34784  $\text{cm}^{-1}$ . The frequency-fixed ionization laser was set to 46838  $\text{cm}^{-1}$  and irradiated 70 ns after the excitation laser. For isolated chromone we reproduced the 0-0 transition at 33896  $\text{cm}^{-1}$  (figure S1). Coordination of one or more methanol molecules leads to a red-shift, resulting in bands at 33292  $\text{cm}^{-1}$  and 33204  $\text{cm}^{-1}$  for the chromone-MeOH and chromone-(MeOH)<sub>2</sub> clusters, respectively. The band broadens significantly upon methanol coordination leading to unstructured spectra for the higher clusters, which are a first hint for UV fragmentation of larger clusters exhibiting similar UV absorption.

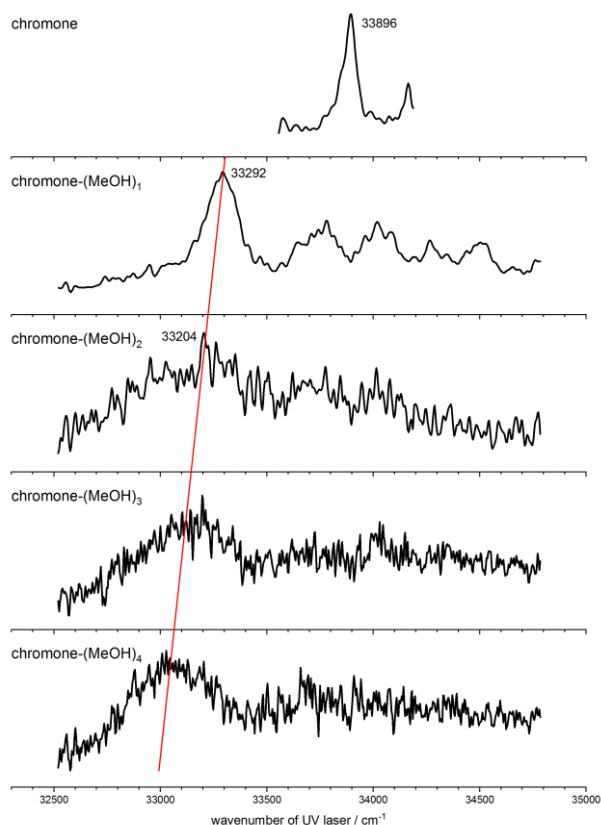


Figure S1: 2C-R2PI spectra for the mass traces of chromone and chromone-(MeOH)<sub>1-4</sub> (from top to bottom), with UV-ionization@46838  $\text{cm}^{-1}$ . The redshift of the 0-0 transition upon addition of methanol is indicated with a red line as a guide to the eye.

Within the context of the expected intersystem crossing with the suspected subsequent “evaporative cooling” mentioned in the main manuscript, mass spectra with different time delays between the excitation and ionization laser pulses were recorded to analyze the cluster distribution over time. For the chromone monomer and the chromone-(MeOH)<sub>n</sub> clusters up to n=6, the integrated signal intensities were determined and illustrated in figure S2.



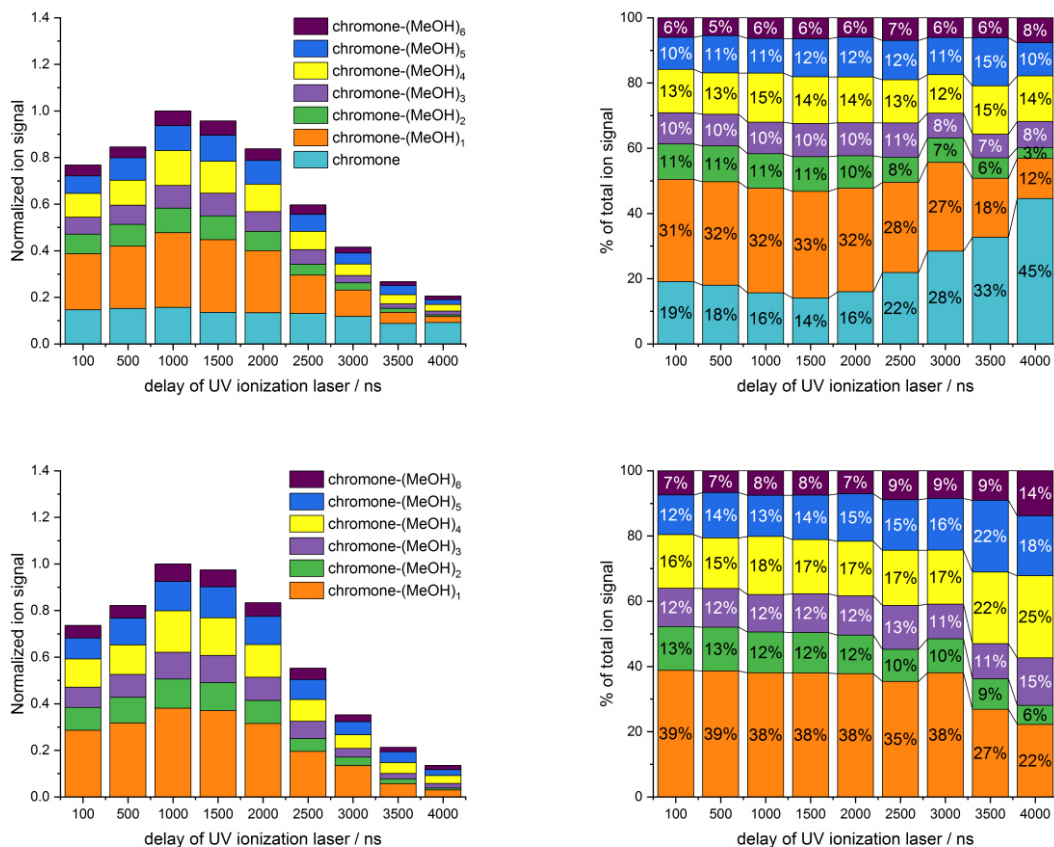


Figure S2: Normalized integrated ion signal intensities as a function of the time delay between the excitation and ionization laser pulses for chromone-(MeOH)<sub>n</sub> clusters (n=1-6) and the chromone monomer (top left, bottom left) and the same as relative proportions of the sum over all signals (top right, bottom right). Despite the significant time-dependence of the total ion signal, the cluster distribution does not change significantly for delays between 100 and 3000 ns, which is especially visible when excluding the chromone monomer mass trace (bottom right).

Focussing on the top left diagram, it is noticeable that the sum of all considered ion signals shows an increase from 100 to 1000 ns and a successive more pronounced decrease towards the final data point at 4000 ns. To determine the cluster distribution, the relative proportion of each species was calculated for each time delay, resulting in the plot at the top right. It can be seen, that only at larger delay times (> 2000 ns), the relative chromone monomer ion signal intensity increases at the cost of the chromone-(MeOH)<sub>1,2</sub> cluster signals, whereas the cluster distribution is constant for delays of 100 ns to 2000 ns. Thus, the “evaporative cooling” process seems to be finished after at most 100 ns, since no significant changes in the cluster distribution can be observed afterwards until a delay of 2000 ns. This is also supported by the nearly constant absolute ion signal of the chromone monomer which should increase if fragmentation of chromone-(MeOH)<sub>n</sub> clusters occurs. It seems challenging to extract any further information from figure S2, as different effects could be responsible for the decrease of the chromone-(MeOH)<sub>n</sub> cluster signals at delays > 2000 ns. For instance, the excited state lifetime of the (potentially hot) clusters (partially originating from fragmentation of larger clusters) is unknown, but can be decisive for ionization *via* R2PI. Furthermore, the excitation and ionization laser beams have to be spatially separated with increasing time delay between excitation and ionization, so that the detection within the Time-of-flight mass spectrometer might also influence this behavior. Nevertheless, omitting the constant chromone monomer signal intensity from the calculation (bottom left, bottom right) reveals that the cluster

distribution of the chromone-(MeOH)<sub>n</sub> clusters can even be considered “stable” until 3000 ns. This indicates that, most importantly, the cluster distribution does not show significant changes for a time frame of 100 ns to 3000 ns and supports our claim that the “evaporative cooling” proposed in the manuscript is already completed at a shorter time scale.

#### IR/UV experiments on chromone-methanol

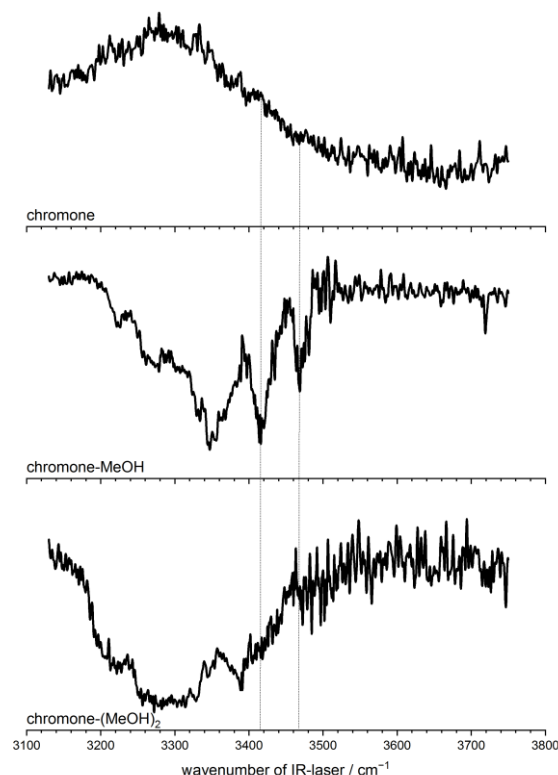


Figure S3: IR/R2PI spectra for the mass traces of chromone and chromone-(MeOH)<sub>1-2</sub>, UV-excitation@33900 cm<sup>-1</sup>, UV-ionization@46838 cm<sup>-1</sup>; emphasizing that the features observed below 3400 cm<sup>-1</sup> on the chromone-MeOH mass trace are due to laser-induced fragmentation from larger clusters.

Analyzing the IR/R2PI spectrum displayed in figure S3, the increase of the signal intensity on the chromone monomer trace can be attributed to IR fragmentation of chromone-solvent clusters. The features below 3400 cm<sup>-1</sup> on the chromone-methanol mass trace are due to fragmentation effects of larger chromone-methanol clusters. Hereby, UV fragmentation effects should dominate, while the influence of (possibly weaker) IR fragmentation effects cannot be excluded. However, the two intense bands standing out at 3419 cm<sup>-1</sup> and at 3470 cm<sup>-1</sup> (highlighted with dashed lines) on the chromone-MeOH trace are unambiguously assigned to the chromone-MeOH species, as the other mass traces show no significant features in that spectral region (above 3400 cm<sup>-1</sup>). The small peak at about 3720 cm<sup>-1</sup> is a sign of fragmentation effects of larger chromone-(MeOH)<sub>n</sub>-H<sub>2</sub>O aggregates. The broad unstructured feature on the chromone-(MeOH)<sub>2</sub> trace is again very likely affected by UV (and possibly IR) fragmentation of larger and less stable clusters.

The UV/IR/UV spectrum (figure S4) shows a broad structured band on the chromone-MeOH mass trace (dashed line), which is definitely blue-shifted relative to the broad dip on the chromone-(MeOH)<sub>2</sub> trace. Thus, the major features on the chromone-MeOH trace can definitely be assigned to the chromone-MeOH species and are not due to fragmentation. The small peak at about 3720 cm<sup>-1</sup> on the chromone-MeOH trace is explained by UV fragmentation of larger chromone-(MeOH)<sub>n</sub>-H<sub>2</sub>O

aggregates. The increase of the signal intensity on the chromone monomer trace is due to IR fragmentation of the chromone-MeOH species (and larger chromone-solvent clusters).

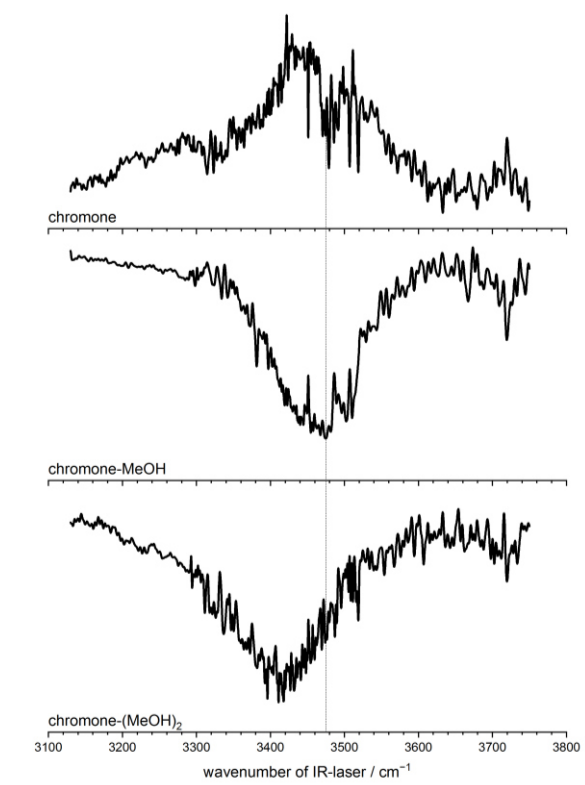


Figure S4: UV/IR/UV spectra for the mass traces of chromone and chromone-(MeOH)<sub>1-2</sub>, UV-excitation@33900 cm<sup>-1</sup>, UV-ionization@46838 cm<sup>-1</sup>.

The sharp spikes which appear in the UV/IR/UV spectrum of chromone-methanol, in the spectral between 3450 and 3510 cm<sup>-1</sup>, are caused by dips in the available IR laser power. For demonstration, the IR laser power curve for that spectral region is depicted in figure S5, together with the UV/IR/UV spectrum measured for chromone-methanol.

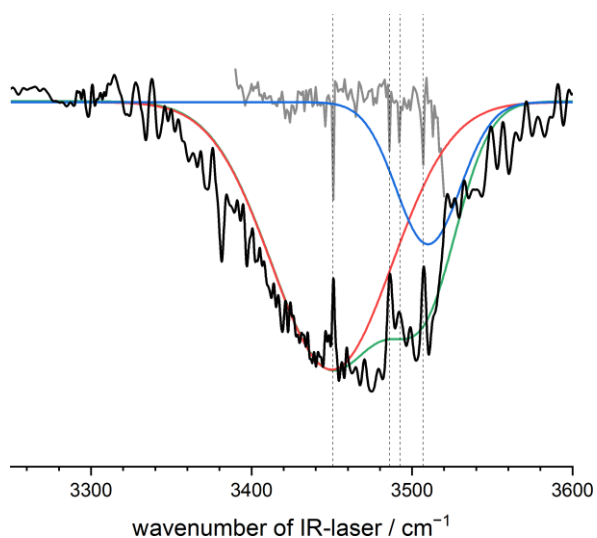


Figure S5: Laser power curve (grey trace) in comparison with the UV/IR/UV spectrum measured on the chromone-methanol trace. The correlation between the dips in the IR laser power curve and the discussed spikes observed in the IR experiment is illustrated by dashed grey lines.



Regarding the IR/R2PI and UV/IR/UV spectra of chromone-methanol a deconvolution with gaussians was performed (figure S6) to obtain a rough estimate for the relative population of the two competing isomers in the  $S_0$  and  $T_1$  state. For the  $S_0$  state the ratio of both peak integrals amounts to 72:28 in favor of the outside isomer. Correcting for the different IR intensity of the bands results in a ratio of 66:34. Similarly, for the  $T_1$  state, a ratio of 78:22 (uncorrected) and 72:28 (corrected) is obtained. Importantly, these values should only be understood as a rough estimate since other relevant factors as R2PI cross-sections, cooling efficiency and depletion efficiency cannot be addressed. Nevertheless, we can expect the increase in outside population to roughly match the increase in  $\Delta E$  for the triplet state, which can be calculated by applying the Boltzmann formula, under the daring assumption that the temperatures in the  $S_0$  and  $T_1$  state are comparable. The preference for the outside isomer is clearly visible in the presented data, as well as the further increased population of the outside isomer in the excited state (see below). Interpretation of this value is difficult due to the inherent experimental errors. Nevertheless, the experimental prediction is close to the DLPNO-CCSD(T) value of 0.636, but differing significantly from the DFT value of 0.382 (DFT).

$$\frac{N(out)}{N(in)} = \exp(-\Delta E/RT)$$

$$\ln\left(\frac{N(out)}{N(in)}\right) = -\Delta E/RT$$

$$\frac{\ln\left(\frac{N(out, S_0)}{N(in, S_0)}\right)}{\ln\left(\frac{N(out, T_1)}{N(in, T_1)}\right)} = \frac{-\Delta E(S_0)/RT}{-\Delta E(T_1)/RT} = \frac{\Delta E(S_0)}{\Delta E(T_1)} = 0.702$$

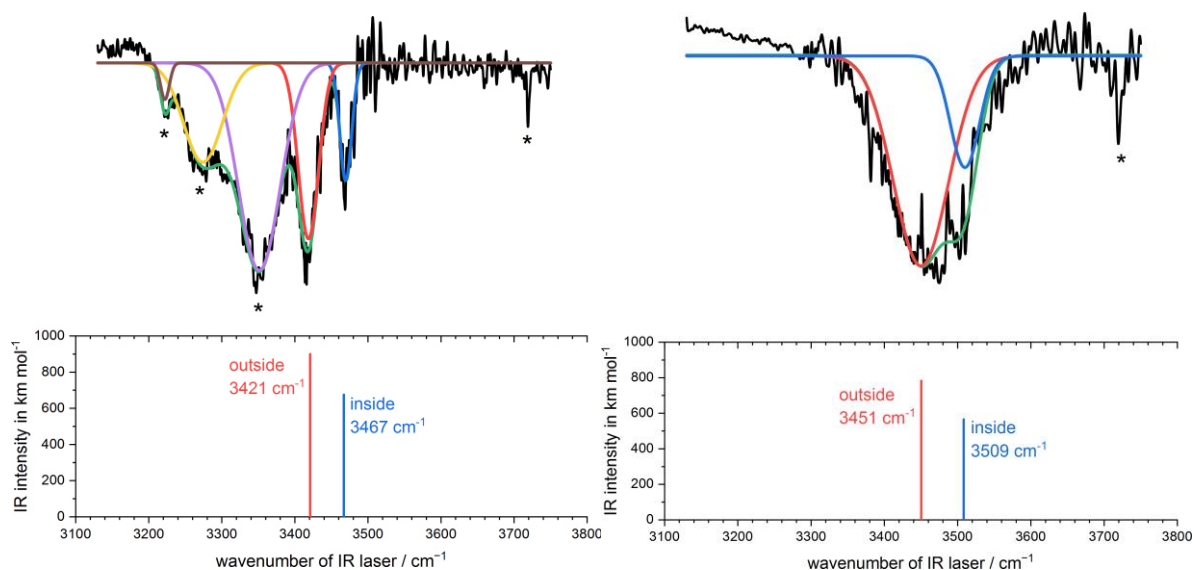


Figure S6: Theoretical and experimental IR spectra for the  $S_0$  (left) and  $T_1$  (right) state including gaussian fit functions to evaluate relative isomer populations. The convolution of all peaks (green) is composed of the inside (blue) and outside (red) peak with additional fragmentation peaks (purple, yellow, brown). Calculated OH stretching frequencies are obtained at CAM-B3LYP-D3(BJ)/def2-TZVP level, scaled by 0.95.

In the main manuscript, the experimental IR/R2PI were compared with the three energetically lowest structures since already the ether-bound cluster is energetically strongly disfavored compared to the carbonyl-bound clusters. Here, a full comparison of the experimental spectrum with all nine calculated isomers is shown (figure S7). All energetically less favored structures ( $\Delta E > 15 \text{ kJ mol}^{-1}$ ) show a strongly blue-shifted OH stretching vibration relative to the experiment. Furthermore, the IR intensity of the considered vibration is significantly lowered because no coordination with the highly polar carbonyl group takes place. Thus, only the first two isomers are taken into consideration.

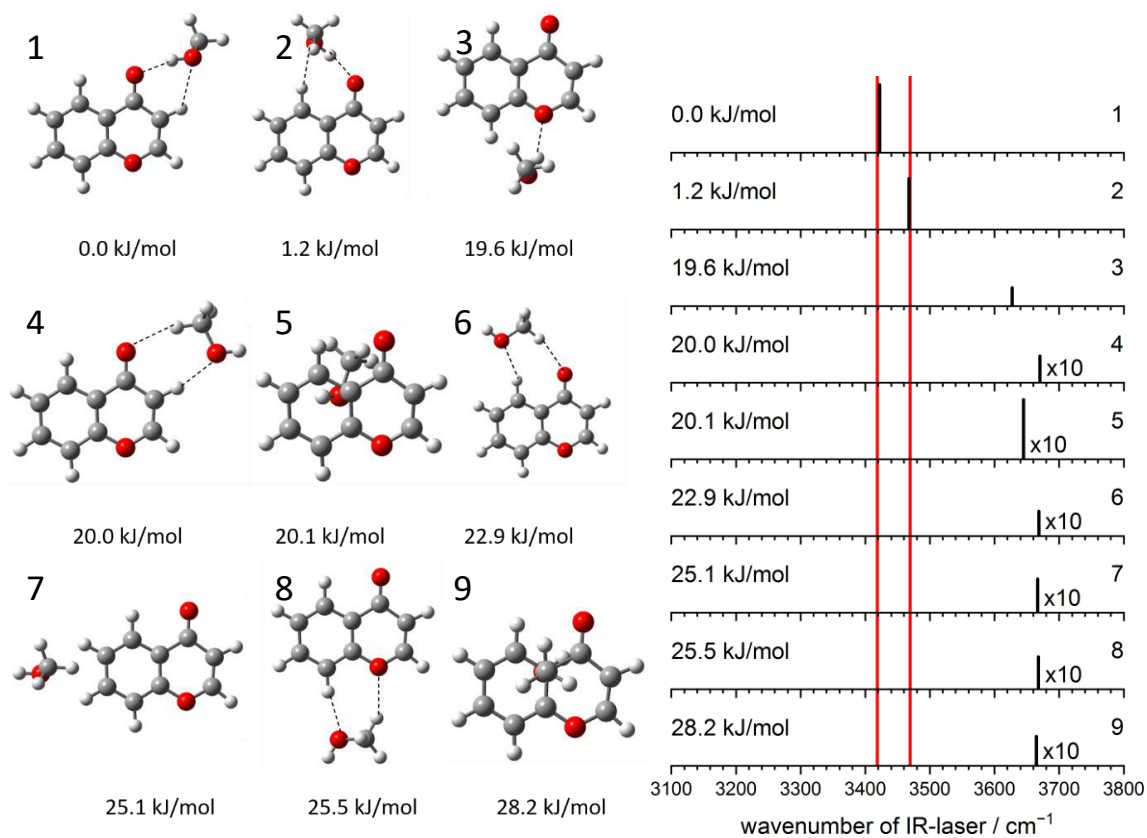


Figure S7: Calculated structures of chromone-MeOH with their respective electronic energies (left) and their respective IR spectra (right), compared with the experiment (red lines), showing that the carbonyl-bound structures exhibit the observed red-shift of the OH stretching band. Geometry optimizations and harmonic frequency calculations were performed at CAM-B3LYP-D3(BJ)/def2-TZVP level. Vibrational frequencies are scaled by 0.95.

### IR/R2PI experiments on higher clusters

We also investigated the chromone-(MeOH)<sub>2</sub> complex in the electronic ground state, with the quantum chemical calculations identifying multiple structure types. For all energetically relevant isomers, a first methanol molecule is linked to the carbonyl group of the chromone unit. The additional methanol molecule is either hydrogen-bonded to the first solvent molecule (isomers 1-10 in figure S9) or can occupy another free binding site of chromone, such as the second free electron pair at the carbonyl oxygen atom (isomers 11-12 in figure S9). Hereby, the calculations clearly show that the first option is energetically advantaged, with a strong preference for the outside binding motif in comparison to the inside type. However, the measured spectrum (in figure S8) is not well resolved, so that we are not able to assign one specific structure to the experiment. Nevertheless, the outside-bound isomers 1 and 2, which are further stabilized *via* C–H···O contacts between chromone and the additional methanol molecule, exhibit the right pattern to be correlated to the spectrum, while (minor) contributions of other isomers, especially isomers 3-5 with occupation of the inside pocket, cannot be excluded. Finally, we cannot assign a specific outside-bound cluster, but may state that this motif contributes strongly to the experimental spectrum. This is further supported by the relative energy, which assigns the global minimum to these structures.

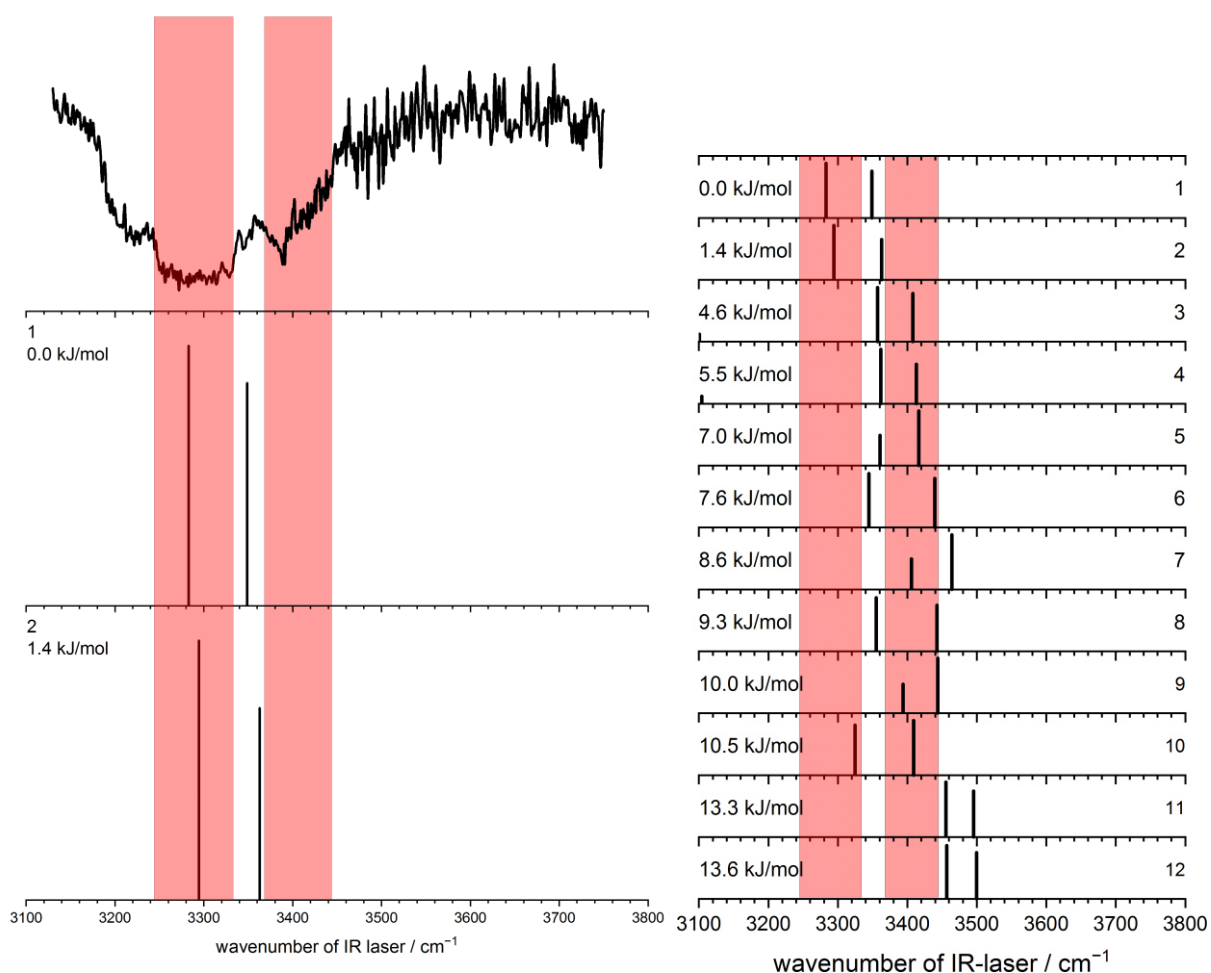


Figure S8: IR/R2PI spectrum of chromone-(MeOH)<sub>2</sub> compared with two calculated spectra of outside-bound clusters (left). A comparison with the IR spectra of all calculated structures is shown on the right, the red areas representing the broad features between 3244/3332 cm<sup>-1</sup> and 3368/3445 cm<sup>-1</sup>. The given energies refer to electronic energies. The two outside-bound structures may correlate with the observed experimental pattern, especially the most red-shifted band, although contributions of

other isomers cannot be excluded. Geometry optimizations and harmonic frequency calculations were performed at CAM-B3LYP-D3(BJ)/def2-TZVP level. Vibrational frequencies are scaled by 0.95.

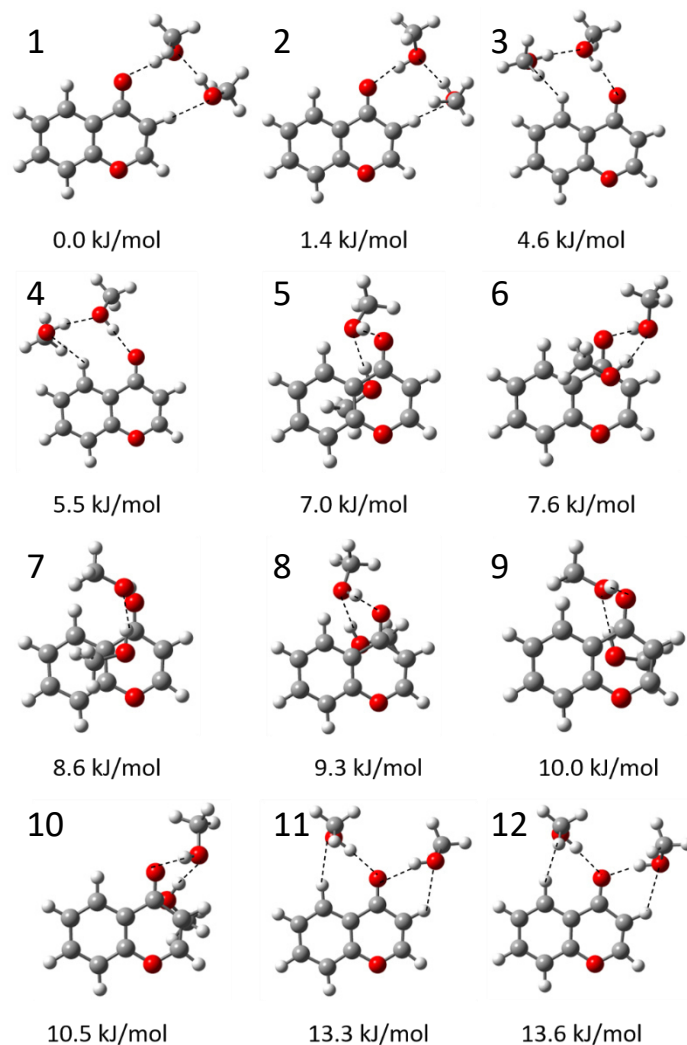


Figure S9: Optimized structures for the chromone-(MeOH)<sub>2</sub> cluster in the S<sub>0</sub> state with their respective electronic energies, as obtained at the CAM-B3LYP-D3(BJ)/def2-TZVP level.

## Theoretical results

### Further analysis of the excited states for chromone-methanol

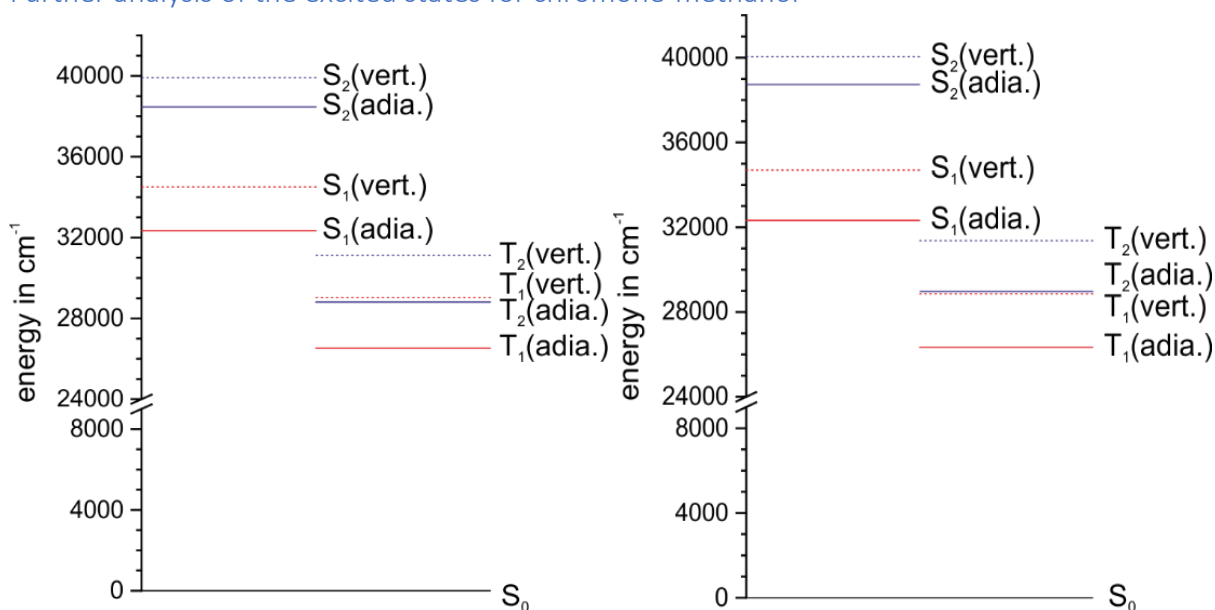


Figure S10: Jablonski diagram showing the first two singlet and triplet states, calculated at the TDDFT/CAM-B3LYP-D3(BJ)/def2-TZVP level; inside binding motif (left) and outside binding motif (right).

To analyze the electronic excitation and subsequent intersystem crossing, we calculated the excitation energies (figure S10) and natural transition orbitals (figures S11-S14) for the inside and outside isomers, for the first two excited singlet and triplet states using TDA-TDDFT/CAM-B3LYP/def2-TZVP. The usage of the Tamm-Dancoff approximation instead of the Random-Phase approximation was necessary to converge the calculations for the triplet states, while CAM-B3LYP was required to converge the excited singlet states. We observe a significant deviation from the experimental values since the band at  $33292\text{ cm}^{-1}$  is assigned to the  $S_2$  state, which is calculated at  $39916\text{ cm}^{-1}$  (inside) and  $40043\text{ cm}^{-1}$  (outside), respectively. Considering the character of the vertical excitations within the singlet manifold, we can state that the  $S_0 \rightarrow S_1$  transition is of  $n, \pi^*$  type, while the  $S_0 \rightarrow S_2$  transition is of  $\pi, \pi^*$  type. The calculations confirm the weakness of the  $S_0 \rightarrow S_1$  transition, with a oscillator strength, which is weaker by a factor of around 8000 in comparison to the  $S_0 \rightarrow S_2$  transition. The  $S_0 \rightarrow S_2$  transition is of similar strength for the inside and outside motif. This should result in a negligible influence on the R2PI cross section, as mentioned in the main manuscript. Natural transition orbitals (NTO)<sup>3</sup> were calculated and are shown below (figures S11-S14). For the triplet manifold the  $S_0 \rightarrow T_1$  transition is of  $\pi, \pi^*$  type while the  $S_0 \rightarrow T_2$  transition is of  $n, \pi^*$  type. Interestingly, the  $T_2$  and  $S_2$  state are of different character, which could serve as an explanation for the observed strong intersystem crossing according to the rule of El-Sayed<sup>4</sup>, leading to the assignment of an  $S_2(\pi, \pi^*) \rightarrow T_2(n, \pi^*)$  intersystem crossing with subsequent internal conversion into the  $T_1$  state, contradicting the assignment of the  $^3(n, \pi^*)$  state as the lowest triplet state.<sup>1</sup> The energetic difference between the unrelaxed  $S_2$  state and relaxed  $T_1$  state amounts to  $13387\text{ cm}^{-1}$  or  $160\text{ kJ mol}^{-1}$  (inside) and  $13709\text{ cm}^{-1}$  or  $164\text{ kJ mol}^{-1}$  (outside), respectively. At this point it should also be noted that the  $T_1$  state is definitely reached in the performed experiment, since the vibrational frequencies predicted for the chromone-methanol cluster in its  $T_2$  state [ $3625\text{ cm}^{-1}$  (inside),  $3651\text{ cm}^{-1}$  (outside),  $3612\text{ cm}^{-1}$  (ether)] do not correlate with the measured UV/IR/UV spectrum.

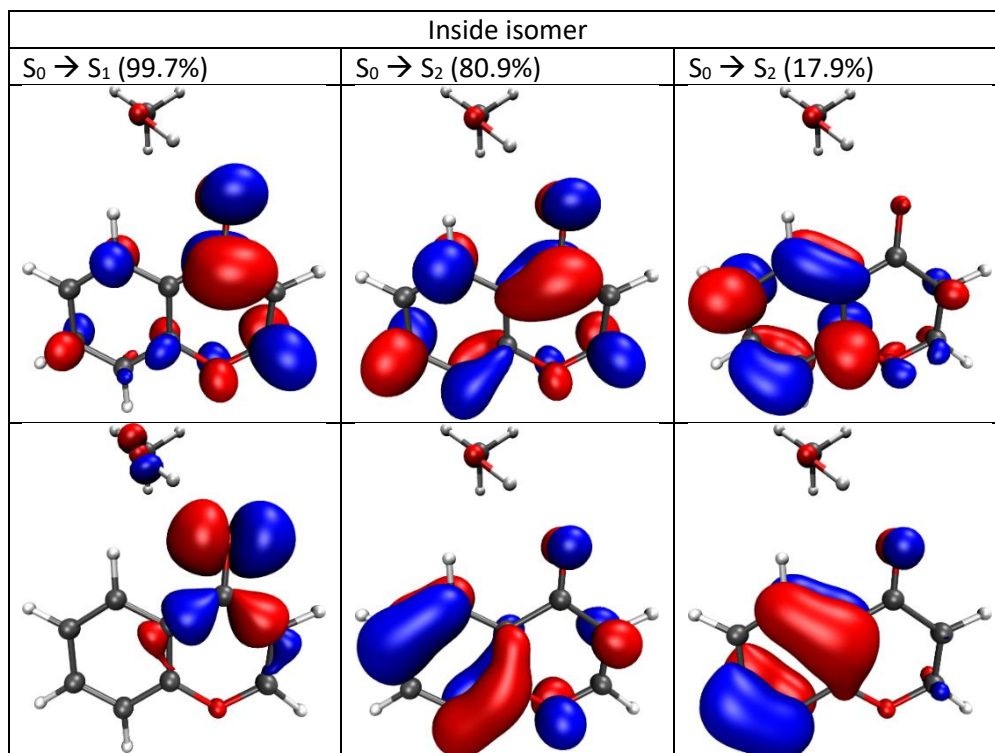


Figure S11: Natural transition orbitals, with occupied (bottom) and virtual (top) orbitals.

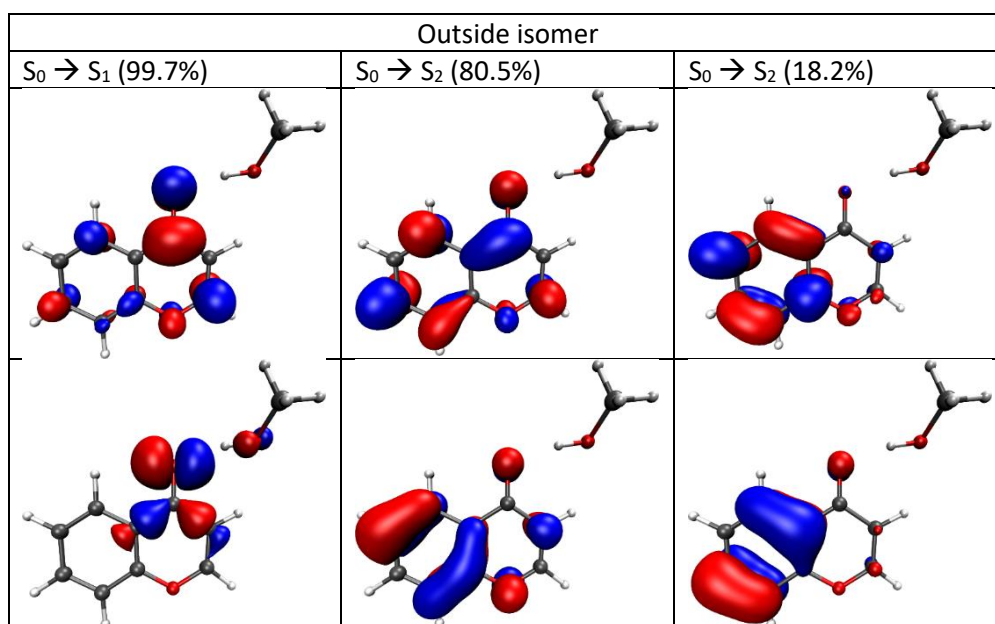


Figure S12: Natural transition orbitals, with occupied (bottom) and virtual (top) orbitals.



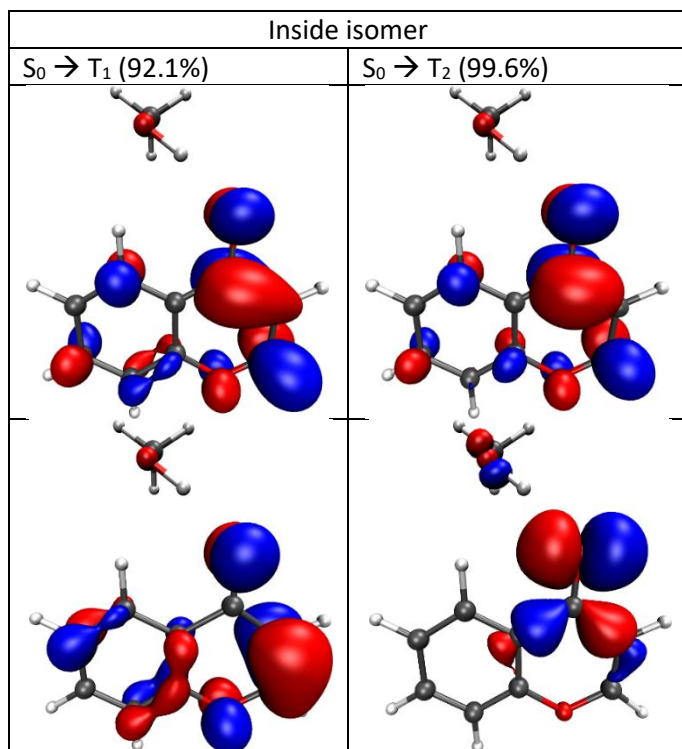


Figure S13: Natural transition orbitals, occupied (bottom) and virtual (top) orbitals.

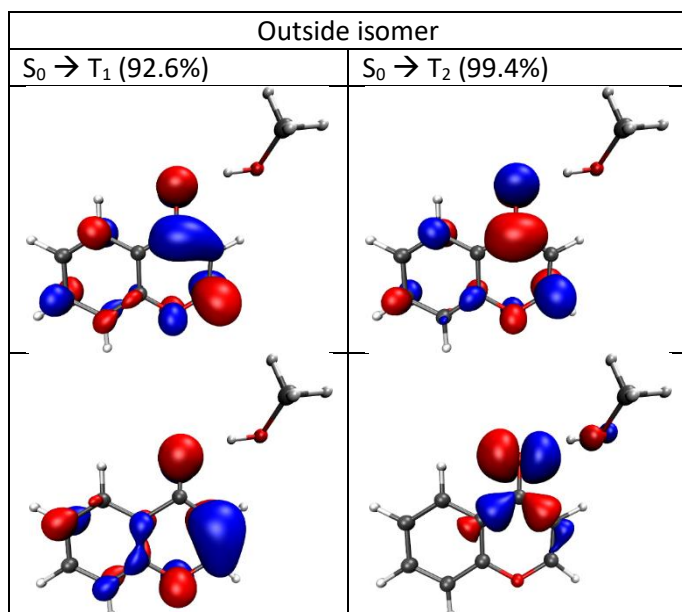


Figure S14: Natural transition orbitals, with occupied (bottom) and virtual (top) orbitals.

In the main manuscript, we refer to the triplet geometries calculated *via* UDFT not TDA-TDDFT, thus we performed TD-DFT calculations utilizing UDFT geometries to confirm that the order of the two triplet states is the same, which is indeed the case. The UDFT calculations allow us to handily extract the spin densities, which are plotted below (figure S15). The spin density is strongly localized on the distorted 4-pyrone ring of the chromone moiety, especially on the carbon atom next to the ether oxygen.

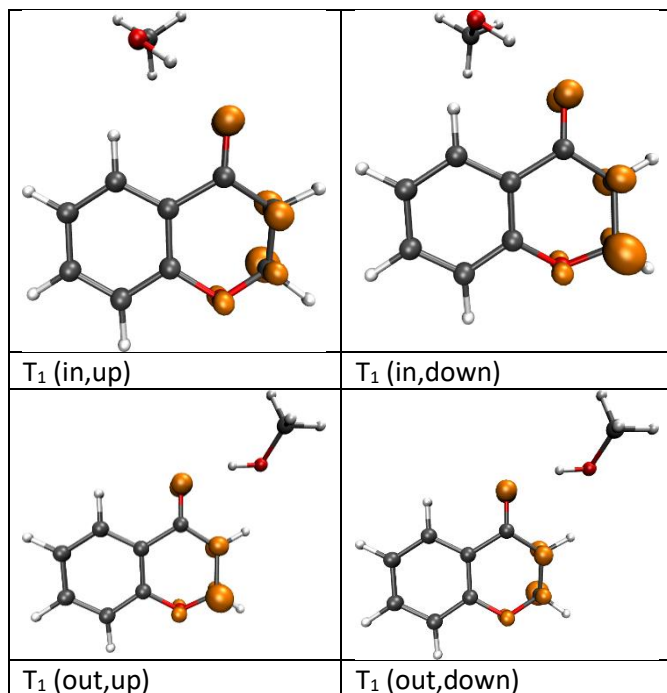


Figure S15: Spin densities of chromone-MeOH in the T<sub>1</sub> state, which are localized onto the 4-pyrone ring of the chromone molecule.

#### Further analysis of the T<sub>1</sub> state

The description of the lowest triplet state (T<sub>1</sub>) is possible by either TD-DFT, using the S<sub>0</sub> as reference or UDFT, using the triplet state as reference. Both methods result in the loss of planarity of the 4-pyrone ring (see figure S16), resulting in “up” and “down” isomers for the triplet state. “Up” is referring to the geometry where the puckered carbon atom is on the same side of the 4-pyrone plane as the solvent molecule, “down” for the inverse configuration. Comparing the geometries calculated by TD-DFT (in red) and UDFT (in blue), the geometric distortion is much more pronounced for the latter (see figure S17). Both methods have in common that the geometric distortion is completely localized onto the 4-pyrone ring, which is demonstrated in figure S17, where all eight possible structures are displayed (UDFT/TD-DFT, in/out, up/down).

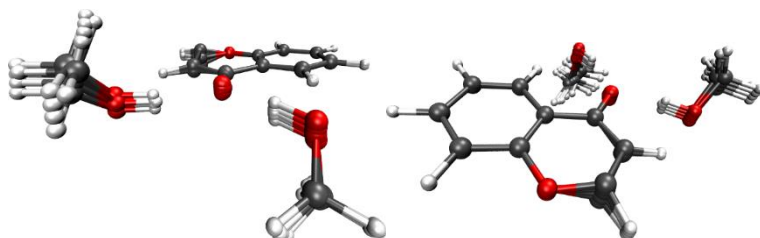


Figure S16: Overlay of all triplet structures, showing the conservation of the benzene ring planarity in chromone



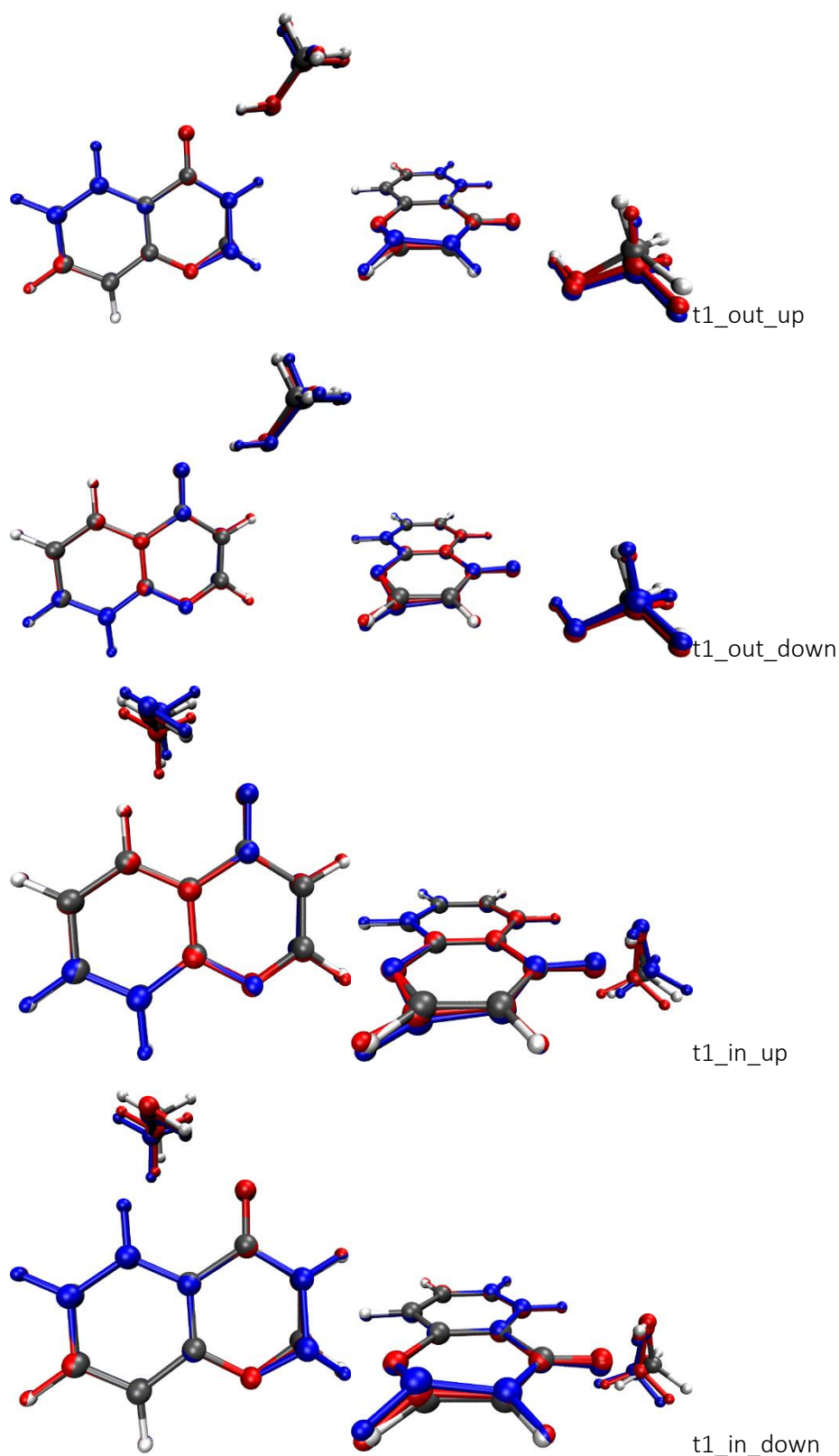


Figure S17: Overlay of multiple structures of chromone-MeOH, ground state (standard colors), TDDFT (red) and UDFT (blue), indicating that ring puckering is stronger in the UDFT case. From top to bottom: outside, up / outside,down / inside,up / inside,down. The stronger distortion of the 4-pyrone ring for the UDFT geometries is clearly visible as well as the conservation of the still planar aromatic ring.

To compare the quality of both approaches, SAPTO/jun-cc-pVTZ and DLPNO-CCSD(T)/def2-TZVP calculations were performed on the relaxed geometries, with the results shown in table S1.

Table S1: Comparison of electronic energies calculated with SAPTO/def2-TZVP and DLPNO-CCSD(T)/def2-TZVP for UDFT and TD-DFT inside/outside geometries in their respective up/down configuration, indicating that UDFT provides a better description of the system since TD-DFT geometries provide worse results (higher energy or failing) in most cases. The relative energies are in reference to the lowest energy of the outside,down structure obtained by UDFT.

Geometry	in	in	out	out	in	in	out	out
Puckering	up	down	up	down	up	down	up	down
Method	UDFT	UDFT	UDFT	UDFT	TD-DFT	TD-DFT	TD-DFT	TD-DFT
E(SAPTO) in kJ/mol	<b>-21.84</b>	<b>-21.82</b>	<b>-24.15</b>	<b>-24.25</b>	n. a.	<b>117.97</b>	<b>-27.86</b>	<b>-27.85</b>
$\Delta E$ (DLPNO-CCSD(T)) in kJ/mol	<b>2.69</b>	<b>2.39</b>	<b>0.07</b>	<b>0.00</b>	<b>7.73</b>	<b>7.30</b>	<b>5.53</b>	<b>5.63</b>

The data show that the UDFT geometries are able to describe both up and down isomers for the inside and outside structures in a satisfactory manner. The relative energies for the outside structure are around 3 kJ/mol higher using the UDFT geometry, but the TD-DFT geometries fail to provide meaningful SAPTO values for inside structures. The DLPNO-CCSD(T) results support this conclusion: The description with TDDFT leads to around 5 kJ/mol higher energies for both isomers, indicating that UDFT provides a better description of the global minimum. Thus, for further analysis in the main manuscript as well as in the supporting information, the UDFT geometries are used.

Still, the question whether the up and down isomer differ significantly remains to be answered. Comparisons of the relative energies and frequencies obtained by UDFT as well as the relative energies obtained *via* SAPTO and LED-DLPNO-CCSD(T) are shown in table S2. No method estimates a  $\Delta E$  greater than 0.3 kJ/mol between the up and down conformation so that the in and out motifs can be interpreted as doubly-degenerated states with respect to the ring puckering. Both configurations exhibit nearly equal OH stretching frequencies, thus differentiating between both structures in the experimental spectrum is not possible.

Table S2: Comparison of energies and frequencies obtained by UDFT, SAPTO and DLPNO-CCSD(T) for the up/down configurations of both inside and outside motif. The corresponding spin expectation value of the UDFT calculation does not show significant spin contamination.

Geo	Puckering	$\langle S^2 \rangle$	$\Delta E$ (UDFT)	$\tilde{\nu}$ (OH) in $\text{cm}^{-1}$	$\Delta E$ (SAPTO) in kJ/mol	$\Delta E$ (DLPNO-CCSD(T)) in kJ/mol
in	up	2.025	0.15	3690	0	0.30
in	down	2.025	0	3693	0.02	0
out	up	2.024	0.02	3635	0.10	0.07
out	down	2.024	0	3632	0	0

A detailed discussion of the energy decomposition analysis obtained *via* SAPTO can be found in the main manuscript, while a complete decomposition of the SAPTO energy is given in table S3. To simplify discussion, only the slightly more stable down configuration is considered when analyzing the triplet states. The results of the LED-DLPNO-CCSD(T) method are discussed in the following.

Table S3: Results of energy decomposition analysis by SAPT0/jun-cc-pVDZ. The raw values for each interaction for the respective electronic state and isomer (col. 2-5), the energy difference between the *inside* and *outside* isomer for each interaction (col. 6,7) and the change in  $\Delta E$  going from the  $S_0$  to  $T_1$  state (col. 8). A detailed explanation and derivation of all contributions can be found in literature.<sup>5</sup> The electrostatic and exchange contribution only consist of one term, the induction interaction consists of three terms  $E_{ind,resp}^{(20)}$ ,  $E_{exch-ind,resp}^{(20)}$ ,  $\delta_{HF}^{(2)}$ . The dispersion interaction is split into  $E_{disp}^{(20)}$  and  $E_{exch-disp}^{(20)}$ , which can be separated further into same-spin and opposite-spin parts. All values in kJ/mol.

	Inside (S0)	Outside (S0)	Inside (T1)	Outside (T1)	$\Delta E(S0)$	$\Delta E(T1)$	$\Delta\Delta E(S0,T1)$
$E_{elst}$	-57.9	-60.4	-43.5	-50.8	2.5	7.3	4.8
$E_{elst}^{(10)}$	-57.9	-60.4	-43.5	-50.8	2.5	7.3	4.8
$E_{exch}$	57.5	58.7	50.4	56.5	-1.2	-6.1	-4.8
$E_{exch}^{(10)}$	57.5	58.7	50.4	56.5	-1.2	-6.1	-4.8
$E_{ind}$	-18.2	-18.9	-13.5	-16.0	0.6	2.4	1.8
$E_{ind,resp}^{(20)}$	-24.1	-27.0	-19.3	-24.0	2.9	4.7	1.8
$E_{exch-ind,resp}^{(20)}$	13.4	15.8	11.6	14.7	-2.4	-3.1	-0.6
$\delta_{HF}^{(2)}$	-7.5	-7.7	-5.9	-6.7	0.2	0.8	0.6
$E_{disp}$	-16.4	-15.2	-15.2	-14.0	-1.3	-1.2	0.0
$E_{disp}^{(20)}$	-20.0	-18.9	-18.2	-17.3	-1.1	-0.9	0.2
$E_{exch-disp}^{(20)}$	3.5	3.7	2.9	3.3	-0.2	-0.4	0.5
$E_{disp,SS}^{(20)}$	-10.0	-9.4			-0.5		
$E_{disp,OS}^{(20)}$	-10.0	-9.4			-0.5		
$E_{exch-disp,SS}^{(20)}$	2.0	2.1			-0.1		
$E_{exch-disp,OS}^{(20)}$	1.5	1.6			-0.1		
$E_{tot}$	-35.1	-35.7	-21.8	-24.2	0.6	2.4	1.8

Table S4: Energy decomposition analysis with LED-DLPNO-CCSD(T)/def2-TZVP,  $\Delta E_{geo-prep}$  is the energetic penalty for distorting the monomers into the dimer geometry,  $\Delta E_{el-prep}^{ref.}$  is the electronic preparation in the reference (Hartree-Fock),  $E_{elstat}^{ref.}$  and  $E_{exch}^{ref.}$  describe the electrostatic and exchange inter-fragment contributions in the reference (HF), while  $E_{disp}^{C-CCSD}$  describe the dispersive contribution from the correlation energy.  $\Delta E_{non-disp}^{C-CCSD}$  contains some electronic preparation from the correlation energy, but also any non-dispersive correlation energy (charge transfer, intrafragment double excitations and singles contributions).  $\Delta E_{int}^{C-(T)}$  describes the change for the triples correction.  $\Delta(S_0)$  and  $\Delta(T_1)$  describe the difference between inside and outside isomer for each contribution, with positive values indicating a preference for the outside isomer. All values in kJ/mol.

	Inside ( $S_0$ )	Outside ( $S_0$ )	Inside ( $T_1$ )	Outside ( $T_1$ )	$\Delta(S_0)$	$\Delta(T_1)$
$\Delta E_{geo-prep}$ (Chromon)	0.6	0.3	0.2	-0.2	0.3	0.5
$\Delta E_{geo-prep}$ (MeOH)	0.1	0.2	0.2	0.5	-0.2	-0.3
$\Delta E_{el-prep}^{ref.}$ (Chromon)	92.5	95.9	72.5	81.9	-3.4	-9.3
$\Delta E_{el-prep}^{ref.}$ (MeOH)	82.0	81.8	70.8	77.4	0.3	-6.6
$E_{elstat}^{ref.}$	-166.1	-171.3	-135.1	-154.8	5.1	19.7
$E_{exch}^{ref.}$	-29.1	-29.1	-26.3	-28.1	0.0	1.9
$\Delta E_{non-disp}^{C-CCSD}$	3.9	3.3	5.8	6.9	0.5	-1.1
$E_{disp}^{C-CCSD}$	-13.7	-12.7	-14.0	-12.5	-1.1	-1.5
$\Delta E_{int}^{C-(T)}$	-2.0	-2.0	-1.5	-0.7	-0.1	-0.8
$\Delta E$ (total)	-31.9	-33.4	-27.4	-29.7	1.5	2.4

As discussed above and in the main manuscript, LED-DLPNO-CCSD(T) predicts the outside isomer as the more stable isomer both in the  $S_0$  and  $T_1$  state. Although SAPT0 and LED-DLPNO-CCSD(T) are difficult to compare directly due to their different approach (SAPT: perturbative, DLPNO: supramolecular), careful analysis is still possible. This shows *e.g.* that, similar to the SAPT0 values, the electrostatic interaction is the strongest attractive interaction with dispersion being significantly weaker. Comparing the contributions for the inside and outside isomer, nearly all contributions are equal in value except the attractive electrostatic interaction as well as the related electronic preparation of the chromone. This can be interpreted as better orbital overlap between the carbonyl group and the OH group of the methanol for the outside motif, resulting in a stronger hydrogen bond and overall higher binding energy in the  $S_0$  state. Analyzing the  $T_1$  state confirms the main theses in the main manuscript. The  $\Delta E$  is mostly influenced by the electronic preparation of both MeOH and chromone as well as the electrostatic interaction. Although the electronic preparation penalty is higher for the outside isomer by 9.3 and 6.6 kJ/mol (15.9 kJ/mol total), this is more than compensated by the increased electrostatic contribution of 19.7 kJ/mol resp. to the inside isomer. We observe again a side dependence in the triplet state, resulting in significantly increased electronic

preparation for the methanol, adapting to the flexible outside pocket. Furthermore, the binding energy is lowered upon electronic excitation, again coinciding with SAPTO results. Finally, the negative geo-prep energy for the chromone molecule is of course unphysical. Since the deformation energy seems to be quite small (< 0.5 kJ/mol), this numeric error occurs due to the accuracy of the DLPNO-CCSD(T) method. Deformation energies calculated by DFT are discussed in the following, and confirm this hypothesis.

### Binding and deformation energies

The OH stretching frequency of an H-donor is closely related to the strength of the hydrogen-bond established with the H-acceptor. Thus, the observed blue-shift of the OH stretching frequency switching from the  $S_0$  to the  $T_1$  state should be visible in binding energy calculations. The binding energy is calculated in following manner:

$$E_{BDE} = E'_{Chromon} + E'_{MeOH} - E_{Dimer}$$

with:  $E'_{Chromon}, E'_{MeOH} =$  Energy of resp. molecule in the dimer geometry

For the discussion of the BDE, we deliberately chose not to apply a BSSE correction. A comparing simulation for the  $S_0$  geometries reveals that the difference between “inside” and “outside” is insignificant (both: 3.9 kJ/mol). Furthermore, it is known that the usual counter-poise correction<sup>6</sup> scheme can lead to deviations from the true BDE<sup>7</sup>. Finally, the deformation energy is calculated in a similar manner by taking the energy difference of the relaxed monomer and the monomer in the dimer geometry.

Table S5: Binding and deformation energies for the chromone-MeOH cluster for the  $S_0$  and  $T_1$  state for both geometries (inside/outside). For the triplet state, the puckering of the 4-pyrone ring is also considered. All values are given in kJ/mol.

State	Geo	Puckering	Method	BDE	$E_{Def}(Chromon)$	$E_{Def}(MeOH)$
$S_0$	in	-	DFT	40.2	0.8	0.5
$S_0$	out	-	DFT	41.2	0.5	0.6
$T_1$	in	up	UDFT	35.5	0.6	0.3
$T_1$	in	down	UDFT	35.6	0.6	0.4
$T_1$	out	up	UDFT	38.6	0.2	0.4
$T_1$	out	down	UDFT	38.6	0.2	0.4

Starting with the deformation energies, it is remarkable how all values are below 1 kJ/mol, indicating low barriers for reorganization. The binding energy is strongest for the outside isomer in general, which is reasonable, since it is the global minimum. The observed blue-shift of the OH stretching frequency can be explained by the reduced binding energy in the triplet state, while the larger splitting of the frequencies of the two relevant isomers is caused by the increased difference in binding energy from 1 kJ/mol to 3 kJ/mol.

### Barriers for isomer interconversion

As explained in the main manuscript, the interconversion barriers between different isomers were calculated by relaxed scans along an appropriate coordinate with the results shown below (fig. S18-22).

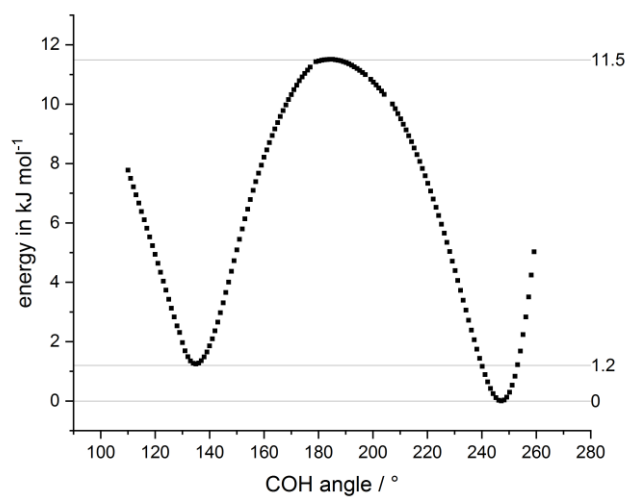


Figure S18: Interconversion barrier between inside and outside isomer in the S0 state

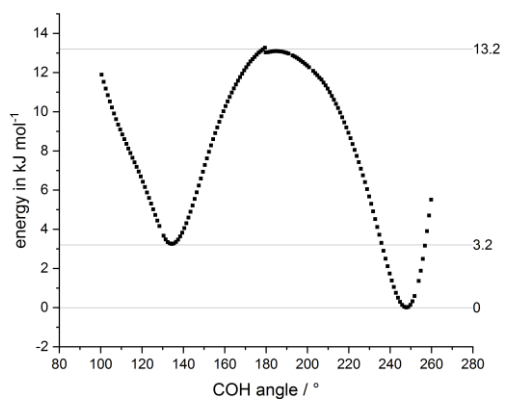


Figure S19: Interconversion barrier between inside and outside isomer in the T1 state (down configuration)

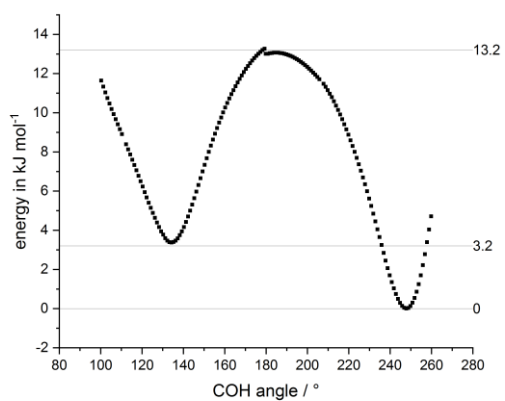


Figure S20: Interconversion barrier between inside and outside isomer in the T1 state (up configuration).

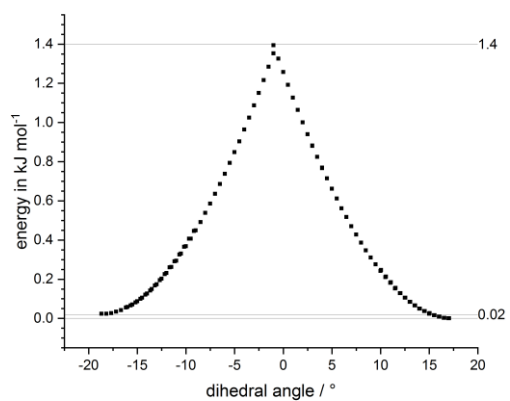


Figure S21: Interconversion barrier between up and down isomer in the T1 state (outside motif), the lowest line denotes the zero (omitted for clarity).

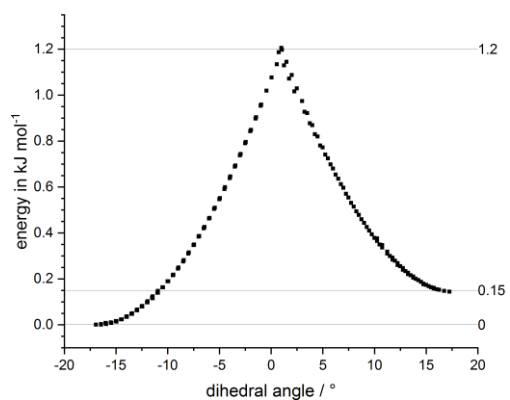


Figure S22: Interconversion barrier between up and down isomer in the T1 state (inside motif)

## References

- 1 T. Itoh, *J. Photochem. Photobiol. A: Chem.*, 2010, **214**, 10–15.
- 2 K. Bartl, A. Funk and M. Gerhards, *ChemPhysChem*, 2009, **10**, 1882–1886.
- 3 R. L. Martin, *J. Chem. Phys.*, 2003, **118**, 4775–4777.
- 4 M. Baba, *J. Phys. Chem. A*, 2011, **115**, 9514–9519.
- 5 B. Jeziorski, R. Moszynski and K. Szalewicz, *Chem. Rev.*, 1994, **94**, 1887–1930.
- 6 S. F. Boys and F. Bernardi, *Mol. Phys.*, 2006, **19**, 553–566.
- 7 a) J. R. Alvarez-Idaboy and A. Galano, *Theor. Chem. Acc.*, 2010, **126**, 75–85; b) A. Galano and J. R. Alvarez-Idaboy, *J. Comput. Chem.*, 2006, **27**, 1203–1210; c) J. C. López, J. L. Alonso, F. J. Lorenzo, V. M. Rayón and J. A. Sordo, *J. Chem. Phys.*, 1999, **111**, 6363–6374; d) H. Valdés and J. A. Sordo, *J. Comput. Chem.*, 2002, **23**, 444–455; e) H. Valdés and J. A. Sordo, *J. Phys. Chem. A*, 2002, **106**, 3690–3701;



### 7.3 Manuscript draft [3]

#### Theoretical and Spectroscopic Investigations on Monovalent Cationic Metal-AcTrpOMe Clusters in the Gas Phase

Pol Boden, Philip Bialach, Markus Becherer, Kirsten Schwing, Markus Gerhards<sup>†</sup>

TU Kaiserslautern, Fachbereich Chemie & Research Center Optimas, Physikalische Chemie, Erwin-Schroedinger-Straße 52, D-67663 Kaiserslautern, Germany

#### Abstract

In this work we performed a combined theoretical and spectroscopic study on the  $[\text{AlAcTrpOMe}]^+$  aggregate, in which a monovalent aluminium(I) ion is coordinated to the protected amino acid AcTrpOMe. The limited stability of Al(I) in combination with the potentially reactive NH group of the Trp side chain may lead to an increased reactivity within the system. Indeed, the performed (DFT-D3 based) conformational search revealed the occurrence of an uncommon and energetically particularly advantageous structure, with the aluminium ion being inserted into the NH bond of the indole substituent. In order to determine if this quite surprising structural motif may be unique to aluminium, geometry optimizations for the so-called “inserted” structure were performed for a series of monovalent metal ions:  $\text{Li}^+$ ,  $\text{Na}^+$ ,  $\text{K}^+$ ,  $\text{Rb}^+$ ,  $\text{Cs}^+$ ,  $\text{Mg}^+$ ,  $\text{Ti}^+$ ,  $\text{Zn}^+$ ,  $\text{Ag}^+$  and  $\text{Ga}^+$ . Indeed, the “inserted” structure seems to be only favoured for systems comprising Al or Ti.

For a comparison with experimental data an IR spectrum was measured in the NH stretching region for the  $[\text{AlAcTrpOMe}]^+$  aggregate/complex by applying the IR+UV technique in a molecular beam experiment. The resulting experimental data can only be explained by the presence of two distinct isomers. Additionally, the formation of the “inserted” structural motif can be postulated.

#### Keywords:

Metal-amino acid aggregates, density functional theory, IR+UV spectroscopy

## **Introduction**

Peptides generally exhibit a great conformational variety, which is responsible for their diverse roles in biochemistry. Their conformation highly depends on intrinsic factors like the sequence of amino acids in the peptide chain. Beyond, structure and functionality are further modulated by the (biological) environment which offers a variety of different aggregation partners (e.g. water as solvent or metal cations) (c.f. e.g. [1-3]). With regard to the latter, it should be noted that almost half of all proteins coordinate metals and thus form so-called metalloproteins (cf. e.g. [1,4]), which play an essential role in various biological processes (cf. e.g. [4]).

Despite their major relevance in nature, the influence of metals on biochemical activities has not been completely understood yet for many processes. In that context the structure-function relationship and thus the structure determination of metal ions bound to biological (macro)molecules is of enormous importance. Since the biological environment is complex it can help to start with a bottom up approach to investigate intrinsic structural properties of a system. The structural analysis of isolated amino acids, peptides and their aggregates with various binding partners (e.g. metal cations [5,6]) by theoretical (mainly DFT) calculations combined with laser spectroscopy in molecular beams can be an important building block of such a bottom up approach [2-4]. Within gas phase experiments, aggregates of (neutral) amino acids/peptides and metal cations are frequently generated by e.g. ESI sources and stored in mostly non-cooled [7-16], but nowadays partly even in cold [17,18] ion traps for laser spectroscopic investigations. Alternatively, metal amino acid aggregates can be analysed within molecular beam experiments [6] which is less frequent than investigations in ion traps. The former requires a more sophisticated source set-up (cf. experimental section) combining e.g. thermal and ablation source.

Several analyses on amino acid metal aggregates under isolated conditions have been performed with a focus on the biologically relevant alkali and earth alkaline metals (e.g. [7-20]). However, in this publication and a former publication of our group [6] we focus on the aggregation behaviour of aluminium cations with protected amino acids. In contrast to alkali and alkaline earth metals like e.g.  $\text{Na}^+$ ,  $\text{K}^+$  or  $\text{Ca}^{2+}$ , aluminium cations have no direct biological function and are not essential. Nevertheless, since the 1970s aluminium is under suspicion to have neurotoxic activities. Indeed, extraordinary high aluminium concentrations are frequently observed in the brain tissue of Alzheimer patients [21-27]. In that context the role of aluminium as trace element in food and drinking water or in form of aluminium salts in everyday items (e.g. deodorants) was and is still controversially discussed.

Due to their limited stability the biological relevance of low valent Al(I) compounds is of course questionable. The low stability also explains the small number of reports on stable Al(I) organometallic

complexes [28-30]. Aluminium(I) can for example be stabilised by complexation with a  $\beta$ -diketiminato ligand (NacNac). Most interestingly, compounds with stable X-H bonds (with X = e.g. H, N, O) can be activated by these so-called NacNacAl complexes, commonly by oxidative addition, yielding aluminium hydride complexes [28,31]. Within this context, it should also be mentioned that isolated aluminium hydride clusters can be generated in a plasma, like e.g. in a pulsed arc cluster ionization source (PACIS), and have been characterised extensively. Performed structural investigations often revealed that geometries incorporating terminal Al-H bonds are among the most stable ones [32-38]. In another IR spectroscopic study on isolated  $\text{Al}^+(\text{CH}_4)_n$  ( $n=1-6$ ) clusters the possible occurrence of structures with an aluminium ion being inserted into the C-H bond of methane was predicted by theory, but the structures could not be found in the experiment [39]. However, IR (multiphoton) photodissociation studies on the isolated transition metal doped aluminium clusters  $\text{Al}_{10}\text{Rh}_2\text{H}_2^+$  and  $\text{Al}_{11}\text{Rh}_2\text{H}_2^+$  revealed the presence of structures comprising terminal Al-H bonds [40], as it is also the case for  $\text{Al}_2\text{H}_6$  embedded in a hydrogen matrix [41].

Against this background aluminium in its different oxidation states is an interesting aggregation partner for amino acids and peptides. Thus, we successfully started our investigations with the aggregation of  $\text{Al}^{+/3+}$  to the protected amino acid AcPheOMe, whose structural preferences as monomer, dimer [42] as well as in aggregates with up to three water molecules [43] were analysed in detail by our working group. In this publication we focus on the aggregation of aluminium to AcTrpOMe. The amino acid Trp differs from Phe by a rather large and  $\pi$ -electron rich [44] heterocyclic indole side chain, whose indolic NH group already causes a different self-aggregation behaviour in comparison to AcPheOMe [42,45]. This NH group offers a certain reactivity towards a metal cation as already realised in the early 1960s by the formation of indole Grignards [46]. Keeping the characteristics of the indole system and discussion of the insertion reactions of  $\text{Al}^+$  in mind, the influence of the side chain on the aggregation remains to be seen.

We have investigated the ionic cluster  $[\text{AlAcTrpOMe}]^+$  both theoretically, by performing geometry optimisations and harmonic frequency calculations at density functional theory (DFT-D3) level as well as CCSD(T) single point energy calculations, and experimentally, by measuring IR+UV photodissociation spectra [6] in a molecular beam apparatus. The theoretical studies were extended to analogous clusters of the type  $[\text{M(I)AcTrpOMe}]^+$  with selected metal centres (where M = Li, Na, K, Rb, Cs, Mg, Ti, Zn, Ag, Ga), to further elucidate the impact of the metal ion with its specific properties (such as redox properties and ion radii) on the structural behaviour and reactivity of the cluster.

### **Spectroscopic Methods**

The experimental spectra were recorded with a setup which was already used for the investigation of the aluminium AcPheOMe aggregates [6] and consists of a three chambered differentially pumped molecular beam apparatus. It is equipped with a reflectron-time-of-flight mass spectrometer and a molecular beam cluster source, which is comprised of a laser ablation source combined with a thermal source. Helium gas (99.999 %) at 2 bar (relative to atmospheric pressure) passes through a heated (up to about 130 °C) reservoir containing the investigated protected amino acid and is injected through a pulsed gas valve (General Valve, Iota One, 300  $\mu$ s/pulse, pulsed at 10 Hz), which is mounted in front of an aluminium block. Triggered by the gas valve, the radiation of a frequency doubled Nd:YAG laser (Lumonics HY 400, 13-15 mJ/pulse, 10 Hz) generates a plasma (containing aluminium ions) by perpendicularly hitting a rotating and translating aluminium rod inside of the aluminium block. This type of source is inspired by the established sources of Smalley [47-49] and Bondybey [50].

At the backside of the ablation source a stack of four electrode plates is attached which functions as a mass filter. The (IR and/or UV) laser beam(s) cross(es) the molecular jet perpendicularly between the second and third plate. About 80 ns after laser interaction a defined ion package is extracted with a voltage of 5 to 15 V, before the ions pass through a skimmer into the Re-TOF mass spectrometer. The investigated clusters are finally detected by an MCP detector. For further and detailed information see previous description [6].

For most cationic compounds, the common IR(M)PD method (e.g. [51-53]) has been successfully applied to elucidate the vibrations of the investigated systems. However, for strongly bound clusters the dissociation barrier may be too high to be surpassed by the absorption of one or a few IR photons. Another limiting factor can be that no efficient dissociative channel may be accessible by the excitation of a certain vibrational mode (dark modes). In such cases, the more complex IR+UV method, illustrated in Figure 1, is applied to enable cluster fragmentation if the IR laser is in resonance with a vibrational mode of the compound. An important advantage of this method is that only one IR photon is used (like in a "normal" IR spectrum) and no influences of multiphoton processes have to be taken into account [6].

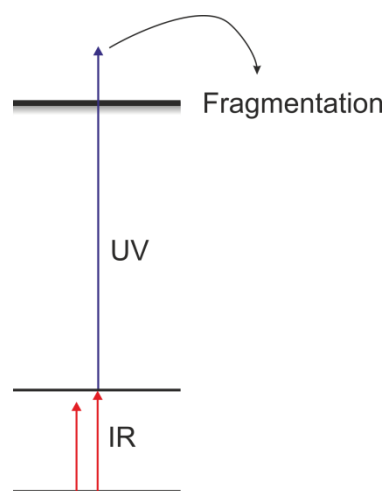


Figure 1: Scheme illustrating the applied IR+UV photofragmentation spectroscopy: The IR laser wavelength is tuned while the UV laser wavelength is fixed at a wavelength (about  $1000\text{ cm}^{-1}$ ) below the dissociation threshold of the cluster. If the IR laser is resonant with a vibrational mode of the aggregate a fragmentation is induced.

When employing the IR+UV method, first a UV photodissociation spectrum of the studied system has to be recorded. Next, the UV laser is set to a wavelength that is clearly lower (around  $1000\text{ cm}^{-1}$ ) than the dissociation limit of the cluster. In this way, no fragmentation can be induced by the UV laser radiation. But, depending on its wavelength, the tuned IR laser, being fired about 10 ns prior to the UV laser, may induce an excitation of a vibrational mode of the system. If the UV laser is fired within the lifetime of the vibrationally excited state (in the nanosecond region under isolated conditions) the sum of the energy of the IR and UV photons can exceed the dissociation limit (IR+UV effect). Thus, an IR depletion spectrum can be obtained by detecting the intensity of the parent ion signal as a function of the IR laser wavelength. For the experiments performed here, the UV radiation in the region of  $36400\text{--}36650\text{ cm}^{-1}$  is generated by a frequency-doubled dye laser, pumped by the second harmonic (532 nm) of a Nd:YAG laser (Innolas Spitlight 600, 10 Hz). The required IR laser radiation in the range of  $3150\text{--}3700\text{ cm}^{-1}$  is obtained by difference frequency mixing (DFM I) in a  $\text{LiNbO}_3$  crystal using the fundamental (1064 nm) of a seeded Nd:YAG laser (Quanta-Ray Pro-230, Spectra-Physics, 10Hz) and the output of a further dye laser (PrecisionScan, Sirah), which is pumped by the second harmonic (532 nm) of the same Nd:YAG laser. Amplification of the resulting IR radiation is generated by an optical parametric amplification (OPA) process in a further  $\text{LiNbO}_3$  crystal using the output of the DFM I process and the fundamental (1064 nm) of the Nd:YAG laser.

It should be mentioned that all the spectra presented here were obtained by performing difference measurements, *i.e.* after one or a few shots averaged with the tuned IR laser “on” the same number of shots with the IR laser “off” is recorded. The effect of the IR laser is finally acquired by subtracting both signals.

### **Theoretical methods and considerations**

Possible starting geometries for [AlAcTrpOMe]<sup>+</sup> were derived from molecular dynamics calculations with the consistent force field as implemented in the Discovery studio [54]. Additional input structures were manually constructed with Avogadro [55] and pre-optimized using the UFF (Universal Force Field) [56]. DFT geometry optimisations as well as harmonic vibrational frequency calculations were realised with the Gaussian09 [57] program package, applying the hybrid functional B3LYP together with the triple zeta basis set TZVP. These calculations were performed including the Grimme D3 dispersion correction [58]. For the resulting DFT energies of the energetically low lying structures relevant for discussion both zero point and basis set superposition error (BSSE) corrections [59] were considered. In case of structure A (cf. Figure 2) only ZPE corrections are taken into account (no reliable BSSE corrections can be performed). The remaining internal energy of the aggregates in the collision free region of the molecular beam is difficult to estimate since the molecular beam is expanded over a plasma which introduces additional internal energy. For amino acids and peptide systems with initial (source) temperatures of 350-500 K it was found that 300 K is a fair estimate to calculate Gibbs energies and thus to account for entropic contributions [3,60-62]. In our analysis we calculated Gibbs energies at 298.15 K. For energetically advantaged DFT-D3 optimised isomers DLPNO-CCSD(T) single point calculations were performed with ORCA 4.2.1 [63] using the def2-TZVP basis set, together with the corresponding def2-TZVP auxiliary basis set for the RI approximation. In addition, the options “TightPNO” [64] and “TightSCF” were applied.

In the way to enable structural assignments an extensive conformational search was performed (cf. SI), resulting in a huge structural variety due to the high flexibility of the investigated system with regard to possible backbone conformations and binding sites for the metal ion. A selection of the optimised geometries is depicted in Figure 2, together with the relative energies predicted by DFT-D3 and DLPNO-CCSD(T) calculations as well as the Gibbs free energies (at 298.15 K; calculated at the same DFT-D3 level).

Interestingly, the clearly most stable structure A (cf. Figure 2) shows a very unique, maybe unexpected binding motif where the aluminium(I) is not only linked to both carbonyl groups of the backbone but is at the same time inserted into the N-H bond of the indole substituent. It should be noted that, considering the relative energies calculated at the DLPNO-CCSD(T) level, this “inserted” structure is almost 5000 cm<sup>-1</sup> lower in energy than the most stable structure with an “intact” indolic NH group. The inclusion of entropy effects at 298.15 K slightly disfavours the rigid inserted structure. Nevertheless, within the computational accuracy it is still (along with isomer B) the most stable structure. Beyond, the inclusion of entropy does not lead to massive changes in the energetic order of

the isomers, so that in the following considerations we refer to the zero-point- and BSSE-corrected electronic energy values.

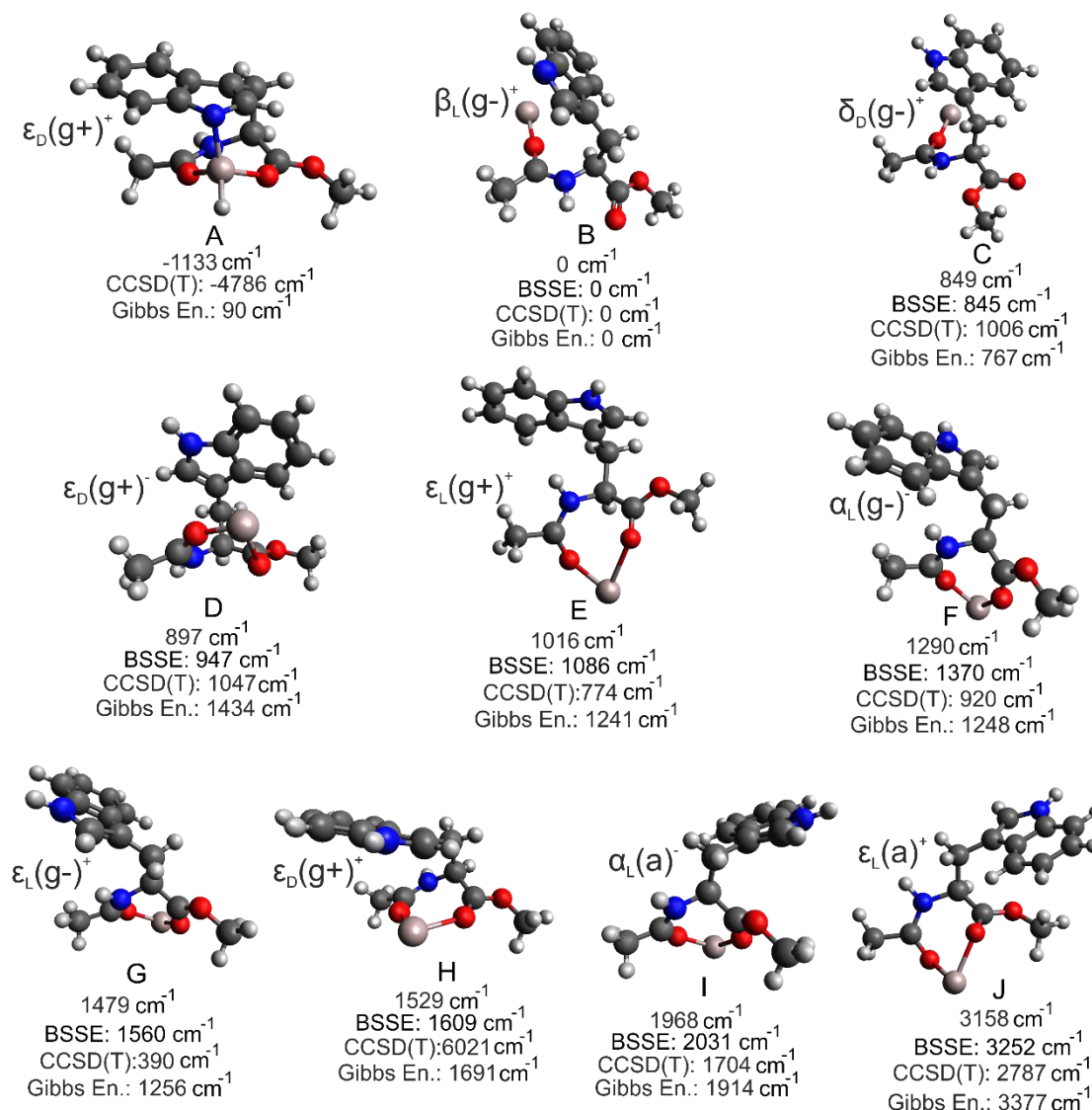


Figure 2: Selected structures of  $[AlAcTrpOMe]^+$  and their relative energies (obtained from DFT, BSSE-corrected DFT, DLPNO-CCSD(T), as well as the Gibbs free energies at 298.15 K (obtained from DFT; including BSSE-correction for all isomers except for structure A)), considered relative to the most stable intact geometry B.

Apart from this (at first sight) quite extraordinary structure A, the three most stable structures with an intact protected amino acid already reveal the special importance of the large, indolic  $\pi$ -system: It strongly stabilises the bound aluminium cation so that even isomers which are only singly bound to one carbonyl group are enormously stable (B) or can energetically compete (C) with a triply bound ( $2x$  CO plus  $\pi$ -interaction) conformer like D. Comparable observations were already made for clusters of alkali metals with the unprotected aromatic amino acids [7,19,20].

A further aspect of interest in metal aggregates is the charge delocalisation. Normally, metal cations are multiply coordinated (cf. [6,7,19,20]) to partly delocalise and thus stabilise their charge. As a consequence, the backbone of the amino acid can differ from its monomeric structure. This was demonstrated for AcPheOMe with the monomer having a stretched  $\beta_L$  structure whereas it is  $\alpha_L$  in the [AlAcPheOMe]<sup>+</sup> aggregates. The distortion of the backbone was overcompensated by the stabilisation achieved by the multiple coordination of the aluminum ion. The same seems to be true for the [AlAcTrpOMe]<sup>+</sup> system: Only isomer B conserves the  $\beta_L$  backbone structure of the AcTrpOMe monomer; however its calculated vibrations cannot describe the experimental spectrum (see further discussion below). In all other isomers the backbone conformation changes to enable the coordination of Al<sup>+</sup> and a partial delocalisation of the positive charge of the metal ion. The charge at the aluminum cation varies between 0.862 (for isomer H) and 0.908 (for isomer C) according to the NBO analysis (cf. SI). An exception is the inserted isomer A in which the charge increases up to 1.738 (cf. SI), so that aluminium approaches its most stable oxidation state (III). Therefore, the formation of isomer A can be considered as a kind of oxidative addition of the protected amino acid to the singly charged aluminum cation. As mentioned in the introduction, the oxidative additions of rather stable H-X bonds (X = H, Si, B, Al, C, N, P, O) to the Al(I) center of NacNacAl complexes (NacNac =  $\beta$ -diketiminato ligand) have already been characterised in solution [28,31]. On top of that, isolated aluminium hydride clusters, e.g. of the type Al<sub>n</sub>H<sub>m</sub><sup>+/-</sup>, with many of them incorporating terminal Al-H bonds, can be formed in a gas phase plasma [32-40].

With regard to its charge distribution but also its high stability isomer A seems to be quite extraordinary among all other isomers having intact indole side chains. However, one should keep in mind that the harsh conditions in the plasma of the ablation source into which the carrier gas (containing AcTrpOMe) is expanded can provide sufficient energy for the formation of such extraordinary structures like A. Nevertheless, we directly assumed that such a structure has no chance to be generated by interconversion from another isomer or (if once formed) to re-isomerise during the further molecular beam expansion. To further analyse and confirm this assumption we roughly estimated an exemplary (lower boundary for an) isomerisation barrier: For this purpose we looked for isomers with structural similarity to A. In this context, it was remarkable that the inserted structure has the same backbone conformation as the triply bound isomer D ( $\epsilon_D(g^+)$ ). A further triply bound isomer only differing from D by the side chain dihedral angle  $\chi_2$  is isomer H. Its calculated vibrations hardly differ from those of isomer D, but it is less stable than D as the stabilisation of the metal cation *via* interactions with the indolic  $\pi$ -system is less effective. Instead, the indolic NH group is placed above the aluminum ion so that this structure could be considered as a kind of “precursor” for the inserted isomer A.



In order to determine a plausible transition state structure and to get an idea about the reaction barrier of the described oxidative addition, transition state calculations were performed by applying the QST3 module implemented in Gaussian09 [65], starting from the cluster geometries of isomers H and A. An initial transition state guess was generated by applying the woelfling module [66] of Turbomole 7.3. (details cf. SI). By running a frequency calculation (yielding one single imaginary frequency) and an intrinsic reaction coordinate calculation (IRC) [67] it was verified that the resulting geometry is indeed a real transition state for the discussed oxidative addition. As expected, the estimated reaction barrier is high, due to the cleavage of the rather stable N-H bond, with around  $16300\text{ cm}^{-1}$  relative to isomer H. From empirical experimental data the isomerisation barriers which can be easily crossed in the molecular beam are given in values of several hundred wavenumbers (e.g. about  $4\text{ kJ mol}^{-1}$  independent of the carrier gas [68], or up to  $800\text{ cm}^{-1}$  [69-71]). Thus, the described reaction from an intact to the inserted structure is quite improbable to occur as isomerisation process in the molecular beam, even though its expansion directly over the aluminum plasma will introduce additional energy which might not be completely extracted from the sample molecules in the further expansion of the beam. However, under our experimental conditions, with the combined thermo-ablation source, the formation of the inserted structure A within the plasma remains a realistic scenario. The obtained transition state structure is further discussed in the supplement information.

Such an “inserted” structure as isomer A is only possible with the amino acid Trp (compared to the other aromatic amino acids Phe and Tyr). This has not been reported in context with former investigations on Trp-metal aggregates [7,19,20]. To get a further idea how extraordinary the role of Al(I) is, DFT geometry optimisations and harmonic vibrational frequency calculations were performed for a series of clusters of the type  $[M(I)AcTrpOMe]^+$  with M(I):  $Li^+$ ,  $Na^+$ ,  $K^+$ ,  $Rb^+$ ,  $Cs^+$ ,  $Mg^+$ ,  $Ti^+$ ,  $Zn^+$ ,  $Ag^+$  and  $Ga^+$ . As for the DFT calculations discussed above, again the B3LYP(-D3) functional was applied, however in combination with the def2-TZVPP basis set, since the TZVP basis set is not available for the metal elements Rb, Cs and Ag. Thus, it can be cleared up if the observed “inserted” structural motif is only advantaged for the  $Al^+$  containing cluster or if it may also occur for clusters comprising other M(I) centers. For this purpose, the inserted structure as well as the isomers B to E obtained for  $[AlAcTrpOMe]^+$  were reoptimised in the presence of the respective monovalent metal cations. The structures of these metal aggregates resulting from the structure A of  $[AlAcTrpOMe]^+$  as starting geometry are depicted in the supplement in Table S1, together with the corresponding relative energies, the geometric data, the atomic partial charges (NBO), the ionisation energies and the respective ionic radii. To give a short overview, the relative energies of the optimised “inserted” structures are summarised in Table 1.

Table 1: Relative energies of the “inserted” structural motifs (DFT/B3LYP-D3/def2-TZVPP) for the Li-, Na-, K-, Rb-, Cs-, Mg-, Ti-, Zn-, Ag-, Al- and Ga-containing clusters, together with a first estimation if the respective structure could indeed be (experimentally) observed or not. Note that the relative energy of a certain aggregate always refers to its most stable isomer with an intact indolic side chain (either structure B or D, cf. SI).

metal element	relative energy of the „inserted“ structural motif/ $\text{cm}^{-1}$	Possibility for the occurrence of the „inserted“ structure based on DFT energies
Li (no Li–H bond!)	-*	X
Na (Indole kept intact!)	-*	X
K	41543	X
Rb	41620	X
Cs	41730	X
Mg	7148	~
Ti	-2959	✓
Zn	7183	~
Ag	26673	X
Al	-1156	✓
Ga	11711	~

\*: No “inserted” structure could be found when exchanging  $\text{Al}^+$  in the isomer A with  $\text{Li}^+$  or  $\text{Na}^+$ . Instead, structures with  $\text{CO}_{\text{Ac}} \cdots$ metal interactions were formed, for  $\text{Na}^+$  comprising additional interactions with the  $\pi$ -system ( $\Delta E = 700 \text{ cm}^{-1}$ ), for  $\text{Li}^+$  the indolic  $\pi$ -system is destroyed leading to  $\Delta E = 11858 \text{ cm}^{-1}$ .

These additional calculations reveal some interesting aspects:

In case of metals having +1 as the most stable oxidation state and additionally having a high second ionisation energy the inserted structure cannot be generated at all as e.g. for Li and Na.

For metals with the preferred oxidation state +1 but a second ionisation energy which is not as high as for lithium or sodium (e.g. K, Rb, Cs, Ag), the inserted structure can in principle be formed but is energetically far of being relevant. Beyond, the charge distribution remains comparable to the non-inserted structures.

The metals which prefer an oxidation state higher than +1 show a slightly different behaviour (Mg, Al, Ga, Zn, Ti): Here, the inserted structure cannot only be formed, it is additionally not as energetically disadvantaged as in case of the larger alkali metals or silver. Beyond, the charge at the metal ion is increased in comparison with the non-inserted isomers, being characteristic for such an oxidative addition. For Mg and Zn this behaviour is in accordance with other reactions observed for these metals like the formation of indole Grignard [46] compounds or zinc hydrides similar to the  $\text{NaNacAl}$  complexes [72-74]. However, only for titanium and aluminium the inserted structure is highly energetically favoured in comparison with a bidentate structure. This is especially the case for titanium, which has the lowest second ionisation energy within the whole series of metals taken into account [75]. Nevertheless, +4 is by far the most stable oxidation state for titanium which is also found

for the titanium hydrides (cf. e.g. [76,77]). In contrast to aluminium no titanium hydride complexes formed by oxidative addition of X-H bonds to Ti(II) seem to be known from literature. The oxidation state +2 to which titanium approaches in the inserted structure is less common than +3 or especially +4 (e.g. [78]). Thus, it is difficult to estimate if the inserted structure could be formed with titanium in the molecular beam. For gallium, however, following Al in the third main group, the inserted structure is much less favoured though the ion radius is in between titanium and aluminium. Thus, the second ionisation energy is the decisive factor here: it increases from aluminum to gallium (in contrast to the tendency within the alkali series). This is due to the fact that between these two elements the 3d sub shell is filled with electrons which are less efficient (compared to s or p electrons) in shielding the increased nuclear charge of gallium. In consequence, the stability of Ga(I) is higher than for Al(I) and the tendency of Ga(I) for an oxidative addition lower. Altogether, the formation of the inserted structure seems to crucially depend on the stability of the oxidation state correlating with the second ionisation energy. Secondly, the ion radius must be adequate to fit into this “binding pocket” formed in the inserted geometry.

### Vibrational frequency calculations

To perform structural assignments the experimental IR data are compared to the calculated vibrational frequencies. In order to compensate for anharmonic effects specific scaling factors were applied to the harmonically calculated frequencies of the DFT-D3 optimized structures. These scaling factors were derived from reference calculations with the extensively investigated neutral systems (AcPheNHMe)<sub>1,2</sub> [79] and (AcPheOMe)<sub>1,2</sub> [42,80]. A comparison of the unscaled vibrational frequencies, obtained within the DFT/B3LYP-D3/TZVP calculations for the AcTrpOMe monomer and the [AlAcTrpOMe]<sup>+</sup> aggregates, already reveals that the binding of aluminium to the CO<sub>Ac</sub> group influences the NH-backbone stretching vibration. The extent of the associated (unscaled) red-shift depends on further interactions of the metal cation with the amino acid and on further intramolecular interactions of the NH group (see below). Due to this red-shift the NH-backbone vibration is scaled by the factor of 0.9563, established for scaling of hydrogen-bonded NH-stretching modes, if aluminium is attached to the CO<sub>Ac</sub> group. In contrast, the backbone NH-stretching vibration is quite unaffected if the Al<sup>+</sup> ion is linked to the ester group of AcTrpOMe and is thus scaled by a factor of 0.9608 for free NH-stretching vibrations. A look at the unscaled indolic NH-stretching mode in the different isomers of the aluminum aggregates reveals a red-shift compared to the value for the AcTrpOMe monomer. Thus, the vibrational stretching mode of the indolic NH group is also influenced by Al<sup>+</sup>, which is also reflected in the experimental data with a red-shift from 3524 cm<sup>-1</sup> for AcTrpOMe [45] to 3488 cm<sup>-1</sup> for the aluminium aggregate (cf. Figure 3). For this reason, the scaling factor for bonded (0.9563) instead of totally free NH-stretching vibrations

(0.9608) was applied here as well. The calculated (scaled) vibrational spectra of selected isomers are depicted further down in Figure 3 (together with the experimental IR+UV spectrum). With regard to the question of the influence of the aluminum binding on the NH-stretching frequency a rough orientation with regard to the application of scaling factors was already given above. In the variety of calculated structures we observed an enormously sensitive interplay between the binding of the metal cation to the carbonyl group(s) and to the  $\pi$ -system along with the “usual” interactions of the NH group within the backbone (e.g. C5 interactions [3],  $\text{NH}\cdots\pi$ ). As seen on former examples [17,18] of e.g. doubly carbonyl coordinated metal amino acid aggregates, the NH-stretching frequency of the backbone is least affected (in comparison with the amino acid monomer) if the metal cation is not only bound to both carbonyl groups but also coordinated to the  $\pi$ -system. The lack of interaction with the  $\pi$ -system leads to a stronger red-shift of the NH-stretching frequency. Taking the NH-stretching backbone vibration of the stretched AcTrpOMe monomer (calculated at  $3452\text{ cm}^{-1}$ , B3LYP-D3/TZVP level; experimental value  $3456\text{ cm}^{-1}$ , cf. Ref. [45]) into account, this effect is also visible here if we compare e.g. the “tridentate” structure D with the bidentate structures E, G and J. Within the latter three isomers, all having an  $\epsilon_L$  backbone, a further trend becomes obvious: In structure E, which is the most stable “bidentate” isomer, with the aluminium cation bound to both carbonyl groups, an additional (strong) interaction between the amide NH group and the  $\pi$ -system of the indole substituent ( $\text{NH}\cdots 6\text{-membered ring: } 3.100\text{ \AA}$ ;  $\text{NH}\cdots 5\text{-membered ring: } 2.863\text{ \AA}$ ) seems to occur, effecting a strong red-shift of the NH mode to values around  $3300\text{ cm}^{-1}$  (cf. Figure 3). When the side chain is successively turned away from the NH group, the  $\text{NH}\cdots\pi$  interaction is reduced ( $\epsilon_L(\text{g-})$ , isomer G) or vanishes completely ( $\epsilon_L(\text{a})$ , isomer J), leading to a reduction of the red-shift (cf. Figure 3\_a, 3\_b). Such interactions like  $\text{NH}\cdots\pi$  or C5 are normally estimated (in comparison to e.g. C7 hydrogen bonding in  $\gamma$ -turns) to be weak and thus to effect only moderate red-shifts (in comparison to the free amidic NH-stretching frequency in the monomer). However, the binding of the aluminum cation (to the  $\text{CO}_{\text{Ac}}$  or both CO groups) influences the NH-stretching frequency and seems to further enhance other NH-interactions like  $\text{NH}\cdots\pi$ .

## **Experimental Results and Discussion**

### **IR/UV experiments**

In the molecular beam expansion an intense [AlAcTrpOMe]<sup>+</sup> cluster mass signal was observed, whereas the triply charged system [AlAcTrpOMe]<sup>3+</sup> was not formed in considerable amounts (in contrast to the observations for [AlAcPheOMe]<sup>3+</sup>, cf. [6], further comparisons see SI).

In order to determine the vibrational pattern of the [AlAcTrpOMe]<sup>+</sup> cluster, attempts were performed to record an IR photodissociation spectrum in the NH-stretching region. However, no depletion effect could be observed in this experiment, either due to a too high dissociation barrier of the investigated clusters or to a dark mode effect. Therefore, the IR+UV technique had to be applied. For this, first a UV photodissociation spectrum of the compound, shown in Figure S5, had to be recorded, where a feature bearing two depletion maxima (of the parent ion) at 36451 and 36516 cm<sup>-1</sup> (blue-shifted with respect to the electronic origin of the AcTrpOMe monomer at 34896 cm<sup>-1</sup> [45]) was observed. Accordingly, the UV laser was fixed at a wavelength of 35335 cm<sup>-1</sup> for the IR+UV experiment (about 1090 cm<sup>-1</sup> lower in energy than the onset of the UV photodissociation band, see Figure S5 in the SI), while the IR laser frequency was tuned between 3150 and 3700 cm<sup>-1</sup>.

In the recorded IR+UV spectrum, depicted in Figure 3 below (together with the vibrational spectra predicted for selected isomers), three clearly separated bands are observed in the NH-stretching region at 3293, 3414 and 3488  $\text{cm}^{-1}$ .

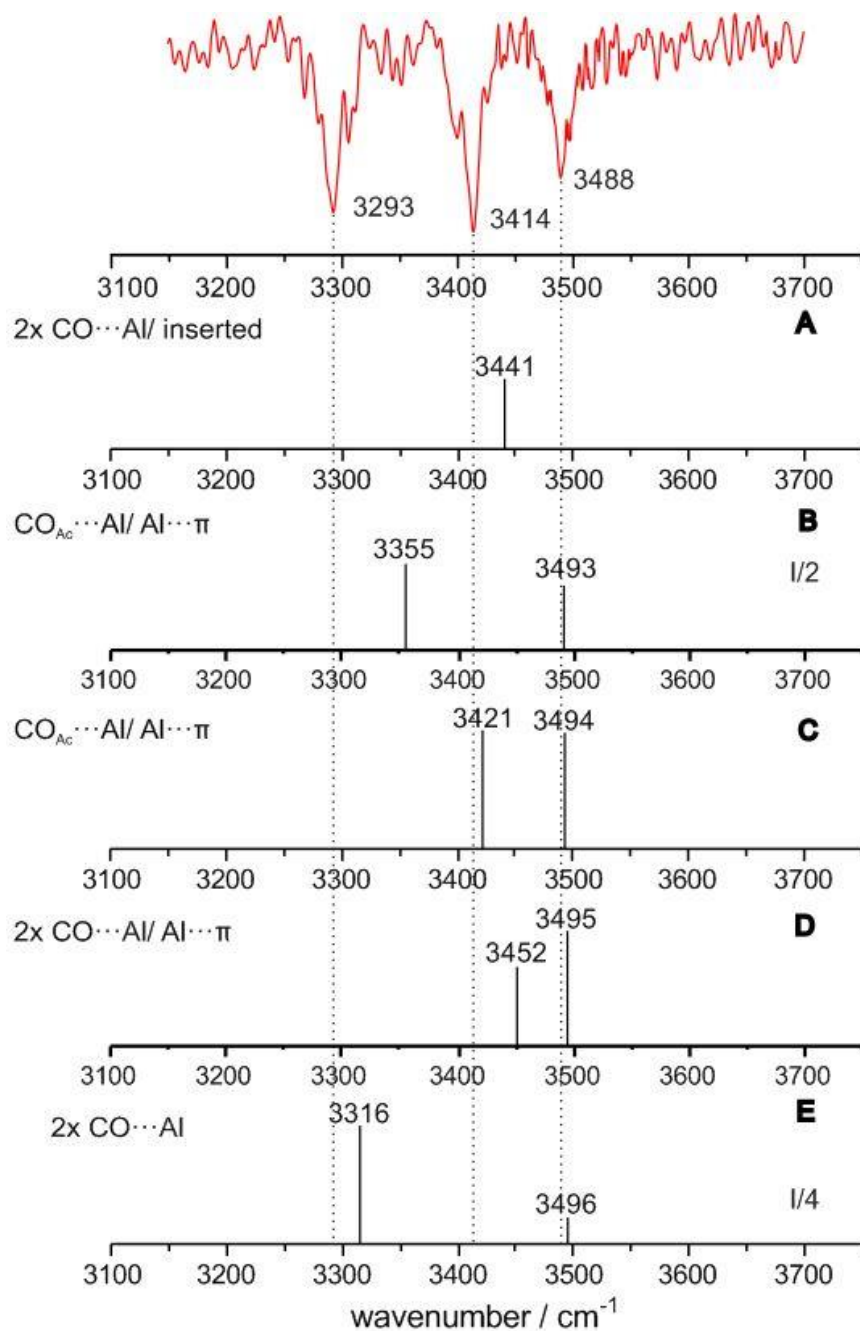


Figure 3\_a: Comparison between the experimental IR+UV spectrum of  $[\text{AlAcTrpOMe}]^+$  and harmonically calculated frequencies obtained from DFT calculations (B3LYP-D3/TZVP) of selected conformers (A-E) of  $[\text{AlAcTrpOMe}]^+$ . For a better illustration the calculated IR intensities for some isomers (B, E) are divided by a factor as indicated in the respective stick spectra.

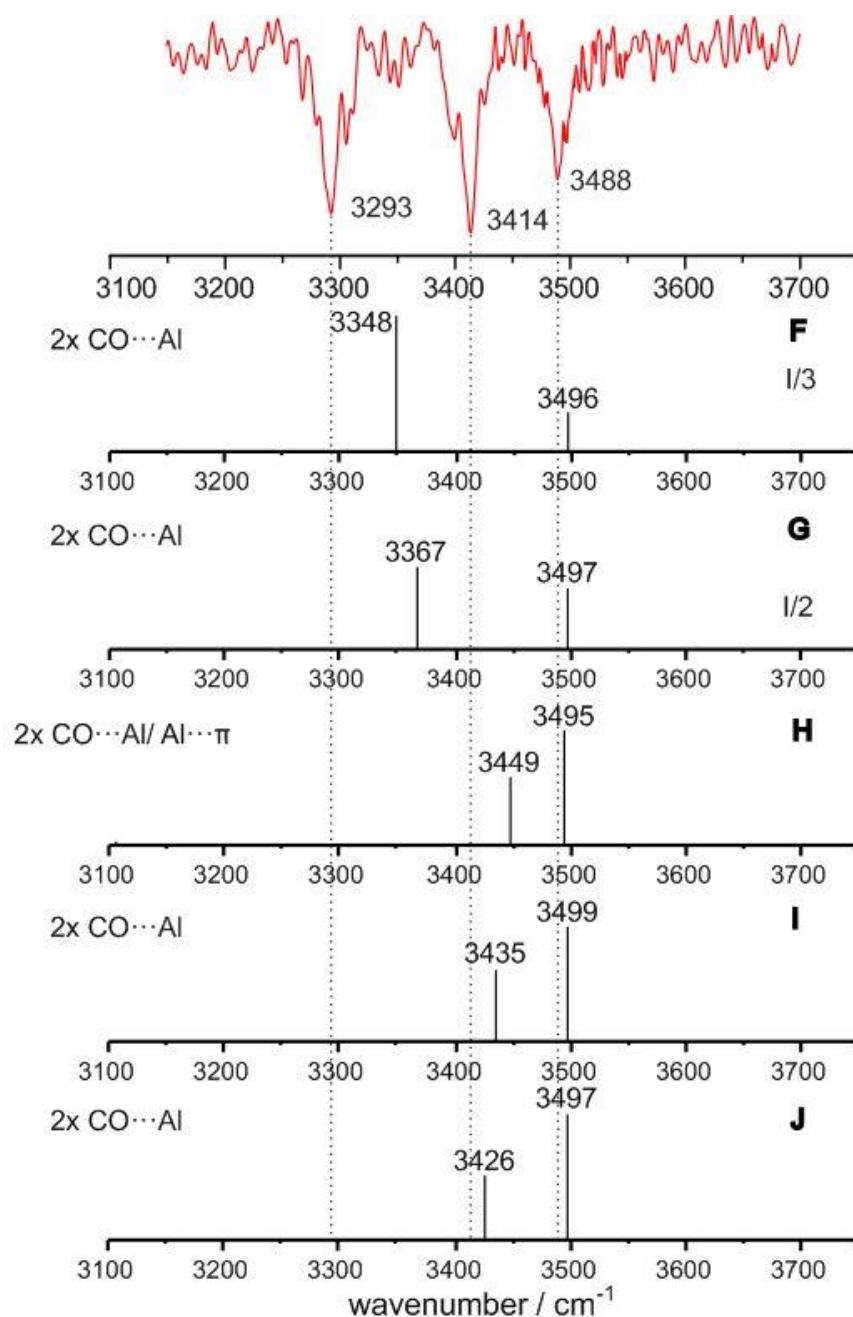


Figure 3\_b: Comparison between the experimental IR+UV spectrum of  $[\text{AlAcTrpOMe}]^+$  and harmonically calculated frequencies obtained from DFT calculations (B3LYP-D3/TZVP) of selected conformers (F-J) of  $[\text{AlAcTrpOMe}]^+$ . For a better illustration the calculated IR intensities for some isomers (F, G) are divided by a factor as indicated in the respective stick spectra.

However, the compound  $[\text{AlAcTrpOMe}]^+$  comprises only two NH groups, so that only two NH-stretching bands would be expected for the presence of one isomer. A possible explanation for this observation could be that only one isomer is present in the molecular beam and that the occurrence of a pattern with three distinct bands results from a Fermi-resonance between the first overtone of a CO-stretching vibration (calculated spectra cf. SI) and one of the NH-stretching fundamentals.

However, the vibrational spectra predicted by DFT for the CO- and NH-stretching regions for all of the energetically relevant structures clearly show that the occurrence of a Fermi-resonance is quite improbable (cf. calculated CO-vibrations in Figure 2\_a, 2\_b). A far more probable explanation for the measured IR spectrum could be that two distinct isomers are present in the molecular beam. The observed vibrational pattern would then be due to the characteristics of the indolic NH group: As long as it is free its stretching frequency is expected to be blue-shifted with respect to the NH frequencies of the backbone. Additionally, the free NH-stretching frequency of the indole moiety should be about the same value for different isomers. These expectations are already supported by the unscaled harmonically calculated frequencies of the different isomers with intact indole side chain. The superposition of the two indolic free NH-stretching frequencies could lead to only three vibrational bands despite the presence of two isomers in the IR spectrum. A further explanation for the observation of the three IR bands could be the presence of only three intact NH groups within two isomers, which would somehow suggest a “reaction” of one of the NH groups when binding to aluminum.

#### Discussion of relevant isomers

The four most stable structures presented in Figure 2 show different vibrational patterns. The most stable structure with an intact indole side chain (B) could be an option to explain the whole IR spectrum in case of a Fermi resonance between the NH-stretch fundamental calculated at  $3355\text{ cm}^{-1}$  and a corresponding CO-stretching overtone, which can be excluded (cf. calculated CO-vibrations in Figure 2\_a, 2\_b). With regard to the calculated CO-vibrations a Fermi resonance for the NH-fundamental (calculated at  $3452\text{ cm}^{-1}$ ) of the triply coordinated isomer D cannot be excluded. This could explain the experimental vibrations at  $3414\text{ cm}^{-1}$  and  $3488\text{ cm}^{-1}$ , but the latter would then even be an overlay of the indolic NH-stretching vibration and the splitting due to the Fermi resonance. Beyond this, an explanation for the most red-shifted band at  $3293\text{ cm}^{-1}$  would still be missing.

In comparison, the remaining NH-backbone vibrations of the inserted structure A and the intact structure C are much closer to the experimental value of  $3414\text{ cm}^{-1}$  (cf. Figure 3). The possibility to form metal aggregates like C, with the cation singly bound to the carbonyl group and additionally stabilised by the indolic  $\pi$ -system, was already demonstrated for the clusters of singly charged alkali metals and the unprotected Trp [7,19,20]. Against this background, conformer C (with a calculated backbone NH-vibration at  $3421\text{ cm}^{-1}$ ) must be taken into account. Nevertheless, the former investigations of Polfer and Rodgers [7,19,20] both agreed that the preference of such a “bidentate” binding of a singly charged alkali cation (carbonyl group/ $\pi$ -system) towards a “tridentate” binding (carbonyl group/NH group/ $\pi$ -system) in unprotected Trp increases with the ion radius. Having a look at the Pauling radius (cf. Table 1 in the SI) of  $\text{Al}^+$  it becomes obvious that the size and charge density of



the singly charged aluminium cation is rather in the range of the corresponding values of  $\text{Li}^+$  and  $\text{Na}^+$  than of  $\text{K}^+$ ,  $\text{Rb}^+$  and  $\text{Cs}^+$ . This makes the structural motif C questionable in case of  $[\text{AlAcTrpOMe}]^+$ . As a consequence, the inserted structure A, whose formation could be considered as a kind of oxidative addition of AcTrpOMe to Al(I) (cf. theory part), must still be seriously considered as possible binding motif. Obviously, only one NH-stretching band is to be expected for this geometry, since the Al–H-stretching frequency is shifted down to  $2069\text{ cm}^{-1}$  in the unscaled harmonic frequency calculation. That predicted value is in line with experimental values observed for other aluminium hydride systems. For example, in IRMPD studies on the transition metal doped aluminium clusters  $\text{Al}_{10}\text{Rh}_2\text{H}_2^+$  and  $\text{Al}_{11}\text{Rh}_2\text{H}_2^+$ , terminal Al–H-stretching modes were observed around  $1900\text{ cm}^{-1}$  [40], while the antisymmetric Al–H<sub>2</sub> stretching modes of  $\text{Al}_2\text{H}_6$  embedded in a hydrogen matrix were observed at  $1932$  and  $1915\text{ cm}^{-1}$  [41].

In general, the binding of aluminum to the  $\text{CO}_{\text{Ac}}$  group (and in structure A also to the second CO group) obviously influences the NH-vibration, so that it was scaled by a factor for bonded NH-modes (cf. theory part). Nevertheless, a binding motif comparable to A was not observed so far, so that a more suitable scaling factor from corresponding reference calculations could not be derived. Thus, the backbone NH-stretching mode of structure A, calculated around  $3440\text{ cm}^{-1}$ , could still correlate with the measured feature at  $3414\text{ cm}^{-1}$ . One should further take into account that the harsh conditions in the plasma of the ablation source into which the AcTrpOMe gas pulse is expanded can provide sufficient energy for the formation of such extraordinary structures like A. As addressed in the theory part such a structure has no chance to be generated by interconversion from another isomer or to re-isomerise during the further molecular beam expansion. As possible starting geometry a tridentate structure has been considered (isomer H). But neither the vibrational frequencies of this structure, nor of its energetically favoured relative D, already addressed above, can sufficiently describe the experimental data. In general, the existence of such tridentate structures seems to be much less probable in our molecular beam experiments than in former investigations [7,17,18,20] using milder source conditions. Thus, one could speculate that the formation of an inserted structure somehow occurs “on the expense of” the triply bound structures.

An additional hint towards the inserted structure could be given by the UV resonances. Among the three aromatic amino acids Trp, with its extended indolic  $\pi$ -system, is known to have the most red-shifted UV absorbance, with typical R2PI (resonant two-photon ionization) resonances found between  $34500\text{--}35300\text{ cm}^{-1}$  [81]. In case of  $[\text{AlAcPheOMe}]^+$  the UV resonance of the metal aggregate was red-shifted in comparison to the AcPheOMe monomer [6]. In general, the UV dissociation behaviour was more difficult to follow for  $[\text{AlAcTrpOMe}]^+$ , since it did not (in contrast to  $[\text{AlAcPheOMe}]^+$ ) generate the singly charged amino acid as fragment whose increase could be parallelly measured to the depletion of the parent ion. The measurements on the parent mass trace resulted into a broad UV PD

spectrum (cf. Figure S5) which is definitely blue-shifted towards the resonance of the AcTrpOMe monomer – a further difference compared to [AlAcPheOMe]<sup>+</sup>, but also a characteristic of the inserted structure. The comparison between the Trp and Phe containing systems as well as the UV absorption spectra predicted by TDDFT are further discussed in the SI.

All these considerations above have taken the isomers A to D into account, finally proposing A or also eventually C as candidates to explain the experimental (backbone) NH-vibration at 3414 cm<sup>-1</sup>. However, an explanation for the band below 3300 cm<sup>-1</sup> is still pending. The IR+UV spectroscopy is applied here in which the UV photon energy is set below the dissociation threshold (see above). However, due to the broad UV photodissociation spectrum, probably bearing more than one isomer, the IR+UV method must not necessarily be isomer-selective in case of [AlAcTrpOMe]<sup>+</sup>. Thus, the excitation of a second isomer by the IR laser finally leading to its dissociation by the IR+UV effect can probably explain the appearance of the most red-shifted experimental vibration at 3293 cm<sup>-1</sup>. The search for an adequate structure is much easier in that case. With the two NH-stretching modes calculated at 3316 and 3496 cm<sup>-1</sup> the doubly bound structure E can well explain the two experimental bands measured at 3293 and 3488 cm<sup>-1</sup>. The assigned isomer, having a ε<sub>L</sub>(g<sup>+</sup>) conformation, is characterised by a strong red-shift of the NH-backbone vibration. As addressed in the theory part this red-shift is partly due to the missing stabilisation of the aluminum by the indolic π-system, but additionally to an NH⋯π-interaction which is enhanced by the binding of the metal cation.

### Final assignment

With regard to all considerations above we can assume the presence of two isomers in our experiments on [AlAcTrpOMe]<sup>+</sup>. Isomer E, with Al<sup>+</sup> doubly bound to both carbonyl groups and an NH⋯π interaction can unambiguously be assigned due to its characteristic red-shifted NH-backbone vibration, well describing the lowest energy band in the experimental spectrum. Concerning the description of the transition at 3414 cm<sup>-1</sup> in the IR+UV spectrum two different isomers can be discussed: either isomer C, with the metal cation bound to the CO<sub>Ac</sub> and stabilised by interactions with the indolic π-system, or the inserted structure A, which additionally is the most stable arrangement, may be assigned. There are indicators that the latter “extraordinary” structure could exist under our experimental conditions. A final experimental proof may be obtained by measurements in the amide I/II region, since the calculated vibrations reveal differences for the relevant discussed isomers (cf. Figures 2\_a to 2\_f).

## Conclusion

In this publication we present our structural proposals for singly charged aggregates of aluminum and the protected amino acid AcTrpOMe based on a combination of (mainly DFT-D3 based) theoretical investigations and IR+UV photodissociation spectroscopy in a molecular beam experiment. The extensive conformational search carried out for [AlAcTrpOMe]<sup>+</sup> revealed a quite unique and unexpected “inserted” structural motif, formed by a kind of oxidative addition, with the aluminium ion being inserted into the NH bond of the indole substituent (and being further coordinated by both carbonyl groups of the backbone). Geometry optimisations performed by exchanging the aluminium ion with the other monovalent ions Li<sup>+</sup>, Na<sup>+</sup>, K<sup>+</sup>, Rb<sup>+</sup>, Cs<sup>+</sup>, Mg<sup>+</sup>, Ti<sup>+</sup>, Zn<sup>+</sup>, Ag<sup>+</sup> and Ga<sup>+</sup> revealed that the formation of this structural motif is energetically favoured only for Ti<sup>+</sup> and Al<sup>+</sup> (compared to structures where the metal cation is coordinated to an intact AcTrpOMe molecule).

With regard to the recorded IR+UV spectrum of [AlAcTrpOMe]<sup>+</sup> in the NH-stretching region, the observed pattern could only be explained by the presence of two isomers: A bidentate structure in which the metal cation is coordinated to both carbonyl groups and additionally stabilised by NH⋯π interactions is unambiguously assigned. For the second isomer two structures can be discussed: In one isomer Al<sup>+</sup> is bound to the CO<sub>Ac</sub> group and is additionally stabilised by interactions with the π-system. However, the measured spectrum could indeed also be explained by the presence of the most stable “inserted” structure being present as a second isomer. In both cases the extraordinary role of the electron-rich and relatively reactive indole side chain becomes obvious. Though the final temperature of the clusters in the molecular beam might be difficult to estimate, transition state optimisations revealed that the mentioned oxidative addition reaction cannot take place as a result of an isomerisation process in the molecular beam, but can only occur under the harsh plasma conditions. This publication reveals that Al(I) shows an interesting, partly extraordinary behaviour which will be interesting to be further analysed in other systems.

## Acknowledgements

The authors thank the Deutsche Forschungsgemeinschaft (DFG:Reference No. GE961/7-2) for financial support and the Hochleistungsrechner Elwetritsch for the granted computer time.

## References

- [1] J. Finkelstein, *Nature*. **460** (7257), 813 (2009).
- [2] K. Schwing and M. Gerhards, *Int. Rev.Phys. Chem.* **35** (4), 569 (2016).
- [3] E. Gloaguen, M. Mons, K. Schwing and M. Gerhards, *Chem. Rev.* **120** (22), 12490 (2020).
- [4] Y. Lu, N. Yeung, N. Sieracki and N. M. Marshall, *Nature*. **460** (7257), 855 (2009).
- [5] S. Habka, V. Brenner, M. Mons and E. Gloaguen, *J. Phys. Chem. Lett.* **7** (7), 1192 (2016).
- [6] P. M. Bialach, T. C. Martin and M. Gerhards, *Phys. Chem. Chem. Phys.* **14**, 8185 (2012).
- [7] Nick C. Polfer, Jos Oomens and Robert C. Dunbar, *Phys. Chem. Chem. Phys.* **8**, 2744 (2006).
- [8] P. B. Armentrout, M. T. Rodgers, J. Oomens and J. D. Steill, *J. Phys. Chem. A.* **112**, 2248 (2008).
- [9] N. C. Polfer, B. Paizs, L. C. Snoek, I. Compagnon, S. Suhai, G. Meijer, G. von Helden and J. Oomens, *J. Am. Chem. Soc.* **127**, 8571 (2005).
- [10] N. C. Polfer, J. Oomens, D. T. Moore, G. von Helden, G. Meijer and R. C. Dunbar, *J. Am. Chem. Soc.* **128**, 517 (2006).
- [11] P. B. Armentrout, *Mass Spec Rev.*, 1 (2021).
- [12] A.Kamariotis, O. V. Boyarkin, S.R. Mercier, R. D. Beck, M. F. Bush, E. R. Williams and T. R. Rizzo, *J. Am. Chem. Soc.* **128**, 905 (2006).
- [13] T. Shoeib, J. Zhao, H. E. Aribi, A. C. Hopkinson and K. W. Michael Siu, *J. Am. Soc. Mass Spectrom.* **24**, 38 (2013).
- [14] G. C. Boles, R. L. Hightower, R. A. Coates, C. P. McNary, G. Berden, J. Oomens and P. B. Armentrout, *J. Phys. Chem. B.* **122**, 3836 (2018).
- [15] R. A., Coates, C. P., McNary, G. C. Boles, G. Berden, J. Oomens and P. B. Armentrout, *Phys. Chem. Chem. Phys.* **17**(39), 25799 (2015).
- [16] M. Citir, E. M.S. Stennett, J. Oomens, J. D. Steill, M.T. Rodgers and P.B. Armentrout, *Int. J. Mass Spectrom.* **297**, 9 (2010).
- [17] R. Otsuka, K. Hirata, Y. Sasaki, J.M. Lisy, S.-I. Ishiuchi and M. Fujii, *Chem. Phys. Chem.* **21**, 712 (2020).
- [18] S.-I. Ishiuchi, Y. Sasaki, J.M. Lisy, and M. Fujii, *Phys. Chem. Chem. Phys.* **21**, 561 (2019).
- [19] R. C. Dunbar, *J. Phys. Chem. A.* **104**, 8067 (2000).

- [20] C. Ruan and M.T. Rodgers, *J. Am. Chem. Soc.* **126**, 14600 (2004).
- [21] V. Rondeau, *Rev. Environ. Health.* **17**, 107 (2002).
- [22] P.C. Ferreira, K. de Almeida Piai, A.M. Magosso Takayanagui and S.I. Segura-Muñoz, *Rev. LatinoAm. Enfermagem.* **16** (1), 151 (2008).
- [23] S. Yumoto, S. Kakimi, A. Ohsaki and A. Ishikawa, *J. Inorg. Biochem.* **103** (11), 1579 (2009).
- [24] C. Exley and E.R. House, *Monatsh. Chem.* **142**, 357 (2011)
- [25] K.A. Jellinger, *Int. Rev. Neurobiol.* **110**, 1 (2013).
- [26] The Federal Institute for Risk Assessment (Bundesinstitut für Risikobewertung): No risk of Alzheimer's disease from aluminium in consumer products, Health Assessment No. 033/ 2007.
- [27] D. R. Crapper, S. S. Krishnan and A. J. Dalton, *Science.* **180** (4085), 511 (1973).
- [28] C. Cui, H. W. Roesky, H.-G. Schmidt, M. Noltemeyer, H. Hao and F. Cimpoesu, *Angew. Chem. Int. Ed.* **39**, 23 (2000).
- [29] C. Dohmeier and D. Loos, H. Schnöckel, *Angew. Chem. Int. Ed. Engl.* **35**, 129 (1996).
- [30] S. Nagendran and H.W. Roesky, *Organometallics.* **27**, 457 (2008).
- [31] T. Chu, I. Korobkov and G. I. Nikonov, *J. Am. Chem. Soc.* **136**, 9195 (2014).
- [32] X. Zhang, L. Wang, G.R. Montone, A.F. Gill, G. Gantefo, B. Eichhorn, A.K. Kandalam and K.H. Bowen, *Phys. Chem. Chem. Phys.* **19**, 15541 (2017).
- [33] X. Zhang, H. Wang, G. Ganteför, B.W. Eichhorn, B. Kiran and K.H. Bowen, *J. Chem. Phys.* **145**, 154305 (2016).
- [34] V. Fontenot, B. Kiran, X. Zhang, H. Wang, G. Ganteför and K. Bowen, *Int. J. Mass Spectrom.* **408**, 56 (2016).
- [35] X. Zhang, G. Ganteför, B. Eichhorn, D. Mayo, W.H. Sawyer, A.F. Gill, A.K. Kandalam, H. Schnöckel and Kit Bowen, *J. Chem. Phys.* **145**, 074305 (2016).
- [36] X. Zhang, H. Wang, G. Ganteför, B.W. Eichhorn and K. Bowen, *Int. J. Mass Spectrom.* **404**, 24 (2016).
- [37] X. Li, A. Grubisic, K.H. Bowen, A.K. Kandalam, B. Kiran, G.F. Gantefoer and P. Jena, *J. Chem. Phys.* **132**, 241103 (2010).
- [38] P.J. Roach, A.C. Reber, W.H. Woodward, S.N. Khanna and A.W. Castleman Jr., *PNAS* September 11 **104** (37), 14565 (2007).

- [39] B.L.J. Poad, C.D. Thompson and E.J. Bieske, *Chem. Phys.* **346**, 176 (2008).
- [40] J. Vanbuel, P. Ferrari and E. Janssens, *Advances in Physics: X.* **5** (1), 1754132 (2020).
- [41] X. Wang, L. Andrews, S. Tam, M.E. DeRose and M.E. Fajardo, *J. Am. Chem. Soc.* **125**, 9218 (2003).
- [42] M. Gerhards, C. Unterberg and A. Gerlach, *Phys. Chem. Chem. Phys.* **4**, 5563 (2002).
- [43] H. Fricke, K. Schwing, A. Gerlach, C. Unterberg, and M. Gerhards, *Phys. Chem. Chem. Phys.* **12**, 3511 (2010).
- [44] S. Lakhdar, M. Westermaier, F. Terrier, R. Goumont, T. Boubaker, A.R. Ofial and H. Mayr, *J. Org. Chem.*, **71**, 9088 (2006).
- [45] A. Gerlach, C. Unterberg, H. Fricke and M. Gerhards, *Mol. Phys.* **103**, 1521 (2005).
- [46] R.A. Heacock and S.Kašpárek, *Adv. Heterocycl. Chem.* **10**, 43 (1969).
- [47] T.G. Dietz, M.A. Duncan, D.E. Powers and R.E. Smalley, *J. Chem. Phys.* **74**, 6511 (1981).
- [48] D.E. Powers, S.G. Hansen, M.E. Geusic, A.C. Puiu, J.B. Hopkins, T.G. Dietz, M.A. Duncan, P.R.R. Langridge-Smith and R.E. Smalley, *J. Phys. Chem.* **86**, 2556 (1982).
- [49] D.E. Powers, S.G. Hansen, M.E. Geusic, D.L. Michalopoulos and R.E. Smalley, *J. Chem. Phys.* **78**, 2866 (1983).
- [50] V.E. Bondybey and J.H. English, *J. Chem. Phys.* **74**, 6978 (1981).
- [51] N.G. Basov, E.P. Markin, A.N. Oraevski, A.V. Pankratov and A.N. Shachkov, *JETP Lett.* **14**, 165 (1971).
- [52] L. Jašíková, J. Roithová, *Chem. Eur. J.* **24**, 3374 (2018).
- [53] N. C. Polfer, *Chem. Soc. Rev.* **40**, 2211 (2011).
- [54] Discovery Studio Client, v2.5.5.9350, Accelrys Software Inc., Copyright 2005–09.
- [55] M.D. Hanwell, D.E. Curtis, D.C. Lonie, T. Vandermeersch, E. Zurek and G.R. Hutchison, *J. Cheminf.* **4**, 17 (2012).
- [56] A.K. Rappe, C.J. Casewit, K.S. Colwell, W.A. III Goddard and W.M. Skiff, *J. Am. Chem. Soc.* **114**, 10024 (1992).
- [57] M. J. Frisch, G. W. Trucks, H. B. Schlegel, G. E. Scuseria, M. A. Robb, J. R. Cheeseman, G. Scalmani, V. Barone, B. Mennucci, G. A. Petersson, H. Nakatsuji, M. Caricato, X. Li, H. P. Hratchian, A. F. Izmaylov, J. Bloino, G. Zheng, J. L. Sonnenberg, M. Hada, M. Ehara, K. Toyota, R. Fukuda, J. Hasegawa,

M. Ishida, T. Nakajima, Y. Honda, O. Kitao, H. Nakai, T. Vreven, J. A. Montgomery Jr., J. E. Peralta, F. Ogliaro, M. J. Bearpark, J. Heyd, E. N. Brothers, K. N. Kudin, V. N. Staroverov, R. Kobayashi, J. Normand, K. Raghavachari, A. P. Rendell, J. C. Burant, S. S. Iyengar, J. Tomasi, M. Cossi, N. Rega, N. J. Millam, M. Klene, J. E. Knox, J. B. Cross, V. Bakken, C. Adamo, J. Jaramillo, R. Gomperts, R. E. Stratmann, O. Yazyev, A. J. Austin, R. Cammi, C. Pomelli, J. W. Ochterski, R. L. Martin, K. Morokuma, V. G. Zakrzewski, G. A. Voth, P. Salvador, J. J. Dannenberg, S. Dapprich, A. D. Daniels, O. Farkas, J. B. Foresman, J. V. Ortiz, J. Cioslowski and D. J. Fox, Gaussian 09, Revision D.01, Gaussian, Inc, Wallingford, CT, USA, 2009.

[58] S. Grimme, J. Antony, S. Ehrlich and H. Krieg, *J. Chem. Phys.* **132**, 154104 (2010).

[59] S.F. Boys and F. Bernardi, *Mol. Phys.* **19**, 553 (2006).

[60] E. Gloaguen, M. Mons and A.M. Rijs, J. Oomens, Eds. **364**, 225 (2015).

[61] B.C. Dian, A. Longarte, S. Mercier, D.A. Evans, D.J. Wales and T.S. Zwier, *J. Chem. Phys.* **117**, 10688 (2002).

[62] D. Řeha, H. Valdés, J. Vondrášek, P. Hobza, A. Abu-Riziq, B. Crews and M.S. de Vries, *Chem. Eur. J.* **11**, 6803 (2005).

[63] F. Neese (2017) Software update: the ORCA program system, version 4.0, *Wiley Interdiscip. Rev.: Comput. Mol. Sci.* **8**, e1327.

[64] D.G. Liakos, M. Sparta, M.K. Kesharwani, J.M.L. Martin and F. Neese, *J. Chem. Theory Comput.* **11**, 1525 (2015).

[65] C. Peng and H. Bernhard Schlegel, *Isr. J. Chem.* **33**, 449 (1993).

[66] P. Plessow, *J. Chem. Theory Comput.* **9**, 1305 (2013).

[67] S. Maeda, Y. Harabuchi, Y. Ono, T. Taketsugu and K. Morokuma, *Int. J. Quantum Chem.* **115**, 258 (2015).

[68] R.S. Ruoff, T.D. Klots, T. Emilsson and H.S. Gutowsky, *J. Chem. Phys.* **93**, 3142 (1990).

[69] A.M. Rijs and J. Oomens, Eds. **364**, 1 (2015).

[70] L.C. Snoek, T. Van Mourik and J.P. Simons, *Mol. Phys.* **101**, 1239 (2003).

[71] J.P. Schermann, Elsevier: Amsterdam (2008).

[72] J. Spielmann, D. Piesik, B. Wittkamp, G. Jansen and S. Harder, *Chem. Commun.* 3455 (2009).

[73] G. Ballmann, S. Grams, H. Elsen and S. Harder, *Organometallics*. **38**, 2824 (2019).

[74] S. Schulz, T. Eisenmann, D. Schuchmann, M. Bolte, M. Kirchner, R. Boese, J. Spielmann and S. Harder, *Z. Naturforsch.* **64b**, 1397 (2009).

[75] WebElements [<http://www.webelements.com/>]

[76] T. Yajima, H. Nakajima, T. Honda, K. Ikeda, T. Otomo, H. Takeda and Z. Hiroi, *Inorg. Chem.* **59**, 4228 (2020).

[77] J. Pinkas, R. Gyepes, I. Císařová, J. Kubišta, M. Horáček, N. Žilková and K. Mach, Dalton Trans. **47**, 8921 (2018).

[78] G.B. Wijeratne, E.M. Zolnhofer, S. Fortier, L.N. Grant, P.J. Carroll, C.-H. Chen, K. Meyer, J. Krzystek, A. Ozarowski, T.A. Jackson, D.J. Mindiola and J. Telser, Inorg. Chem., **54**, 10380 (2015).

[79] M. Gerhards, C. Unterberg, A. Gerlach and A. Jansen, Phys. Chem. Chem. Phys. **6**, 2682 (2004).

[80] M. Gerhards and C. Unterberg, Phys. Chem. Chem. Phys. **4**, 1760 (2002).



## Supplementary information

## Table of contents

Additional geometries and the corresponding vibrational spectra for the NH-stretching region....	202
Geometries and the corresponding vibrational spectra for the CO-stretching region.....	206
Estimation of a possible isomerisation barrier towards the inserted structure.....	212
Structural and electronic data for the considered $\text{Li}^+$ , $\text{Na}^+$ , $\text{K}^+$ , $\text{Rb}^+$ , $\text{Cs}^+$ , $\text{Mg}^+$ , $\text{Ti}^+$ , $\text{Zn}^+$ , $\text{Ag}^+$ and $\text{Ga}^+$ -containing clusters.....	213
Calculated vibrational (NH-stretching) frequencies obtained for the $\text{Li}^+$ , $\text{Na}^+$ , $\text{K}^+$ , $\text{Rb}^+$ , $\text{Cs}^+$ , $\text{Mg}^+$ , $\text{Ti}^+$ , $\text{Zn}^+$ , $\text{Ag}^+$ and $\text{Ga}^+$ -containing clusters.....	223
Measured UV photodissociation spectrum.....	226
Calculated UV/VIS absorption spectra.....	227
Atomic partial charges predicted by natural bond orbital and Mulliken population analyses.....	229
Geometric data for selected isomers of $[\text{AlAcTrpOMe}]^+$ .....	233
Comparison of $[\text{AlAcTrpOMe}]^+$ and $[\text{AlAcPheOMe}]^+$ .....	235
References.....	236

## Additional geometries and the corresponding vibrational spectra for the NH-stretching region

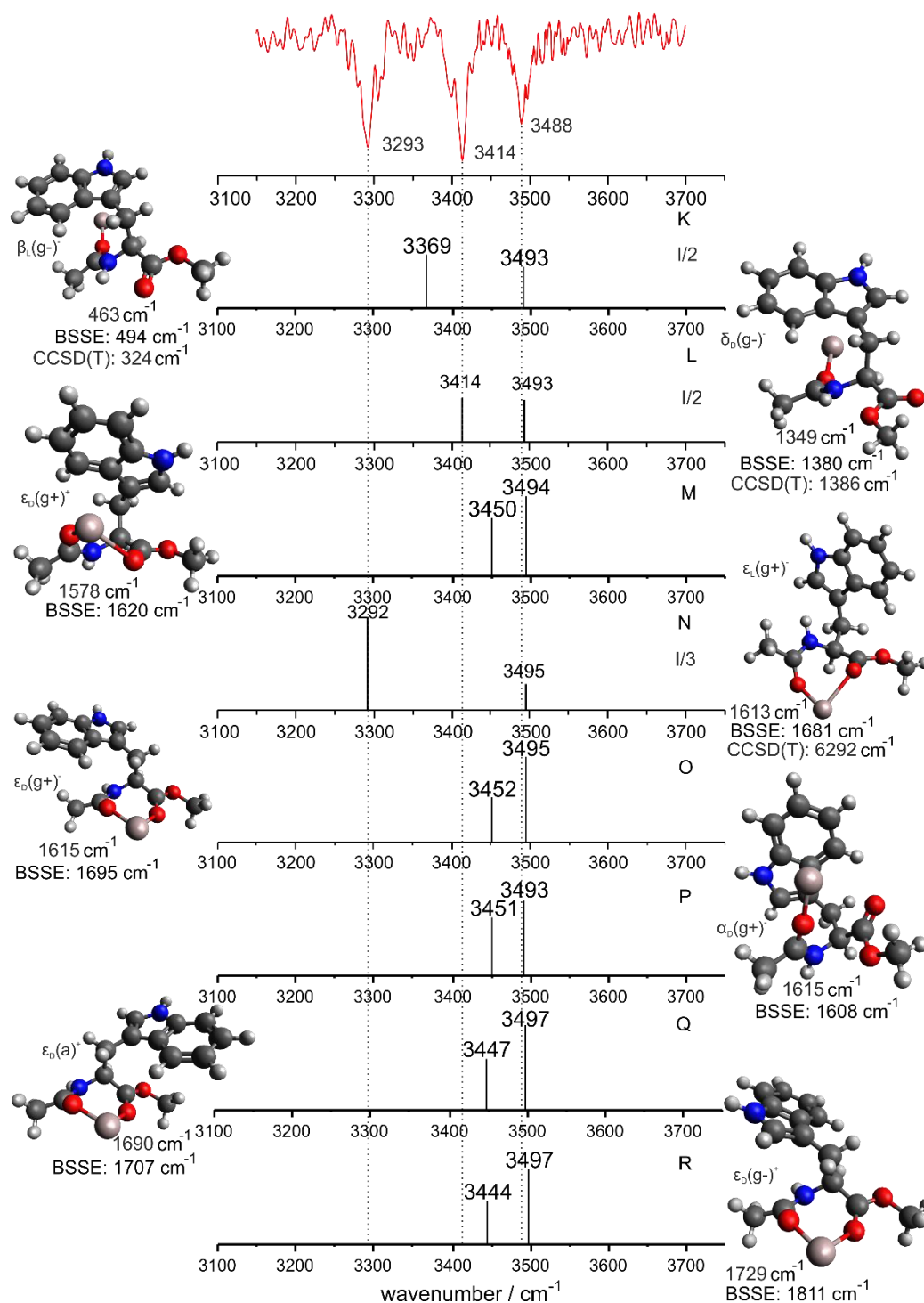


Fig. S1\_a: Comparison between the experimental IR+UV spectrum of  $[\text{AlAcTrpOMe}]^+$  and harmonically calculated frequencies obtained from DFT calculations (B3LYP-D3/TZVP) of conformers K-R of  $[\text{AlAcTrpOMe}]^+$ . For a better illustration the calculated IR intensities for some isomers (K, L, N) are divided by a factor as indicated in the respective stick spectra. The given relative energies (obtained from DFT, BSSE-corrected DFT as well as DLPNO-CCSD(T)), are considered relative to the most stable intact geometry B.

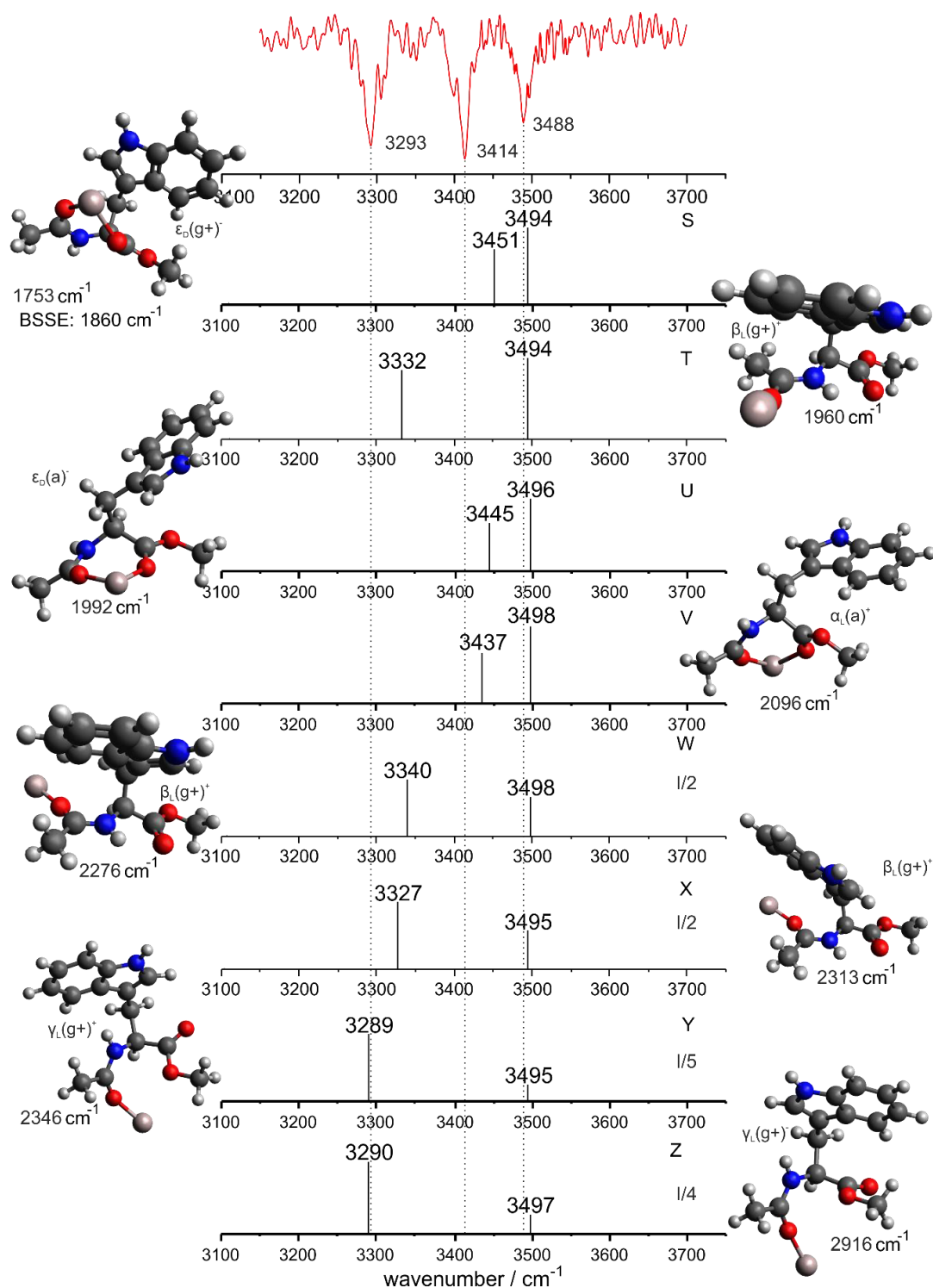


Fig. S1\_b: Comparison between the experimental IR+UV spectrum of  $[\text{AlAcTrpOMe}]^+$  and harmonically calculated frequencies obtained from DFT calculations (B3LYP-D3/TZVP) of conformers S-Z of  $[\text{AlAcTrpOMe}]^+$ . For a better illustration the calculated IR intensities for some isomers (W, X, Y, Z) are divided by a factor as indicated in the respective stick spectra. The given relative energies (obtained from DFT and BSSE-corrected DFT) are considered relative to the most stable intact geometry B.

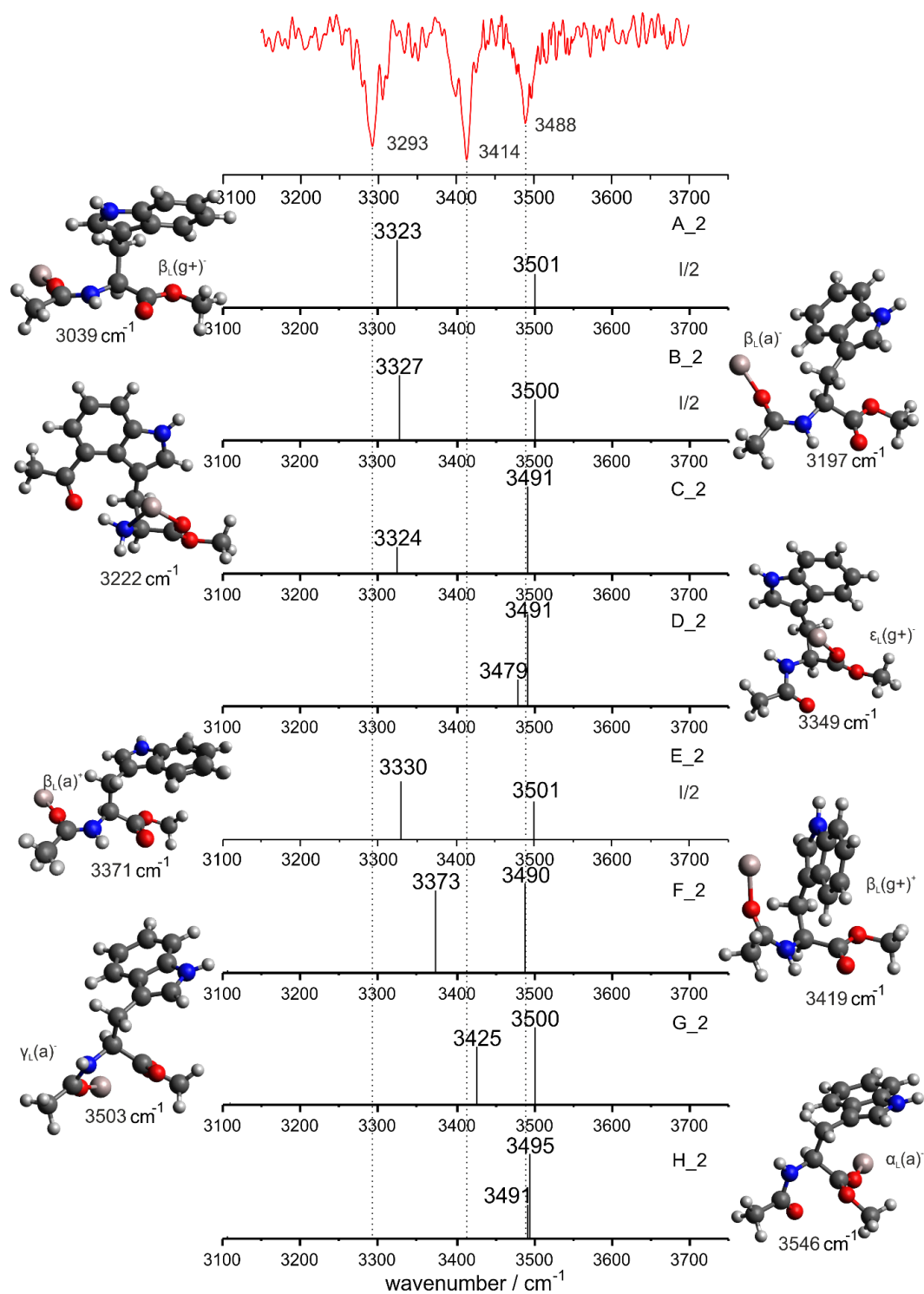


Fig. S1\_c: Comparison between the experimental IR+UV spectrum of [AlAcTrpOMe]<sup>+</sup> and harmonically calculated frequencies obtained from DFT calculations (B3LYP-D3/TZVP) of conformers A<sub>2</sub>-H<sub>2</sub> of [AlAcTrpOMe]<sup>+</sup>. For a better illustration the calculated IR intensities for some isomers (A<sub>2</sub>, B<sub>2</sub>, E<sub>2</sub>) are divided by a factor as indicated in the respective stick spectra. The given relative energies (obtained from DFT) are considered relative to the most stable intact geometry B.

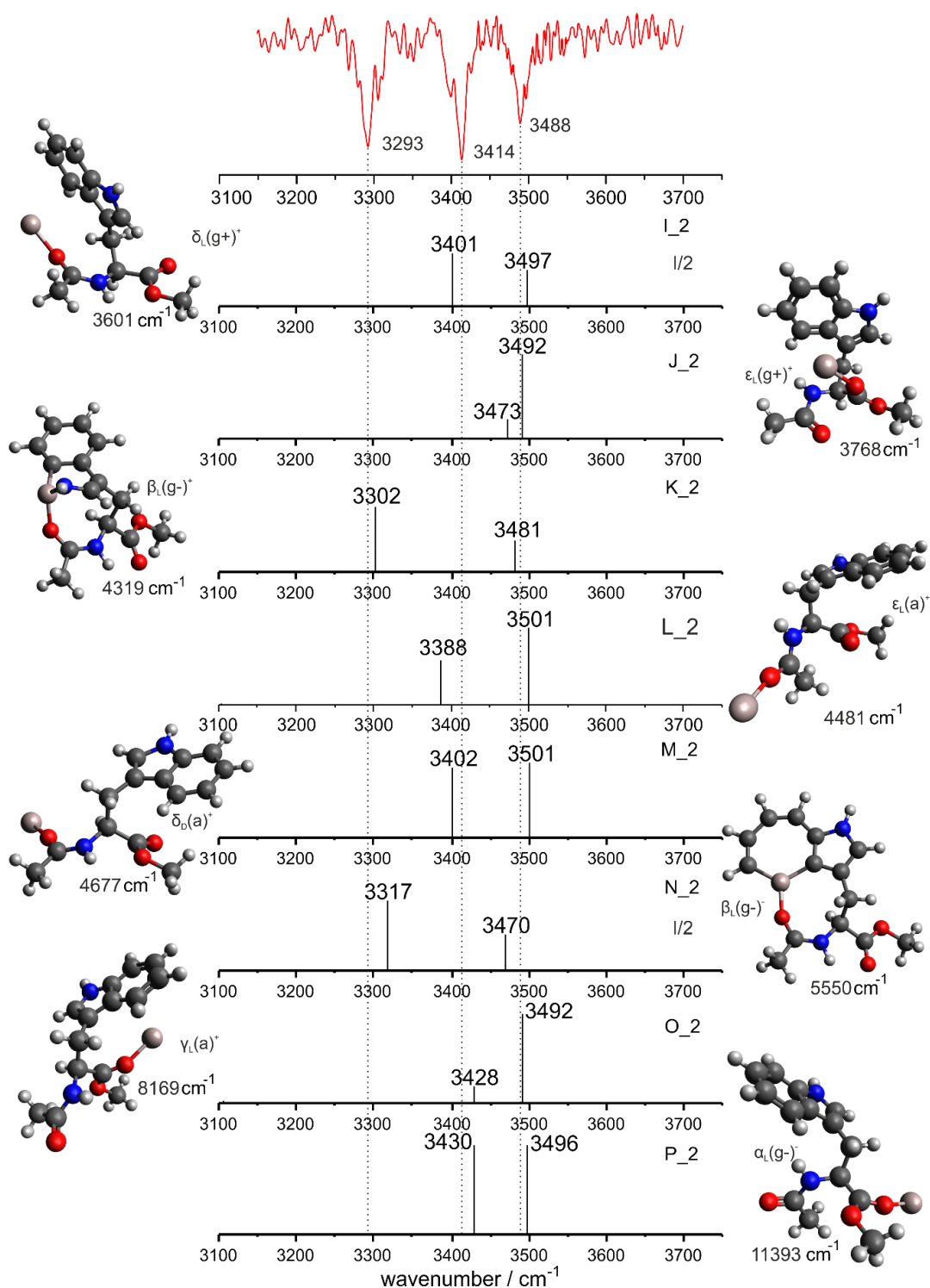


Fig. S1\_d: Comparison between the experimental IR+UV spectrum of  $[\text{AlAcTrpOMe}]^+$  and harmonically calculated frequencies obtained from DFT calculations (B3LYP-D3/TZVP) of conformers  $\text{I}_2$ - $\text{P}_2$  of  $[\text{AlAcTrpOMe}]^+$ . For a better illustration the calculated IR intensities for some isomers ( $\text{I}_2$ ,  $\text{N}_2$ ) are divided by a factor as indicated in the respective stick spectra. The given relative energies (obtained from DFT) are considered relative to the most stable intact geometry B.

## Additional geometries and the corresponding vibrational spectra for the CO-stretching region

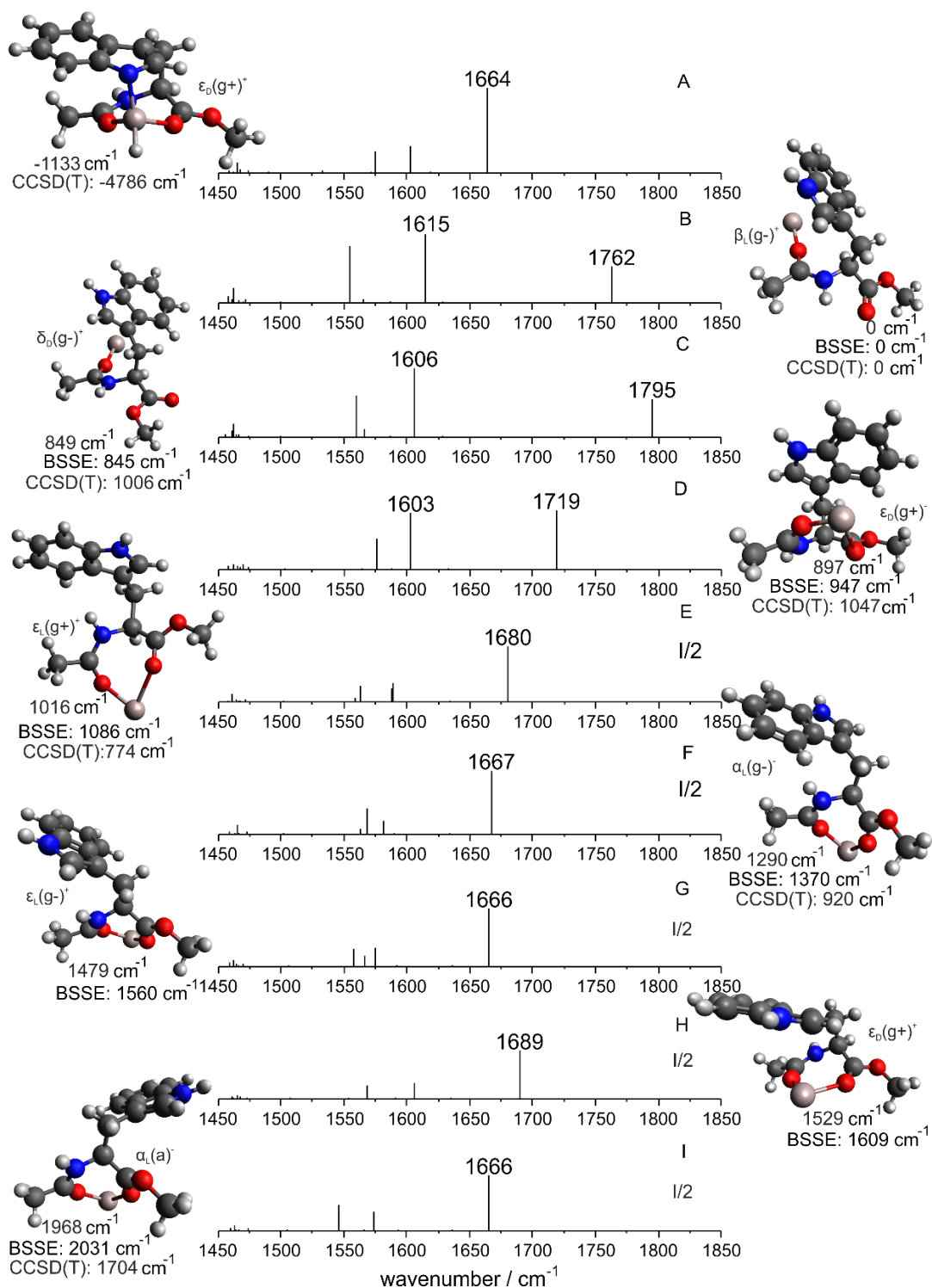


Fig. S2\_a: Harmonically calculated vibrational spectra for the CO stretching region (DFT/B3LYP/TZVP; scal.: 0.9850) of selected conformers (A-I) of [AlAcTrpOMe]<sup>+</sup>. For a better illustration the calculated IR intensities for some isomers (E, F, G, H, I) are divided by a factor as indicated in the respective stick spectra.

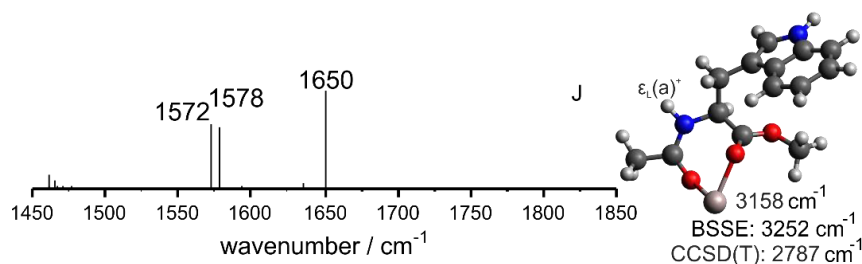


Fig. S2\_b: Harmonically calculated vibrational spectra for the CO stretching region (DFT/B3LYP/TZVP; scal.: 0.9850) of selected conformers (J) of [AlAcTrpOMe]<sup>+</sup>.

In the main part of the paper it is briefly hinted that the measured vibrational pattern (with three NH-stretching bands) might be explained by the presence of only one single isomer (comprising two NH groups) in the molecular beam if Fermi resonance effects are involved, in which the superposition of a CO-stretching overtone and an NH-stretching fundamental effects a coupling of these modes and finally a splitting into two observable vibrational bands.

Concerning the energetically rather favoured isomer B, the predicted NH-stretching frequency at 3355 cm<sup>-1</sup> falls indeed between the two measured bands at 3293 and 3414 cm<sup>-1</sup>. That is why the calculated vibrational pattern in the CO-stretching region should be consulted to determine if the occurrence of a Fermi resonance between the first overtone of one of the C=O-stretching vibrations and the fundamental of the NH-stretching vibration (of the amide group) is likely or not. If a Fermi resonance should occur for the mentioned isomer, a CO-stretching band has to be located around 1677-1678 cm<sup>-1</sup>. However, the CO-stretching mode of the amide carbonyl group is shifted down to 1615 cm<sup>-1</sup>, due to the coordination of Al<sup>+</sup>, while the free CO-stretching vibration of the ester group is predicted at 1762 cm<sup>-1</sup>. Thus, obviously no overtone of one of both CO-vibrations may undergo a Fermi resonance with the NH-stretching mode in question, so that the occurrence of a Fermi resonance is to be excluded.

Similarly, the NH-stretching vibration predicted for isomer D at 3452 cm<sup>-1</sup> might explain the measured bands at 3414 and 3488 cm<sup>-1</sup> (then overlaying with the NH-vibration of the indolic NH group), but CO stretching bands at 1603 cm<sup>-1</sup> and at 1719 cm<sup>-1</sup> show that a Fermi resonance effect is again rather unlikely, but cannot be completely excluded. However, it should also be evoked that this isomer cannot be responsible for the measured band at 3293 cm<sup>-1</sup>, so that the presence of a second isomer would again be crucial to explain this experimental feature.

Finally, the above mentioned considerations could be verified experimentally by recording IR photodissociation spectra in the amide I/II region. However, these experiments cannot be performed



with our current experimental setup due to the insufficient IR laser power available at the position of the corresponding molecular beam apparatus.

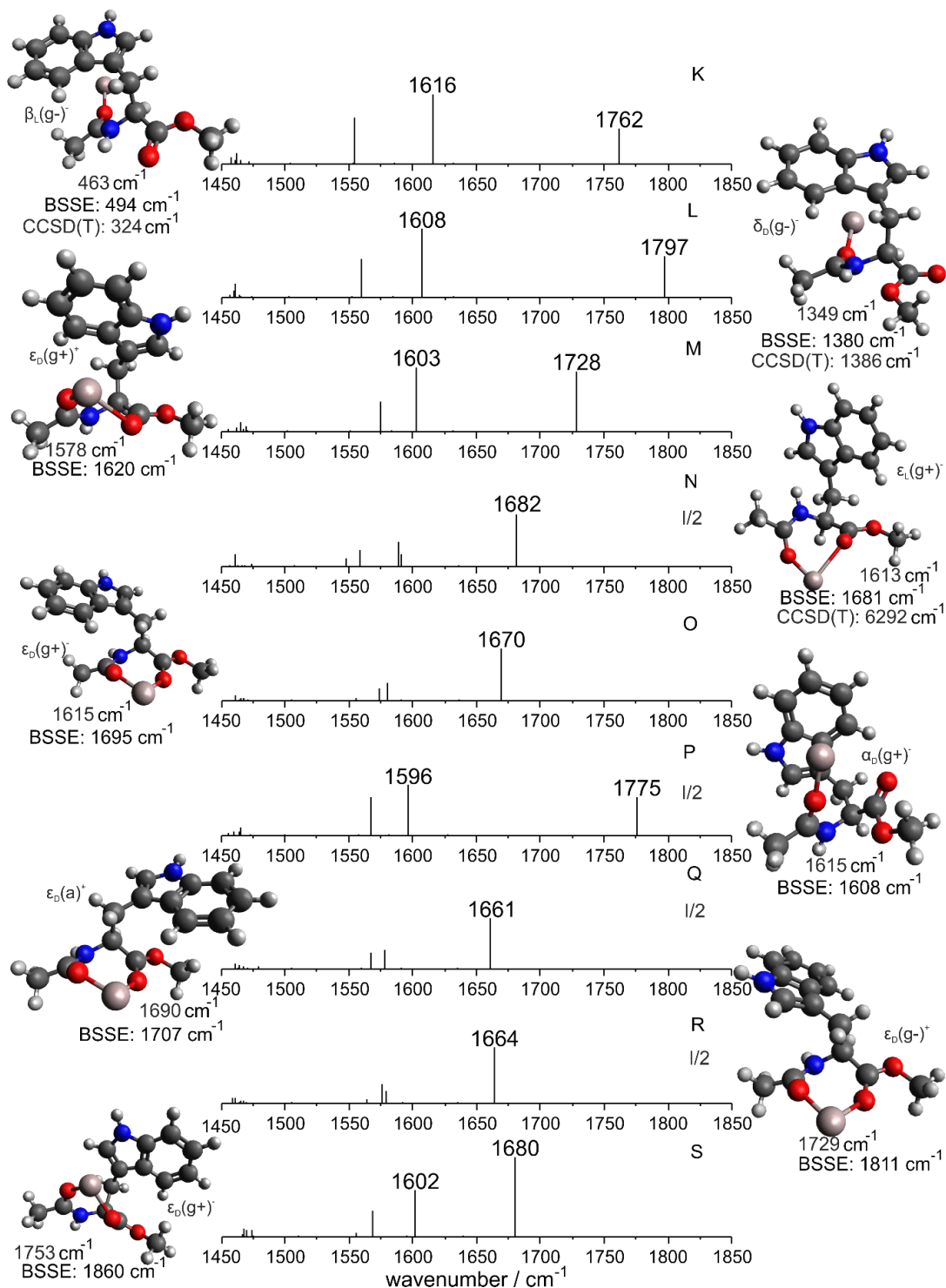


Fig. S2\_c: Harmonically calculated vibrational spectra for the CO stretching region (DFT/B3LYP/TZVP; scal.: 0.9850) of conformers K–S of [AlAcTrpOMe]<sup>+</sup>. For a better illustration the calculated IR intensities for some isomers (N, P, Q, R) are divided by a factor as indicated in the respective stick spectra.



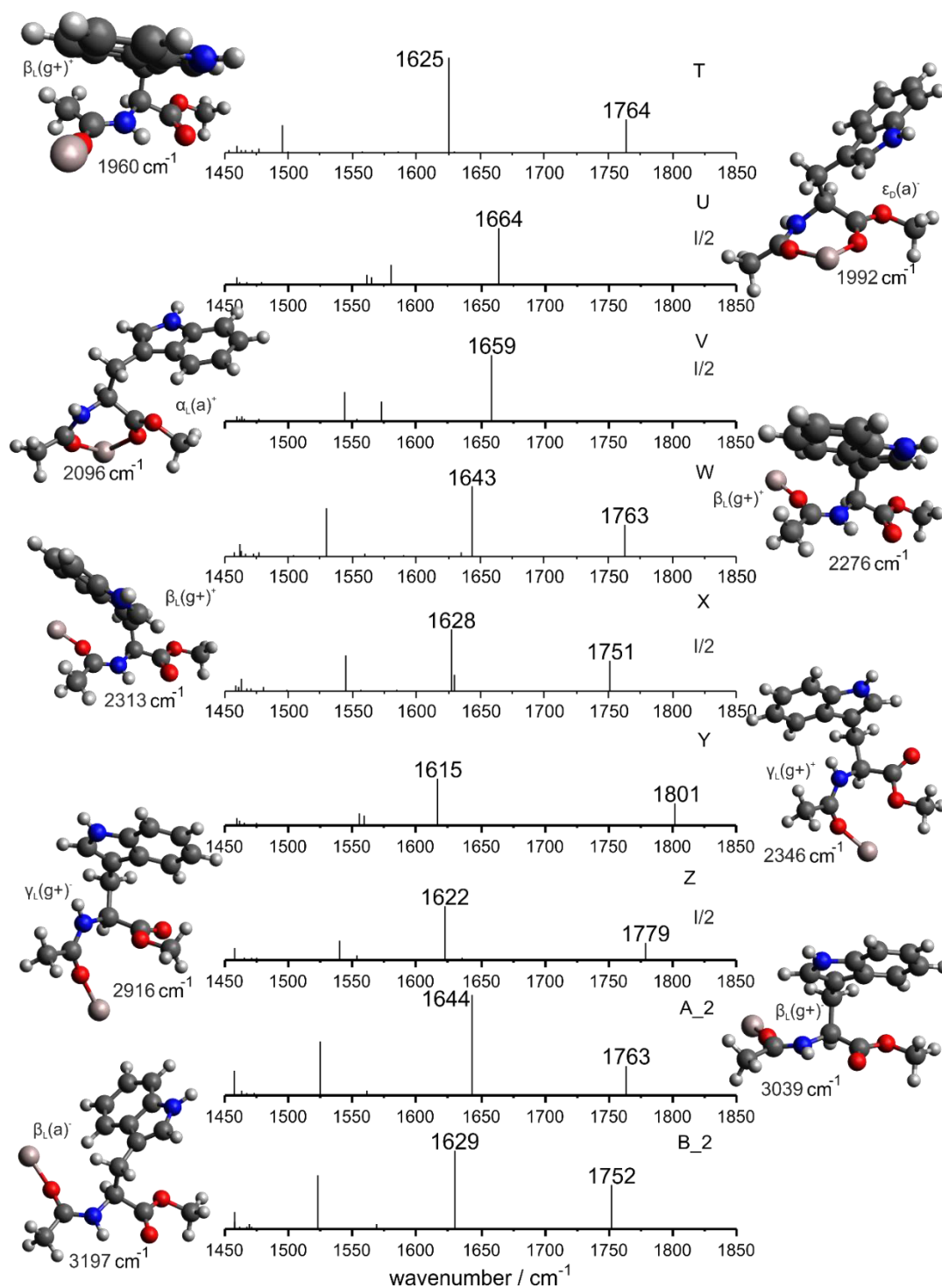


Fig. S2\_d: Harmonically calculated vibrational spectra for the CO stretching region (DFT/B3LYP/TZVP; scal.: 0.9850) of conformers T-B<sub>2</sub> of [AlAcTrpOMe]<sup>+</sup>. For a better illustration the calculated IR intensities for some isomers (U, V, X, Z) are divided by a factor as indicated in the respective stick spectra.

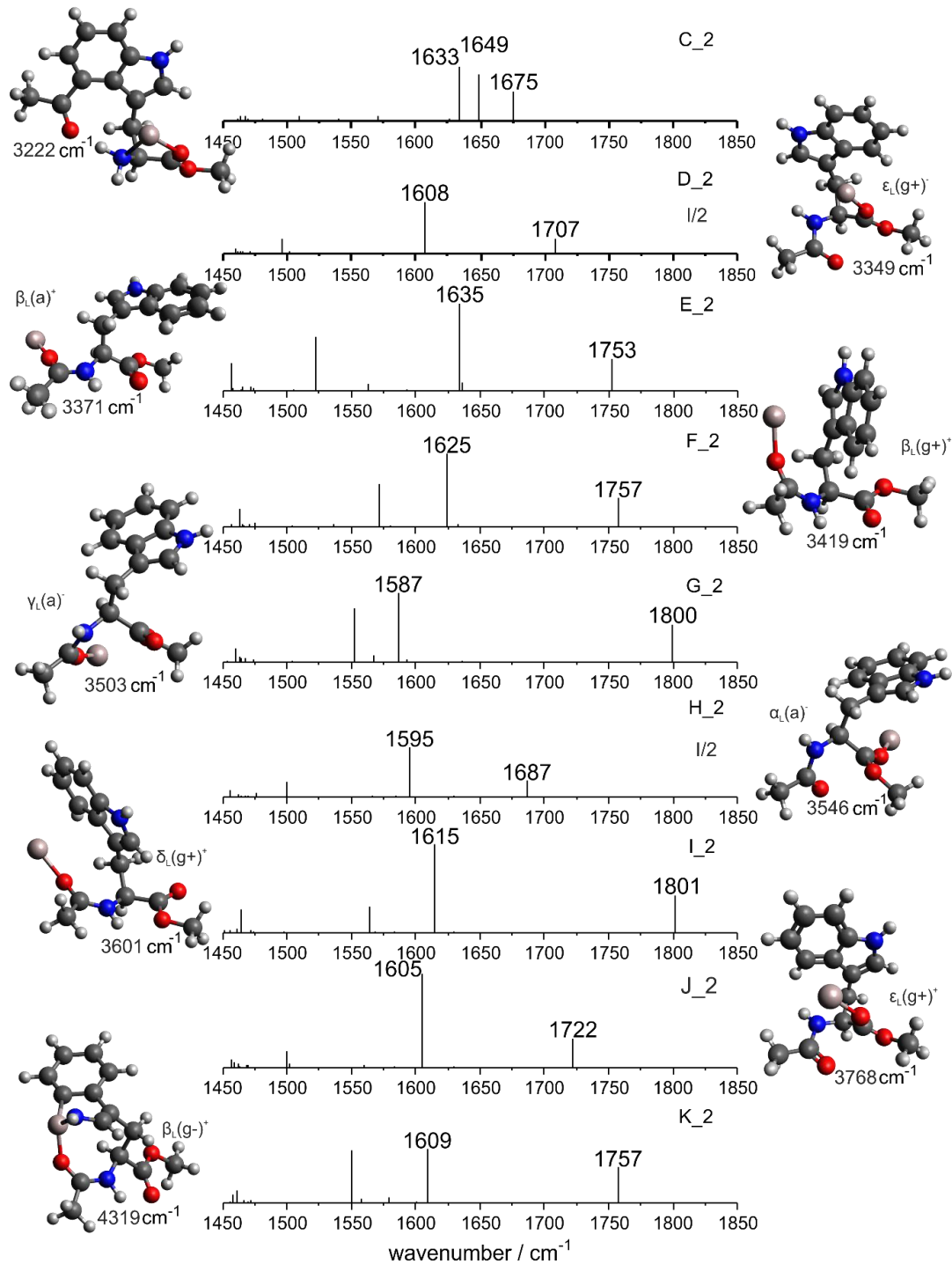


Fig. S2\_e: Harmonically calculated vibrational spectra for the CO stretching region (DFT/B3LYP/TZVP; scal.: 0.9850) of conformers C<sub>2</sub>-K<sub>2</sub> of [AlAcTrpOMe]<sup>+</sup>. For a better illustration the calculated IR intensities for some isomers (D<sub>2</sub>, H<sub>2</sub>) are divided by a factor as indicated in the respective stick spectra.

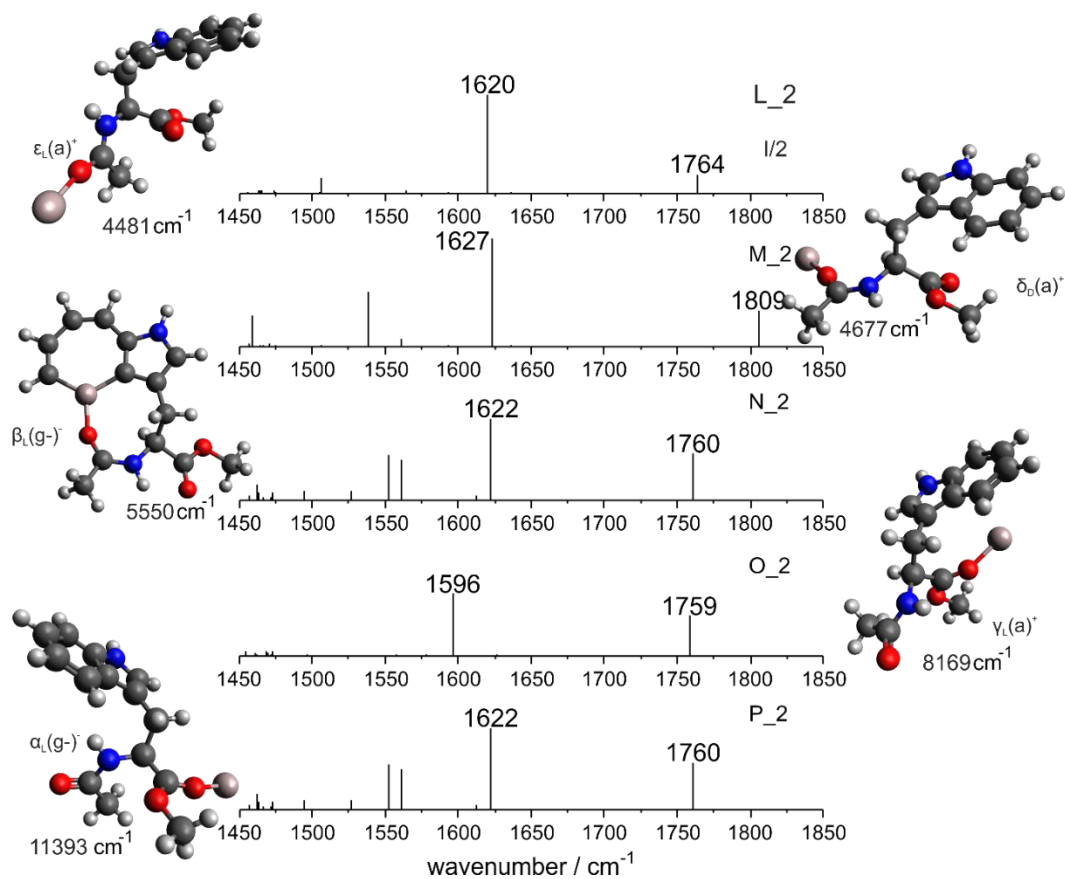


Fig. S2\_f: Harmonically calculated vibrational spectra for the CO stretching region (DFT/B3LYP/TZVP; scal.: 0.9850) of conformers L\_2-P\_2 of [AlAcTrpOMe]<sup>+</sup>. For a better illustration the calculated IR intensities for one isomer (L\_2) is divided by a factor as indicated in the respective stick spectrum.

### Estimation of a possible isomerisation barrier towards the inserted structure

In the figure below, the predicted transition state for the possible oxidative addition within  $[\text{AlAcTrpOMe}]^+$  is depicted. For this, the tridentate geometry H, having the same  $\epsilon_D(g^+)$  backbone geometry as the considerably more stable isomer D, has been selected as starting geometry. The only structural difference between isomers H and D consists in the different side chain orientation, with the indolic NH group, interestingly, being placed just above the aluminium ion in the case of isomer H. Thus, structure H can be considered as a possible starting geometry to calculate a conceivable reaction path towards the inserted structural motif A.

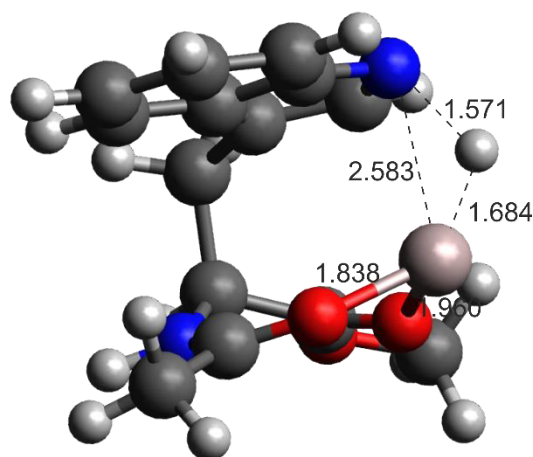


Fig. S3: Transition state structure ( $\epsilon_D(g^+)^+$ ) predicted by a QST3 calculation (performed within Gaussian 09). The  $\text{Al}\cdots\text{N}_{\text{ind-}}$ ,  $\text{N}_{\text{ind}}\cdots\text{H-}$ ,  $\text{Al}\cdots\text{H-}$ ,  $\text{O}_{\text{Ac}}-\text{Al-}$  and  $\text{O}_{\text{E}}-\text{Al-}$  bond lengths are indicated.


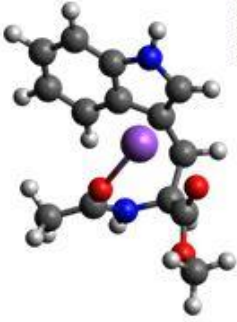
Compared to the starting geometry H, the  $\text{Al}^+$  ion has significantly approached the five-membered ring of the indole system ( $\text{Al}^+\cdots\text{N}$ : only 2.583 Å) in the transition state, while the hydrogen atom of the indole NH group is not localized in the aromatic indole plane anymore, but is pointing towards the metal ion. The involved NH bond is considerably elongated, with a bond length of 1.571 Å compared to only 1.006 Å within the starting geometry, while the  $\text{Al}\cdots\text{H}$  gap is already as small as 1.684 Å.

Considering the mechanism of the discussed oxidative addition, the predicted transition state structure may give a hint towards a concerted reaction path, where the N-H bond is cleaved while the Al-H bond is formed simultaneously (as indicated by dashed lines in fig. S3).

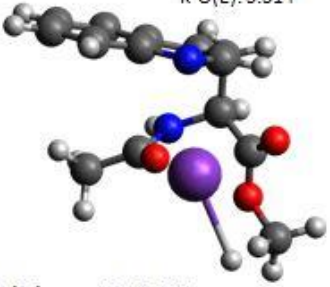
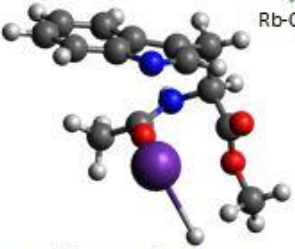
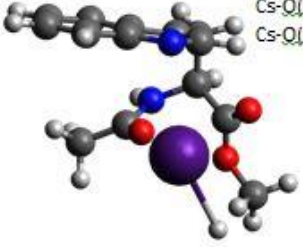
### Structural and electronic data for the considered Li<sup>+</sup>, Na<sup>+</sup>, K<sup>+</sup>, Rb<sup>+</sup>, Cs<sup>+</sup>, Mg<sup>+</sup>, Ti<sup>+</sup>, Zn<sup>+</sup>, Ag<sup>+</sup> and Ga<sup>+</sup>-containing clusters

Tab. S1\_a-S1\_d: Optimized cluster geometries obtained by exchanging Al<sup>+</sup> with the monovalent ions Li<sup>+</sup>, Na<sup>+</sup>, K<sup>+</sup>, Rb<sup>+</sup>, Cs<sup>+</sup>, Mg<sup>+</sup>, Ti<sup>+</sup>, Zn<sup>+</sup>, Ag<sup>+</sup> and Ga<sup>+</sup>; together with the corresponding relative energies (calculated at the level B3LYP-D3/def2-TZVPP), the geometric data, the atomic partial charges (NBO), the ionization energies [1] and the respective ionic radii [1].

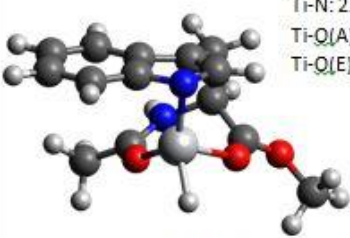
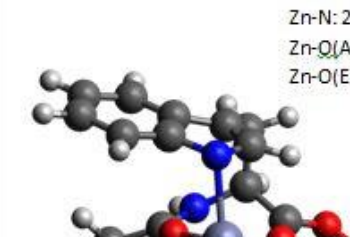
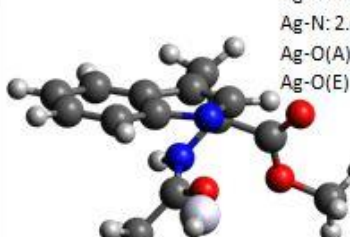
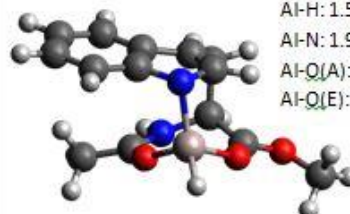
Tab. S1\_a

Structure/selected bond length (M...N <sub>indole</sub> ; M...O(A;amide); M...O(E;ester))/partial charge on the metal ion of the "inserted" structure	energy of the inserted structure relative to the most stable "intact" structure/cm <sup>-1</sup>	Geom.	2 <sup>nd</sup> ionization energy/ kJ/mol <sup>1</sup>	Pauling radii for ox. state (+I)/pm <sup>1</sup>
Li no Al-H bond! Li-N: 1.972 Li-O(A): 1.821 Li-O(E): 4.076  partial charge Li: 0.951	+11858 cm <sup>-1</sup>	α <sub>D</sub> (g <sup>+</sup> )	7298.16	60
Na Indole kept intact! Na-N: 3.031 Na-O(A): 2.187 Na-O(E): 2.317  partial charge Na: 0.966	700 cm <sup>-1</sup>	α <sub>D</sub> (g <sup>+</sup> )	4562.44	95

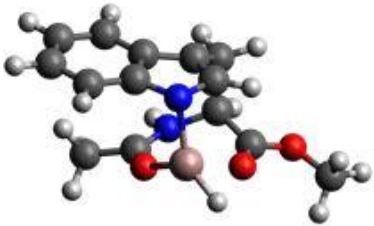
Tab. S1\_b

<p>K</p> <p>K-H: 2.503 K-N: 3.003 K-O(A): 2.639 K-O(E): 3.314</p>  <p>partial charge K: 0.943</p>	41543 cm <sup>-1</sup>	$\alpha_D(g^+)$	3051.35	133
<p>Rb</p> <p>Rb-H: 2.662 Rb-N: 3.177 Rb-Q(A): 2.815 Rb-O(E): 3.450</p>  <p>partial charge Rb: 0.958</p>	41620 cm <sup>-1</sup>	$\alpha_D(g^+)$	2633.04	148
<p>Cs</p> <p>Cs-H: 2.745 Cs-N: 3.307 Cs-Q(A): 2.980 Cs-Q(E): 3.634</p>  <p>partial charge Cs: 0.975</p>	41730 cm <sup>-1</sup>	$\alpha_D(g^+)$	2234.35	181

Tab. S1\_c

<p>Ti</p>  <p>Ti-H: 1.725 Ti-N: 2.130 Ti-O(A): 2.052 Ti-O(E): 2.115</p> <p>partial charge Ti: 1.295</p>	-2959 cm <sup>-1</sup>	$\alpha_D(g^+)$	1309.84	96
<p>Zn</p>  <p>Zn-H: 1.528 Zn-N: 2.292 Zn-O(A): 2.015 Zn-O(E): 2.345</p> <p>partial charge Zn: 1.351</p>	7183 cm <sup>-1</sup>	$\epsilon_D(g^+)$	1733.30	88
<p>Ag</p>  <p>Ag-H: 1.592 Ag-N: 2.637 Ag-O(A): 2.225 Ag-O(E): 4.853</p> <p>partial charge Ag: 0.622</p>	26673 cm <sup>-1</sup>	$\alpha_D(g^+)$	2072.93	126
<p>Al</p>  <p>Al-H: 1.546 Al-N: 1.920 Al-O(A): 1.810 Al-O(E): 1.952</p> <p>partial charge Al: 1.747</p>	-1156 cm <sup>-1</sup>	$\epsilon_D(g^+)$	1816.68	72

Tab. S1\_d

<p>Ga</p> <p>Ga-H: 1.530 Ga-N: 1.958 Ga-Q(A): 1.923 Ga-O(E): 2.126</p>  <p>partial charge Ga: 1.596</p>	11711 cm <sup>-1</sup>	$\epsilon_D(g^+)$	1979.41	81
--	------------------------	-------------------	---------	----



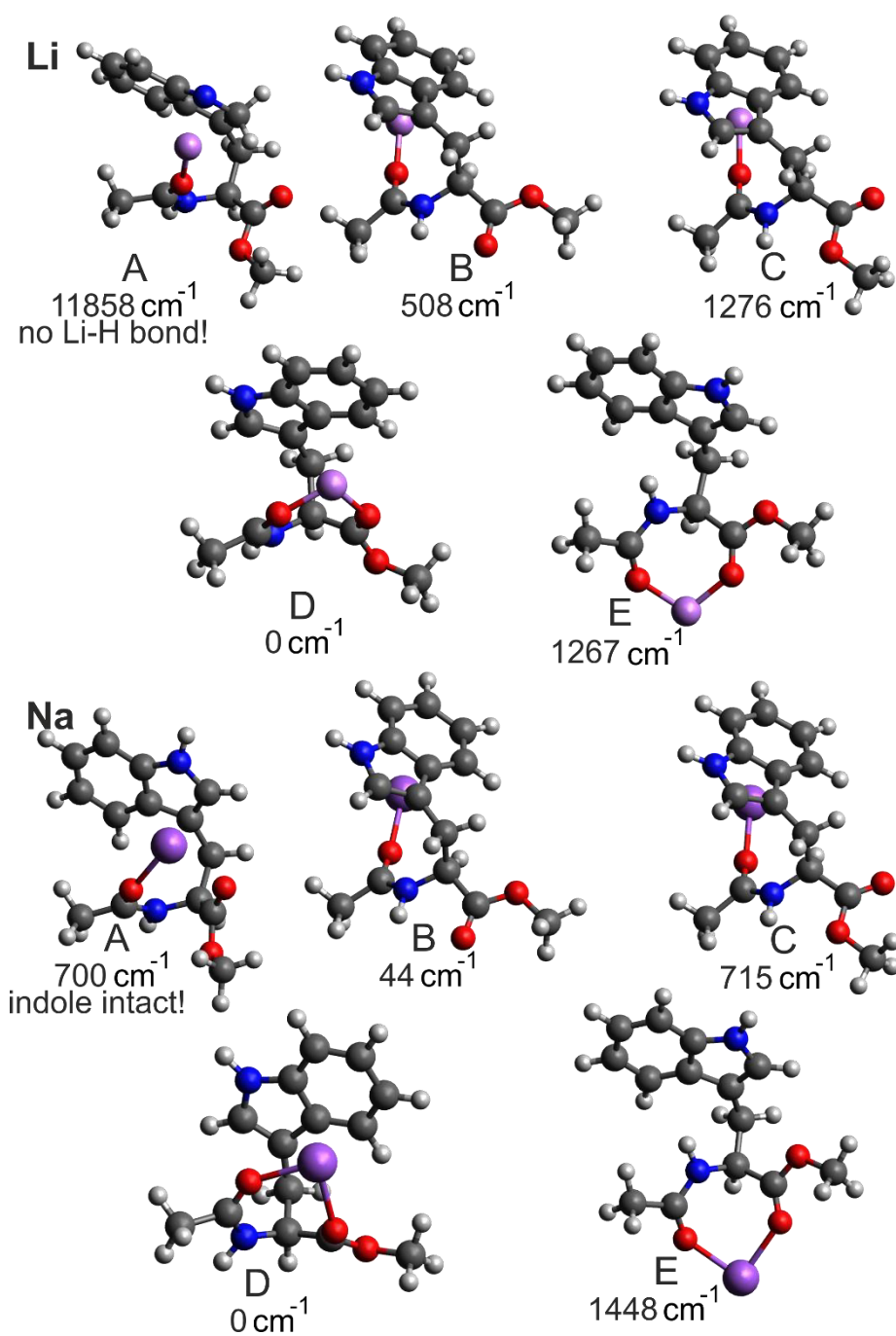


Fig. S4\_a: Calculated cluster geometries (DFT/B3LYP-D3/def2-TZVPP) with their respective (zero point corrected) relative energies. For each cluster geometry, the energy is indicated relative to the most stable „intact“ geometry obtained for the respective metal elements (Li, Na).

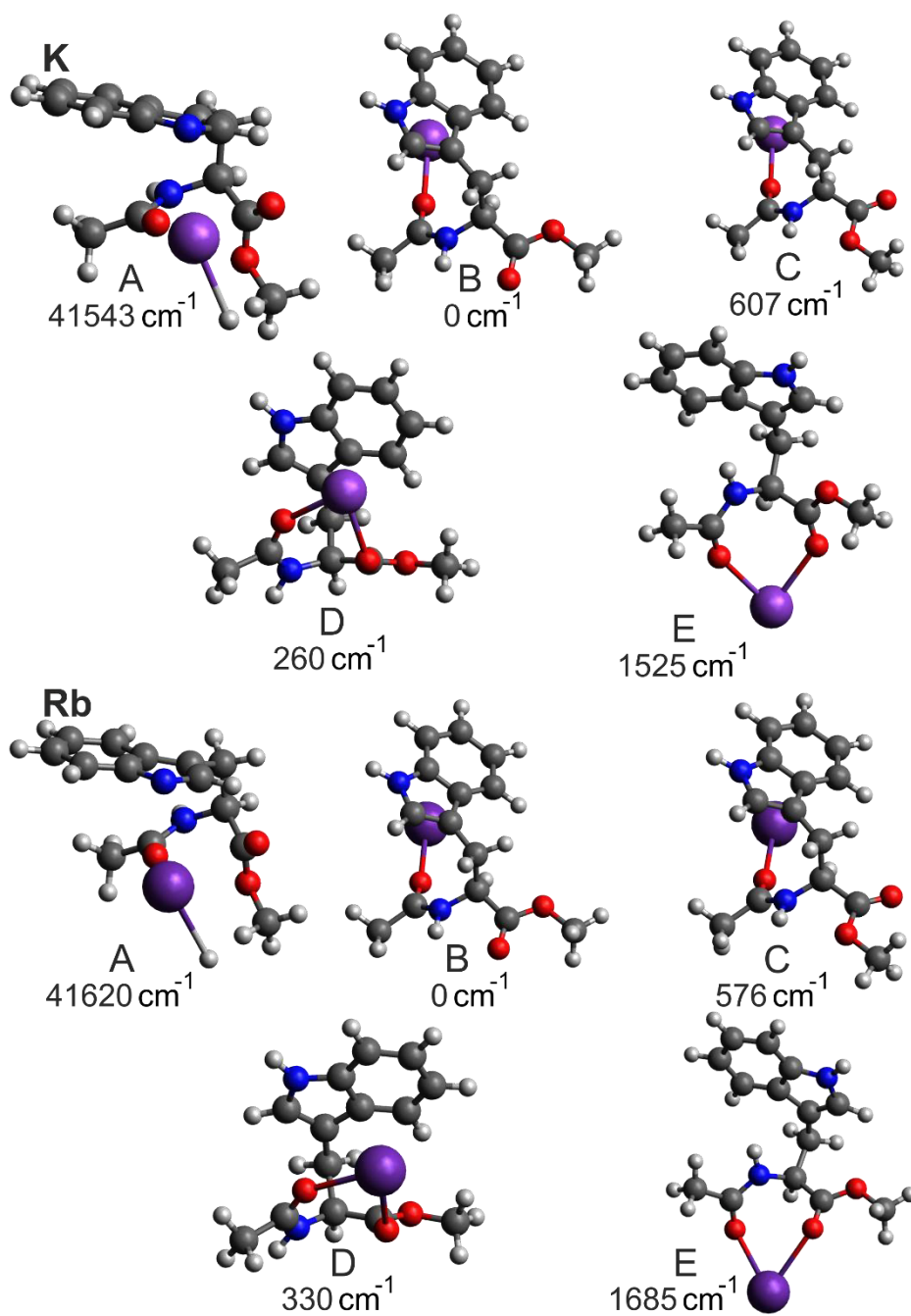


Fig. S4\_b: Calculated cluster geometries (DFT/B3LYP-D3/def2-TZVPP) with their respective (zero point corrected) relative energies. For each cluster geometry, the energy is indicated relative to the most stable „intact“ geometry obtained for the respective metal elements (K, Rb).

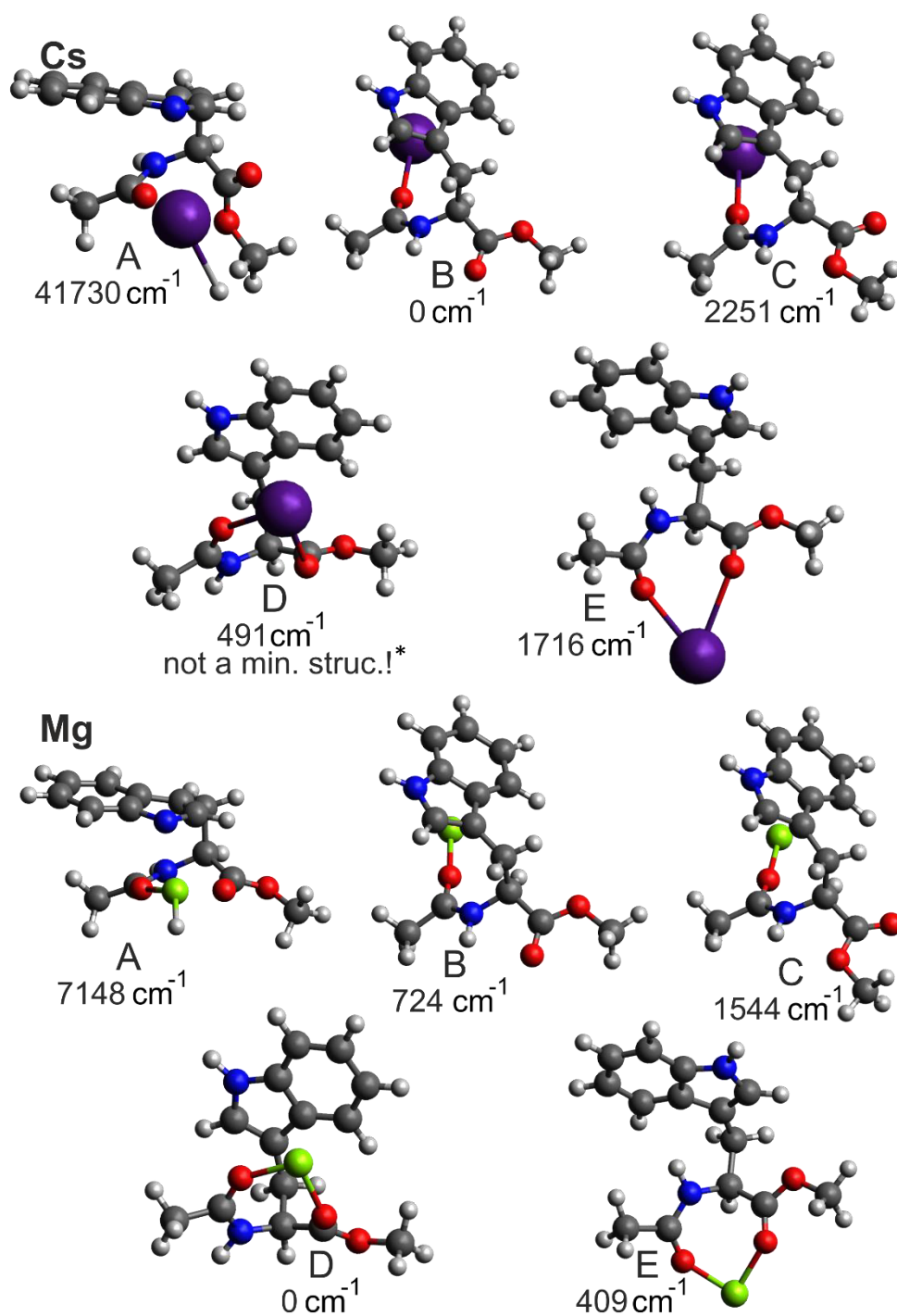


Fig. S4\_c: Calculated cluster geometries (DFT/B3LYP-D3/def2-TZVPP) with their respective (zero point corrected) relative energies. For each cluster geometry, the energy is indicated relative to the most stable „intact“ geometry obtained for the respective metal elements (Cs, Mg).

\*: structure yielded an imaginary frequency

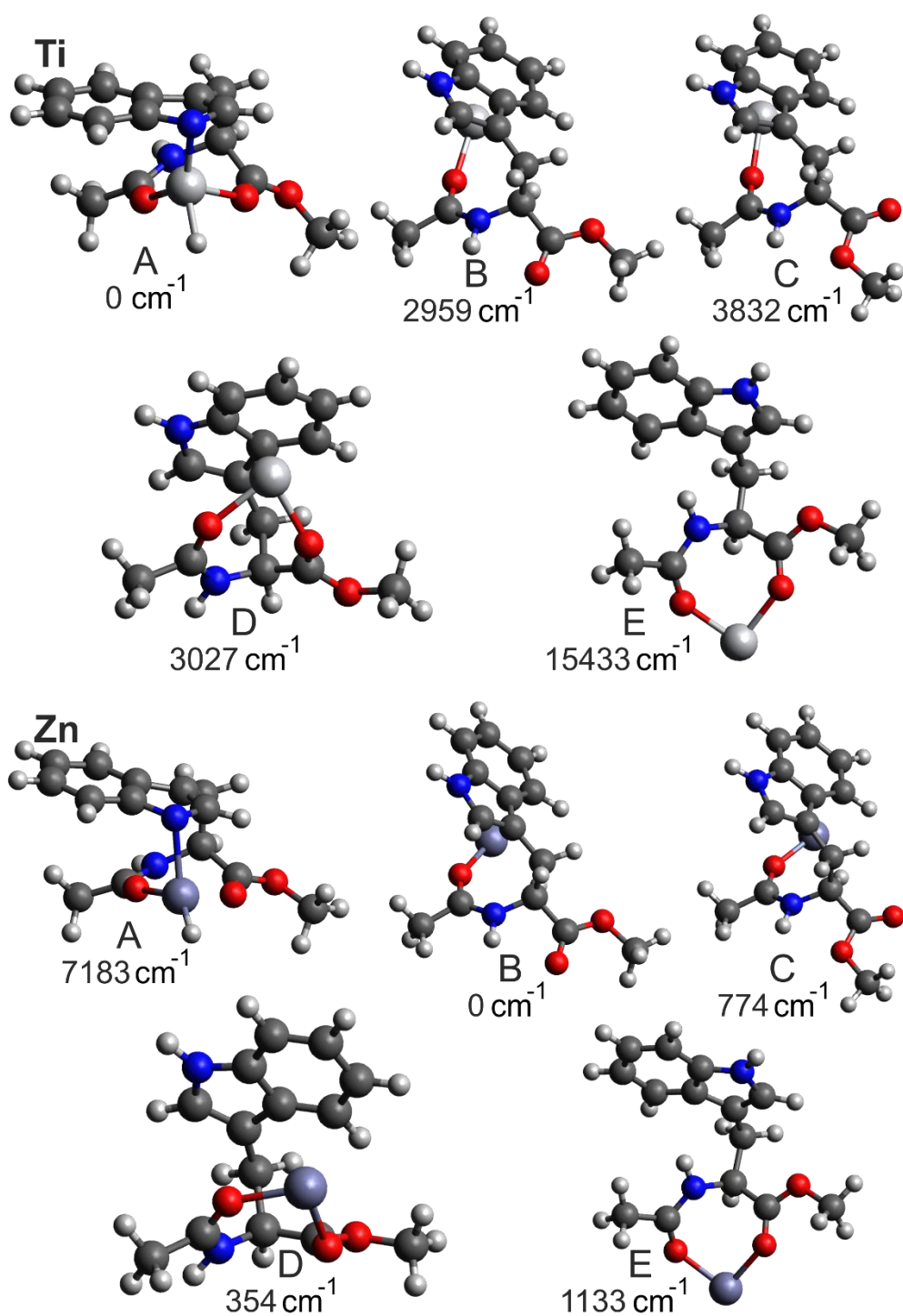


Fig. S4\_d: Calculated cluster geometries (DFT/B3LYP-D3/def2-TZVPP) with their respective (zero point corrected) relative energies. For each cluster geometry, the energy is indicated relative to the most stable „intact“ geometry obtained for the respective metal elements (Ti, Zn).

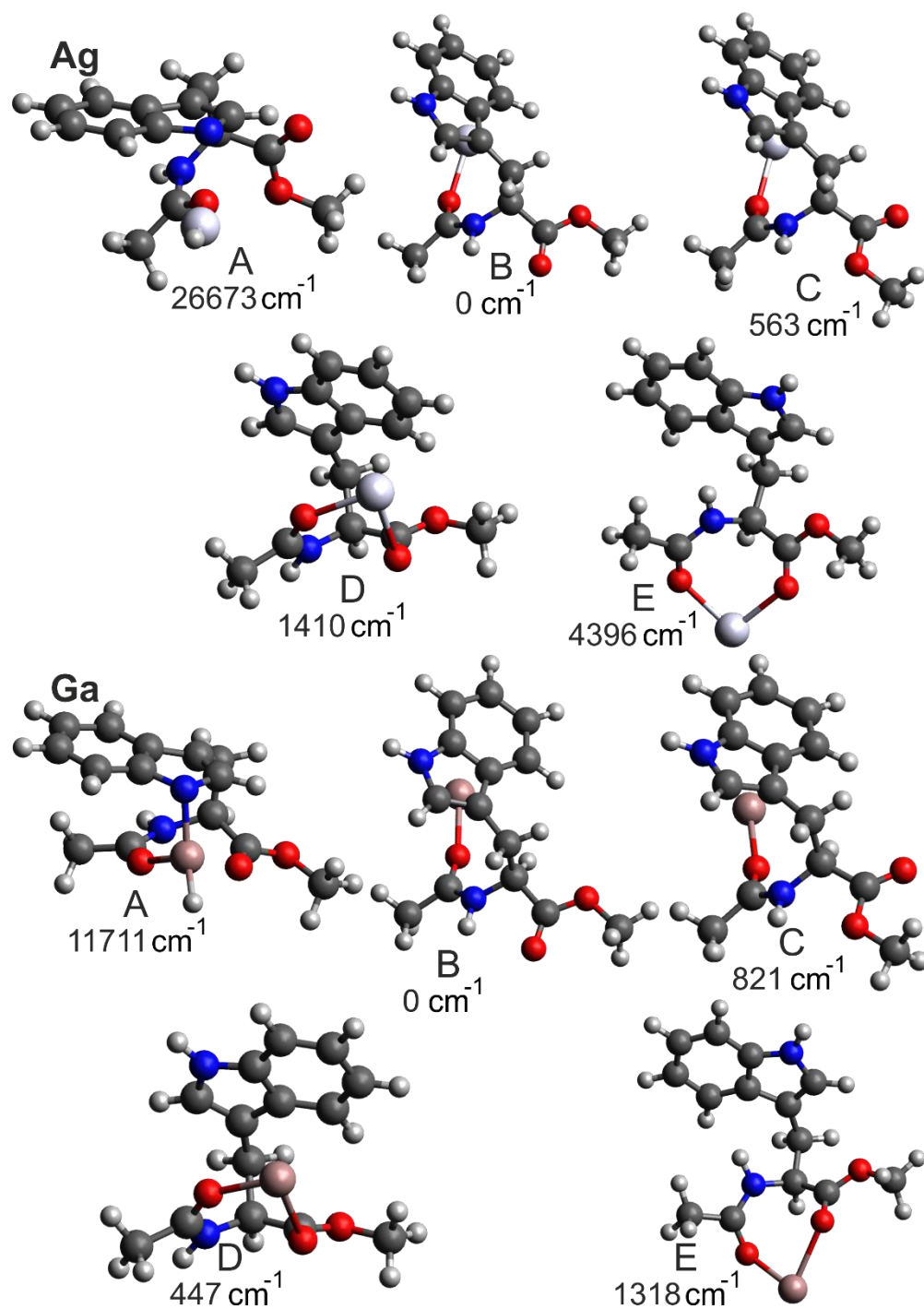


Fig. S4\_e: Calculated cluster geometries (DFT/B3LYP-D3/def2-TZVPP) with their respective (zero point corrected) relative energies. For each cluster geometry, the energy is indicated relative to the most stable „intact“ geometry obtained for the respective metal elements (Ag, Ga).

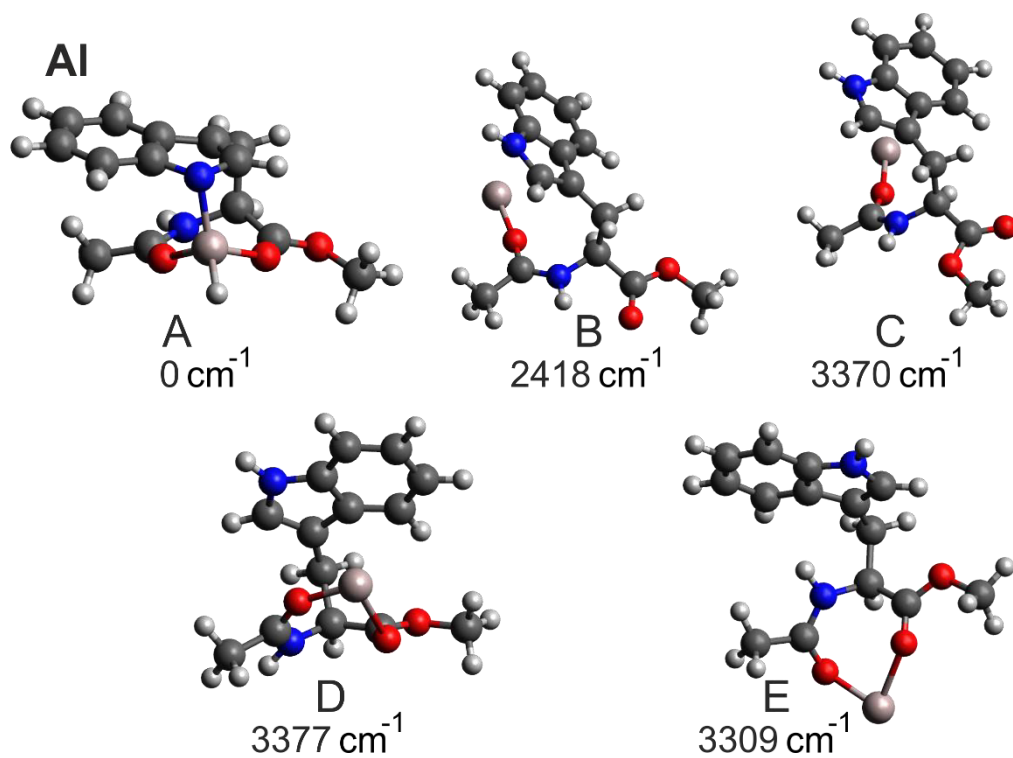


Fig. S4\_f: Calculated cluster geometries (DFT/B3LYP-D3/def2-TZVPP) with their respective (zero point corrected) relative energies. For each cluster geometry, the energy is indicated relative to the most stable „intact“ geometry obtained for the respective metal element (Al).

**Calculated vibrational (NH-stretching) frequencies obtained for the Li<sup>+</sup>, Na<sup>+</sup>, K<sup>+</sup>, Rb<sup>+</sup>, Cs<sup>+</sup>, Mg<sup>+</sup>, Ti<sup>+</sup>, Zn<sup>+</sup>, Ag<sup>+</sup> and Ga<sup>+</sup>-containing clusters**

Tab. S2\_a-S2\_k: Harmonically calculated vibrational frequencies (DFT/B3LYP-D3/def2-TZVPP; scal. 0.9551) for the NH stretching region obtained for the different geometries (A, B, C, D, E), comprising the considered metal elements Li, Na, K, Rb, Cs, Mg, Ti, Zn, Ag, Ga, Al.

**Li**

isomer	NH <sub>ind</sub>	NH <sub>bb</sub>
A (no Li-H bond!)	-	3469
B	3493	3403
C	3493	3451
D	3496	3467
E	3499	3366

**Na**

isomer	NH <sub>ind</sub>	NH <sub>bb</sub>
A (indole intact!)	-	3481
B	3494	3414
C	3496	3457
D	3499	3470
E	3502	3385

**K**

isomer	NH <sub>ind</sub>	NH <sub>bb</sub>
A	-	3470
B	3496	3421
C	3496	3461
D	3500	3474
E	3502	3400

**Rb**

isomer	NH <sub>ind</sub>	NH <sub>bb</sub>
A	-	3471
B	3497	3424
C	3497	3462
D	3501	3476
E	3502	3409

**Cs**

isomer	NH <sub>ind</sub>	NH <sub>bb</sub>
A	-	3470
B	3498	3426
C	3485	3451
D (not a min. struc.!)	3501	3475
E	3502	3412

**Mg**

isomer	NH <sub>ind</sub>	NH <sub>bb</sub>
A	-	3459
B	3496	3394
C	3496	3443
D	3498	3459
E	3498	3351

**Ti**

isomer	NH <sub>ind</sub>	NH <sub>bb</sub>
A	-	3456
B	3491	3387
C	3492	3438
D	3492	3461
E	3497	3336

**Zn**

isomer	NH <sub>ind</sub>	NH <sub>bb</sub>
A	-	3461
B	3493	3398
C	3493	3446
D	3497	3466
E	3498	3350

**Ag**

isomer	NH <sub>ind</sub>	NH <sub>bb</sub>
A	-	3470
B	3492	3418
C	3492	3450
D	3496	3474
E	3499	3375



**Ga**

isomer	NH <sub>ind</sub>	NH <sub>bb</sub>
A	-	3444
B	3496	3395
C	3496	3442
D	3498	3463
E	3499	3349

**Al**

isomer	NH <sub>ind</sub>	NH <sub>bb</sub>
A	-	3443
B	3496	3370
C	3496	3427
D	3497	3454
E	3498	3325

The presented structures, relative energies and vibrational frequencies were determined mainly for comparison with the results obtained for [AlAcTrpOMe]<sup>+</sup>. However, some trends can be observed, especially for the alkali clusters, since the “bidentate” structural motif B, with the metal ion being linked to the CO<sub>Ac</sub> group and at the same time interacting with the  $\pi$ -system, is increasingly favoured (especially over the “tridentate” geometry D) when going from Li down to Cs. In other words, the “tridentate” structural motif is favoured for small ions of high charge density like Li<sup>+</sup> and Na<sup>+</sup> (in contrast to the aggregates with K<sup>+</sup>, Rb<sup>+</sup>, Cs<sup>+</sup>). This result is in accordance with earlier theoretical and experimental studies on systems of isolated Trp linked to alkali ions [2,3,4]. Furthermore, the alkali clusters show a clear trend concerning the corresponding NH-stretching frequencies, as the mentioned vibrational modes tend to undergo, considering any of the structural motifs B to E, (almost without exception) a successive blue-shift from Li to Cs. This effect may be explained mainly by the decreasing ion charge density (when going from Li to Cs), leading to a weakening of the M<sup>+</sup>... $\pi$ - and M<sup>+</sup>...O=C- interactions.

Another very interesting aspect is the observation that for all the structural motifs (A-E) the predicted NH<sub>bb</sub>-stretching frequencies are particularly red-shifted in the clusters with Al<sup>+</sup>, which are in the focus of this project. Thus, the influence of Al<sup>+</sup> on the electronic structure of AcTrpOMe is comparatively pronounced compared to clusters comprising other metal centers of comparable ion size/positive charge density, so that aluminium shows a somehow unique behaviour.

**Measured UV photodissociation spectrum**

The UV/VIS photo dissociation spectrum in the region between 36400 and 36600  $\text{cm}^{-1}$ , showing an onset at about 36425 $\text{cm}^{-1}$ , is depicted in figure S5 below.

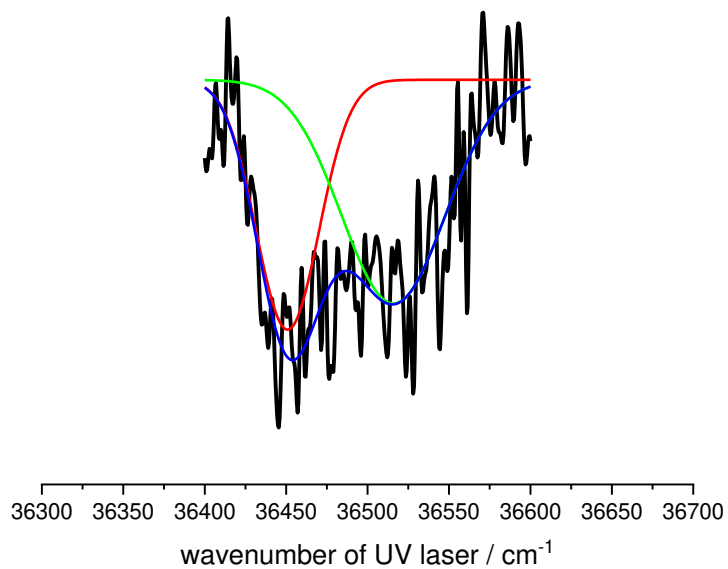


Fig. S5: UV/VIS photo dissociation spectrum of [Al-AcTrpOMe]<sup>+</sup> with Gaussian fits (red and green curves with maxima at 36451 and 36516  $\text{cm}^{-1}$ ) and their envelope (blue curve).

## Calculated UV/VIS absorption spectra

In the following figure S6 the predicted UV/VIS spectra (calculated at the TDDFT/B3LYP-D3/TZVP level) for isomers A-J are presented.

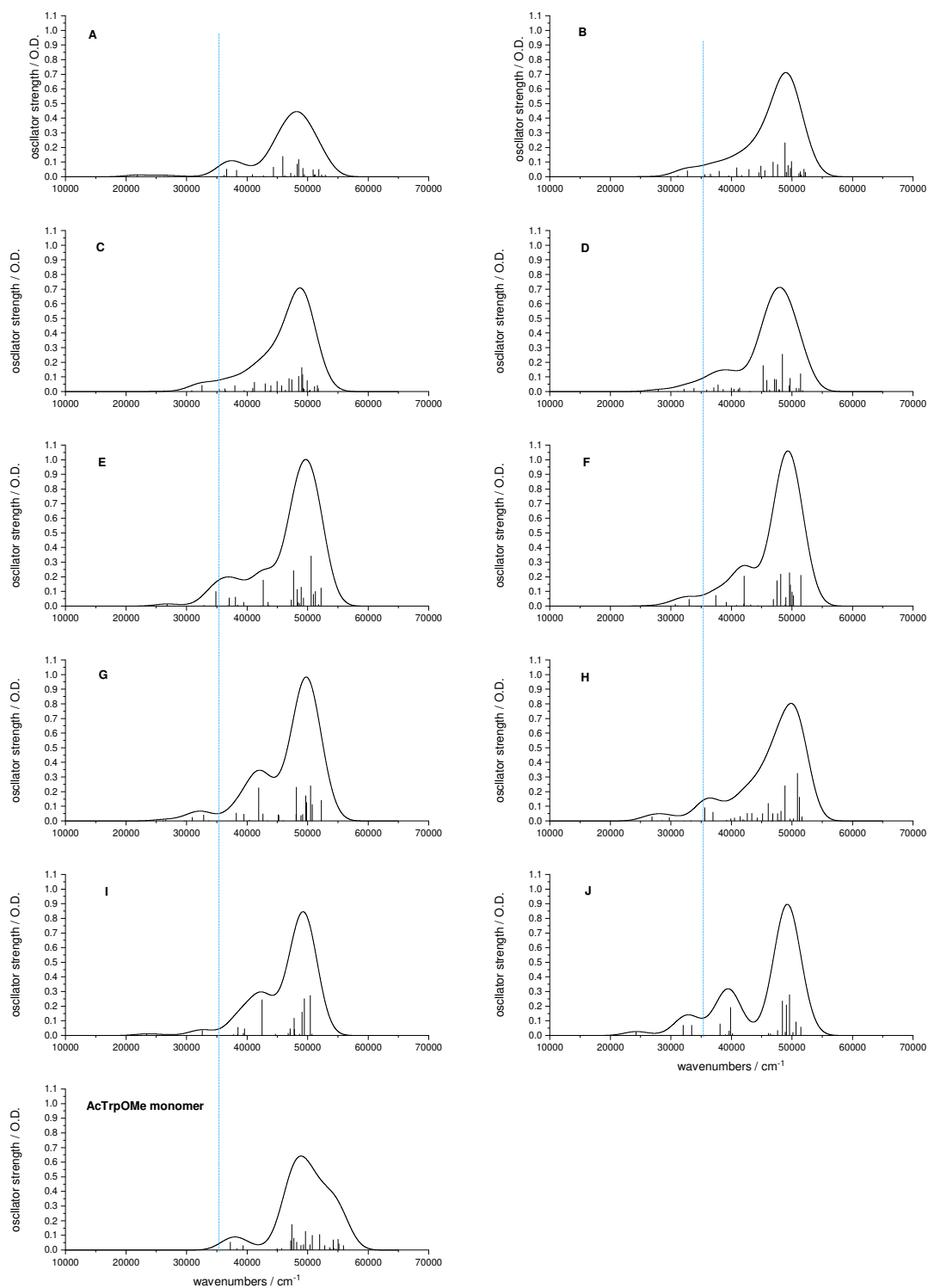


Fig S6: Calculated UV/VIS absorbance frequencies and theoretical UV/VIS spectrum (at the level TDDFT/B3LYP-D3/TZVP) of isomers A-J and the structure assigned for the isolated AcTrpOMe monomer (gaussian conv.  $2000\text{ cm}^{-1}$ ). The UV laser wavelength ( $35335\text{ cm}^{-1}$ ) applied within the IR+UV experiment is indicated by the blue dashed line.

The UV/VIS spectra of selected isomers presented in figure S6 show the spin-allowed transitions predicted by the TDDFT/B3LYP-D3/TZVP calculations (unshifted, values directly taken from the calculation). Interestingly, the two maxima observed in the measured UV photodissociation spectrum (at about 36451 and 36516  $\text{cm}^{-1}$ ) could be explained by the folded UV/VIS spectra predicted for the “inserted” energetic minimum structure A as well as for isomer E. At the same time, the pattern for isomer C, which could principally be assigned according to the measured and predicted IR spectra, shows no considerable absorption peak in the respective UV/VIS absorption range, but only a rather gentle increase in UV absorption intensity. This aspect could be considered as a further hint that the inserted energetic minimum structure A is actually formed in the experiment.

It should also be noted that the other isomers comprising an intact AcTrpOMe molecule show a UV absorption peak which is red-shifted relative to the band of structure A. Thus, all the discussed isomers can principally be probed within the performed IR+UV experiment if the vibrational excitation followed by UV excitation leads to a dissociative channel.

**Atomic partial charges predicted by natural bond orbital (NBO) and Mulliken population analyses**

In the following the most relevant atomic partial charges are given for selected isomers, obtained by performing natural bond orbital (NBO) and Mulliken population analyses.

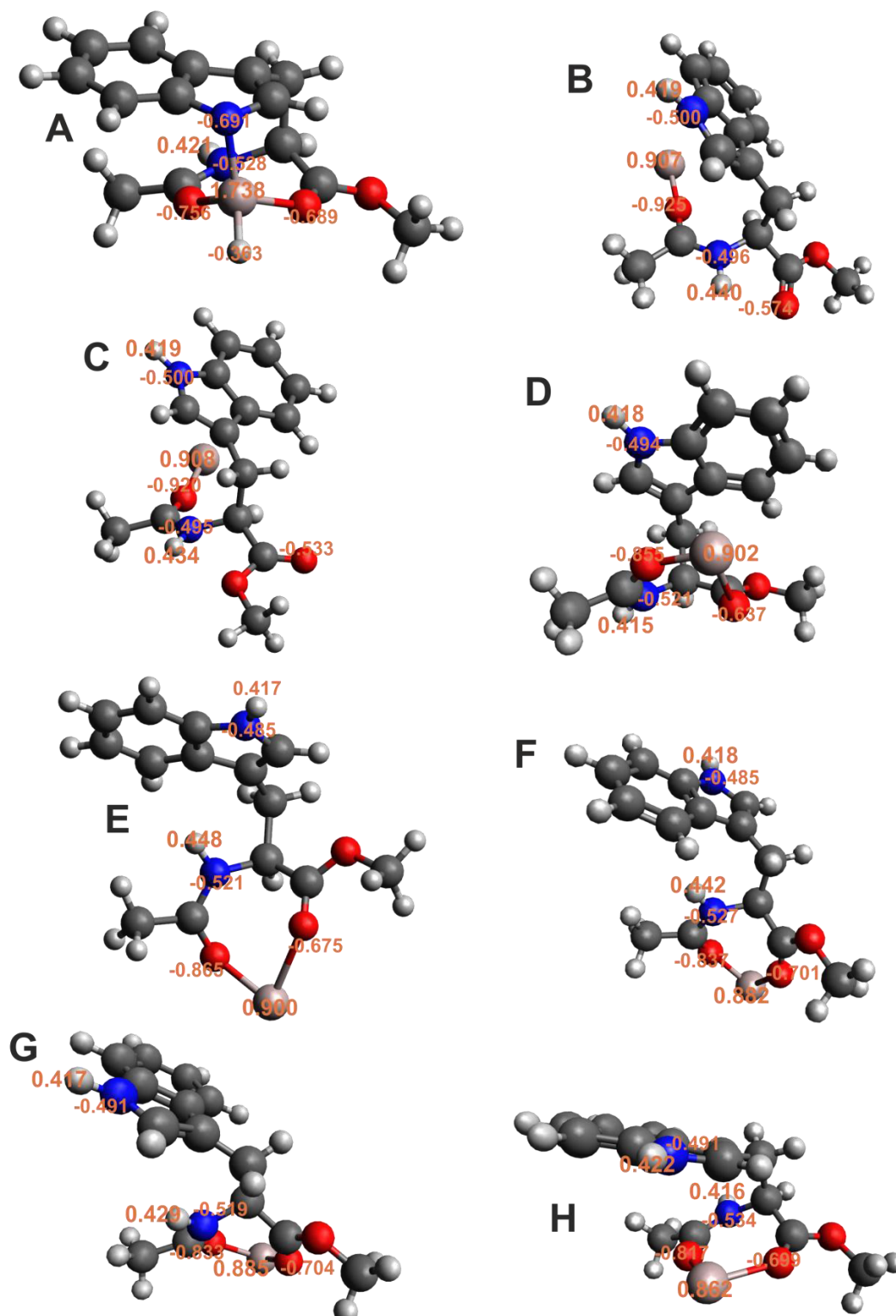


Fig. S7\_a: Atomic partial charges for selected atoms (Al<sup>+</sup>, amide N atom, amide H atom, indole N atom, indole (N)H atom, carbonyl O atoms of peptide bond and ester) of isomers A-H, obtained within a natural bond orbital (NBO) analysis performed at the level B3LYP-D3/TZVP.

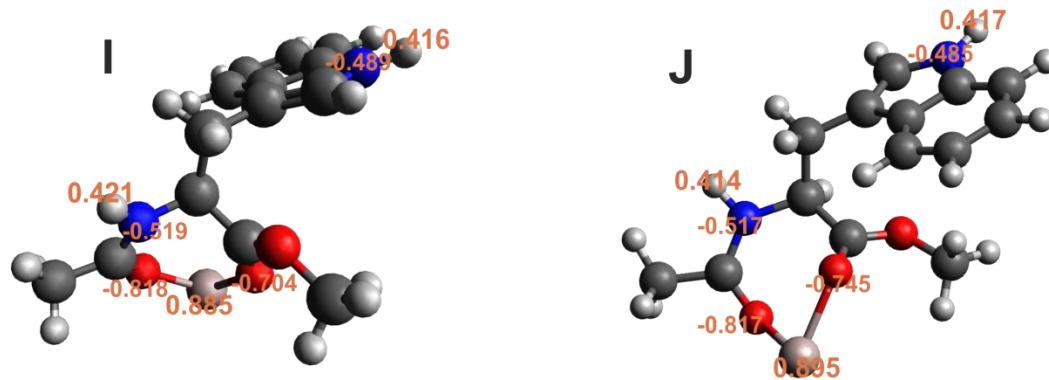


Fig. S7\_b: Atomic partial charges for selected atoms ( $\text{Al}^+$ , amide N atom, amide H atom, indole N atom, indole (N)H atom, carbonyl O atoms of peptide bond and ester) of isomers I-J, obtained within a natural bond orbital (NBO) analysis performed at the level B3LYP-D3/TZVP.

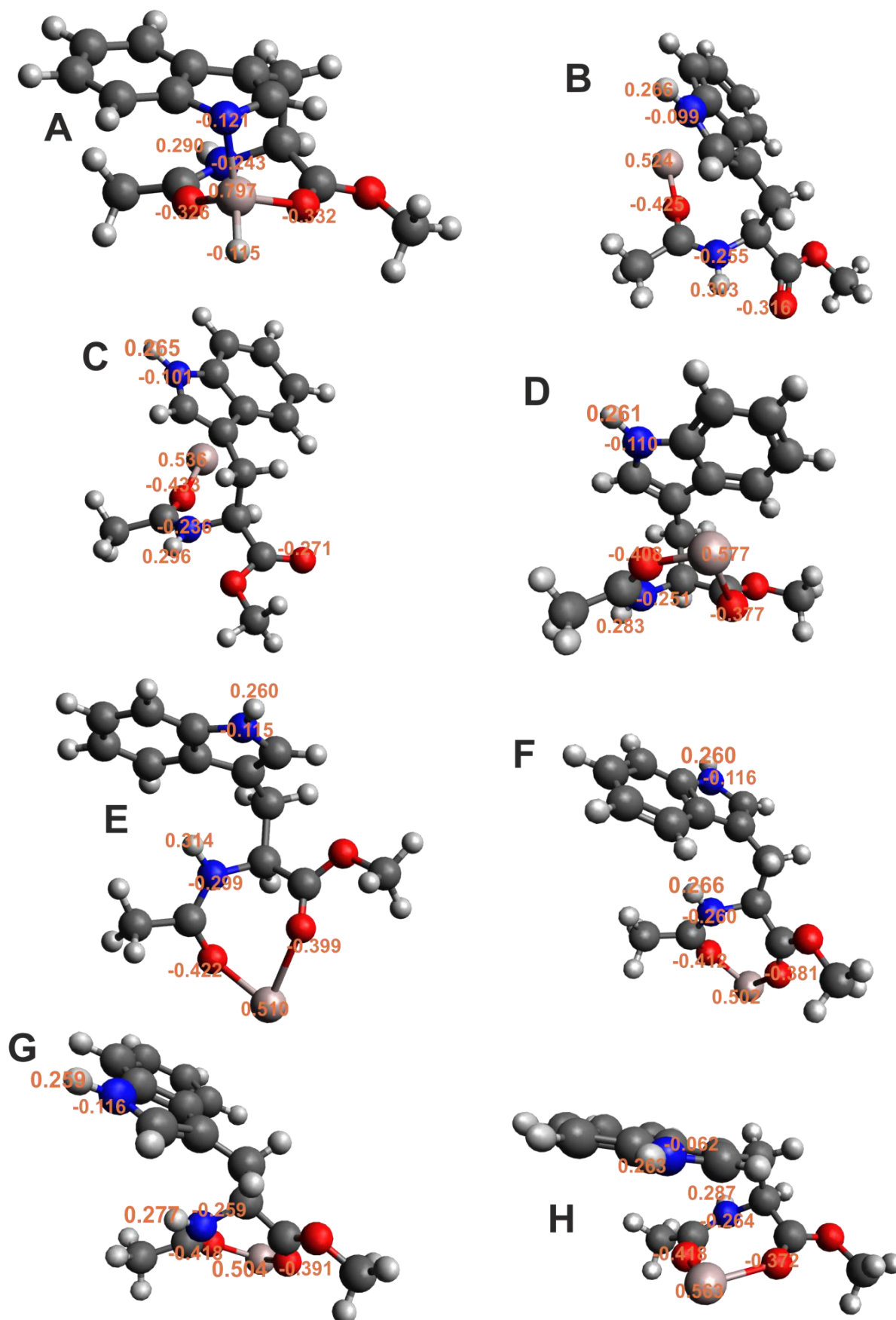


Fig. S8\_a: Atomic partial charges for selected atoms (Al<sup>+</sup>, amide N atom, amide H atom, indole N atom, indole (N)H atom, carbonyl O atoms of peptide bond and ester) of isomers A-H, obtained within a Mulliken population analysis performed at the level B3LYP-D3/TZVP.

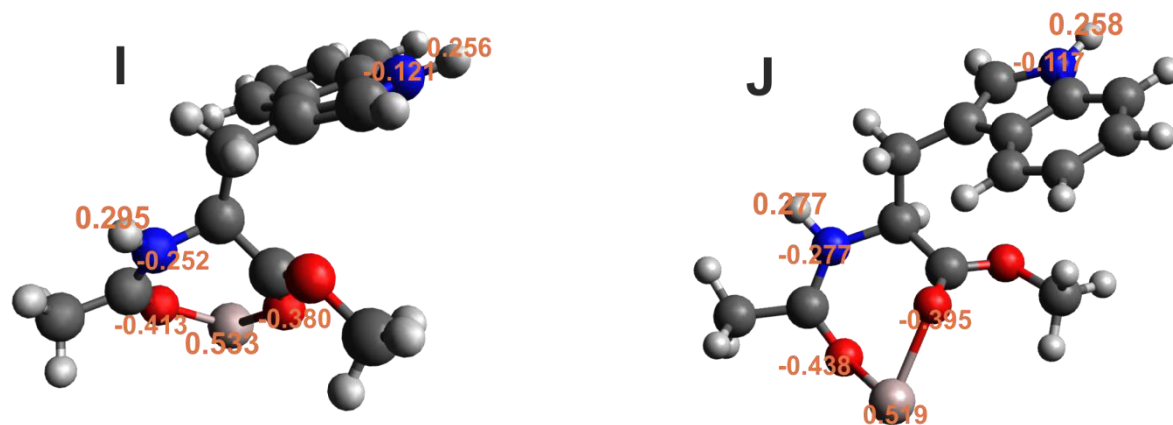


Fig. S8\_b: Atomic partial charges for selected atoms ( $\text{Al}^+$ , amide N atom, amide H atom, indole N atom, indole (N)H atom, carbonyl O atoms of peptide bond and ester) of isomers I-J, obtained within a Mulliken population analysis performed at the level B3LYP-D3/TZVP.



**Geometric data for the most relevant isomers of [AlAcTrpOMe]<sup>+</sup>**

Tab. 2: Geometric data (calculated at the level B3LYP-D3/TZVP) for selected isomers (A-J) of [AlAcTrpOMe]<sup>+</sup>, together with the predicted transition state geometry as well as the structure assigned for the isolated AcTrpOMe monomer.

isomer	Backbone geometry	$\Psi/^\circ$	$\Phi/^\circ$	$\chi_1/^\circ$	$\chi_2/^\circ$
<b>A</b>	$\varepsilon_D(g^+)^+$	133.8	45.5	60.0	69.7
<b>B</b>	$\beta_L(g^-)^+$	164.3	-147.3	-62.3	105.0
<b>C</b>	$\delta_D(g^-)^+$	-23.0	-142.4	-63.8	105.9
<b>D</b>	$\varepsilon_D(g^+)^-$	164.9	55.8	59.8	-98.3
<b>E</b>	$\varepsilon_L(g^+)^+$	-138.7	-76.5	48.7	91.0
<b>F</b>	$\alpha_L(g^-)^-$	-113.6	-76.5	-49.9	-87.3
<b>G</b>	$\varepsilon_L(g^-)^+$	-120.9	-77.5	-47.0	117.0
<b>H</b>	$\varepsilon_D(g^+)^+$	126.7	51.8	52.5	99.0
<b>I</b>	$\alpha_L(a)^-$	-92.4	-73.2	-172.9	-111.7
<b>J</b>	$\varepsilon_L(a)^+$	151.1	-33.8	178.6	89.3
<b>transition state</b>	$\varepsilon_D(g^+)^+$	139.6	53.5	56.5	79.2
<b>isolated AcTrpOMe monomer</b>	$\beta_L(g^+)^-$	171.7	-162.1	63.7	-83.2

Tab. 3: Calculated distances (Å) (B3LYP-D3/TZVP level) for selected isomers (A-J) of [AlAcTrpOMe]<sup>+</sup> and for the predicted transition state (TS): between the Al ion and the carbonyl O atom of the amide group; between the Al ion and the carbonyl O atom of the ester; between the Al ion and the N atom of the indole substituent; of the Al–H bond; between the Al ion and the  $\pi$ -system (Al $\cdots$ 6-ring/Al $\cdots$ 5-ring); between the backbone NH group and the OMe group of the ester; between the backbone NH group and the carbonyl O atom of the ester; between the backbone NH group and the  $\pi$ -system (Al $\cdots$ 6-ring/Al $\cdots$ 5-ring).

isomer	O <sub>Ac</sub> $\cdots$ Al	O <sub>E</sub> $\cdots$ Al	Al $\cdots$ N <sub>ind</sub>	Al–H	Al $\cdots$ $\pi$ (6-ring/5-ring)	NH <sub>bb</sub> $\cdots$ OMe	NH <sub>bb</sub> $\cdots$ O <sub>E</sub>	NH <sub>bb</sub> $\cdots$ $\pi$ (6-ring/5-ring)
A	1.827	1.977	1.923	1.550	-	-	-	-
B	1.874	-	-	-	3.13/3.62	-	2.221	-
C	1.882	-	-	-	3.10/3.60	2.246	-	-
D	1.933	2.538	-	-	3.35/3.69	-	-	-
E	1.915	2.427	-	-	-	-	-	3.11/2.82
F	1.947	2.242	-	-	-	-	-	3.17/3.12
G	1.948	2.236	-	-	-	-	-	-/2.92
H	1.946	2.191	-	-	-/3.38	-	-	-
I	1.997	2.224	-	-	-	-	-	-
J	1.990	2.134	-	-	-	-	-	-
TS	1.838	1.960	2.583	1.684	-	-	-	-

### Comparison of [AlAcTrpOMe]<sup>+</sup> and [AlAcPheOMe]<sup>+</sup>

In the main part of this paper the comparison between [AlAcTrpOMe]<sup>+</sup> and [AlAcPheOMe]<sup>+</sup> or isolated AcTrpOMe is briefly addressed several times and reveals a different structural behaviour of [AlAcTrpOMe]<sup>+</sup> compared to the Phe-containing aluminum aggregate. Isomers with Al<sup>+</sup> being linked to both CO groups were assigned to [AlAcPheOMe]<sup>+</sup>, with the conformations  $\alpha_{\text{I}}(\text{g-})$  and  $\alpha_{\text{I}}(\text{a})$ . Those conformers were also calculated for [AlAcTrpOMe]<sup>+</sup> (F and I), but for the former (F) the calculated NH-backbone vibration cannot describe one of the corresponding experimental bands (at 3293 cm<sup>-1</sup> or 3414 cm<sup>-1</sup>); for the latter (I) a description of the experimental vibration of 3414 cm<sup>-1</sup> might be given, but its relatively high energy makes its presence less probable. With regard to the special characteristics of the indole chromophore and observed insertion reactions for Al(I) [5,6] an assignment of other isomers than for [AlAcPheOMe]<sup>+</sup> is not very surprising. A further difference between [AlAcPheOMe]<sup>+</sup> and [AlAcTrpOMe]<sup>+</sup> is the dissociation behaviour (already briefly mentioned in context with the UV PD spectroscopy): For gas phase peptide ions in general the loss of aromatic side chains for Tyr and Trp (together with H-atoms) is a frequent consequence of UV radiation between 193 and 260 nm, strongly depending on the wavelength, peptide sequence and protonation state [7-11]. For [AlAcPheOMe]<sup>+</sup>, AcPheOMe<sup>+</sup> could always be observed as fragment signal for the UV as well as for the IR photodissociation spectroscopy [12]. This was already a characteristic dissociation behaviour since Willey et al. found in their experiments that [Ag-benzene]<sup>+</sup> undergoes a dissociative charge transfer process into benzene<sup>+</sup> and Ag<sup>0</sup>, but [Al-benzene]<sup>+</sup> dissociated into Al<sup>+</sup> and benzene<sup>0</sup>, independent of the laser wavelength used to initiate the dissociation [13]. The dissociative charge transfer process in UV PD was later on also observed for [Ag-Trp]<sup>+</sup> in literature. In addition, other channels including the fragmentation of the side chain were observed, probably because the binding energy of the silver cation was higher than the energy needed to activate the fragmentation of the side chain [14]. However, we could not find comparable studies with singly charged aluminium in literature. For [AlAcTrpOMe]<sup>+</sup>, neither in the UV PD nor the IR+UV process AcTrpOMe<sup>+</sup> was found as fragment ion; both spectra were merely recorded as depletion spectra of the parent [AlAcTrpOMe]<sup>+</sup> ion. A further difference to the singly charged [AlAcPheOMe]<sup>+</sup> is that the IRPMD method did not work for [AlAcTrpOMe]<sup>+</sup>. These observations could be an indicator for a higher dissociation energy in [AlAcTrpOMe]<sup>+</sup> and a different dissociation behaviour, both associated to other isomers than those assigned for [AlAcPheOMe]<sup>+</sup>.

## References

- [1] WebElements [<http://www.webelements.com/>]
- [2] Nick C. Polfer, Jos Oomens and Robert C. Dunbar, *Phys. Chem. Chem. Phys.*, **8**, 2744 (2006).
- [3] C. Ruan and M.T. Rodgers, *J. Am. Chem. Soc.*, **126**, 14600 (2004).
- [4] R. C. Dunbar, *J. Phys. Chem. A*, **104**, 8067 (2000).
- [5] C. Cui, H. W. Roesky, H.-G. Schmidt, M. Noltemeyer, H. Hao and F. Cimpoesu, *Angew. Chem. Int. Ed.* **39**, 23 (2000).
- [6] T. Chu, I. Korobkov and G. I. Nikonov, *J. Am. Chem. Soc.* **136**, 9195 (2014).
- [7] R. Antoine and P. Dugourd, *Phys. Chem. Chem. Phys.* **13**, 16494 (2011).
- [8] T. Tabarin, R. Antoine, M. Broyer and P. Dugourd, *Rapid Commun. Mass Spectrom.* **19**, 2883 (2005).
- [9] H. Kang, C. Dedonder-Lardeux, C. Jouvét, S. Martrenchard, G. Gregoire, C. Desfrancois, J. P. Schermann, M. Barat and J. A. Fayeton, *Phys. Chem. Chem. Phys.* **6**, 2628 (2004).
- [10] L. Joly, R. Antoine, M. Broyer, P. Dugourd and J. Lemoine, *J. Mass Spectrom.* **42**, 818 (2007).
- [11] E.R. Williams, J.J.P. Furlong and F.W. McLafferty, *J. Am. Soc. Mass Spectrom.* **1**, 288 (1990).
- [12] P. M. Bialach, T. C. Martin and M. Gerhards, *Phys. Chem. Chem. Phys.* **14**, 8185 (2012).
- [13] K.F. Willey, P.Y. Cheng, K.D. Pearce and M.A. Duncan, *J. Phys. Chem.* **94**, 4769 (1990).
- [14] M. Broyer, P. Dugourd, R. Mitrić and V. Bonačić-Koutecký, *Chem. Phys. Chem.* **7**, 524 (2006).
- [15] E. K. U. Gross, L. N. Oliveira, and W. Kohn, *Phys Rev A Gen Phys.*, 37(8), 2805 (1988).

## 8 Summary and Outlook

The present work deals with the investigation of (mainly neutral) cold, isolated molecules, aggregates and metal complexes in the gas phase by applying UV- and combined IR/UV laser spectroscopic techniques in molecular beams, and partially supported by quantum chemical analyses. Using these methods, three main projects are described in this thesis. In the first project, spectroscopic investigations were performed in combination with a newly established laser desorption source. After successful optimization of this setup, the focus was put on the investigation of neutral isolated contact ion pairs, which presents still a new field in molecular beam spectroscopy. In the second project, aromatic molecule–solvent aggregates were investigated with regard to non-covalent (and especially dispersion) interactions. And finally in the last project, cationic clusters, formed by aggregation of monovalent metal ions (mainly aluminium) and the protected amino acid AcTrpOMe, were studied. For the latter subject, distinct theoretical approaches (mainly density functional theory (DFT)) were applied in addition to the spectroscopic investigations performed by former group members. In the following paragraphs, the corresponding projects are summarized in more detail.

### Laser desorption studies and spectroscopic characterization of contact ion pairs

The often pioneering gas phase experiments on neutral systems performed in the Gerhards group were usually conducted by using a thermal molecular beam source. However, molecules exhibiting an insufficient vapor pressure or a significant thermal lability cannot be transferred into the gas phase through simple heating. In such cases, the laser desorption technique is a convenient alternative. Such a laser desorption source was designed by the former group member Dr. Markus Becherer and implemented into one of the two molecular beam machines available in the Gerhards group. However, at the beginning of the present thesis, the experimental achievements were still limited to at most some mass spectra and no spectroscopic results were available. The obtained ion signals were weak in intensity and too unstable to perform spectroscopic investigation. Thus, some major experimental refinements were required.

First, the preparation of the used laser desorption samples was crucially optimized within this work. In the initial experiments, the respective compound was mixed with soot or graphite powder as matrix (in a ratio of approximately 1:1). The ion signal intensity was then increased by a factor of 3-4 and the ion signal stability was clearly improved using active charcoal powder as matrix. Furthermore, the expansion conditions were optimized, whereby it turned out that well-resolved UV- and IR spectra are

only obtained if argon is used as carrier gas for efficient supersonic cooling. Despite these crucial experimental improvements, the ion signal fluctuations were still too pronounced to record any useful IR/(1C-)R2PI spectra. Therefore, a so-called “reference signal correction” technique was established, which is very briefly described in the following lines. After crossing the molecular beam, the UV laser beam is redirected through the interaction region to ionize a second packet of molecules. Within that, the molecular beam is crossed at two slightly distinct heights (difference  $\sim 5$  mm), which leads to two clearly separated mass signals for the same  $m/z$ . The IR laser beam is spatially overlapped with the UV laser beam at the first interaction point with the molecular beam. At the same time, the “second” ion signal is untouched by the IR-radiation and is only subjected to the unavoidable ion signal fluctuations. Thus, the second mass peak can be used as “reference signal” in the data evaluation, in the way to account for ion signal fluctuations.

The described optimization steps were realized within investigations of *para*-aminobenzoic acid and its homodimer, as well as of the cyclic dipeptide cyclo Trp-Tyr. Hereby, the recorded spectra show nicely resolved resonances and are absolutely in accordance with literature data. This underlines that the experimental conditions had been successfully optimized. In the following, the next aim was to investigate larger organic molecules of higher  $m/z$ . For this, the cyclic depsipeptide beauvericin and in particular the calixarene derivatives 4-*tert*-butylcalix[6]arene and its smaller homologue 4-*tert*-butylcalix[4]arene were chosen. These compounds could all be successfully transferred into the gas phase and detected in the mass spectrometer. However, even after further optimization, the obtained ion signals were drastically smaller than for compounds with lower  $m/z$ . Furthermore, no clear and convincing features were found in the R2PI- and IR/R2PI experiments. Thus, the limits of the current experimental setup were probably gradually reached. Some suggestions regarding further technical optimizations are evoked in the last paragraph.

In the following, the focus was turned towards the investigation of neutral isolated contact ion pairs (CIPs), using the newly established laser desorption setup. Ion pairing plays a key role *e.g.* in biochemical processes or in catalysis. Up to now, most studies on CIPs were limited to condensed phase experiments, which are always underlying the fluctuations between different types of ion pairing (solvent separated ion pairs, solvent shared ion pairs,...) and interactions with the environment. Therefore, the intrinsic properties of ion pairs are not yet well understood for many systems. Within this context, the alkali (from  $\text{Li}^+$  to  $\text{Cs}^+$ ) *para*-aminobenzoate ion pairs were investigated by applying various spectroscopic approaches. First, one color R2PI spectra were recorded for all species, in which a small but considerable spectral red-shift of the electronic origin transition was observed towards ion pairs with heavier alkali ions. The same is valid for the IR/R2PI experiments (for the  $S_0$  state) in the NH-stretching region. By probing the vibrational frequency of the  $\text{NH}_2$  substituent in *para* position, the influence of a variation of the alkali ion could be analyzed. In addition, IR photodissociation spectra of

the photoionized ion pairs (in the  $D_0$  state) were recorded, whereby a blue-shift, and thus an opposite trend relative to the effects in the electronic ground state, was obtained. These inverse trends may not be provoked by pure electrostatic effects, but rather by electronic effects induced by the Coulomb potential of the metal ion. This interpretation is based on the results of a natural bond orbital (NBO) analysis performed at the DFT level. Particularly strong shifts (red-shift from  $\text{Li}^+$  to  $\text{Cs}^+$ ) by thousands of wavenumbers upon substitution of the alkali cation were observed for the ionization potentials, which were estimated by performing two color R2PI experiments. Over all, the measured trends are in perfect agreement with the results from DFT (and partially ADC(2)) calculations. Finally, the ion radius of the coordinating alkali ion turned out to be the most decisive factor for the spectroscopic behavior of the *para*-aminobenzoate chromophore. In order to increase molecular complexity and pave the way for studies on isolated metal complexes in the gas phase, the earth alkaline *para*-aminobenzoate complexes, (composed of the bivalent cation and two *para*-aminobenzoate anions), were investigated *via* R2PI spectroscopy. Here, the obtained spectra are fully in line with the observations made for the respective alkali species. In the following, these studies were extended to the alkali *para*-methoxybenzoate as well as to alkali benzoate ion pairs. For these species, R2PI spectra were recorded, which again show very sharp features. In contrast to the alkali *para*-aminobenzoate ion pairs, these species however exhibit a significantly reduced (photo)stability. A reduced mesomeric donor (+M) effect exhibited by the substituent in *para*-position goes along with a lowered cation...anion binding energy and thus with a decreased ion pair stability. Therefore, merely one color R2PI experiments could be performed here, that are partly limited to the respective ion pairs with smaller cations. The observed vibronic resonance shifts could not be understood to full extent up to now, but it was observed that the spectral shifts upon cation substitution are most pronounced for the alkali benzoate species. This may again be due to the absence of any substituent exhibiting a mesomeric donor effect in *para*-position.

On top of all this, the neutral OLED relevant complex tris(8-hydroxyquinolato)aluminium ( $\text{Alq}_3$ ) could be successfully desorbed, subsequently photoionized and detected in the time-of-flight mass spectrometer.

#### Ketone-solvation balances with regard to non-covalent interactions

The second topic of this thesis dealt with the spectroscopic investigation of isolated aromatic molecule–solvent clusters with regard to non-covalent interactions. These studies were performed within the DFG priority program on the “Control of London dispersion in molecular chemistry” (SPP 1807). Within that, one aim is the quantification of non-covalent and especially dispersion interactions. Since theoretical methods often struggle with the description of subtle energetic differences,

spectroscopic data on small isolated model aggregates are at the same time convenient benchmark values. In this way, theoretical approaches can be evaluated and further refined or newly developed. In the past, in-depth studies on so-called “solvation balances” had been performed on the example of aromatic ether–alcohol aggregates. In the following, these studies were extended to ketone-solvation balances, featuring two very similar carbonyl docking sites for an alcohol molecule. Hereby, the preference for a specific structural arrangement is decided by non-covalent interactions with neighboring aromatic or alkyl moieties. Studies on carbonyl–solvent clusters have the further advantage that the competing isomers are both of C=O⋯H-O type, which leads to an almost error cancellation for the zero point vibrational energy (ZPVE). Several analyses on such systems had already been performed (among others within the SPP), but up to that point all investigations on ketone–alcohol aggregates were limited to clusters in their electronic ground state.

Within this context, studies on chromone–methanol clusters were performed here. The structure of chromone exhibits two very similar carbonyl oxygen lone pairs as docking sites, in which the methanol molecule is stabilized *via* distinct (either 1,2- or 1,3-like) CH⋯O contacts. Since chromone undergoes a fast and efficient intersystem crossing (ISC) into the triplet manifold upon electronic excitation, spectroscopic investigations could for the first time be applied to a neutral cluster in its lowest excited triplet state ( $T_1$ ). Although (especially larger) chromone–methanol clusters tended to undergo fragmentation, *i.e.*, evaporative cooling, upon ISC into the triplet manifold, it could be demonstrated here that the UV/IR/UV technique can be applied to investigate neutral clusters in an electronically excited triplet state. Hereby, these experiments may be supported by the mentioned evaporative cooling process. Since this lowest triplet state is of ground state character, sophisticated energy decomposition approaches such as SAPT (symmetry-adapted perturbation theory) and DLPNO-CCSD(T)/LED (local energy decomposition domain-based local pair natural orbital coupled-cluster method) could be applied. Extensive theoretical analyses were performed by my colleagues Patrick Strebert and Marcel Meta. The IR/R2PI experiments, in combination with the calculated harmonic frequencies, confirm the occurrence of both competing isomers in the molecular beam, whereby the energetically favored motif with an 1,2-like CH⋯O contact seems to have a higher contribution. Similar structural arrangements and isomer populations are maintained after electronic excitation and subsequent ISC. Interestingly, the excited state geometry optimizations however unveiled a loss of planarity (puckering) of the 4-pyrone ring when reaching the  $T_1$  state, with the spin-density being mostly localized on the puckered C atom. This structural effect leads to an increased energetic gap between both minimum structures. Finally, the energy decomposition analyses revealed that this energetic effect (increase of  $\Delta E$ ) is mainly driven by electrostatic and inductive interactions rather than by dispersion forces.



Alongside the studies on chromone–methanol, the aggregation of the protected amino acid AcTyr(Me)OMe with methanol was also investigated. Amino acid– or small peptide–solvent clusters are again convenient model systems to study the delicate interplay of non-covalent interactions. Furthermore, these systems give the possibility to probe potential structural rearrangements of peptide structures upon stepwise microsolvation. As the polar N- and C-termini are capped within protected amino acids such as AcTyr(Me)OMe, these model systems are ideally suited to explore peptide backbone solvations. Particularly, a solvent molecule (such as water or an alcohol) may only interact with the NH and CO groups of the backbone or with the  $\pi$ -system of the protected tyrosine (Tyr) residue. However, for the AcTyr(Me)OMe–methanol aggregate, the IR/R2PI spectra recorded in the NH- and OH-stretching region suggest the dominance of only one specific isomer in the molecular beam. Finally, a structure with the methanol molecule being coordinated to both the NH and ester C=O groups is suggested. Thus, the OH group of the methanol molecule simultaneously acts as hydrogen bond donor (towards C=O) and acceptor, whereby the initially stretched backbone ( $\beta_L$ ) conformation of AcTyr(Me)OMe is maintained.

#### Investigations of metal ion–peptide interactions

In the last part of this thesis, structural investigations on the cationic aggregate of monovalent aluminium ( $Al^+$ ) and the protected amino acid AcTrpOMe were performed. In nature, a vast number of proteins coordinate metal atoms to form so-called metalloproteins, with the biomolecular function of such a complex often critically depending on its structural arrangement. The role of  $Al^+$  in nature is of course questionable, but its low stability (compared to *e.g.* alkali cations), in combination with the relatively high reactivity of the indole chromophore of tryptophane, could lead to unique and maybe unexpected structural effects. Indeed, the performed conformational search yielded, among others, an extraordinary geometry, in which the  $Al^+$  ion is inserted into the N–H bond of the Trp residue and at the same time linked to both carbonyl groups of the backbone. One should note that this structural motif is (according to DFT-D3 and DLPNO-CCSD(T)) even one of the energetically most favored geometries. Transition state optimizations revealed that this “inserted” structure may not be formed within an isomerization process in the cold molecular beam. Nevertheless, such a strong rearrangement within the harsh plasma conditions of the used combined thermal and laser ablation source remains conceivable. Furthermore, the harmonic vibrational frequencies predicted for this geometry are principally in accordance with the experimental IR+UV spectrum, measured by the former group members Dr. Philip Bialach and Dr. Markus Becherer. The experiment also shows that a further isomer has to be present in the molecular beam. Here, a structural motif with the  $Al^+$  ion being linked to both backbone C=O groups was assigned. In order to elucidate if the discussed unexpected

structural motif with an insertion of the metal cation into the indolic NH bond may be unique to aggregates with  $\text{Al}^+$ , the DFT studies were extended to a series of clusters with other monovalent metal ions ( $\text{Li}^+$ ,  $\text{Na}^+$ ,  $\text{K}^+$ ,  $\text{Rb}^+$ ,  $\text{Cs}^+$ ,  $\text{Mg}^+$ ,  $\text{Ti}^+$ ,  $\text{Zn}^+$ ,  $\text{Ag}^+$ ,  $\text{Ga}^+$ ). These calculations predicted that such an “inserted” geometry may only be favored in combination with  $\text{Al}^+$  or  $\text{Ti}^+$ .

### Outlook

With respect to future molecular beam studies, it can be noted that promising results were obtained within this work, especially regarding the laser desorption experiments. The first spectroscopic studies using the laser desorption setup can definitely be considered as an experimental breakthrough in the Gerhards group. The extended investigations on alkali *para*-aminobenzoate ion pairs yielded unambiguous spectral effects that may trigger further studies on these systems as well as on related analytes. For instance, the IR/UV experiments could be extended to the CO-stretching region, as pronounced spectral shifts upon substitution of the alkali ion are expected for this spectral region. Furthermore, the (micro)solvation of the alkali *para*-aminobenzoates could be investigated by *e.g.* probing their respective hydrate clusters, to elucidate (possible) separation mechanisms between cation and anion upon attachment of water molecules. Beyond that, analyses on the alkali *ortho*- and alkali *meta*-aminobenzoate derivatives may also be of interest.

However, the performed measurements at the same time unveiled technical limits, showing which further refinements could be beneficial. In particular, the R2PI- and IR/R2PI experiments on molecules of higher molecular weight turned out to be difficult. This limitation could be due to inefficient vibrational cooling of these large molecules, exhibiting a bath of low-frequency modes. Therefore, alternative pulsed valve types, designed for the application of higher backing pressures, shorter opening times (*e.g.* piezo valves) and thus providing particularly cold expansion conditions, may be applied. It should, however, be pointed out that the successful desorption, subsequent photoionization and detection of a larger metal complex promises a high potential for future investigations on neutral metal complexes in the gas phase by using laser desorption setups.

The other topics treated in the present thesis demonstrate that further studies on aggregates in electronically excited triplet states could be performed and that clusters comprising monovalent aluminium ions may be of particular interest for future research.

## 9 Zusammenfassung und Ausblick

Die vorliegende Arbeit befasst sich mit der Untersuchung von (insbesondere neutralen) kalten, isolierten Molekülen, Aggregaten und Metallkomplexen in der Gasphase mittels UV- und kombinierter IR/UV-Laserspektroskopie im Molekularstrahl. Die Arbeit setzt sich im Wesentlichen aus drei Teilprojekten zusammen. Im ersten Teil wurden erste spektroskopische Untersuchungen in Kombination mit einer neu etablierten Laserdesorptionsquelle durchgeführt. Nach erfolgreicher Optimierung dieses Aufbaus wurde der Fokus auf die Analyse neutraler isolierter Kontaktionenpaare gelegt, die ein noch neues Feld in der Molekularstrahlspektroskopie darstellen. Im zweiten Projekt wurden Aggregate, bestehend aus einem aromatischen Molekül und einem Lösungsmittelmolekül, im Hinblick auf nicht-kovalente (und insbesondere Dispersions-) Wechselwirkungen untersucht. Im letzten Teil wurden kationische Cluster analysiert, die durch Aggregation von einwertigen Metallionen (insbesondere Aluminium) und der geschützten Aminosäure AcTrpOMe gebildet werden. Diesbezüglich wurden, komplementär zu den von ehemaligen Gruppenmitgliedern durchgeführten spektroskopischen Untersuchungen, verschiedene theoretische Ansätze (hauptsächlich Dichtefunktionaltheorie (DFT)) angewandt. In den folgenden Abschnitten werden die unterschiedlichen Teilprojekte ausführlicher zusammengefasst.

### Experimente mittels Laser-Desorption und spektroskopische Charakterisierung von Kontaktionenpaaren

Die oft initiierten Gasphasenexperimente an neutralen Systemen, die im Arbeitskreis von Prof. Gerhards durchgeführt wurden, wurden alle mit Hilfe einer thermischen Molekularstrahlquelle realisiert. Allerdings können Moleküle, die einen unzureichenden Dampfdruck oder eine signifikante thermische Labilität aufweisen, nicht durch einfaches Erhitzen in die Gasphase überführt werden. In diesen Fällen stellt die Technik der Laserdesorption eine geeignete Alternative dar. In dem Zusammenhang wurde vom ehemaligen Mitarbeiter Dr. Markus Becherer eine solche Laser-Desorptionsquelle entwickelt und in eine der in der Arbeitsgruppe vorhandenen Molekularstrahlapparaturen implementiert. Jedoch beschränkten sich die experimentellen Ergebnisse bis zu Beginn der vorliegenden Arbeit auf höchstens ein paar Massenspektren, wobei die detektierten Ionensignale zu schwach und zu instabil waren für tiefgründigere spektroskopische Untersuchungen. Somit waren bedeutende experimentelle Anpassungen unabdingbar.

Bezüglich der Laserdesorption wurde die Probenvorbereitung im Rahmen dieser Arbeit entscheidend optimiert. In den ersten Experimenten wurde die jeweilige Verbindung mit Ruß- oder Graphitpulver

als Matrix gemischt (in einem Verhältnis von etwa 1:1). Es stellte sich jedoch heraus, dass die Ionensignalintensität um den Faktor 3-4 höher ist und die Stabilität des Ionensignals bedeutend besser ist, wenn Aktivkohlepulver als Matrix verwendet wird. Weiterhin wurden die Expansionsbedingungen optimiert, wobei gut aufgelöste UV- und IR-Spektren nur unter Verwendung von Argon als Trägergas für eine effiziente adiabatische Abkühlung erreicht wurden. Trotz dieser entscheidenden experimentellen Verbesserungen waren die Fluktuationen der Ionensignale immer noch zu ausgeprägt, um aussagekräftige IR/(1C-)R2PI-Spektren aufzunehmen. Daraufhin wurde eine sogenannte „Referenzsignal-Korrektur“ eingeführt, die in folgenden Zeilen kurz beschrieben wird. Nachdem der UV-Laserstrahl den Molekularstrahl durchquert hat, wird er umgelenkt und ein zweites Mal mit dem Molekularstrahl überlappt, um ein zweites Molekülpaket zu ionisieren. Dabei wird der Molekularstrahl in zwei leicht unterschiedlichen Höhen gekreuzt (Unterschied  $\sim 5$  mm), was zu zwei klar separierten Massensignalen für dasselbe Masse-zu-Ladung-Verhältnis ( $m/z$ ) führt. Der IR-Laserstrahl wird am ersten Kreuzungspunkt von Molekularstrahl und UV-Laserstrahl mit dem UV-Laserstrahl überlappt. Gleichzeitig bleibt das „zweite“ Ionensignal von der IR-Strahlung unberührt und ist nur den unvermeidlichen Ionensignalschwankungen unterworfen. Somit kann der zweite Massenpeak als „Referenzsignal“ bei der Datenauswertung verwendet werden, um auf diese Weise die Ionensignalschwankungen zu berücksichtigen.

Die beschriebenen Optimierungsschritte wurden im Rahmen von Untersuchungen an *para*-Aminobenzoesäure und deren Homodimer, sowie am cyclischen Dipeptid cyclo Trp-Tyr durchgeführt. Hierbei zeigen die aufgenommenen Spektren gut aufgelöste Resonanzen und stimmen absolut mit Literaturdaten überein. Dies unterstreicht die erfolgreiche Optimierung der experimentellen Bedingungen. Das nächste Ziel bestand darin, größere organische Moleküle mit höherem  $m/z$  zu untersuchen. Hierfür wurden das cyclische Depsipeptid Beauvericin und insbesondere die Calixaren-Derivate 4-*tert*-Butylcalix[6]aren sowie dessen kleineres Homolog 4-*tert*-Butylcalix[4]aren ausgewählt. Diese Verbindungen konnten alle erfolgreich in die Gasphase überführt werden und im Massenspektrometer nachgewiesen werden. Doch auch nach weiterer Optimierung waren die erhaltenen Ionensignale deutlich kleiner als für Verbindungen mit niedrigem  $m/z$ . Außerdem waren in den R2PI- und IR/R2PI-Experimenten keine eindeutigen Resonanzeffekte festzustellen. Somit waren die Grenzen des derzeitigen Versuchsaufbaus wohl allmählich erreicht. Einige Vorschläge bezüglich weiterer technischer Optimierungen werden im letzten Absatz erläutert.

Im Folgenden wurde der Fokus auf die Untersuchung von neutralen, isolierten Kontaktionenpaaren (CIPs) gerichtet, wozu der neu etablierte Laser-Desorptions-Aufbau verwendet wurde. Die Ionenpaarung spielt zum Beispiel in biochemischen Prozessen oder in der Katalyse eine wichtige Rolle. Bislang beschränkten sich die meisten Studien zu CIPs jedoch auf Experimente in kondensierter Phase, die stets Fluktuationen zwischen verschiedenen Arten von Ionenpaaren (durch das Lösungsmittel

separiertes Ionenpaar (SSIPs), Ionenpaar mit einer einzelnen Solvatschicht zwischen Kation und Anion (SIPs),...) und Wechselwirkungen mit der Umgebung unterliegen. Daher sind die intrinsischen Eigenschaften von Ionenpaaren für viele Systeme noch nicht gut verstanden. In diesem Zusammenhang wurden die Alkali-Ionenpaare (von  $\text{Li}^+$  bis  $\text{Cs}^+$ ) des *para*-Aminobenzoats mit Hilfe verschiedener spektroskopischer Ansätze untersucht. Zunächst wurden für alle Spezies einfarbige R2PI-Spektren aufgenommen, bei denen von den Ionenpaaren mit kleinem Kation ( $\text{Li}^+$ ) hin zu den Spezies mit größerem Kation ( $\text{Cs}^+$ ) eine kleine aber bedeutende Rotverschiebung des ersten reinen elektronischen Übergangs (ohne Schwingungsanregung) zu sehen war. Das Gleiche gilt für die IR/R2PI-Experimente (für den  $S_0$ -Zustand) im NH-Streckschwingungsbereich. Indem im Experiment die Schwingungsfrequenzen des  $\text{NH}_2$ -Substituenten in *para*-Position abgefragt wurden, konnten die Auswirkungen einer Substitution des Alkaliions in größerer Entfernung zum Metallion analysiert werden. Zusätzlich dazu wurden IR-Photodissoziationsspektren der photoionisierten Ionenpaare (im  $D_0$ -Zustand) aufgenommen, wobei, im Gegensatz zu den Effekten im elektronischen Grundzustand, eine Blauverschiebung festgestellt wurde. Hierbei sind die entgegengesetzten Trends wahrscheinlich nicht auf rein elektrostatische Effekte zurückzuführen, sondern auf elektronische Effekte, die durch das Coulomb-Potential des Metallions hervorgerufen werden. Diese Interpretation stützt sich unter anderem auf die Ergebnisse einer auf DFT-Niveau durchgeführten „Natural Bond Orbital“ (NBO)-Analyse. Besonders starke Verschiebungen (Rotverschiebung von  $\text{Li}^+$  zu  $\text{Cs}^+$ ) um mehrere tausend Wellenzahlen bei Substitution des Alkaliions wurden für die Ionisierungspotentiale beobachtet, die in zwei Farben R2PI-Experimenten abgeschätzt wurden. Alles in allem stehen die gemessenen Trends in perfekter Übereinstimmung mit den Ergebnissen aus DFT- (und teilweise ADC(2))-Rechnungen. Schlussendlich erwies sich der Ionenradius des koordinierenden Alkaliions als der entscheidende Faktor für das spektroskopische Verhalten des *para*-Aminobenzoat-Chromophors. Um einen weiteren Schritt in Richtung von Studien an isolierten Metallkomplexen in der Gasphase zu machen, wurden die Erdalkali-*para*-aminobenzoat-Komplexe (bestehend aus dem zweiwertigen Kation und zwei *para*-aminobenzoat-Anionen) mittels R2PI-Spektroskopie untersucht. Die hierbei gemessenen Spektren stimmen sehr gut mit den Beobachtungen, wie sie bei den entsprechenden Alkali-Spezies gemacht wurden, überein. Im Folgenden wurden diese Studien auf die Alkali-*para*-methoxybenzoate sowie auf die Alkali-benzoate ausgedehnt. Für diese Spezies wurden R2PI-Spektren aufgenommen, die ebenfalls sehr scharfe Resonanzen aufweisen. Im Gegensatz zu den Alkali-*para*-Aminobenzoat-Ionenpaaren weisen diese Spezies jedoch eine deutlich geringere (Photo)stabilität auf. Ein schwächerer elektronenschiebender mesomerer Donoreffekt (+M-Effekt) des Substituenten in *para*-Stellung geht mit einer verringerten Kation-Anion-Bindungsenergie und somit mit einer verringerten Ionenpaar-Stabilität einher. Daher konnten für die letztgenannten Spezies lediglich einfarbige R2PI-Experimente durchgeführt werden, die teilweise auf die jeweiligen Ionenpaare mit kleineren Kationen beschränkt

sind. Die beobachteten Verschiebungen vibronischer Übergänge konnten bisher nicht in vollem Umfang verstanden werden. Trotzdem wurde deutlich, dass die spektralen Verschiebungen bei Substitution des Kations für die Alkalibenzoat-Spezies am stärksten ausgeprägt sind. Dies ist womöglich auf das Fehlen eines Substituenten mit einem mesomeren Donoreffekt (+M-Effekt) in *para*-Position zurückzuführen.

Darüber hinaus konnte der neutrale OLED-relevante Komplex Tris(8-hydroxychinolinato)aluminium ( $\text{Alq}_3$ ) erfolgreich desorbiert, anschließend photoionisiert und im Flugzeitmassenspektrometer nachgewiesen werden.

#### „Keton-Lösungsmittel-Waagen“ in Bezug auf nicht-kovalente Wechselwirkungen

Das zweite Thema dieser Arbeit befasste sich mit der spektroskopischen Untersuchung von isolierten aromatischen Molekül-Lösungsmittel-Clustern im Hinblick auf nicht-kovalente Wechselwirkungen. Diese Untersuchungen wurden im Rahmen des DFG-Schwerpunktprogramms SPP 1807 mit dem Titel „Control of London dispersion in molecular chemistry“ durchgeführt. Ein Hauptziel dabei ist die Quantifizierung von nicht-kovalenten und insbesondere von Dispersions-Wechselwirkungen. Da theoretische Methoden bei der Beschreibung subtiler Energieunterschiede oft an ihre Grenzen stoßen, stellen spektroskopische Daten zu kleinen molekularen Clustern gleichzeitig geeignete Referenzsysteme („benchmarks“) dar. Auf diese Weise können theoretische Methoden evaluiert und weiterentwickelt werden. In der Vergangenheit wurden in der Arbeitsgruppe am Beispiel von aromatischen Ether-Alkohol-Aggregaten bereits vertiefte Studien an sogenannten „Solvations-Waagen“ („solvation balances“) durchgeführt. In der Folgezeit wurden diese Untersuchungen auf „Keton-Lösungsmittel-Waagen“ ausgedehnt, welche zwei sehr ähnliche Carbonyl-Andockstellen für ein Alkoholmolekül aufweisen. Bei diesen Systemen wird die Präferenz für eine spezifische strukturelle Anordnung durch nicht-kovalente Wechselwirkungen mit benachbarten aromatischen Gruppen oder Alkylgruppen bestimmt. In dem Zusammenhang wurden bereits mehrere Untersuchungen an derartigen Systemen durchgeführt (unter anderem im Rahmen des SPP), die sich bisher aber alle auf die Analyse von Clustern im elektronischen Grundzustand beschränkten.

In dem Kontext wurden hier Untersuchungen an Chromon-Methanol-Clustern durchgeführt. Die Struktur von Chromon weist zwei sehr ähnliche freie Elektronenpaare am Carbonylsauerstoff als Andockstellen auf, womit die entsprechenden Alkohol-Komplexe entweder über 1,2- oder 1,3-ähnliche  $\text{CH}\cdots\text{O}$ -Kontakte stabilisiert werden. Da Chromon nach elektronischer Anregung über einen besonders schnellen und effizienten Interkombinationsprozess (ISC) in die Triplet-Mannigfaltigkeit übergeht, konnten erstmalig spektroskopische Untersuchungen an einem neutralen Cluster in seinem niedrigsten angeregten Triplett-Zustand ( $T_1$ ) durchgeführt werden. Obschon (insbesondere die

größeren) Chromon–Methanol-Aggregate nach ISC in die Triplet-Mannigfaltigkeit zur Fragmentation, das heißt zur Abspaltung von Lösungsmittelmolekülen („evaporative cooling“) neigen, konnte hier gezeigt werden, dass die UV/IR/UV-Technik zur Untersuchung neutraler Cluster in einem elektronisch angeregten Triplett-Zustand eingesetzt werden kann. Dabei kann es sein, dass die Experimente durch den „evaporative cooling“-Prozess unterstützt werden. Da dieser niedrigste Triplett-Zustand Grundzustandscharakter aufweist, konnten aufwendige theoretische Methoden, wie SAPT (symmetry-adapted perturbation theory) und DLPNO-CCSD(T)/LED (local energy decomposition domain-based local pair natural orbital coupled-cluster method), zur Zerlegung der Gesamtenergie in einzelne Energiebeiträge angewandt werden. Umfangreiche theoretische Analysen wurden von meinen Kollegen Patrick Strebert und Marcel Meta durchgeführt. Die IR/R2PI-Experimente, in Kombination mit den berechneten harmonischen Frequenzen, bestätigen die Koexistenz beider konkurrierender Isomere im Molekularstrahl, wobei das energetisch bevorzugte Motiv mit einem 1,2-ähnlichen CH...O-Kontakt einen größeren Beitrag zu haben scheint. Ähnliche strukturelle Anordnungen und Isomerenpopulationen wurden nach elektronischer Anregung und anschließendem ISC beobachtet. Interessanterweise enthüllten die Geometrieoptimierungen im angeregten  $T_1$ -Zustand jedoch einen Verlust der Planarität („puckering“) des 4-Pyron-Rings, wobei die Spindichte hauptsächlich auf dem „gepuckerten“ C-Atom lokalisiert ist. Dieser strukturelle Effekt führt zu einem vergrößerten energetischen Abstand zwischen den beiden Minimumstrukturen. Die Zerlegung in einzelne Energiebeiträge ergab schließlich, dass dieser energetische Effekt (Vergrößerung von  $\Delta E$ ) nicht durch Dispersionskräfte, sondern in erster Linie durch elektrostatische und induktive Wechselwirkungen verursacht wird.

Neben den Studien zu Chromon–Methanol wurde auch die Aggregation der geschützten Aminosäure AcTyr(Me)OMe mit Methanol untersucht. Cluster aus einer Aminosäure oder einem kleinen Peptid und einem Lösungsmittelmolekül sind ebenfalls geeignete Modellsysteme, um das sensitive Zusammenspiel nicht-kovalenter Wechselwirkungen zu untersuchen. Außerdem bieten diese Systeme die Möglichkeit potenzielle strukturelle Umlagerungen von Peptidstrukturen bei schrittweiser Mikrosolvatation zu untersuchen. Da die polaren N- und C-Termini in geschützten Aminosäuren wie AcTyr(Me)OMe verkappt sind, eignen sich diese Modellsysteme ideal für die Untersuchung von Peptidrückgrat-Solvatationen. Konkret kann ein Lösungsmittelmolekül (wie Wasser oder ein Alkohol) nur mit den NH- und CO-Gruppen des Rückgrats oder mit dem  $\pi$ -System des geschützten Tyrosin (Tyr)-Rests wechselwirken. Für das AcTyr(Me)OMe–Methanol-Aggregat deuten die IR/R2PI-Spektren im NH- und OH-Streckschwingungsbereich auf die Bildung eines einzigen Isomers im Molekularstrahl hin. Schlussendlich wird eine Struktur vorgeschlagen, bei der das Methanolmolekül sowohl an die NH-Gruppe als auch an die C=O-Gruppe des Esters koordiniert ist. Somit fungiert die OH-Gruppe des Methanols gleichzeitig als Wasserstoffbrücken-Donor (an die C=O-Gruppe) und -Akzeptor (an die N-H-

Gruppe), wobei die ursprünglich gestreckte Rückgratkonformation ( $\beta_L$ ) von AcTyr(Me)OMe erhalten bleibt.

#### Untersuchungen von Metall–Peptid-Wechselwirkungen

Im letzten Teil dieser Arbeit wurden strukturelle Untersuchungen am kationischen Aggregat aus einwertigem Aluminium ( $Al^+$ ) und der geschützten Aminosäure AcTrpOMe durchgeführt. In der Natur koordinieren eine Vielzahl von Proteinen Metallatome und bilden dabei sogenannte Metalloproteine, wobei die biomolekulare Funktion eines solchen Komplexes oft entscheidend von seiner Struktur abhängig ist. Die Rolle von  $Al^+$  in der Natur ist natürlich fraglich, jedoch könnte dessen geringe Stabilität (im Vergleich mit beispielsweise Alkalikationen) in Verbindung mit der relativ hohen Reaktivität des Indol-Chromophors von Tryptophan zu besonderen strukturellen Effekten führen. In der Tat hat die Konformerensuche unter anderem eine außergewöhnliche Geometrie ergeben, bei der das  $Al^+$ -Ion in die NH-Bindung des Trp-Rests inseriert und gleichzeitig an beide Carbonylgruppen des Rückgrats gebunden ist. Dabei ist hervorzuheben, dass dieses Strukturmotiv (nach DFT-D3 und DLPNO-CCSD(T)) sogar eine der energetisch günstigsten Geometrien darstellt. Laut theoretischer Berechnungen wird bei der Bildung dieser Spezies ein energiereicher Übergangszustand durchlaufen, womit diese „insertierte“ Struktur wohl nicht in einem Isomerisierungsprozess im kalten Molekularstrahl gebildet werden kann. Dennoch ist eine derartige strukturelle Änderung unter den harschen Plasmabedingungen der verwendeten kombinierten Thermo-Laserablationsquelle denkbar. Darüber hinaus stimmen die für diese Geometrie vorhergesagten harmonischen Schwingungsfrequenzen prinzipiell mit dem experimentellen IR+UV-Spektrum, welches von den ehemaligen Gruppenmitgliedern Dr. Philip Bialach und Dr. Markus Becherer gemessen wurde, überein. Das Experiment zeigt auch, dass ein weiteres Isomer im Molekularstrahl vorhanden sein muss. Hier wurde ein strukturelles Motiv zugeordnet, bei dem das  $Al^+$ -Ion an beide C=O-Gruppen des Rückgrats gebunden ist. Um zu klären, ob das diskutierte unerwartete strukturelle Motiv mit einer Insertion des Metallkations in die indolische NH-Bindung nur im Fall von Aggregaten mit  $Al^+$  vorkommt, wurden die DFT-Studien auf eine Reihe von Clustern mit anderen einwertigen Metallionen ( $Li^+$ ,  $Na^+$ ,  $K^+$ ,  $Rb^+$ ,  $Cs^+$ ,  $Mg^+$ ,  $Ti^+$ ,  $Zn^+$ ,  $Ag^+$ ,  $Ga^+$ ) ausgedehnt. Diese Rechnungen haben gezeigt, dass eine solche „insertierte“ Geometrie lediglich in Kombination mit  $Al^+$  oder  $Ti^+$  bevorzugt gebildet wird.



## Ausblick

Im Hinblick auf zukünftige Molekularstrahlstudien kann festgehalten werden, dass im Rahmen dieser Arbeit vielversprechende Ergebnisse erzielt wurden, insbesondere was Experimente mit der Laserdesorptionsquelle angeht. Die ersten spektroskopischen Untersuchungen mit dem Laserdesorptionsaufbau können durchaus als experimenteller Durchbruch im Arbeitskreis von Prof. Gerhards angesehen werden. Die ausgedehnten Experimente an Alkali-*para*-aminobenzoat-Ionenpaaren ergaben eindeutige spektrale Effekte, die als Ansporn für weitere Untersuchungen an diesen Systemen sowie an verwandten Analyten dienen können. Zum Beispiel könnten die IR/UV-Experimente auf den CO-Streckschwingungsbereich ausgedehnt werden, da für diesen Spektralbereich ausgeprägte spektrale Verschiebungen bei der Substitution des Alkaliions zu erwarten sind. Darüber hinaus könnte die (Mikro-)Solvatation der Alkali-*para*-Aminobenzoate analysiert werden, indem beispielsweise deren Hydratcluster spektroskopiert werden, um (mögliche) Trennungsmechanismen zwischen Kation und Anion bei Anlagerung von Wassermolekülen aufzuklären. Außerdem können auch Untersuchungen an den Derivaten Alkali-*ortho*- sowie Alkali-*meta*-aminobenzoat von Interesse sein. Gleichzeitig enthüllen diese Messungen aber auch technische Grenzen, die zeigen welche weiteren experimentellen Anpassungen sinnvoll sein könnten. Insbesondere die R2PI- und IR/R2PI-Experimente an Molekülen mit höherem Molekulargewicht haben sich als problematisch erwiesen. Diese Beschränkung könnte auf eine unzureichende Schwingungsabkühlung dieser großen Moleküle zurückzuführen sein, die eine Vielzahl von niederfrequenten Moden aufweisen. Daher wäre es durchaus sinnvoll alternative Pulsdüsentypen einzusetzen, die für die Verwendung höherer Hintergründrücke und kürzerer Öffnungszeiten ausgelegt sind (zum Beispiel Piezoventile), um auf die Weise besonders kalte Expansionsbedingungen zu erreichen. Es ist jedoch auch hervorzuheben, dass die erfolgreiche Desorption, die anschließende Photoionisierung und der Nachweis eines größeren Metallkomplexes das hohe Potenzial für zukünftige Untersuchungen an neutralen Metallkomplexen in der Gasphase mittels Laserdesorption darlegen. Die anderen in dieser Arbeit behandelten Themen zeigen, dass weitere Studien an Aggregaten in elektronisch angeregten Triplett-Zuständen greifbar sind und dass Cluster, die monovalente Aluminiumionen enthalten, von besonderem Interesse für die zukünftige Forschung sein könnten.

## Conference contributions

### **DPG Conference SAMOP Kaiserslautern (virtually), 20. – 24.09.2021**

“Combined IR/UV spectroscopic investigations on neutral isolated ion pairs in a molecular beam”,  
Talk

### **Busentagung Regensburg (virtually), 10. – 12.05.2021**

“Combined IR/UV spectroscopic and quantum chemical studies on chromone/methanol aggregates –  
investigation of dispersion interactions”, Poster

### **Horizons in Hydrogen Bond Research (HBOND2019), Amsterdam, 24. – 27.09.2019**

“Investigation of isolated aggregates of coumarin derivatives in the gas phase by applying combined  
IR/UV spectroscopy”, Poster

# Lebenslauf

**Pol Jean Boden**

## **Ausbildung:**

10 / 2018 – Heute	Promotion TU Kaiserslautern, Physikalische Chemie
10 / 2016 – 09 / 2018	Masterstudium Chemie, TU Kaiserslautern, Vertiefung in Physikalischer Chemie, Abschlussarbeit: „Laser-Desorption und theoretische Berechnungen an neutralen Übergangsmetallhaltigen Clustern und Untersuchung von $[Al(AcTrpOMe)]^+$ “
10 / 2013 – 09 / 2016	Bachelorstudium Chemie, TU Kaiserslautern, Abschlussarbeit in Physikalischer Chemie: „Untersuchung von Eisen(II)-Komplexen mit N-heterocyclischen Carben Liganden mittels Fluoreszenz- und Absorptionsspektroskopie“
09 / 2006 – 07 / 2013	Gymnasium in Mersch bzw. Diekirch (Luxemburg)
09 / 2000 – 07 / 2006	Grundschule in Mersch (Luxemburg)